

Dissertation

Minderung von Schallausbreitung durch Mikroperforierte Absorber in unterschiedlichen Schallfeldarten - Design und Evaluierung

ausgeführt zum Zwecke der Erlangung des akademischen Grades
eines Doktors der technischen Wissenschaften unter der Leitung von

Univ.-Prof. Dipl.-Ing. Dr.techn. Manfred Kaltenbacher
Institut für Grundlagen und Theorie der Elektrotechnik
TU Graz

eingereicht an der Technischen Universität Wien
Fakultät für Maschinenwesen und Betriebswissenschaften

von

Dipl.-Ing. Sebastian Floß

Mat.Nr. 01027524



Wien, Januar 2022

Kurzfassung

Lärm in von Menschen bewohnten Räumen ist zu einer immer größeren Herausforderung geworden. Bei der Auslegung von Maschinen spielt die Betrachtung der Schallemissionen in der Regel eine untergeordnete Rolle, und erst wenn sie im Betrieb als "zu laut" wahrgenommen werden, kommt die Akustik ins Spiel. In solchen Fällen werden üblicherweise die standardmäßigen schaum- oder faserbasierten Dämpfungsmaterialien in zu großem Maße eingesetzt. Besonders bei Anwendungen in Klimaanlageanlagen können diese Materialien unter starken Nutzeneinbußen leiden, wenn sie Wasser und Staubpartikeln ausgesetzt sind, und das Anbringen von Schutzmaßnahmen, welche die Langlebigkeit erhöhen sollen, die akustische Performance deutlich reduziert. Metallbasierte mikroperforierte Absorber (MPA) bieten eine Alternative, um Lärmprobleme vor Ort oder generisch zu lösen. Sie können in gefährlichen Umgebungen eingesetzt und umweltfreundlich aus Metallschrott recyclebar hergestellt werden. Um eine generische und genaue Auslegung der Absorber für spezifische Lärmprobleme zu ermöglichen, sollte die akustische Leistung im Voraus durch Simulationen mit nur geringer Abweichung von der gemessenen Schallreduzierung bewertet werden. In dieser Arbeit wurde ein auf dem Johnson-Champoux-Allard-Lafarge-Modell basierender Ansatz entwickelt und auf MPAs angewandt. Die Grundlage bildet die Ermittlung äquivalenter akustischer Materialparameter aus Impedanzrohrmessungen durch inverse Anpassung mit einem genetischen Evolutionsalgorithmus. Mit diesen Parametern werden dedizierte MPA-Designs in hochdiffusen Schallfeldern bis zu 8 kHz getestet. Die Anwendbarkeit des Ansatzes und die Leistung verschiedener MPA-Konfigurationen werden anhand von Simulationen und Beispielen demonstriert. Die Untersuchungen erlauben es auch, bestimmte Designempfehlungen in Abhängigkeit vom Frequenzbereich zu geben.

Da eine der möglichen Anwendungen mikroperforierter Absorber in Klimaanlageanlagen liegt, wurde die Dämpfungsleistung eines MPA unter Strömungsbedingungen und in direkter Nähe zu einem Niederdruck-Axialventilator untersucht. Die Messungen ergaben, dass sich die Wirksamkeit des MPA in Abhängigkeit von der relativen Position zum Ventilator stark verändert. Auch die aerodynamische Leistung des Ventilators hängt von den konstruktiven Details des MPA ab. Unter bestimmten Bedingungen emittiert der mikroperforierte Absorber auch Schall. Diese Bedingungen wurden untersucht und es zeigte sich, dass das akustische Leistungsspektrum des Absorbers auch den Pegel der Eigengeräuschemissionen unter Strömungsbedingungen bestimmt.

Ehrenwörtliche Erklärung

Ich nehme zur Kenntnis, dass ich zur Drucklegung meiner Arbeit unter der Bezeichnung

Dissertation

nur mit Bewilligung der Prüfungskommission berechtigt bin.

Ich erkläre ehrenwörtlich, dass ich die vorliegende wissenschaftliche Arbeit selbstständig angefertigt und die mit ihr unmittelbar verbundenen Tätigkeiten selbst erbracht habe. Ich erkläre weiters, dass ich keine anderen als die angegebenen Hilfsmittel benutzt habe. Alle aus gedruckten, ungedruckten oder dem Internet im Wortlaut oder im wesentlichen Inhalt übernommenen Formulierungen und Konzepte sind gemäß den Regeln für wissenschaftliche Arbeiten zitiert und durch Fußnoten bzw. durch andere genaue Quellenangaben gekennzeichnet.

Die während des Arbeitsvorganges gewährte Unterstützung einschließlich signifikanter Betreuungshinweise ist vollständig angegeben. Die wissenschaftliche Arbeit ist noch keiner anderen Prüfungsbehörde vorgelegt worden. Diese Arbeit wurde in gedruckter und elektronischer Form abgegeben. Ich bestätige, dass der Inhalt der digitalen Version vollständig mit dem der gedruckten Version übereinstimmt.

Ich bin mir bewusst, dass eine falsche Erklärung rechtliche Folgen haben wird.

(Unterschrift)

(Ort, Datum)

Dissertation

Mitigation of sound by micro-perforated absorbers in different types of sound fields - Design and evaluation

performed for the purpose of obtaining the academic degree
of Doctor of Technical Science
under the supervision of

Univ.-Prof. Dipl.-Ing. Dr.techn. Manfred Kaltenbacher
Institute of Fundamentals and Theory in Electrical Engineering, TU Graz, Austria

submitted to the Vienna University of Technology
Faculty of Mechanical and Industrial Engineering

by

Dipl.-Ing. Sebastian Floß

Mat.Nr. 01027524

Formanekgasse 1A/3/13

1190 Wien

Vienna, January 2022

Abstract

Noise in human-occupied areas has become an increasing challenge. Usually, in the design process or application scenario of machines, the consideration of noise emissions plays a minor role. Only if the experience is "too loud" in operation, the acoustic at play is considered. In such cases, the standard foam or fiber-based attenuation materials are applied to an excessive extent. Especially in HVAC application, these materials can suffer from severe performance restraints if exposed to water, dust particles and by the protective measures used for persistence. Metal based micro-perforated absorbers (MPA) offer an alternative means for solving noise challenges in situ or generically. They can be applied in hazardous environments and can be produced eco-friendly from scrap metal. In order to allow a generic accurate absorber design for specific noise challenges, the acoustic performance should be pre-evaluated by simulations with only a small disparity to the measured sound reduction. In this thesis, a simulation framework based on the Johnson-Champoux-Allard-Lafarge model has been developed and applied to MPAs. The basis is obtaining equivalent acoustic material parameters from impedance tube measurements by inverse-fitting with a evolutionary genetic algorithm. With these parameters, more dedicated MPA designs are tested in highly diffuse sound fields up to 8 kHz. The applicability of the approach and the performance of several MPA configurations will be demonstrated through simulations and examples. The investigations also allow to give specific design recommendations depending on the frequency range.

Since a possible application involves HVAC ducts, the performance of an MPA under grazing flow conditions and next to a low-pressure axial fan has been investigated. The measurements showed severe changes in MPA effectiveness depending on the relative position to the fan. The fan's aerodynamic performance is also sensitive to the constructive details of the MPA. Under certain conditions, the micro-perforated absorber will emit sound. These conditions have been investigated, and it is shown that the absorber's acoustic performance also determines its self-noise emission level in a grazing flow scenario.

Danksagung

Mein Dank gilt zunächst Univ.-Prof. Dr.techn. Manfred Kaltenbacher für die Betreuung dieser Arbeit, sowie für das durch ihn geschaffene sehr motivierende und freundschaftliche Arbeitsumfeld in der Arbeitsgruppe. Darüber hinaus bin ich ihm für die kontinuierliche Unterstützung und die Freiräume zur Bearbeitung der verschiedenen Themengebiete der Akustik und Strömungsmechanik sehr zu Dank verpflichtet.

Zudem möchte ich mich bei apl. Prof. Dr.-Ing. habil. Stefan Becker und Priv.-Doz. Dipl.-Ing. Dr.techn. Andreas Marn für das Interesse an meiner Arbeit und die Übernahme der Gutachten bedanken.

Ein besonderer Dank gebührt meinen Kollegen in der Arbeitsgruppe für das tolle Arbeitsumfeld. Besonders möchte ich hier meine Bürokollegen Stefan Gombots ("Der Weise aus dem Burgenland"), Jonathan Nowak (Wiener Oberschmähführer) und meinen Diplomarbeitsbetreuer Clemens Junger ("Wir gründen die links-konservative Partei noch!") erwähnen. Aber auch bei allen anderen Kollegen, die ich während der Zeit am Institut kennenlernen durfte und die zu guten Freunden geworden sind, danke ich für die Unterstützung und die anregenden Diskussionen. Ebenfalls gilt mein besonderer Dank den Herren Peter Unterkreuter, Johann Schindele, Christoph Keppel, Manfred Neumann und Reinhold Wagner für ihre große Unterstützung und ihr Engagement bei der Auslegung und dem Aufbau diverser Messanordnungen innerhalb der verschiedenen gemeinsamen Projekte. Auch möchte ich mich bei Birgit Pimperl, Renate Mühlberger und Ruth Tscherne für die zuverlässige Erledigung von allen organisatorischen Angelegenheiten bedanken - bei Ruth noch im Speziellen für die vielen Abende mit Schnitzel.

In besonderen Maße möchte hier die fachliche und freundschaftliche Zusammenarbeit mit Felix Czwielong von der FAU Erlangen hervorheben. Ohne seine Tatkraft, Kollegialität, Neugier und Motivation auch während spät abendlicher Messungen wären große Teile dieser Arbeit nicht möglich gewesen.

Ein sehr, sehr großes Dankeschön gilt meinen Eltern Gabriele und Eduard, die mich während des Studiums hervorragend unterstützt haben. Meinem Bruder Simon danke ich für seine vielen Besuche in Wien und die schönen gemeinsamen Streifzüge durch die Stadt. Meinem Nachbarn und Freund Claus Hubrich danke ich für sein reges Interesse an Akustik und die vielen gemeinsamen Diskussionen.

Contents

1	Introduction	1
1.1	State of the art	2
1.2	Motivation for the thesis	6
1.3	Structure of the thesis	6
2	Fundamentals	8
2.1	Governing equations	10
2.1.1	Conservation equations	10
2.1.2	Ideal gas equation of state and the incompressible substance	12
2.1.3	Linearized equations - towards acoustics	14
2.1.4	Dissipation in bounded and unbounded media	16
2.1.5	Sound field composition in a quiescent medium	17
2.2	Attenuation of the acoustic mode in a semi-infinite homogeneous medium	18
2.2.1	Biot-modeling of fluid-structure interaction	18
2.2.2	Morphology of porous materials	19
2.2.3	MPP modeling	20
2.3	Acoustic field characterization	26
2.4	Excitation of an aperture under grazing flow influence	27
2.4.1	Modeling turbulent wall pressure spectra	28
2.4.2	Ansatz for cavity sound	28
2.4.3	Ansatz for emitted sound of a circular aperture	29
3	Predictive design	30
3.1	Material characterization using an impedance tube	30
3.1.1	Materials	31
3.1.2	Fitting procedure	32
3.1.3	Impedance tube measurement results	36

3.1.4	Fitting results	38
3.2	MPA measurements using an expansion chamber	44
3.2.1	Measurement setup	44
3.2.2	Features of the measurement setup	48
3.2.3	Influence of pore obstructions	49
3.2.4	Influence of cavity configuration, sound field character and MPP type	51
3.2.5	Circular MPP in expansion chamber	56
3.3	Characterization by simulation	58
3.3.1	Validation	58
3.3.2	Changing the MPA configuration	62
3.3.3	Mesh sensitivity study	66
3.4	Review of the general findings	68
4	In-duct application adjacent to an axial fan	69
4.1	Measurement setup	70
4.1.1	Fan setups	71
4.1.2	MPA setups	72
4.2	Acoustic analysis - Duct setup pre-characterization	73
4.2.1	Aeroacoustic sources	73
4.2.2	Acoustic simulation setup	75
4.2.3	Radiated sound and directivity	77
4.3	Overall measured sound reduction and fan efficiency	79
4.4	MPA configuration effectiveness	85
4.4.1	Simulated acoustics at the design point	85
4.4.2	Unsteady (partial) load range	90
4.4.3	High flow speed steady range	92
4.5	Cavity setup effects on fan aerodynamics	96
4.6	Review of the general findings	97
5	Evaluation in the free-far field and grazing flow	99
5.1	Measurement setup and MPA configuration	99
5.2	Results	102
5.2.1	Boundary layer measurements	102
5.2.2	Self-noise measurements	107
5.3	Simulations	110
5.3.1	Analytical models	110
5.3.2	Comparison to measurements	112
5.4	Consequences for MPA application in flow	114
6	Conclusion and outlook	115
	Bibliography	141

Notations and Abbreviations

In this thesis, scalars are represented by normal letters (b), Cartesian or data vectors, matrices and tensors are set in bold-italic letters \mathbf{b} .

Abbreviations

–MPP	Configuration without a micro-perforated panel
ABC	Absorbing Boundary Condition
Al	Aluminum
B	Backward skewed axial fan
BPF	Blade passing frequency
CAA	Computational Aeroacoustics
CAD	Computer-aided design
CFD	Computational Fluid Dynamics
DES	Detached Eddy Simulation
F	Forward skewed axial fan
FE	Finite Element
FFT	Fast Fourier Transform
HVAC	Heating, Ventilation and Air Conditioning
IL	Insertion loss
JCAL	Johnson-Champoux-Allard-Lafarge
JCAPL	Johnson-Champoux-Allard-Pride-Lafarge
MCFS	Short MPA duct with free inflow, reduced backvolume, $L_c = 35$ mm
MCTS	Short MPA duct with turbulent inflow, reduced backvolume, $L_c = 35$ mm
MDFS	Short MPA duct with free inflow, $D_{\text{MPA}} = D_{\text{duct}}$, $L_c = 140$ mm

MDTS	Short MPA duct with turbulent inflow, $D_{\text{MPA}} = D_{\text{duct}}, L_c = 140$ mm
MFL	Long MPA duct with free inflow, $L_c = 140$ mm
MFS	Short MPA duct with free inflow, $L_c = 140$ mm
MHFS	Short MPA duct with free inflow, honeycomb backvolume, $L_c = 40$ mm
MHTS	Short MPA duct with turbulent inflow, honeycomb backvolume, $L_c = 40$ mm
MLS	Maximum Length Sequence
MMFS	Short MPA duct with free inflow, $L_c = 140$ mm, azimuthal and axial backvolume segmentation, MPP with double thickness added in fan segment
MMTS	Short MPA duct with turbulent inflow, $L_c = 140$ mm, azimuthal and axial backvolume segmentation, MPP with double thickness added in fan segment
MPA	Micro-perforated absorber
MPP	Micro-perforated panel
MTL	Long MPA duct with turbulent inflow, $L_c = 140$ mm
MTS	Short MPA duct with turbulent inflow, $L_c = 140$ mm
MXFS	Short MPA duct with free inflow, $L_c = 140$ mm, azimuthal and axial backvolume segmentation
MXTS	Short MPA duct with turbulent inflow, $L_c = 140$ mm, azimuthal and axial backvolume segmentation
NACA	National Advisory Committee for Aeronautics
openCFS	Open Finite Element solver for Coupled Field Simulation
PML	Perfectly Matched Layer
RFL	Long reference duct with free inflow
RFS	Short reference duct with free inflow
RTL	Long reference duct with turbulent inflow
RTS	Short reference duct with turbulent inflow
SPL	Sound pressure level
SS	Stainless steel
TL	Transmission loss

Fluid mechanics

$()'$	Hydraulic (random) field quantity fluctuation
$()_0$	Ambient field quantity or transport property at ambient conditions
β_{ex}	Bulk expansion coefficient
σ	Total stress tensor
τ	Viscous stress tensor
\boldsymbol{x}	Cartesian coordinates vector
δ^*	Displacement thickness

Notations and Abbreviations

δ_{99}	Boundary layer thickness
\dot{V}	Volume flow rate
γ	Isentropic exponent
κ	Thermal conductivity
κ_T	Isothermal compressibility
μ	Dynamic viscosity
ν	Kinematic viscosity
Ω_{fan}	Angular speed of the fan
Φ_{bot}	Power spectral density of the acoustic pressure at the MPA cavity bottom
Φ_f	Power spectrum of fluctuation force in slits
Φ_{surf}	Power spectral density of the hydraulic pressure at the wall beneath the boundary layer
Ψ	Additional function for modulating the Rayleigh conductivity
ρ	Density
σ_1, σ_2	Kelvin-Helmholtz wavenumbers
τ_w	Wall shear stress
Θ	Momentum thickness
ϑ	Circumferential incremental angle
A_{duct}	Cross section of the fan duct
C_{fan}	Circumference of the fan
c_p	Specific heat of air at constant pressure
c_v	Specific heat of air at constant volume
D_{duct}	Duct diameter
D_{fan}	Total fan diameter
D_{MPP}	Duct diameter of MPP duct
e	Specific inner energy
h	Specific enthalpy
K_R	Rayleigh conductivity
K_s	Adiabatic bulk modulus
K_T	Isothermal bulk modulus
L_d	Distance from nozzle to fan hub center
L_{MPA}	Length of MPA section (expansion chamber)
$l_{\text{corr,H-S}}$	Length correction function
l_{pore}	Slit length
N	Number of apertures in the screen
n_{blade}	Number of fan blades

n_{rot}	Number of revolutions
p	Pressure
p_{stat}	Static pressure
Pr	Prandtl number
$Q(\omega)$	Volume flux across an aperture
$Q_{\text{mono}}, Q(\omega)_i$	Mass flux across an aperture, monopole source strength
R	Universal gas constant
R_{duct}	Duct radius
r_{ap}	Radius of circular aperture
$r_{\text{corr,H-S}}$	Radiation correction function
Re	Reynolds number
s	Specific entropy
S_{ap}	Cross section area of singular circular aperture
S_{neck}	Slit area cross section
$S_{\text{piston,rigid}}$	Weighting, correlation function
S_{plate}	Surface area of micro-perforated plate
St	Strouhal number
T	Absolute temperature
t_{rough}	Average height of MPP surface waviness
Tu	Turbulence level
u	Velocity
U_0	Flow velocity far from the wall
U_c	Convection velocity
U_e	Flow velocity at the edge of the boundary layer
$U_{\text{fan,tip}}$	Velocity of the fan's blade tips
u_{norm}	Velocity within the hydraulic boundary layer, normalized with U_0
v	Specific volume
v	Velocity component perpendicular to a single aperture
w_{pore}	Slit width

Mathematics

e_i	Unit vector in i -direction
\Im	Imaginary part
e	Natural exponential function
i	Imaginary unit
\Re	Real part

a	Unspecified field variable
J_i	Bessel function of the first kind and i th order
Acoustics	
$()'$	Thermal acoustic model parameter
$(a, b, c)_{\text{JCAL}}$	Additional fitting parameters for JCAL model
α	Absorption coefficient
$\alpha(\omega)$	Dynamic tortuosity
α_∞	High frequency limit of tortuosity
α_\pm	Acoustic wave attenuation due to convective flow effects
$\alpha_{\text{cl}}, \alpha_{\text{walls}}$	Attenuation coefficient in the unbounded fluid and at the walls of a duct
$\beta(\omega)$	Dynamic compressibility
β_{mr}	Argument of the Bessel function solution to the wave equation in the duct
$\mathbf{T}()$	Transfer matrix
δ_t	Thermal acoustic boundary layer thickness
δ_v	Viscous acoustic boundary layer thickness
γ_{mod}	Density coupling factor
Λ	Viscous characteristic length
λ	Wavelength
Λ'	Thermal characteristic length
ω	Angular frequency
$\bar{L}_{\text{p,sim}}$	Simulated overall sound pressure level
\bar{L}_{p}	Overall sound pressure level
ϕ	Porosity
Φ_{mic}	Angle between microphones
$\rho()$	Density depending on material
$\rho_{\text{eq,scr}}$	Equivalent density of the semi-infinite extended MPP
σ	Static air flow resistivity
τ	Transmission coefficient
τ_{drag}	Time constant of exponential decay of fluid particle velocity
$\tau_{\text{ent,vor}}$	Relaxation time of the entropy and vorticity mode
Z_0	Characteristic impedance of air at ambient conditions
$\tilde{()}$	Coherent field quantity fluctuation, acoustic quantity
$\tilde{\tau}_w$	Coherent part of the wall shear stress
$\tilde{k}()$	Wave number

\tilde{k}_{mr}	Modal wavenumber in circumferential m and radial direction r with order (m, r)
a_i	Source strength of source i
$a_{\text{ex}}, b_{\text{ex}}, l_{\text{ex}}$	Dimensions of the small-scale expansion chamber setup
b_{form}	Pore shape drag fitting parameter
c_0	Speed of sound at standard ambient conditions
d	General acoustic characteristic length, diameter of circular MPP pores
D_{imp}	Inner diameter of impedance tube
f	Frequency
$F(\epsilon)$	Fok-like power series [135] with weighting parameter ϵ
f_{BPF}	Blade passing frequency of the axial fan
f_c	Cut-off frequency
$f_{\lambda/4,i}$	i th resonance frequency due to expansion chamber cross-section jumps, multiples of chamber length l_{ex}
f_c, f_1, f_2	Frequency limits separating different sound fields
f_d	Decoupling frequency
f_{low}	Low frequency limit
f_{mid}	Center frequency of noise frequency band
f_t	Thermal Biot frequency
f_{up}	High frequency limit
f_v	Viscous Biot frequency
h	Mesh size for FE simulation
He	Helmholtz number
k_0	Static viscous permeability
k'_0	Static thermal permeability
$K_{\text{eq,scr}}$	Equivalent bulk modulus of the semi-infinite extended MPP
k_{per}	Viscous permeability
k'_{per}	Thermal permeability
l	Unspecified symbol for length scale of acoustic and hydraulic order
L_c	Cavity length
L_p	Sound pressure level, referenced with p_{ref}
n	Integer multiples
N_{near}	Near field length
p_0	Ambient pressure
$P_{(a)}$	Sound power portion
p_{ref}	Reference sound pressure at ambient conditions, $p_{\text{ref}} = 20 \mu\text{Pa}$

q	Element order of FE ansatz functions
r	Reflection coefficient
R_{imp}	Radius of the impedance tube
R_{mic}	Radius of the microphone setup, distance of microphones
r_{pore}	Hydraulic pore radius, characteristic length for circular pores
St	Stokes number or acoustic Reynolds number
$t_{()}$	Porous media sample thickness
w	Distance of circular pores to each other
$Z_{()}$	Impedance with its corresponding definition
z_{τ}	Normalized shear stress impedance
Z_{eff}	Effective surface impedance
z_q	Normalized heat conduction impedance
z_{rad}	Normalized radiation impedance of a slit
Z_m	Equivalent characteristic impedance of the (porous) material m

Data fitting

\mathbf{x}	Vector of design variables
f_{lim}	Fitness limit
f_{tol}	Function tolerance
a_i, b_i	Constraints for design variables
$G_{\text{max, stall}}$	Maximum number of stall generations
G_{max}	Maximum number of generations
$J(\mathbf{x})$	Objective function

Mechanics

σ_s	Solid media stress
\mathbf{u}_{fr}	Frame displacement
Φ	Potential energy
ε	Solid media strain
$E_{()}$	Young's modulus
t	Time

CHAPTER 1

Introduction

Long-term exposure to elevated noise can bring about several adverse consequences to individual human health (e.g. cardiovascular diseases, hearing loss) and psyche (e.g. sleep disorder) [156] [63] [51]. Unwanted sound is omnipresent in inner city living and workspace areas and is caused by many different source mechanisms [42]. The sound emission into enclosed spaces is especially important, since there, people go about their daily lives for a fair amount of the day. Fans in duct systems, mostly for application with low-pressure rises and high volume flow rate (e.g. HVAC systems) are such noise contributors in e.g. office areas or daily commuting. Many people have experienced background noises caused by the emission of small scale fans in 3D-printers, PC cooling systems or beamers at lower dB levels, but long exposure time, and the accompanying feelings of annoyance and of discomfort.

Therefore, best-practice guidelines [157] for low noise levels exist in the EU. Mainly concerned with traffic and aircraft noise, there exist no thresholds for the sound emission of fans or from duct systems. Nevertheless, the determination of sound power radiated into a duct by fans or other air-circulating devices is an ISO standard [52]. When faced with the challenge of lowering threshold sound exposure in human occupied areas, the acoustic engineer has two solution strategies. On the one hand, he or she can identify the sources of the unwanted sound emissions and try to mend them. For example optimize the blade geometry of a fan or study the tyre noise mechanisms and make re-design recommendations. But in a lot of cases, e.g. in HVAC systems or living space areas, the potential of sound source reduction is limited: physically - acoustic measures demand space which has a worsening influence on the aerodynamics - and monetary - reworking the fan-duct system, the operating fan (characteristics) conditions might be unchangeable for thermodynamic and efficiency reasons, or the inflow boundary conditions are not ideal and thus adding to aerodynamic sound production. Traffic noise sources are more or less unswayable by the individual in its quest for lowering noise exposure in enclosed spaces.

Passive sound reduction by absorption (by dissipation or interference sound cancelling) is the other strategy of dealing with noise in situ. An efficient sound absorber has a broad frequency band application spectrum and is compact in geometric dimensions. Compactness is crucial in duct acoustics with a mean background flow, since any additional pressure drop will reduce the efficiency of the turbo-machine providing the static pressure difference. The absorber material should have a low-cost manufacturing process and be easy to apply in rooms and ducts. Hence, a large variety of acoustic absorber materials are available on the market. Melamin foams and fibrous materials are the standard choices for broadband sound reduction application, e.g. in anechoic chambers, liners and edifice sound insulation. More advanced absorber design concerns the porous micro-structure, the predictive in-situ-dedicated design with simulation tools and a broader applicability range including hazardous environments and low Mach number duct flows.

1.1 State of the art

Application requirements for technical acoustic passive sound absorbers include the selection of a suitable and cost-efficient producible absorber material and its physical modeling. Most of the available absorber materials are derived from porous foams or are based on fibers. With an in-duct acoustic wave-guide, a mean background flow is encountered almost all the time and not exceptionally. Specifically the perforated liner has been studied extensively in aircraft applications.

Micro-perforated material

The basal configuration of the micro-perforated absorber (MPA) is a thin micro-perforated plate-like structure (MPP), which is placed in front of an empty air-tight cavity of length L_c . Preferable the semi-finished product is made of metal, due to its durability and machining quality. The materials that were investigated in this study are commercially available. The production process is well-established, meaning that acoustically significant parameters can be changed straightforward, e.g. for optimization, and the production costs per square meter are similar to the standard porous foam or fibrous materials. However, the physical parameters governing the acoustic response of these materials are either not known exactly by the manufacturer, rather difficult to determine without significant variances or the pore geometry is not suitable for the established acoustic modeling.

The MPP can be categorized by its basal semi-finished good, the plate thickness, the size of the pores, their shape and the porosity, which is the ratio of pore area to the entire plate area (see Tab. 1.1). The micro-perforated materials that were investigated are depicted in Fig. 1.1 and Fig. 3.2 and are either based on Aluminum (Al) or stainless steel (SS).

These commercially available materials were chosen since they are rather cheap in production due to being only plastically deformed by milling or braiding. Therefore material is conserved. Slit shaped perforations ease the deforming procedure. However the acoustically rel-

evant material parameters are difficult to obtain. Either there were no parameters provided at all or merely parameters without the necessary degree of precision for an accurate acoustic modeling.

The investigated MPPs were subjected to different types of sound fields and flow conditions as they would in a common HVAC application scenario or in architectural acoustics. Therefore, the selected basal scientific literature is categorized into a general review of porous materials and their modeling, the acoustic liner with a background mean flow and specifically

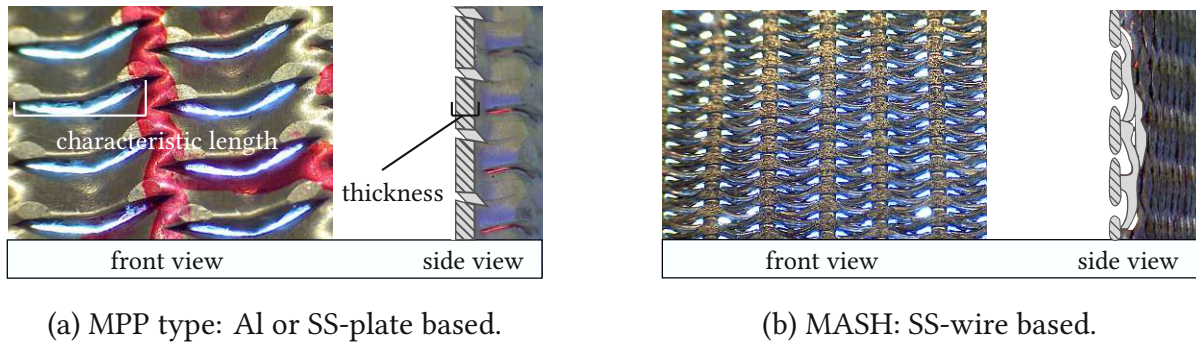


Figure 1.1: Close-up image of the investigated materials.

MPP type (semi-finished good)	t_{MPP}	char. length	shape	porosity
C (Al)	≈ 1 mm	< 0.5 mm	slit	1 - 2 %
B (SS)	≈ 0.5 mm	< 0.5 mm	slit	1 - 2 %
LSE2 (Al)	≈ 1 mm	< 0.5 mm	slit	10 %
LSE3 (Al)	≈ 1 mm	< 0.3 mm	slit	3.5 %
LSE4 (Al)	≈ 1 mm	< 0.2 mm	slit	1.5 %
LSE7 (SS)	≈ 0.5 mm	< 0.2 mm	slit	1.0 %
MASH (SS)	< 1 mm	n/a	slit	n/a

Table 1.1: Investigated materials, named with an acronym, with parameter description; porosity measured by the manufacturer and characteristic (char.) length estimated or measured with high-resolution camera.

the application of MPPs and MPPs in-duct with flow wave-guide acoustics. The literature on axial fan aerodynamics is referenced accordingly in the relevant chapter. So is the relevant background scientific literature on the measurement techniques used.

Porous materials

An overview of the scientific publications on porous materials and the modeling of their micro-scale are marked according to the focus of the investigations in Tab. 1.2, e.g. appli-

cation, development or augmentation of models (mod. type), whether an analytical or numerical approach was used (analyt./num.), whether experiments were conducted (exp.) or an absorber material parameter fitting was performed (mat. param. fit.). The development of the presented porous material models stretches over the last four decades [12] and is still an ongoing field of research with the advent of new ways of material production (e.g. 3D printers). The porous media and sound attenuation modeling procedures usually make use of electro-acoustic analogies (see [131]) for low-frequency sound transmission modeling. These analogies are valid if the acoustic wave length and geometrical dimension of the wave guide are of comparable scale.

source	year	mod. type	analyt./num.	exp.	mat. param. fit.
Tijdeman [150]	1975	■	■		
Knutsson [93]	2008	■	■	■	
Berggren [24]	2018	■	■	■	
Allard et al. [13]	1992	■	■		
Lafarge [101]	1993	■	■	■	
Lee et al. [105]	2005	■		■	
Atalla et al. [15]	2007	■	■	■	
Jaouen et al. [80]	2011	■	■	■	■
Beltman [23]	1998	■	■	■	
Randeberg [134]	2000	■	■	■	
Zielinski et al. [169]	2015				■

Table 1.2: Selected literature on modeling micro-scale acoustics.

Acoustic liners with flow

Liner investigations with flow use semi-infinite plate setups for far field measurements or wave guides where the plane wave mode and a few higher order modes are calculated by wave-decomposition [140] with the pressure data of various microphones. The literature in Tab. 1.3 is marked according to whether liner-flow interaction modeling was used or developed (mod.), experiments were conducted (exp.), liners were investigated (liners) or merely theoretical analyses were done; whether a numerical simulation was performed (num.) and if the self-noise of the investigated materials has been measured (self-noise).

Application of MPPs and MPPs in duct flow acoustics

The MPP literature (Tab. 1.4) is categorized as before with the additional focus of the impact of grazing flow or treating fan noise (flow-fans). The works include the original MPP idea by Maa, extensive MPP-flow interaction studies in duct arrangements, optimized locally-reacting MPAs enforced by honeycomb-segmented cavities and numerical simulations to

source	year	mod.	exp.	liners	numeric.	self-noise
Ffowcs Williams [53]	1972	■		■		
Tsui et al. [152]	1977	■	■	■		■
Bauer et al. [20]	1977		■	■		■
Nelson et al. [125]	1982	■	■	■		■
Liu et al. [111]	2008	■	■			■
Weng [155]	2013	■	■		■	
Zhang et al. [168]	2016	■	■	■	■	
Stein et al. [146]	2019	■	■		■	
Howe [76]	1995	■	■			
Jing et al. [82]	2001	■	■			
Knutsson et al. [94]	2010	■	■			
Schulz [144]	2018	■	■	■	■	

Table 1.3: Selected literature on acoustic liners (in ducts), duct acoustics with a background flow and acoustic-flow interaction modeling.

identify the influence of flow on the real and imaginary part of the MPA's impedance. The lists are far from complete and additional sources are referenced throughout the text.

source	year	mod.	exp.	flow-fans	numeric.	mod. param. fit.
Maa [112], [113]	1975/1998	■	■			
Liu et al. [110]	2013	■	■			■
Denayer et al. [48]	2016	■	■		■	
Laly et al. [103]	2017	■	■			■
Bolton et al. [31]	2017	■	■		■	■
Allam et al. [9], [10], [11]	2011/14/15	■	■	■	■	
Sacks, Kabral [141], [86]	2016	■	■	■	■	
Bravo et al. [32]	2017	■	■	■	■	
Xiaoqi et al. [164]	2019	■	■	■	■	
Xiaoqi et al. [165]	2020		■	■		
Xi et al. [163]	2014		■	■	■	
Lee et al. [104]	2015		■	■	■	

Table 1.4: Selected literature on application of MPPs, MPPs in duct acoustics with and without fans.

1.2 Motivation for the thesis

As discussed above, the scientific background leading to now available micro-perforated materials and absorbers is substantial. There have been individual studies covering certain aspects of the MPA, but so far no comprehensive studies by simulations and in situ evaluation in various sound fields have been performed.

The purpose of the thesis is to give detailed description of the design framework and application considerations of the MPA based on metal micro-perforated plates. Porous material modeling in combination with Finite Element simulation forms the basis for more dedicated absorber designs. A systematic experimental study of three application scenarios in different sound fields (*free field with flow, wave guides with flow and diffuse field without flow*) was conducted and allowed to assess the absorbers' acoustic behavior with and without flow and its impact on the aerodynamics of an adjacent axial fan. The considered flow velocities are of a low Mach number ($Ma < 0.3$). The main questions that guided the MPAs' scrutiny imply:

- Suitability of efficient and accurate numerical simulation in a wide frequency range for sound reduction and space requirement optimization.
- Robustness and accuracy of the material parameter fitting procedure.
- Influence of sound field character in front (*direct and plane wavefronts vs. diffuse*) and within the MPA (*local vs. non-local*).
- Aerodynamic effects of an MPA adjacent on an axial fan in a duct.
- MPA characterization under grazing flow concerning self-noise and the influence of flow-MPP-interaction on effectiveness of the MPA.
- Derivation of recommendations for MPA usage in various sound field and flow field scenarios.

1.3 Structure of the thesis

The literature presented above shows the initial situation for the following investigations. The outlined research represents duct acoustics wave propagation and measurement theory, acoustic liner characterization experimental and simulation results as well as theoretical and experimental investigations on the equivalent fluid based Finite Element framework.

Chapter 2 deals with the governing equation describing the acoustic field quantities inside and outside of porous materials with or without a background mean flow field. Thereby, the equations are simplified and modeling solutions for the acoustic pressure field are presented. The influences of flow on the acoustic field are discussed. The porous material parameter determination and a discussion of the occurring modal fields conclude the chapter.

Chapter 3 elaborates the equivalent fluid based simulation approach. The fitting procedure

based on a genetic evolutionary algorithm is presented [115]. The impact of various models and number of fitting parameters on the simulated sound field is discussed. Differently modeled MPA structures and geometrical sensitivity studies show the robustness of the FE framework and its limits. The simulations were carried out with the open source Finite Element code openCFS [5, 87]. By variation of MPPs arrangements relative to the sound source, measurement and simulation studies show how frequency range and absorber morphology determine its efficacy in terms of sound mitigation. The MPPs investigated are type C, B and MASH. Some parts of the content haven been published in two papers: [56, 89].

Chapter 4 summarizes investigations of a circumferential MPP arrangement in the direct vicinity of an axial fan. The measurements were performed at an axial fan test rig that allowed to measure fan characteristic curves with and without the circular MPP liner. The used MPP was type B. Major parts of the content have been published in two papers: [46, 57].

Chapter 5 deals with investigations of flow grazed compact MPP liners under free field acoustic boundary conditions. Flow induced self-noise and flow velocity profile measurements were used to characterize the impact of flow direction, flow velocity and MPP parameters on the acoustic behaviour of the MPA under laminar and turbulent flow conditions. The investigated MPPs are type LSE2, LSE3, LSE4 and LSE7.

Chapter 6 contains the summary of the general findings and concludes the thesis with recommendations for future work on MPAs.

CHAPTER 2

Fundamentals

The main goal of MPP application is the attenuation of acoustic wave energy. However, in the common application scenario, besides the fluctuating coherent acoustic field quantities, laminar and/or turbulent fluid flow field structures will be present [78]. The interaction of both fields is to be considered depending on the spatial scale, flow characteristics in the presence of a porous structure, but most importantly, on the local flow velocity in excess of the speed of sound (Mach number Ma). The simplification of the general conservation equations of mass, momentum and energy, leads to models for sound absorption, aeroacoustic source description, the influence of fluid flow on sound propagation and attenuation under specific physical boundary conditions. These simplified descriptive models require in part certain approximate assumptions [144]:

Compactness:

An object that is exposed to an acoustic wave is said to be compact if the fluid region occupied by its volume with characteristic length scale l is much smaller than the acoustic wavelength $\lambda = 2\pi c_0/\omega$ [77]. This means for the Helmholtz number: $He = \omega l/c_0 = \tilde{k}_0 l \ll 1$. Compactness is necessary for the electro-acoustical analogies, used for semi-infinite absorber modelling and wave-guide analysis by lumped element models [131].

Local and non-local reaction:

Suppose the reaction of a surface's portion to an incident acoustic field quantity is dependent only on the quantity incident on that portion and independent of the quantities on any other part of the surface. In that case, it is said that the surface is locally reacting [122]. Hence, such a surface is independent of the spatial distribution (wavenumber $\tilde{\mathbf{k}}$) of the incident acoustic wave field and thus the angle of incident [144]. A locally reacting surface can be sufficiently described by the ratio of the local acoustic pressure and surface normal particle velocity - its normal incident impedance. Since the impedance is a feature of the surface and not the

acoustic field, different modal sound field solutions can lead to the same impedance [144]. Compactness is a sufficient but not a necessary condition for a local reaction. Concretely e.g. porous foam materials are considered locally-reacting because of a very large specific flow resistance (decoupling by inner damping). The single pores in the slotted MPPs (MPP type B, C, etc. and MASH) are not connected parallel to the plate surface. Therefore, the real MPP can be assumed to be locally-reacting. This does not apply to the combination of MPP and an adjacent air cavity.

Homogeneity:

Suppose the assumption holds that the acoustic reaction is spatially invariant and equally distributed across the surface. In that case, one can describe it as homogeneous. The surfaces' single pore impedances are represented by a "smeared" impedance [84]. For a porous surface, the local reaction of each perforation, described by a local impedance, is scaled with the entire surface area by the perforation ratio or porosity ϕ . Homogeneity can be assumed if all the MPP's structural elements (openings with characteristic length d) react with the same amplitude and phase response to an incident sound pressure, and if $\lambda \geq 2.8d$ [84]. In this case, compactness of the acoustic object (pores) is necessary. By these definitions, *the MPA can not be assumed homogeneous due to its air cavity*. Depending on the frequency and He number, the sound field in the cavity will not be spatially homogeneous. According to Allard [12], compactness and homogeneity, however, justify the usage of an equivalent fluid at the macroscopic scale and of the semi-empirical models described in the following sections.

Linearity:

If the ratio between complex-valued local acoustic pressure and particle velocity is constant over the surface and only dependent on frequency and therefore on the wavenumber, but not on the pressure or particle velocity amplitude, then the assumption of a linear reaction is valid. Experience shows that for larger amplitudes, a physical system reacts increasingly non-linear. In the MPP domain for small amplitudes, the effect of viscous friction can be described as a linear function of the acoustic particle velocity. An example for a non-linear behavior at larger amplitudes is the eddy detachment from an orifice flowed through at very high sound pressure levels [79, 118, 144].

Separation of scales:

When the background flow velocity is significantly lower than the local speed of sound c_0 , the aeroacoustic source field exists on (characteristic) length scale l and the resulting acoustic field on scale l/Ma [53], with $l = 1/k'$ and where k' is the hydraulic (flow) wavenumber. The resulting acoustic wave length is the spatial equivalent to the time periodicity of a fluctuating coherent (acoustic) flow field variable.

2.1 Governing equations

For the interpretation of the acoustic experiments involving a moving background flow and the derivation of the sound wave attenuation models, at first, the governing equations for the flow field quantities are presented.

2.1.1 Conservation equations

The description of the fluid dynamic (thermodynamic) state quantities is carried out in terms of substantial quantities (Eulerian framework) of a field variable a . The transformation operator D/Dt is called substantial derivative of a . Thereby, the total differential computes by:

$$\frac{Da}{Dt} = \frac{\partial a}{\partial t} + u_i \frac{\partial a}{\partial x_i} = \frac{\partial a}{\partial t} + (\mathbf{u} \cdot \nabla)a. \quad (2.1)$$

The underlying equations are the conservation of mass, momentum and energy:[19, 50, 50, 131]

Conservation of mass:

For fluids in general, the mass balance over a moving fluid material control volume is

$$\frac{D\rho}{Dt} + \rho \nabla \cdot \mathbf{u} = \frac{\partial \rho}{\partial t} + u_i \frac{\partial \rho}{\partial x_i} + \rho \frac{\partial u_i}{\partial x_i} = 0, \quad (2.2)$$

with total fluid density ρ and the velocity component u_i of \mathbf{u} in x_i -direction.

Conservation of momentum: (Cauchy equation) [50] [19] [108]

$$\rho \frac{D\mathbf{u}}{Dt} = \mathbf{f} - \nabla p + \nabla \cdot \boldsymbol{\tau} \quad \text{or} \quad \rho \left(\frac{\partial u_i}{\partial t} + u_j \frac{\partial u_i}{\partial x_j} \right) = f_j - \frac{\partial p}{\partial x_i} - \frac{\partial \tau_{ij}}{\partial x_j} \quad (2.3)$$

Thereby, for directions $i, j = 1, 2, 3$, f_j is acting on the enclosed volume of a fluid particle, with \mathbf{f} representing a body force per unit volume. τ_{ij} is the molecular-dependent momentum input, indicating transport of momentum j in x_i -direction, represented by the tensor $\boldsymbol{\tau}$ which is also known as viscous stress tensor. The only surface forces that can exist are those imposed by the spatial change of the static pressure $\partial p / \partial x_j$. The right-hand side of (2.3) is balanced by the momentum increase per time and addition of momentum by convection velocity (\mathbf{u}). Common fluids, like air and water, are classified as Newtonian fluids. Here the shear and normal parts of $\boldsymbol{\tau}$ are linearly connected to the gradient velocity field via a fluid specific proportionality constant called dynamic viscosity μ . The momentum equation is then called the Navier-Stokes equation, and the molecule-dependent momentum input becomes

$$\tau_{ij} = \left[(\mu_B - \frac{2}{3}\mu) \frac{\partial u_k}{\partial x_k} \right] \delta_{ij} + 2\mu S_{ij}, \quad \text{with} \quad S_{ij} = \frac{1}{2} \left(\frac{\partial u_i}{\partial x_j} + \frac{\partial u_j}{\partial x_i} \right) \quad (2.4)$$

Steady body forces like ρg_i due to gravitational pull g_i in constant density flows are usually compensated by the gradient of the hydrostatic pressure, which is subtracted from the fluid dynamic pressure. They are therefore omitted further on [100]. The total pressure in the fluid is the sum of static (thermodynamic) pressure, hydrostatic pressure, and dynamic pressure. Dynamic viscosity μ is also called shear viscosity and a well-characterized fluid property. The bulk viscosity is often neglected ($\mu_B = 0$), which is a valid assumption for many applications. However e.g., in the higher frequency range (ultrasonic), the influence of humidity, temperature, and pressure on bulk viscosity significantly affects acoustic absorption in the fluid medium [108]. In a fluid element at the molecular scale and at thermal equilibrium the molecular energy modes (internal energy: translational, rotational and vibrational) are equal. If the departure from internal equilibrium is not too large, a transport property like viscosity can be expressed as a function of the local thermodynamic (equilibrium) state (defined by any two-state variables such as T , ρ , s or p) [69, 149]. The time that it takes for the disturbed local thermodynamic state quantity to regain equilibrium is called the relaxation time. If the relaxation time is much shorter than a change in fluid field quantities (e.g., static pressure or velocity gradient field) than the local equilibrium assumption is valid. The fluid reacts "slow" compared to the molecular processes (e.g. at $p = 1$ atm, 300K H_2O -vibrational mode relaxation time: 1.6×10^{-8} s, [149]). The process of relaxation of rotational and vibrational energy modes to thermodynamic equilibrium can then be expressed with the effective transport property coefficient of bulk viscosity μ_B . The relaxation of translational molecular energy modes happens much faster and is represented by the shear viscosity μ . So, in "slow" fluids the bulk motion (\mathbf{u}) does not affect the statistical averages of the molecular properties - the thermodynamic state [129].

Conservation of energy: [19, 70, 100, 121, 129]

The energy equation (for fluids with constant specific heat capacity) follows from the first law of thermodynamics. The total energy dE within a thermodynamically enclosed material volume dV is composed of the inner energy $dV \rho e_i$, the kinetic energy $dV \rho \mathbf{u}^2/2$ and the specific potential energy Φ . The substantial rate of change of total energy DE/Dt is equal to the rate that energy is received by heat $\dot{Q} = -dV \nabla \cdot \mathbf{q}$ and surface work transfers $\dot{W} = dV \nabla \cdot (\boldsymbol{\sigma} \mathbf{u})$ [129]:

$$\frac{DE}{Dt} = \dot{Q} + \dot{W} \quad \text{or} \quad \rho \frac{D(e_i + \frac{1}{2} \mathbf{u}^2 + \Phi)}{Dt} = -\nabla \cdot \mathbf{q} + \nabla \cdot (\boldsymbol{\sigma} \mathbf{u}) + \mathbf{u} \cdot \mathbf{f} \quad (2.5)$$

with \mathbf{q} as the heat flux and $\boldsymbol{\sigma} = -\delta p + \boldsymbol{\tau}$ as the total stress tensor with static pressure p and $\boldsymbol{\tau}$ as the viscous stress tensor. If one omits the specific potential energy, then the total energy has a thermal and a kinetic portion. Here, the work of the body forces $\mathbf{u} \cdot \mathbf{f}$ contributes solely to the kinetic portion. However, the total work of surface forces $\boldsymbol{\sigma} \mathbf{u}$ can be separated into

pressure work and viscous work:

$$\nabla \cdot ((-\delta p + \boldsymbol{\tau})\mathbf{u}) = \underbrace{-p \nabla \cdot \mathbf{u} - \mathbf{u} \cdot \nabla p}_{\text{pressure work}} \quad + \quad \underbrace{\boldsymbol{\tau} : \nabla \mathbf{u} + \mathbf{u} \cdot (\nabla \cdot \boldsymbol{\tau})}_{\text{viscous work}} \quad (2.6)$$

In terms (2) and (4), the gradients indicate force imbalances that accelerate the fluid element and cause a change in kinetic energy. These terms appear in the mechanical energy equation, which is the result of the scalar product of the momentum equation with convection velocity \mathbf{u} . Terms (1) and (3) appear in the thermal energy equation and they are forces multiplied by fluid element deformations. Term 1 can be interpreted as the volumetric rate of expansion and contraction. Thermodynamically, this corresponds to heating or cooling of the fluid element by compression and expansion. Separating the kinetic from the thermal part of the total energy, one arrives at the thermal energy equation

$$\rho \frac{De}{Dt} = -\nabla \cdot \mathbf{q} - p \nabla \cdot \mathbf{u} + \boldsymbol{\tau} : \nabla \mathbf{u}. \quad (2.7)$$

The specific inner energy e can be rewritten by the enthalpy $h = e + \rho^{-1}p$. Therefore, for convenience in the fluid dynamics domain, the inner energy for a Newtonian fluid separated from the kinetic energy in (2.5) can be rewritten with the enthalpy relation $dh = c_p dT + \rho^{-1}[1 - T\beta]dp$, describing heat transfer in terms of temperature T [129, 131]:

$$\rho c_p \frac{DT}{Dt} = \nabla \cdot (\kappa \nabla T) + \beta_{\text{ex}} T \frac{Dp}{Dt} + \beta_{\text{ex}} T \mathbf{u} \cdot \nabla p + \boldsymbol{\tau} : \nabla \mathbf{u}, \quad (2.8)$$

where according to Fourier's law $\mathbf{q} = -\kappa \nabla T$, with κ as thermal conductivity and β_{ex} as bulk (or volume) expansion coefficient defined in (2.13). Also the dissipation term in (2.8) can be rewritten by

$$\boldsymbol{\tau} : \nabla \mathbf{u} = (\mu_B - \frac{2}{3}\mu)(\nabla \cdot \mathbf{u})^2 + 2\mu \mathbf{S} : \mathbf{S}, \quad (2.9)$$

with the velocity gradient or strain rate tensor $\mathbf{S} := S_{ij}$.

It can be advantageous for the study of acoustic-fluid interaction or aeroacoustic phenomena to rewrite (2.7) with the entropy s by using the combined first and second law of thermodynamics $de = Tds + p/\rho^2 d\rho$ [87, 129]

$$\rho T \frac{Ds}{Dt} = \nabla \cdot (\kappa \nabla T) + \boldsymbol{\tau} : \nabla \mathbf{u}. \quad (2.10)$$

2.1.2 Ideal gas equation of state and the incompressible substance

The complete description of flow and acoustic fields requires the elaboration of the specific equation of state for the fluid air and the concept of the incompressible substance .

Ideal gas: Depending on the physical boundary conditions the equation relates thermodynamic (static) pressure p , absolute temperature T and specific volume v by the universal gas constant R in the state equation

$$pv = RT. \quad (2.11)$$

Air can be assumed to behave like an ideal gas, depending on the humidity level. For an ideal gas $\beta_{\text{ex}} = 1/T$ in (2.8) and the relation $R = c_p - c_v$ holds, where c_p is the specific heat at constant pressure and c_v at constant volume and $\gamma = c_p/c_v$ is the specific heat ratio. For the isentropic case ($ds = 0$), one can relate pressure and density via the isentropic speed of sound c_0 at standard ambient conditions

$$c_0 = \sqrt{\gamma p / \rho} = \sqrt{\gamma RT} = \sqrt{(\partial p / \partial \rho)_s} = \sqrt{K_s / \rho}, \quad (2.12)$$

where K_s is the adiabatic bulk modulus. Its reciprocal $1/K_s$ is called the adiabatic compressibility.

Incompressible substance [129]: The sensitivity of a substance to density changes is specified by [121, 129]

$$\frac{d\rho}{\rho} = \kappa_T dp - \beta_{\text{ex}} dT \quad \text{with} \quad \kappa_T = \left. \frac{1}{\rho} \frac{\partial \rho}{\partial p} \right|_T \quad \text{and} \quad \beta_{\text{ex}} = - \left. \frac{1}{\rho} \frac{\partial \rho}{\partial T} \right|_p, \quad (2.13)$$

where κ_T is the isothermal compressibility coefficient with its reciprocal $1/\kappa_T = K_T$, the isothermal bulk modulus. Both compression moduli are related by [131]:

$$\frac{K_s - K_T}{K_T} = \frac{T \beta_{\text{ex}}^2 K_T}{\rho c_p} = \frac{\gamma - 1}{\gamma} = \frac{c_p - c_v}{c_p} \quad (2.14)$$

The thermodynamic (static) pressure p_t is the force on the wall of a box containing a fluid at equilibrium. Surface forces are a mechanical force concept. When a substance is not moving, the normal stress is the same as the thermodynamic pressure, giving the effective pressure because the normal stress is a sum of pressure and normal viscous stress.

In an incompressible substance, thermodynamically called *fluid* or mechanically called *flow*, the pressure variable is interpreted as the mechanical pressure p_m . For a compressible substance, in a first approximation, the difference between the two pressures can be related to the rate of expansion with the continuity equation combined with the momentum (2.3) and energy (2.7) equation by [129, 149]:

$$p_m - p_t = \mu_B \nabla \cdot \mathbf{u} \\ \nabla \cdot \mathbf{u} = - \frac{1}{\rho} \frac{D\rho}{Dt} = \frac{1}{2c_0^2} \mathbf{u} \cdot \nabla \mathbf{u}^2 + \frac{1}{c_0^2} \left[\frac{1}{2} \frac{\partial u^2}{\partial t} - \frac{1}{\rho} \frac{\partial p}{\partial t} \right] + [\dots] \quad (2.15)$$

One important consequence for the incompressible flow assumption is that fluid flow events

are independent of heat transfer events, and the specific heats are equal ($c_p = c_v$). The energy equation (2.8) can then be disregarded. The density in an incompressible flow is constant. The (static) mechanical pressure is determined by the momentum equation. Also, the pressure work term in (2.8) vanishes. With (2.15), it is understandable that at low Mach numbers, compressibility can be neglected and that only local fluid velocity fluctuations in the order of c_0 introduce non-linearity (e.g., due to high local pressure fluctuations).

Newtonian fluid [129]: Stokes assumption of the equality of thermodynamic and mechanical pressure is commonly taken as one of the characteristics of the Newtonian fluid simplification. Yet rapid changes of state variables of pressure and density (expansion and compression) associated with the propagation of sound in a free-field lead at first to an increase in the translational molecular energy mode and only after several collisions the energy is distributed to rotational and vibrational modes. The translational mode is only associated with the mechanical pressure, which is therefore not the equilibrium thermodynamic value. If the relaxation time scale is long compared to the flow fluctuation time scale, the bulk viscosity coefficient μ_B can be used to model these non-equilibrium effects for sound waves [129]. For example, the absorption in noble gases follows Stoke's assumption, and in air μ_B is non-zero, but its value depends strongly on the water vapor content. Generally it is stated that a Newtonian fluid has the following essential properties:

1. Stress is a linear function of the strain rate.
2. Transport coefficients are a function of the thermodynamic state and usually constant.
3. When the fluid is stationary, the stress is the thermodynamic pressure.
4. The fluid is isotropic.
5. Stokes's assumption applies ($\mu_B = 0$): the mechanical and thermodynamic pressures are equal. The average normal viscous stress is zero.

In the following investigations, the sound-wave-carrying medium is air at ambient (humidity) conditions and assumed to be Newtonian. The investigated sound frequency ranges (100 Hz to 10 kHz) are way below the ultrasonic range. The bulk medium flow velocities are sufficiently low ($Ma < 0.1$) to allow envisioning the flow as incompressible.

2.1.3 Linearized equations - towards acoustics

Sound waves in free air have small amplitudes, are fast and have coherent changes of pressure \tilde{p} , velocity $\tilde{\mathbf{u}}$ and density $\tilde{\rho}$ around an ambient state $(p_0, \rho_0, \mathbf{u}_0, T_0, s_0)$, which occur isentropically (reversibly and adiabatically, $Ds/Dt = 0$ - Laplace's hypothesis).

Inserting the perturbed field quantities $\rho = \tilde{\rho} + \rho_0$, $p = \tilde{p} + p_0$ and $\mathbf{u} = \tilde{\mathbf{u}} + \mathbf{u}_0$ in the continuity equation (2.2), momentum equation (2.3) without viscosity and the isentropic relation

of pressure and density (2.12) and assuming a quiescent medium ($\mathbf{u}_0 = 0$), leads to the Euler equations [47, 131, 136]:

$$\begin{aligned} \frac{\partial}{\partial t}(\rho_0 + \tilde{\rho}) + \nabla \cdot ((\rho_0 + \tilde{\rho})\tilde{\mathbf{u}}) &= 0 \\ (\rho_0 + \tilde{\rho})(\partial/\partial t + \tilde{\mathbf{u}} \cdot \nabla)\tilde{\mathbf{u}} &= -\nabla(p_0 + \tilde{p}) \\ p_0 + \tilde{p} &= p(\rho_0 + \tilde{\rho}, s_0) \end{aligned} \quad (2.16)$$

Using the so-called acoustic (or linear) approximation and transferring the combined equations (2.16) into the frequency domain for harmonic perturbations $d/dt = -i\omega$, with ω as the angular frequency, results in the Helmholtz equation. To be more general, the equation for an inhomogeneous medium is [88, 89]

$$\frac{\omega^2}{K_0}\tilde{p} + \nabla \cdot \left(\frac{1}{\rho_0}\nabla\tilde{p}\right) = 0. \quad (2.17)$$

For acoustic wave propagation $K_s = K_0$ and the solution for \tilde{p} in an unbounded plane wave field defined by cartesian coordinates $\mathbf{x} = xe_x + ye_y + ze_z$ is $\tilde{p}(\mathbf{x}, t) = \Re(\hat{p}e^{-i\omega t + i\tilde{\mathbf{k}} \cdot \mathbf{x}})$. Accordingly, the solution for $\tilde{\mathbf{u}}$ is $\tilde{\mathbf{u}}(\mathbf{x}, t) = \Re(\hat{\mathbf{u}}e^{-i\omega t + i\tilde{\mathbf{k}} \cdot \mathbf{x}})$, with $\tilde{\mathbf{k}} = \omega/c_0\mathbf{n}$ as the acoustic wave number vector, \mathbf{n} is the unit vector in the direction of propagation, and $\omega = 2\pi f$ with f as the frequency. The wavelength λ is related to the frequency via $c_0 = \lambda f$.

To describe sound wave propagation through an MPP (or more generally of a porous absorber) and its frequency-dependent attenuation, which is linked to thermal and viscous dissipation, one can rewrite the acoustic approximations of continuity and momentum with the linearized isentropic state relation $\tilde{p} = c_0^2\tilde{\rho}$ (2.16) to arrive at [101]

$$\begin{aligned} \rho(\omega)\frac{\partial}{\partial t}\phi\langle\tilde{\mathbf{u}}\rangle &= -\nabla\langle\tilde{p}\rangle \text{ viscous effects and} \\ K(\omega)^{-1}\frac{\partial}{\partial t}\langle\tilde{p}\rangle &= -\phi\nabla \cdot \langle\tilde{\mathbf{u}}\rangle \text{ thermal effects.} \end{aligned} \quad (2.18)$$

Here, $\langle\tilde{\mathbf{u}}\rangle$ and $\langle\tilde{p}\rangle$ denote the macroscopic phase averages of the local periodic fluctuation in the microscopic pores over an homogenized volume. The phase average allows to differentiate between periodic ($\langle\tilde{\cdot}\rangle$, coherent) and random ($\langle\tilde{\cdot}\rangle'$) fluctuations. It is usually accomplished by correlating e.g., measured pressure/ velocity data to a reference signal.

Thereby it is defined that $\rho(\omega) = \rho_0\alpha(\omega)$ and $K(\omega)^{-1} = K_0^{-1}\beta(\omega)$, with $\alpha(\omega)$ as the dynamic tortuosity and $\beta(\omega)$ as the dynamic compressibility. This means that in (2.17), $K_0 \rightarrow K(\omega)$ and $\rho_0 \rightarrow \rho(\omega)$. A more descriptive explanation of $\alpha(\omega)$ and $\beta(\omega)$ can be given by a generalization of Darcy's law (Stokes equation for creeping incompressible flow and neglecting the convective terms in (2.3)) [101], which describes the single-phase flow of a fluid through a

porous medium:

$$\begin{aligned}\langle \tilde{\mathbf{u}} \rangle \phi &= -\frac{1}{\mu_0} k_{\text{per}}(\omega) \nabla \langle \tilde{p} \rangle \\ \langle \tilde{T} \rangle \phi &= -\frac{1}{\kappa} k'_{\text{per}}(\omega) \frac{\partial}{\partial t} \beta_{\text{ex}} T_0 \langle \tilde{p} \rangle.\end{aligned}\quad (2.19)$$

In (2.19), μ_0 is the dynamic shear viscosity, κ the thermal conductivity, \tilde{T} the excess temperature fluctuation and $k_{\text{per}}(\omega), k'_{\text{per}}(\omega)$ are the viscous and thermal permeabilities [12, 101]. Darcy's law and the wave equation for (in)homogeneous media are related by

$$\alpha(\omega) = \frac{i\nu_0\phi}{\omega k_{\text{per}}(\omega)}, \quad \beta(\omega) = \gamma \left(1 + i\omega \frac{(\gamma-1)Pr}{\gamma\nu_0\phi} \right) k'_{\text{per}}(\omega), \quad (2.20)$$

with $\nu_0 = \mu_0/\rho_0$ as kinematic shear viscosity and $Pr = \mu_0 c_p/\kappa$ as the Prandtl number. Porosity ϕ is the area fraction that is in contact with the fluid.

2.1.4 Dissipation in bounded and unbounded media

At relevant sound propagating distances, e.g. in duct systems or rooms, one can neglect energy dissipation of the plane wave sound energy due to energy transfer between the three molecular energy degrees of freedom when not being in mutual thermodynamic equilibrium. This, however, becomes relevant at higher levels of humidity or multi-atomic gases and at more considerable wave propagation distances (see [131]) and can be modeled with a temperature- and pressure-dependent bulk viscosity μ_B [108]. The attenuation of a plane wave then computes by

$$\alpha_{\text{cl}} = \frac{\omega^2}{2\rho_0 c_0^3} \left[\frac{4}{3} \mu + \frac{(\gamma-1)^2 \kappa}{\gamma R} + \mu_B \right]. \quad (2.21)$$

Here, the absorption due to relaxation processes of the molecular vibrational energies to thermodynamical equilibrium of each molecular species (O_2, N_2 etc.) has been neglected. Additionally, sound perturbation waves that propagate along solid structures manifest the formation of viscous (δ_v) and thermal acoustic boundary layers (δ_t) with

$$\delta_v = \sqrt{\frac{2\mu_0}{\rho_0\omega}} \quad \text{and} \quad \delta_t = \sqrt{\frac{2\kappa}{\omega\rho_0 c_p}}. \quad (2.22)$$

The Prandtl number for air is of the order of one and assumed to be constant, therefore $\delta_v \approx \delta_t$. The boundary layer formation manifests in the micro-meter order of distance from the wall. The attenuation of acoustic energy is associated with viscous and thermal dissipation effects in the vicinity of the solid structure. A thermal wave is created due to successive compression and rarefaction of the sound wave, and thermal dissipation occurs when there

is heat exchange between fluid particles and the solid structure. Viscous dissipation occurs due to friction of air particles within a micro-meter range from the solid wall.

2.1.5 Sound field composition in a quiescent medium

The plane wave sound field in the linear approximation is composed of the acoustic (modal) wave, the vorticity and the entropy modal wave field, $\tilde{F} = \tilde{F}_{ac} + \tilde{F}_{vor} + \tilde{F}_{ent}$. The individual modal fields are uncoupled in the linear approximation except at boundaries. The formulations for each mode are derived from the acoustic approximation of the governing equations (2.16) with viscosity included and an entropy and temperature perturbation \tilde{s}, \tilde{T} [131, 158]. **Entropy mode:** In this mode the fluid flows from colder to hotter regions due to density changes. Entropy mode changes do not appear in the vorticity mode and rather small compared to the temperature perturbations in the acoustic mode

$$\begin{aligned} \tilde{k}^2 &= i\omega\rho_0c_p/\kappa, \text{ with solution and the linear relations:} & (2.23) \\ \tilde{s}_{ent} &= \tilde{s}_{ent,w}e^{-(1+i)z/\delta_v}, \tilde{p}_{ent} = 0, \tilde{\mathbf{u}}_{ent} = \left(\frac{\beta_{ex}T_0\kappa}{\rho_0c_p}\right)\nabla\tilde{s}_{ent}, \nabla\times\tilde{\mathbf{u}}_{ent} = 0, \\ \tilde{T}_{ent} &= \left(\frac{T_0}{c_p}\right)\tilde{s}_{ent}, \tilde{\rho}_{ent} = -\left(\frac{\rho_0\beta_{ex}T_0}{c_p}\right). \end{aligned}$$

Vorticity mode: The dispersion relation and linear relations of the vorticity mode correspond to an incompressible flow that is decoupled from the thermodynamic state of the fluid.

$$\begin{aligned} \tilde{k}^2 &= i\omega\rho_0/\mu_0, \text{ with solution and the linear relations:} & (2.24) \\ \tilde{\mathbf{u}}_{vor} &= \tilde{\mathbf{u}}_{vor,w}e^{-(1+i)z/\delta_v}, \nabla\cdot\tilde{\mathbf{u}}_{vor} = 0, \tilde{p}_{vor} = \tilde{s}_{vor} = \tilde{T}_{vor} = \tilde{\rho}_{vor} = 0 \end{aligned}$$

Acoustic mode: The acoustic mode solution for $\tilde{\mathbf{u}}$ and \tilde{p} has been presented in (2.17). The wavenumber for the acoustic mode is modulated by visco-thermal dissipation (imaginary part of the first term in (2.25)) in a finite medium (e.g. MPP) or in the unbounded medium due to relaxation processes in the molecular energy modes by

$$\begin{aligned} \tilde{k}^2 &= \frac{\omega^2\rho(\omega)}{K(\omega)} + \frac{2i\omega}{c_0}[\alpha_{cl} + (1-i)\alpha_{walls}], \text{ with the linear relations:} & (2.25) \\ \nabla\times\tilde{\mathbf{u}}_{ac} &= 0, s_{ac} = 0, \rho_0\frac{\partial\tilde{\mathbf{u}}_{ac}}{\partial t} = -\nabla\tilde{p}_{ac}, \tilde{T}_{ac} = \frac{T_0\beta_{ex}}{\rho_0c_p}\tilde{p}_{ac}, \tilde{\rho}_{ac} = \frac{\tilde{p}_{ac}}{c_0^2}. \end{aligned}$$

The influence of absorption in the acoustic boundary layer can be incorporated by the Kirchhoff solution for a circular duct with circumference $D_{duct}\pi$ and cross section area $D_{duct}^2\pi/4$ by [131, 138, 155]

$$\alpha_{walls} = \frac{2i}{\rho_0c_0D_{duct}}\left(z_\tau + \frac{\gamma-1}{c_p}z_q\right). \quad (2.26)$$

Here, the wall shear stress impedance z_τ and wall heat conduction impedance z_q , evaluated at the wall (subscript w), are defined by

$$z_\tau = \tilde{\tau}_w / \tilde{u}_w = \left(\frac{\mu_0 \partial \tilde{u}_{\text{vor},x} / \partial z}{\tilde{u}_{\text{vor},x}} \right)_w, \quad z_q = \left(\frac{\kappa \partial \tilde{T}_{\text{ent}} / \partial z}{\tilde{T}_{\text{ent}}} \right)_w, \quad (2.27)$$

with z as the normal direction towards the wall and $\tilde{\tau}_w$ as the coherent part of wall shear stress. The wall stress impedance is calculated from the vorticity field and therefore also the shear stress induced by a mean flow field (τ_w) and turbulent perturbations in the vicinity of the wall would contribute.

2.2 Attenuation of the acoustic mode in a semi-infinite homogeneous medium

The following models allow the simulation of the first term on the right-hand side of (2.25). An isotropic, homogeneous medium is assumed that has a finite thickness but infinite extension to the other two space coordinates. The local fluid velocity and pressure in the microscopic porous domain are averaged to macroscopic values and homogenized over the finite thickness (see (2.19)). The frequency-dependent bulk modulus and density in (2.25) constitute an equivalent isotropic, homogeneous fluid that has the same visco-thermal behavior as the real material (e.g., the MPP). Henceforth, $K(\omega)$ is named K_{eq} and $\rho(\omega)$ becomes ρ_{eq} .

2.2.1 Biot-modeling of fluid-structure interaction

Biot's poroelasticity equations [12, 25, 26] govern the elasto-acoustic behavior of fluid saturated porous isotropic medium with an elastic frame where viscous effects are accounted for with a structure factor. The porous material bulk movement consists of a longitudinal wave in the fluid and a longitudinal and transversal wave in the solid phase. The equivalent fluid density ρ_{eq} accounts for drag related dissipation and the equivalent bulk modulus K_{eq} for thermal-dissipative effects [22]. The drag effects are dominated by fluid viscosity for low frequencies and fluid particle inertia in the high-frequency range, depending on the Stokes number (see (2.32)). The elastic behavior is related to mechanical parameters of the frame material and may also be modulated by structural losses. With the partial stress tensor σ_s of a frame continuum element and by using the so-called $(\mathbf{u}_{\text{fr}}, \tilde{p})$ -formulation [16], where \mathbf{u}_{fr} is the frame displacement and \tilde{p} is the fluid pressure in the pores, the poroelastic behavior is described by

$$\nabla \cdot \sigma_s + \omega^2 \rho_{\text{mod}} \mathbf{u}_{\text{fr}} = -\gamma_{\text{mod}} \nabla \tilde{p} \quad (2.28)$$

$$\nabla^2 \tilde{p} + \frac{\rho_{\text{eq}}}{K_{\text{eq}}} \omega^2 \tilde{p} = \rho_{\text{eq}} \gamma_{\text{mod}} \omega^2 \nabla \cdot \mathbf{u}_{\text{fr}}, \quad (2.29)$$

with the modified density $\rho_{\text{mod}} = \rho_1 + \phi\rho_0 - \rho_0^2/\rho_{\text{eq}}$ and modified $\gamma_{\text{mod}} = \rho_0/\rho_{\text{eq}} - 1 = \alpha(\omega) - 1$. Also, $\rho_1 = (1 - \phi)\rho_s$ denote the frame density and ρ_s the density of the solid constituting the frame.

For a rigid and motionless frame the second equation becomes (2.17). When the frame is allowed to move, the complex mass density ρ_{eq} can be modified to account for additional inertia effects. Either the frame moves as a whole without deformation (stiff material, $E_s/\rho_s \gg 1$) or is limp ($E_s/\rho_s \ll 1$), where the porous frame is so soft that the coupling between the frame and the interstitial fluid is weak. For the MPP (coupling between air and metal) both of these cases do not apply, since they will be clamped and $E_s/\rho_s \gg 1$. One can assume a rigid frame of the porous material, characterized by static air flow resistivity σ and porosity ϕ , if the decoupling frequency is exceeded [12]:

$$f_d = \frac{\sigma\phi^2}{2\pi\rho_s} \quad (2.30)$$

The decoupling frequency for the MPP made of aluminum can initially be estimated below 1 Hz.

2.2.2 Morphology of porous materials

Each of the porous media models relies on different morphological parameters by which sound-absorbing porous materials can be categorized. There are structural and elastic parameters. Pore structure-related parameters are associated with the fluid and solid phase. The elastic parameters describe the visco-elastic behavior of the solid phase of the bulk material. Usually, in acoustic application studies, the vibration and deformations are kept small, with Young's modulus, Poisson's ratio and structural damping parameters describing the solid phase vibration behavior. On the other hand, up to nine pore structure parameters can be discerned that govern the acoustic attenuation behavior of a porous absorber [101]. The modeling assumption for the velocity field is normally a non-viscous fluid with boundary layer δ_v forming near the solid walls [12, 41, 127]:

- open porosity ϕ : ratio of the fluid volume to bulk volume (fluid plus solid phase of the porous material); portion of the area that is covered by the fluid (see (3.2) and Fig.3.2).
- high-frequency limit of tortuosity α_∞ : also known as sinuosity of the pore domain and is partly correlated to inertia drag effects in the high-frequency regime where the acoustic boundary layer is much smaller than the pore size. The apparent equivalent density due to drag forces is related to the dynamic tortuosity by $\rho_{\text{eq}}/\rho_0 = \alpha(\omega)$. The high frequency limit of ρ_{eq} is $\rho_0\alpha_\infty$. The porous frame is envisioned saturated by a non-viscous fluid. This fluid flows through the porous frame and the macroscopic velocity is obtained by averaging the microscopic local velocity over a representative elementary volume.

As far as the macroscopic velocity is considered, the non-viscous fluid must be replaced

by a fluid of density $\rho_0\alpha(\omega)$. Thus, the value of the tortuosity is an intrinsic property of the porous frame that depends on the micro-geometry [12].

- static air-flow resistivity $\sigma = \mu_0/k_0 = \Delta\tilde{p}_{\omega\rightarrow 0}/(ut_{\text{mat}})$: reflects fluid permeability through the porous material, depends on the fluid and is also defined as the resistance within a unit thickness t_{mat} of a porous material.
- viscous characteristic length Λ : [83] [36] represents the surface-to-pore-volume ratio. Each area or volume element is weighted according to the local pore velocity of the non-viscous fluid, since the viscous effects are located in a very small region close to solid walls of the pore; hence there is a connection to the scope of the inter-connection between two pores. Λ controls viscous effects at medium to high frequencies.
- thermal characteristic length Λ' : [36] surface-to-pore-volume ratio without the local velocity weighting.
- static viscous permeability k_0 : reflects fluid permeability through the porous material, independent of the fluid and is defined with Darcy's law [83]:

$$\langle \tilde{\mathbf{u}} \rangle \phi = -\frac{k_{\text{per}}(\omega)}{\eta_0} \nabla \tilde{p}; k_0 = \lim_{\omega \rightarrow 0} k_{\text{per}}(\omega). \quad (2.31)$$

An important factor in the low-frequency, viscous regime and related to the geometry of the micro-structure and controlling thermal effects at medium and high frequencies.

- static thermal permeability k'_0 : has a similar role in the description of thermal exchanges as viscous permeability has in the case of viscous forces. Characterizes partly the thermal effects of excess temperature \tilde{T} at low frequencies when the size of boundary layer δ_v is of the order of the pore size:

$$\langle \tilde{T} \rangle \phi = -\frac{k'_{\text{per}}(\omega)}{\kappa} \frac{\partial p}{\partial t}; k'_0 = \lim_{\omega \rightarrow 0} k'_{\text{per}}(\omega); k'_0 \geq k_0.$$

- static viscous tortuosity α_0 or low frequency limit of tortuosity: is defined as α_∞ , but in the static flow field at $\omega = 0$ (a viscous fluid is assumed). One has found that $\alpha_0 \geq \alpha_\infty$ [12].
- static thermal tortuosity $\alpha'_0 \simeq \alpha_0/\alpha_\infty$ [142].

2.2.3 MPP modeling

For the following four MPP models, a rigid porous material is assumed, because of the low decoupling frequency f_d . The Maa model describes the effective surface impedance of a single MPP pore scaled to the extended screen with porosity ϕ , whereas the other three can model

the equivalent characteristic impedance Z_m of the MPP domain. The model of Delany-Bazely-Miki describes locally-reacting porous materials with a very high porosity.

Analytical model: impedance of an MPP

According to Maa [113] an MPP "...is a lattice of short narrow tubes, separated by distances much larger than their diameter, but small compared to the wavelength of impinging sound waves". Based on the treatment of sound waves in tubes, he solved the momentum equation in circular coordinates in the frequency domain and calculated thereby the impedance of a single hole. The equation was later adapted to account for hole-to-hole-interaction (over perforation) with a Fok-like function $F(\epsilon)$ [38]. The over perforation function diminishes the length correction (see Fig. 2.1) excess due to fluid flow interaction between neighboring holes. The impedance consists of two parts: the resistive part of the surface resistance of one hole due to friction of the fluid flow at the edges and the reactive part due to the piston-like movement of the envisioned air plug at both edges (see Fig. 2.1) linked to acoustic radiation. The effective surface impedance of an infinite MPP sample with thickness t_{MPP} in front of an air cavity of length L_c computes by

$$Z_{\text{Maa}} = \frac{1}{\phi} \underbrace{\left(\frac{\sqrt{2\rho_0\omega\mu_0}}{2} + i\omega\rho_0 0.85 \frac{d}{F(\epsilon)} \right)}_{\text{hole edge length + added mass correction}} + \frac{1}{\phi} \underbrace{i\omega\rho_0 t_{\text{MPP}} \left[1 - \frac{2}{St\sqrt{-i}} \frac{J_1(St\sqrt{-i})}{J_0(St\sqrt{-i})} \right]^{-1}}_{Z_{\text{hole}}} - iZ_0 \cot(\tilde{k}_0 L_c), \quad (2.32)$$

where $St = d\sqrt{\omega\rho_0/4\mu_0} = d/(2\delta_v)$ is the acoustical Reynolds number. It is defined as the ratio of the diameter of perforations d to the boundary layer thickness. It is also called the Stokes number St and J_1, J_0 are Bessel functions of first kind and first and zeroth order. The function F is a power series with the parameter $\epsilon = \sqrt{\phi}$ that weights the influence of ϕ on the length correction [38] and Z_0 is the characteristic impedance of air. In fluid dynamics the Stokes number is a measure of the characteristic time of a fluid particle to the characteristic time of the flow:

$$St = \frac{\tau_{\text{drag}} |\mathbf{u}|}{d}, \quad (2.33)$$

where τ_{drag} is the time constant in the exponential decay of a fluid particle velocity due to drag. A fluid particle with a Stokes number less than unity follows the streamlines of the flow \mathbf{u} and if greater than unity, the particle in the fluid is more and more dominated by its inertia and differs from the streamline path. The Stokes number in acoustics is the ratio of the characteristic pore dimension d to the acoustic boundary layer δ_v . If the ratio is low, then the entire flow profile in the pore is formed by viscous friction or drag (Hagen-Poiseuille profile). If the ratio is high, then friction is only concentrated in a small domain near the solid surface, and the flow profile resembles that of a turbulent macroscopic flow profile. This

regime is dominated by inertial drag. The imaginary (reactance) part of the surface impedance Z_{Maa} is associated with inertia drag, the real (resistance) part with viscous drag. The porous media models each account for the two impedance portions with different expressions [15, 118]. From a macroscopic point of view, the flow through an MPP or generally a porous material is governed by Darcy's law (2.19) (or (2.18)), if the Stokes number is low, respectively, if the frequency is low.

Empirical Model: Delany-Bazely-Miki

The empirical models by Delany and Bazely [41] and their modifications by Miki [119] were derived by curve-fitting of the real and imaginary part of measured surface impedances of a large number of porous materials. The equation describe how the complex surface impedance and complex propagating wave number vary with static flow resistivity σ . They are able to produce accurate predictions of porous materials with a porosity ϕ close to unity and are applicable in the range of $0.01 < f/\sigma < 1.00$

$$Z_{\text{Miki}} = \rho_0 c_0 \left[1 + 5.50 \left(10^3 \frac{f}{\sigma} \right)^{-0.632} - i 8.43 \left(10^3 \frac{f}{\sigma} \right)^{-0.632} \right], \quad (2.34)$$

$$\tilde{k}_{\text{Miki}} = \frac{\omega}{c_0} \left[1 + 7.81 \left(10^3 \frac{f}{\sigma} \right)^{-0.618} - i 11.41 \left(10^3 \frac{f}{\sigma} \right)^{-0.618} \right], \quad (2.35)$$

where Z_{Miki} is the characteristic impedance and \tilde{k}_{Miki} the wave number of the porous material. This model is mentioned for completeness and can not reproduce the MPP behavior, because the investigated MPPs are of much lower porosity than unity.

Semi-empirical equivalent fluid: Biot-rigid frame-JCAL

Asymptotic low and high-frequency matching is an inherent part of semi-empirical modeling. The bulk fluid can be regarded as inviscid and adiabatic except for a lossy boundary layer at the pore walls in the high-frequency regime. By tortuosity α_∞ and thermal (Λ') and viscous characteristic (Λ) length of the pores, the inertia effects, and thermal dissipative effects can be incorporated in a frequency-dependent model [36]. In the low-frequency regime, the fluid in the pores behaves more viscous and isothermal [74]. The viscous and inertia effects are described by the static viscous permeability k_0 and the static viscous tortuosity α_0 . The thermal effects are described by the static thermal permeability k'_0 and the static thermal tortuosity α'_0 [137][169] [36]. The low- and high-frequency regime for a porous material of circular characteristic length (pore size) $r_{\text{pore}} = d/2$ and straight pores ($\alpha_\infty = 1$) can be

determined by the viscous and thermal Biot frequency [74]

$$\omega_v = \frac{8\mu_0}{r_{\text{pore}}^2 \rho_0} = \frac{\mu_0 \phi}{\rho_0 \alpha_\infty k_0} \quad \text{with} \quad \sigma = \frac{8\mu_0}{\phi r_{\text{pore}}^2} \quad \text{and} \quad \omega_t = \frac{\kappa}{r_{\text{pore}}^2 \rho_0 c_p}. \quad (2.36)$$

The low-frequency viscous-isothermal regime applies for $\omega \ll \omega_v, \omega_t$ and is to be separated from the high-frequency regime ($\omega \gg \omega_v, \omega_t$), where the fluid behaves adiabatic and inertia effects dominate. The JCAL modeled equivalent density is present in the Biot-Allard model for poroelastic media which must be used when the wave propagation in the solid frame cannot be neglected. The equivalent fluid model also uses tortuosity to account for overperforation effects and hole-to-hole-interaction effects [80] [81] with a Fok-like function and the length correction parameter ϵ . The expression for ρ_{eq} was derived by Johnson et al. [83] and later by Champoux et al. [36] and accounts for drag effects (viscous and inertia) due to the micro-structure [14]. The equation for K_{eq} was derived by Lafarge et al. [102]. The effective impedance of one MPP pore (basically a one pore-MPA) connected to an air cavity of length L_c is

$$Z_{\text{MPP, one hole}} = i\omega \rho_{\text{eq}} t_{\text{MPP}} - i\phi Z_0 \cot(\tilde{k}_0 L_c). \quad (2.37)$$

For an entire screen or plate made up of pores with impedance $Z_{\text{MPP, one hole}}$ and porosity ϕ , the density of the equivalent fluid is

$$\rho_{\text{eq,scr}} = \frac{\rho_0 \alpha(\omega)}{\phi} = \frac{\alpha_\infty \rho_0}{\phi} \left[1 + \frac{\sigma \phi}{i\omega \rho_0 \alpha_\infty} \sqrt{1 + i \frac{4\alpha_\infty^2 \mu_0 \rho_0 \omega}{\sigma^2 \Lambda^2 \phi^2}} \right] \quad \text{with} \quad \alpha_\infty = 1 + \frac{2\epsilon}{t_{\text{MPP}}}, \quad (2.38)$$

and (2.38) becomes

$$Z_{\text{MPA}} = i\omega \rho_{\text{eq,scr}} t_{\text{MPP}} - iZ_0 \cot(\tilde{k}_0 L_c).$$

The formulation for $K_{\text{eq,scr}}$ to incorporate the thermal-dissipation effects by the acoustic boundary layer contains the angular frequency weighted with the Prandtl number $Pr = \mu_0 c_p / \kappa$

$$K_{\text{eq,scr}} = \frac{\gamma p_0}{\phi} \frac{1}{\beta(\omega)} = \frac{\gamma p_0 / \phi}{\gamma - (\gamma - 1) \left[1 + \frac{\phi \mu_0}{i\omega k_0' Pr \rho_0} \sqrt{1 + i \frac{4\omega Pr k_0'^2 \rho_0}{\mu_0 \Lambda^2 \phi^2}} \right]^{-1}}. \quad (2.39)$$

Here $\beta(\omega)$ is the dynamic compressibility [102] and $K_0 = \gamma p_0$, as in the ideal gas. Similarly, as in the Maa model $\epsilon(\sqrt{\phi})$ is a power series that weights the influence of perforation rate on the correction lengths for the moving air piston in a single pore. The complex valued equivalent impedance can be computed by $Z_m = \sqrt{\rho_{\text{eq,scr}} K_{\text{eq,scr}}}$ and the complex valued

propagating wave number $\tilde{k} = \omega \sqrt{\rho_{\text{eq,scr}}/K_{\text{eq,scr}}}$. The low and high frequency limits in first order approximation [12] for $\rho_{\text{eq,scr}}$ are

$$\lim_{\omega \rightarrow 0} \rho_{\text{eq,scr}} = \frac{\alpha_{\infty} \rho_0}{\phi} \left(1 + \frac{2\alpha_{\infty} \mu_0}{\sigma \Lambda^2 \phi} \right) - i \frac{\sigma}{\omega} \quad (2.40)$$

$$\lim_{\omega \rightarrow \infty} \rho_{\text{eq,scr}} = \alpha_{\infty} \rho_0 \left(1 + \frac{\delta_v}{\Lambda} \right) - i \alpha_{\infty} \rho_0 \frac{\delta_v}{\Lambda}. \quad (2.41)$$

For identical cylindrical pores with characteristic length $r_{\text{pore}} = d/2$, the flow through the pores (assuming Poiseuille flow, no convective term in the momentum equation) is perpendicular to the cross section and the pressure is uniform over the cross section, then the viscous and thermal problem happen to have the same mathematical form and the following relations hold [102]:

$$\begin{aligned} k'(\omega) &= k(Pr\omega) & \Lambda &= \Lambda' = r_{\text{pore}} \\ k_0 &= k'_0 = \phi r_{\text{pore}}^2 / 8 & \sigma &= 8\mu_0 / (\phi r_{\text{pore}}^2) \end{aligned} \quad (2.42)$$

The roughness of the surface within the slits could affect the high-frequency permeability, respectively the static flow resistance, as described in [40]. However, due to the thinness of the MPP, such an influence was not further considered.

Semi-empirical equivalent fluid: Biot-rigid frame-JCAPL

The JCAL and Biot model approach lead to an underestimation of the imaginary part of the dynamic permeability at low frequencies with the amount of discrepancy increasing with the magnitude of the maximum pore-wall slope relative to the (circular) perforation channel axis [133]. The drag within pores of variable shape is considered in this model. Form drag always contributes to drag forces when there is a non-constant channel width. Thereby, the contribution increases with an increasing slope of the walls of the channel. Friction drag mainly appears in the smallest apertures (pores).

The low-frequency corrected expression for the equivalent density is [12]

$$\rho_{\text{eq,scr}} = \frac{\alpha_{\infty} \rho_0}{\phi} \left[1 + \frac{\sigma \phi}{i \omega \rho_0 \alpha_{\infty}} \left(1 - b_{\text{form}} + b_{\text{form}} \sqrt{1 + i \frac{4\alpha_{\infty}^2 \mu_0 \rho_0 \omega}{b_{\text{form}}^2 \sigma^2 \Lambda^2 \phi^2}} \right) \right] \quad (2.43)$$

The factor b_{form} can be identified as the maximum channel-wall or streamline slope within the pores of the bulk material [12]. Generally the following relation holds

$$b_{\text{form}} = \frac{2k_0 \alpha_{\infty}^2}{\phi \Lambda^2 (\alpha_0 - \alpha_{\infty})}. \quad (2.44)$$

For straight pores, the form factor is $b_{\text{form}} = 1$.

Relaxational Model

This model is intended to match sound wave relaxation characteristics and not to fit the asymptotic behavior at high and low frequencies as the models before [12]. The parameters τ_{vor} and τ_{ent} are the vorticity-mode and entropy-mode relaxation time. The simplified form of the equations for circular pore geometry are

$$\rho_{\text{eq,scr}}(\omega) = \rho_{\infty} \frac{(1 + i\omega\tau_{\text{vor}})^{1/2}}{(1 + i\omega\tau_{\text{vor}})^{1/2} - 1}, \quad K_{\text{eq,scr}}(\omega) = K_{\infty} \frac{(1 + i\omega\tau_{\text{ent}})^{1/2}}{(1 + i\omega\tau_{\text{ent}})^{1/2} + \gamma - 1}. \quad (2.45)$$

Approximated estimations (compared with the JCAL model) for $\tau_{\text{vor/ent}}$ are based on parameters of the porous material [158]

$$\begin{aligned} \tau_{\text{vor}} &= \rho_0 \mu_0 \left(\frac{2\alpha_{\infty}}{\phi \sigma \Lambda} \right)^2 & \tau_{\text{ent}} &= \frac{\rho_0 P r \Lambda^2}{\mu_0 4} \\ \rho_{\infty} &= \frac{\rho_0 \alpha_{\infty}}{\phi} & K_{\infty} &= \frac{\gamma P_0}{\phi}. \end{aligned} \quad (2.46)$$

The acoustic mode propagation is modeled without the influence of drag, and the process is seen as an adiabatic change of thermodynamic state variables. Therefore it is unaffected by the presence of the porous frame. The interaction with the porous frame only takes place within the thin boundary layer manifesting near the pore surface. The relaxation time τ_{vor} is the time that the velocity field takes to establish equilibrium with the counteracting frictional forces across the porous medium pore surface. The time τ_{ent} is needed for the heated fluid in the pore to establish thermal equilibrium by heat conduction with the frame material [17, 126, 128, 158, 159].

Schematic of oscillating flow through an MPP pore

The models emulating the measured data each involve certain assumptions about the influence of viscous and inertia drag a fluid particle is exposed to in the oscillating wave motion through a micro-perforated. The distortion of the flow streamlines is cast into resistive correction lengths that account for surface and inner viscous effects near a pore, as well as reactive correction lengths that express additional mass loading of the envisioned moving air plug in the pore (see Fig. 2.1). Both physical phenomenons manifest in the aforementioned apparent equivalent frequency-dependent density ρ_{eq} . Depending on the Stokes number, the interpolating weighting function in the JCAL model, either augments the viscous or inertial correction. For $K_{\text{eq,scr}}$ either the isothermal or adiabatic correction is affected. The characteristic pore size r_{pore} , whether measured or fitted, has been shown to greatly affect the

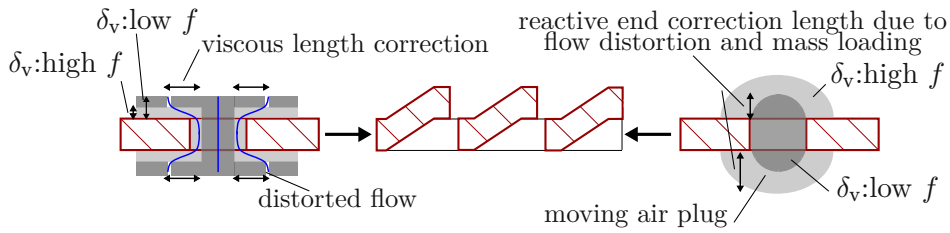


Figure 2.1: Near the MPP pore oscillating flow streamlines (blue) and the length corrections to account for viscous and inertia drag portions for the ideal circular straight pore [15, 118]; MPP material under investigation depicted in the center.

visco-inertial limiting frequency $f_v = 2\pi\omega_v$. The larger the characteristic pore size, the lower is f_v . This means that if the pore size is large, viscosity-driven friction/drag merely plays a role in the lower-frequency spectrum. Here, the viscous boundary layer thickness δ_v is also larger and in the order of the pore size. With a smaller boundary layer thickness in the higher-frequency range, the inertia-driven drag is predominant.

The following investigations with different sound fields aim to determine whether the two drag regimes can be discerned. And if they can, which drag mechanisms dominate absorption in case of the very thin MPP and more dedicated MPA configurations.

2.3 Acoustic field characterization

Near and far field in the quiescent medium

Already in one millimeter away from any solid structure in a quiescent medium, it is valid to assume the sole presence of an inviscid flow-dominated acoustic mode field. Depending on the nature of the boundary conditions, one can discern a *direct* acoustic wave field (free wave propagation, no reflections eigenmode shapes, just plane wave fronts) and a *diffuse* acoustic field due to multiple reflections in a duct or at solid boundaries in a room and the manifestation of higher order mode shapes [106]. In the free field the sound pressure level decays by 6 dB per doubling the distance from the source, whereas in the diffuse field, a spatially homogeneous sound pressure level develops. The level of homogeneity depends on the frequency and modal density of the bounded space. Generally, in a diffuse sound field acoustic particle velocity and pressure appear to be uncorrelated signals [139]. Depending on the compactness of a sound source, the distance from the source and the wavelength, one can also discern the *near* field (being reactive, particle velocity and pressure are out of phase) and the *far* field (being active, particle velocity and pressure are out of phase) relative to a source. The diffuse sound field is neither active nor reactive. The *far* field is approximately either a *diffuse* or a *direct* sound field. The directionality of the sound field emitted into the far field from a piston radiator with characteristic length l , can be defined by the Helmholtz number $He = k_0 l$. If $k_0 l \ll 1$, the sound is more or less isotropically emitted (half sphere

pattern). However, if $\tilde{k}_0 l \gg 1$ then the sound emission is bundled with a maximum of sound pressure on the perpendicular bisector of the piston. The near field length $N_{\text{near}} = l^2/\lambda$ defines the boundary between the *near* and the *far* field. In the far field the sound field is much more homogeneous than in the near field.

Duct acoustics

For the acoustic mode sound wave propagating along the longitudinal axis x of a duct without dissipation, bounded in y, z -direction by its circumference (rectangular or circular), the wave equation (2.17), its solution and the axial propagating wavenumber \tilde{k}_x are given by:

$$\begin{aligned} \nabla^2 \tilde{p} + \left(\frac{\omega^2}{c_0^2} - \tilde{k}_{mr}^2 \right) \tilde{p} &= 0 & -\nabla_{y,z}^2 \tilde{p} &= \tilde{k}_{mr}^2 \tilde{p} \\ \tilde{k}_x &= \sqrt{(\omega/c_0)^2 - \tilde{k}_{mr}^2} = \sqrt{\tilde{k}_0^2 - \tilde{k}_{mr}^2}. \end{aligned} \quad (2.47)$$

Here \tilde{k}_{mr} is the cross section modal wavenumber with mode order (m, r) . The plane-wave mode is always propagating (order $(0, 0)$). The modes that have $\tilde{k}_{mr}^2 > \tilde{k}_0^2$ are evanescent ("cut-off"), but are propagating if $\tilde{k}_{mr}^2 < \tilde{k}_0^2$. For the rectangular duct with maximum cross sectional length L_{max} and the circular duct with radius R_{duct} , all higher modes are cut-off if the following inequality holds [106, 131, 136]

$$\omega < c_0 \pi / L_{\text{max}} \quad \text{or} \quad \omega < 1.841 c_0 / R_{\text{duct}}. \quad (2.48)$$

2.4 Excitation of an aperture under grazing flow influence

So far, the dissipation of wave propagation due to influences of the viscous and thermal effects in a boundary layer near a solid surface or on the pore surface of a finite porous material has been discussed. However, the wave propagation is also influenced by mean flow convection, mean flow refraction and turbulent absorption [155], especially for an acoustic wave in a wave guide with propagating wave number \tilde{k}_x (for convenience only the plane wave relation is considered). It is assumed that the acoustic mode wavenumber \tilde{k} is already modulated by the effects of the acoustic boundary layer forming at the walls (cf. α_{walls} in (2.24)). Depending on the Mach number Ma , the downstream (+) and upstream (-) propagating waves are modulated by

$$\tilde{k}_{x,\pm} = -\tilde{k} \frac{-Ma \pm 1}{1 - Ma^2} \quad \text{and} \quad \alpha_{\pm} = -\Im(\tilde{k}_{x,\pm}). \quad (2.49)$$

The convection effect would then decrease attenuation for the downstream wave and cause more attenuation of the upstream acoustic wave. Refraction would guide the downstream wave toward the wave guide walls and the upstream wave towards the wave guide's center. This would result in an increase in attenuation of the downstream wave and a decrease in

attenuation of the upstream wave. Convection would also be more important in the low He number range, and as the Helmholtz numbers increase, refraction would dominate α_{\pm} . [155] The wave attenuation α_{\pm} due to fluid convection is neglected in the following investigations due to the rather small Mach numbers.

2.4.1 Modeling turbulent wall pressure spectra

The random hydraulic pressure fluctuations p' convecting with the bulk flow and impinging on the solid walls of a duct can be simulated by a model developed by Goody [68]. It is a semi-empirical model for the frequency-dependent power spectral density of the pressure field $\Phi_{\text{surf}}(\omega)$ beneath the hydraulic boundary layer:

$$\frac{\Phi_{\text{surf}}(\omega)U_e}{\delta_{99}\tau_w^2} = \frac{C_2(\omega\delta_{99}/U_e)^2}{[(\omega\delta_{99}/U_e)^{0.75} + C_1]^{3.7} + [C_3(\omega\delta_{99}/U_e)]^7}, \quad (2.50)$$

where C_1 , C_2 and C_3 are empirical constants, which will be explained in the corresponding chapter. The boundary layer thickness δ_{99} , the velocity at the boundary layer's edge U_e , and the wall shear stress τ_w will be measured. Thus, the model can be tuned to the observed wall pressure levels.

2.4.2 Ansatz for cavity sound

The model for the simulation of the sound in a single overflowed cavity can be reviewed in the works of Howe, Golliard and Gloorfelt [61, 66, 77]. It is based on the simulation of fluctuations of a one-sided flow past an aperture represented by a vortex sheet. The key idea is the modulation of the volume flux $Q(\omega)$ across an aperture, with (hydraulic, random) pressure p_+ and p_- on either side. The volume flux is driven by the pressure differential across the aperture and expressed as a vortex sheet displacement.

The displacement of the vortex sheet is represented by Kelvin-Helmholtz wave numbers σ_1 and σ_2 , which are calculated by

$$\sigma_1 = \frac{\omega 2l_{\text{pore}}(1+i)}{U_+ + iU_-} \text{ and } \sigma_2 = \frac{\omega 2l_{\text{pore}}(1-i)}{U_+ - iU_-}, \quad (2.51)$$

where $U_+ = U_0$ and $U_- = 0$. With U_0 as the bulk flow velocity. The fluctuating mass flow, now affects the Rayleigh conductivity K_R , which is the inverse of the impedance of an aperture under grazing flow [61]:

$$K_R = \frac{i\omega Q(\omega)}{p_+ - p_-} = \frac{\pi b_{\text{pore}}}{2F(\sigma_1, \sigma_2) + \Psi}, \text{ with } \Psi = \ln(4b_{\text{pore}}/e^1 l_{\text{pore}}). \quad (2.52)$$

Here, l_{pore} and b_{pore} are the dimensions of the MPP slit, and the function $F(\sigma_1, \sigma_2)$ can be found in Appendix E (cf. (6.11)). This function can signify the energy transfer from the mean flow towards the vortex sheet fluctuations. It is found that $F(\sigma_1, \sigma_2)_{U_0=0} = -2$ [146].

2.4.3 Ansatz for emitted sound of a circular aperture

In [53], Ffowcs Williams argues that an overflown screen with low porosity and N perforations supports a monopole at each aperture with radius r_{ap} . Then in each aperture, he envisioned a rigid piston that can move perpendicular to the screen surface (z -direction) with an average impedance Z_0 . The pressure and fluid (particle) velocity v at the i th aperture located at \mathbf{y}_i on the screen surface are then related by:

$$-\frac{1}{\pi r_{\text{ap}}^2} \int p dS_{r_{\text{ap},i}} = Z_0 v = \frac{Z_0}{i\omega\rho_0} \frac{\partial \tilde{p}}{\partial z} = \frac{Z_0 Q(\omega)_i}{i\tilde{k}_0 \rho_0 c_0 \pi r_{\text{ap}}^2}, \quad (2.53)$$

where the acting pressure on the piston p is made up of a slowly varying acoustic part and a rapidly varying hydraulic part p' , and $Q(\omega)_i$ is i th monopole strength associated with the mass flow through an infinitely baffled circular aperture. The mass flow results in a force on the piston. This force accordingly also has an "acoustic" and a separated "hydraulic" part. The monopole strength $Q(\omega)_i$ can be interpreted as follows. The pressure on the rigid baffle with cross section areas $S_{r_{\text{ap},i}}$ is twice the pressure in the free field. This pressure induces a motion of the envisioned piston which supplements the local (hydraulic) pressure p' by an "acoustic" amount $(8/3\pi)i\rho_0 c_0 \tilde{k}_0 r_{\text{ap}} v$. It follows that

$$2p' + (8/3\pi)i\rho_0 c_0 \tilde{k}_0 r_{\text{ap}} v = Z_0 v, \quad \text{thus } v = \frac{2p'}{Z_0 - (8/3\pi)i\rho_0 c_0 \tilde{k}_0 r_{\text{ap}}}. \quad (2.54)$$

Each piston moving with this velocity then induces a monopole of strength

$$Q(\omega)_i = i\tilde{k}_0 r_{\text{ap}}^2 \rho_0 c_0 \pi v = \frac{i\tilde{k}_0 r_{\text{ap}}^2 \rho_0 c_0 \pi 2p'}{Z_0 - (8/3\pi)i\rho_0 c_0 \tilde{k}_0 r_{\text{ap}}}. \quad (2.55)$$

Each monopole radiates through the screen with $1-r$ a field $(\exp(i\tilde{k}_0 R_{\text{Mic}})/4\pi R_{\text{Mic}})Q(\omega)_i(1-r)$. Here, for N circular apertures, the homogeneous surface impedance is

$$Z_{\text{eff}} = \frac{Z_0 - (8/3\pi)i\tilde{k}_0 r_{\text{ap}} \rho_0 c_0}{\pi r_{\text{ap}}^2 N} \quad \text{and } r = \frac{Z_{\text{eff}} - \rho_0 c_0}{Z_{\text{eff}} + \rho_0 c_0}. \quad (2.56)$$

The monopoles radiate and are reflected in the screen surface with reflection coefficient r so that the scattered, respectively emitted field at position \mathbf{x} from all pistons is

$$-\sum_i^N (1-r) \frac{2p' i\tilde{k}_0 r_{\text{ap}}^2 \rho_0 c_0 \pi}{Z_0 - (8/3\pi)i\tilde{k}_0 r_{\text{ap}} \rho_0 c_0} \frac{\exp(i\tilde{k}_0 |\mathbf{x} - \mathbf{y}_i|)}{4\pi |\mathbf{x} - \mathbf{y}_i|}, \quad \text{here } |\mathbf{x} - \mathbf{y}_i| \approx R_{\text{Mic}}. \quad (2.57)$$

Predictive design

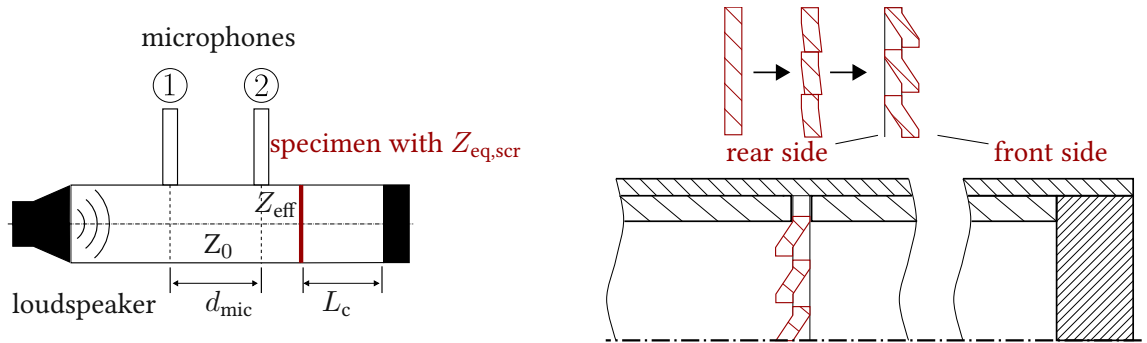
In this section, the procedure of obtaining MPP material parameters for the acoustic simulation of more advanced MPAs is described. Following this, design studies of MPA structures and sensitivity-to-sound-field investigations are conducted using the equivalent fluid approach combined with the Finite Element (FE) Method. The influence of the MPA on reflected, absorbed and transmitted sound power are assessed separately by comparing simulated and measured data.

3.1 Material characterization using an impedance tube

The reproducibility of standing wave impedance tube measurements (Fig. 3.1,[37]) of porous materials with an effective surface impedance Z_{eff} , characteristic impedance $Z_{\text{eq,scr}}$, thickness t_{MPP} and cavity length L_c is influenced a.o. by the mounting conditions of the specimen, sample preparation, excitation signal and the signal processing and the microphone distance d_{mic} [43, 75, 132]. In particular, the main sources of error in the two and four microphone impedance tube measurements are [2, 4]:

- the microphone phase mismatch error,
- the bias error of the measurement system or the impedance tube setup,
- the tube attenuation α_{cl} and α_{walls} (2.21, 2.26) and
- a vibrating sample, due to unfavorable mounting conditions (6.10).

The accuracy depends on the stationarity of electronic systems and FFT averages. For materials with a high sound power transmission, the phase mismatch between the microphones



(a) Impedance tube with MPP specimen, characterized by its surface impedance Z_{eff} , characteristic impedance $Z_{eq,scr}$ and microphone distance d_{mic} .

(b) Enlarged view of MPP mounting in the impedance tube; process of plastically deforming semi-finished (plate) good to MPP.

Figure 3.1: Sheet material parameter characterization, production process and mounting in the impedance tube.

is a major biasing concern. Bias and random errors can be avoided by choosing an optimal $\tilde{k}_0 d_{mic}$, a non-reflective source and a not too long impedance tube [30]. One can further reduce the phase mismatch by calculating a correction transfer function between the microphones by performing microphone switching. The vibrating part can either be accounted for with correcting the MPP characteristic impedance with the impedance of the MPP panel Z_p under eigenexcitation (6.10), or by clamping the specimen or by using adhesive for mounting the specimen rather rigidly in the tube section (see Fig. 3.1 (b)). The excitation signal in the measurements was either white noise or a Maximum Length Sequence (MLS) with a power level of 90 dB. 400 FFT averages have been used for a total measurement time of 16 s. The measured frequency range was 100 Hz to 6400 Hz. The tube attenuation α_{cl} and α_{walls} was neglected due to the rather short impedance tube length of 30 cm, as it is recommended in EN ISO norm [2]. The microphone phase mismatch issue can lead to erroneous results due the high sensitivity to errors in the microphone data input in the frequency regions below f_{low} and beyond f_{up} [30]:

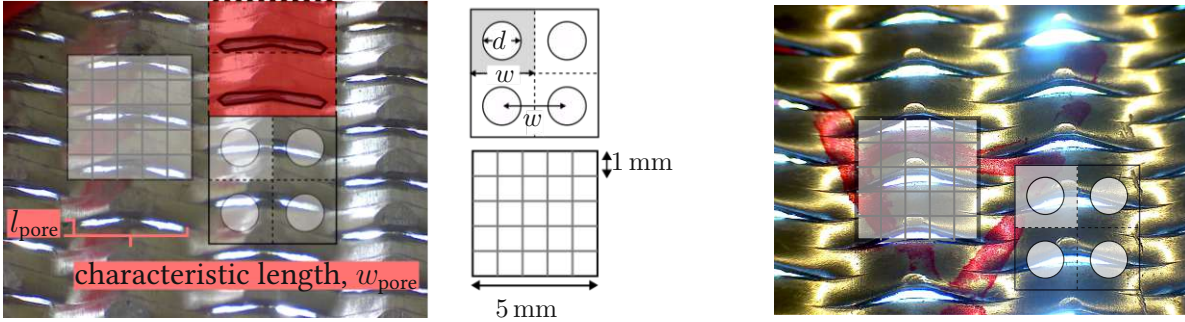
- $f_{low} < 857$ Hz and $f_{up} > 6860$ Hz for $d_{mic} = 20$ mm and
- $f_{low} < 952$ Hz and $f_{up} > 7622$ Hz for $d_{mic} = 18$ mm

(3.1)

3.1.1 Materials

Seven micro-perforated materials based on different semi-finished goods were investigated. As can be seen in Fig. 1.1 (b) MASH is a wire-like material. The perforates shown in Fig. 3.2 (a) are MPP type C which is based on a 1 mm thick aluminum plate and MPP type B (Fig. 3.2 (b))

based on a 0.55 mm stainless steel plate. In comparison, the MASH has a stainless steel wire frame with an effective thickness of ≈ 0.7 mm. The schematic view in Fig. 3.2 (a) with a unit



(a) MPP type C: Aluminum plate based with slit-shaped perforations; rear view.

(b) MPP type B: stainless steel based; rear view

Figure 3.2: Close-up image of plate-based MPP materials. Indicated slit lengths l_{pore} , w_{pore} and square of 25 mm^2 to compare slotted perforations with uniformly distributed circles with pore diameter d and distance w of the pores to each other.

rectangle shows the understanding of the perforation ratio ϕ and ϵ as [113][38]

$$\phi = \frac{\pi}{4} \left(\frac{d}{w} \right)^2 \quad \text{and} \quad \epsilon = \sqrt{\phi} \approx \frac{d}{w}. \quad (3.2)$$

In (3.2) w denotes the separation between circular holes uniformly distributed and characteristic length $d = 2r_{\text{pore}}$ is the diameter of the circular perforation. The slotted plate material is characterized by the manufacturer-provided porosity and a length l_{pore} and width w_{pore} of the slits. Following Fig. 3.1 (b), it is noteworthy that due to the manufacturing process a rear and front side of the plate-based MPPs can be discerned.

3.1.2 Fitting procedure

The measured impedance tube data was inversely fitted to a 1D simulation of a semi-infinite MPP domain modeled via aforementioned equivalent fluid models [80, 170]. The procedure is comparable to that of Zielinski [169] or Jaouen-Bécot [80]. However, the fitting was accomplished with a genetic algorithm that minimizes a cost function containing the measured impedance tube and simulated data.

Generally in an optimization task the goal is to find $\mathbf{x}^* \in \mathcal{X}$ from a given set $\mathcal{X} \in \mathbb{R}^P$. The

basic optimization problem can be written mathematically as

$$\begin{aligned} & \min_{\mathbf{x} \in \mathcal{X}} J(\mathbf{x}) \\ \text{subject to} & \quad a_i(\mathbf{x}) \leq 0 \quad i = 1, \dots, m \\ & \quad b_j(\mathbf{x}) = 0 \quad j = 1, \dots, n. \end{aligned} \tag{3.3}$$

In (3.3) $J(\mathbf{x})$ is the (objective) function to be minimized. Additionally, $a_i(\mathbf{x})$ and $b_j(\mathbf{x})$ represent constraints for the design variables x_1, \dots, x_p in a tuple $\mathbf{x} = (x_1, \dots, x_p) \in \mathcal{X}$. The algorithm applied [115] uses a gradient-free method of selecting among a population of individuals the "fittest" members to minimize the objective function [64, 73]. This synthetic evolutionary process is steered by preserving "fit" members of the population and eliminating "unfit" ones (the term "fit" is to be understood in the sense of "well adapted"). The members of the population are restricted by the constraints of the search space for the design variables. Here, the limits for the MPP parameters (ϕ , r_{pore} etc.) set by the investigator. Within these limitations, the optimization algorithm searches for a global minimum. So, each individual is a certain combination of constraint values within the design variable tuple \mathbf{x} . The algorithm consists of these basic steps:

1. Creating a random initial population
2. Determining the fitness of each individual of the current population by evaluation of the objective function. If the fitness of an individual meets a stopping criteria the algorithm stops.
3. Creating the next generation. This involves using the current population to create the children who represent the next generation. In the selection process, parents are selected that will contribute their genes to the next population. The applied version of the algorithm only uses elite children, which are individuals with the best fitness value.

The creation of a next generation from the current population is stopped when one of the stopping criteria is met:

- Exceeding the maximum number of generations G_{max} (here $G_{\text{max}} = 250$).
- Undershooting the fitness limit f_{lim} (here $f_{\text{lim}} = 1.5$, default $-\infty$). The best fitness value of the current population is less than or equal to f_{lim} .
- Exceeding the maximum number of stall generations $G_{\text{max, stall}}$ (default $G_{\text{max, stall}} = 50$). The average relative change of the best fitness value over $G_{\text{max, stall}}$ generations is less than or equal to the function tolerance f_{tol} .
- Undershooting the function tolerance f_{tol} (here $f_{\text{tol}} = 10^{-8}$). The average relative change in the fitness value over $G_{\text{max, stall}}$ generations is less than f_{tol} .

The evolutionary selection here is based on rank selection [18, 29, 33]. By using this selection technique, the search will not be dominated by few individuals with a high fitness value, which hinders the algorithm from converging too quickly towards a possible local minimum. Therefore, the search is prolonged and the probability of finding a global minimum increases. These kinds of algorithms are used if the cost function is stochastic or highly non-linear [67].

In this case the cost function was the vector norm of the reflection coefficient (see (3.6)). The reflection coefficient was chosen since the inverse problem of fitting is ill-posed. Several sets of parameters could lead to the same solution, especially when if one uses the absorption coefficient. The 1D analytic solution for the real-valued absorption coefficient α , respectively the complex-valued reflection coefficient r , computes by (3.4) and (3.5).

$$Z_m(\omega) = \sqrt{\rho_m(\omega) K_m(\omega)} = \frac{T_{m,11}}{T_{m,21}}; \quad m = 0, 1; \quad \alpha = 1 - |r|^2 = 1 - \left| \frac{Z_{\text{eff}} - Z_0}{Z_{\text{eff}} + Z_0} \right|^2 \quad (3.4)$$

$$\mathbf{T}_{\text{eff}} = \begin{bmatrix} T_{11} & T_{12} \\ T_{21} & T_{22} \end{bmatrix} = \mathbf{T}_1 \cdot \mathbf{T}_0; \quad \mathbf{T}_m = \begin{bmatrix} \cos(\tilde{k}_m t_m) & i Z_m \sin(\tilde{k}_m t_m) \\ i \frac{1}{Z_m} \sin(\tilde{k}_m t_m) & \cos(\tilde{k}_m t_m) \end{bmatrix} \quad (3.5)$$

The genetic algorithm searches for a combination of design variable values that minimize the error between the simulated reflection coefficient curve r_A and the measured values r_M . With the frequency f_i as an independent parameter and measured data set $[f_i, r_{M,i}]$. With N data points the error computes by the cost function.

$$J(\mathbf{x}) = \sum_{i=1}^N \|r_{M,i} - r_A(f_i, \mathbf{x})\|. \quad (3.6)$$

Here $Z_1(\omega) = Z_{\text{eq,scr}}$, $Z_0(\omega)$ is the characteristic impedance of the cavity with length L_c and Z_0 is the characteristic impedance of air at ambient conditions. The range of physically reasonable parameter values determines the range for the design parameter constraints. The equivalent fluid model mimics the acoustic behavior of the real MPP material. On the one hand, the investigated models assume uniformly distributed circular pores, so the equivalent model parameter limits must be in the range of those of the real values. For example the perforation ratio ϕ according to the manufacturer does not exceed 10% and the slit length l_{pore} is below 1 mm (see App. A for entire set of constraints).

Beside the perforation ratio, the other prominent design variable is in the case of the JCAL model, and the Wilson model, the hydraulic radius r_{pore} . When using the JCAPL model, the parameter b_{form} in the range of 0 to 1 is added. The length L_c of the cavity has to be considered with a geometric error margin of ± 3 mm. For the fitting procedure, the equivalent material was assumed to be rigid due to the very low decoupling frequency (2.30) of ≈ 1 Hz.

The entire set of the most important design variables (model parameters) therefore contains:

$$\mathbf{x} = (\phi, r_{\text{pore}}, L_c, b_{\text{form}}) \quad (3.7)$$

The extended MPP can be assumed to be acoustically compact and homogeneous, since $\tilde{k}_0 r_{\text{pore}} \ll 1$, $\tilde{k}_0 t_{\text{MPP}} \ll 1$ and $\lambda \gg 2.8 r_{\text{pore}}$. In the impedance tube, there is no diffuse sound field in the cavity, only the plane wave mode can propagate towards the plate. The acoustic pressure distribution along the tube's cross-section and along the MPP specimen surface is therefore also homogeneous. The real metal frame MPP domain is locally-reacting because an acoustic wave cannot travel within the MPP domain perpendicular to the impinging sound. Thus, the MPA in the impedance tube is locally-reacting. It is obvious however from (3.5) that the same characteristic impedance $Z_m(\omega)$ can be calculated from different combinations of the equivalent density and compression modulus in the plane-wave case and thus different combinations of design parameters ϕ , r_{pore} , etc. may occur. Here, the direction of wave propagation in the MPP domain and the MPA cavity are the same, and sound pressure, and particle velocity wave fronts are always spatially in phase (homogeneity over cross section). Thus, different equivalent densities and compression moduli can lead to the same plane wave sound field.

Now, what happens if the absorber domain (MPP + L_c) in-depth direction (of L_c or t_{MPP}) is not anymore locally reacting because sound waves impinge from various directions (non-homogeneity over cross section or along the MPP surface)?

- The synthetic wave propagation in the simulated absorber domain other than in the direction of the impinging sound wave can have an influence on the responsive synthetic field (on the reflected and absorbed power portions, see (3.8)). Also, the MPP domain is then not locally reacting anymore.
- In such a case, different combinations of the equivalent density and compression modulus would yield different synthetic responsive sound fields because they influence the synthetic wave propagation in the MPP domain.
- However, depending on the evaluation parameters (TL or IL of a larger-scale sound absorber configuration), different local sound fields near the MPP might yield the same global acoustic response. But also, sound fields with different modal components can lead to the same surface impedance because it is linearly connected to the acoustic field.

Therefore, the follow-up questions for the design stage of an MPA are:

- How much is the measured MPA's effectiveness influenced by the non-local reaction in the air volume cavity? There is no parallel sound propagation within the real MPP material. The effects of the non-local reaction would manifest, especially in a diffuse sound field.

- How accurately can the plane-wave fitted MPP absorption characteristics emulate the acoustic behavior of more dedicated MPA configurations in a diffuse sound field in the FE simulations? This is dependent on how much the MPP modeling and the non-local reaction (due to the parallel wave propagation in its volume domain) affects the synthetic acoustic response of the MPP to an impinging sound wave.

3.1.3 Impedance tube measurement results

To ease the interpretation of the measurement results, it helps to recall the power balance of a material specimen exposed to an impinging plane sound wave of power $P_{a,+}$. A part of this power is reflected ($P_{a,-}$). The non-reflected power consists of a dissipated ($P_{a,diss}$) and transmitted part ($P_{a,t}$). Some of the power portions can be calculated from the measured pressure data and be put into context via the following balance equations, with τ as the transmission coefficient.

$$P_{a,+} = P_{a,-} + P_{a,diss} + P_{a,t} \quad | \quad : P_{a,+}$$

$$1 - |r|^2 = \alpha = \frac{P_{a,diss}}{P_{a,+}} + |\tau|^2 \quad (3.8)$$

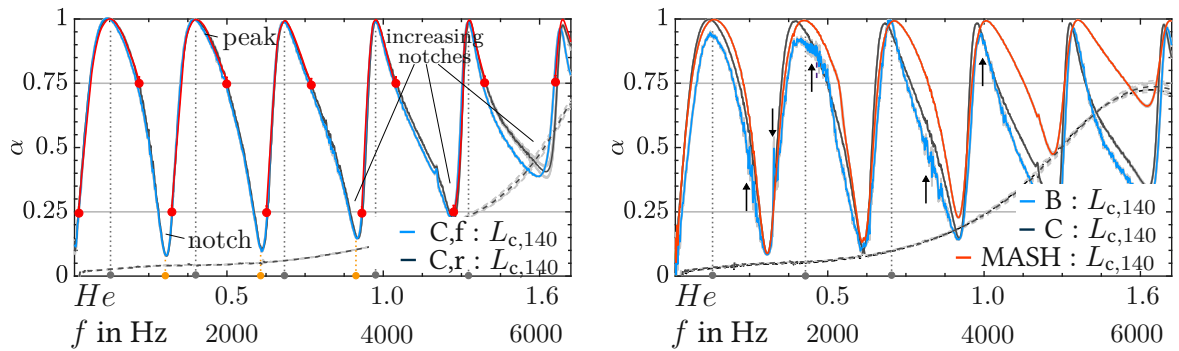
For impedance tube measurements with a hard backed end the transmitted sound power is zero ($\tau = 0$), so α solely represents the dissipated sound power.

Investigated MPPs and comparison to porous material

Figure 3.3 (a) shows the absorption curve of MPP type C with rear (r) and front (f) side pointing towards the loudspeaker with $L_{c,140} = 140$ mm (see Fig. 3.1 (a,b)). The red lines indicate the "left flank" of the absorption curve between $\alpha \in [0.25; 1.0; 0.75]$. The blacked-dashed line indicates the absorption trend if $L_c = 0$ mm. The dimensionless frequency is computed via $He = \tilde{k}_0 R_{imp}$, where R_{imp} is the radius of the impedance tube. The vertical grey and yellow dotted lines mark resonance-related absorption peaks, respectively absorption notches.

The rear and front sides of the MPP only differ significantly, starting at $He = 1.6$. The trend of the dashed line is visible in the light- and dark blue curves. The seemingly increasing absorption at resonance notches is attributed to a low coherence between the microphones due to a standing wave pressure node at one of the microphones in the range of $He = 1.6$. Here, large bias and random errors can occur [30], because of the high reflectiveness of the MPA. However, the measurement results are quite reproducible which can be seen on the low variations of the grey curves (standard deviation).

A comparison between MPP type C, B, and MASH in Fig. 3.3 (b) reveals that type B is much more prone to excitation of its frame (black arrows indicate frame vibration). Further investigations revealed, however, that these vibrations are more correlated to the mounting conditions and the finiteness of the MPP specimen (edge effects) than the eigenfrequencies

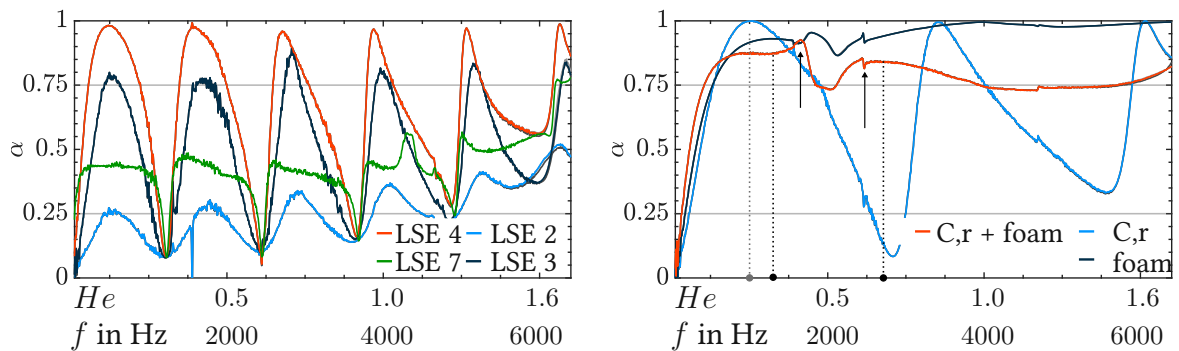


(a) Type C, rear (r) and front (f) side:
 $L_{c,140} = 140$ mm.

(b) Type C, type B and MASH: $L_{c,140} = 140$ mm.

Figure 3.3: Measured α -curves for type C, B and MASH; black dashed line shows $L_c \approx 0$ mm; grey α -curves show the standard deviations.

of the circular specimen. Type B also has a lower maximum absorption than type C. Only type C, and MASH have comparable maximum absorption, with MASH being seemingly more broadband effective. However, this could again be an effect of the error influence near $He = 1.6$ and above (compare dashed line to absorption notches at $L_{c,140} = 140$ mm). The absorption curves of the MPP types LSE are displayed in Fig. 3.4 (a). The absorption of LSE



(a) LSE types with strongly varying porosity and characteristic length:
 $L_{c,140} = 140$ mm.

(b) Type C in comparison to porous foam and a combination of MPP and foam;
 $L_{c,60} = 60$ mm.

Figure 3.4: Absorption of MPAs with LSE MPP types 2,3,4 and 7; and type C in combination with porous foam material in the cavity.

4 is comparable to type C, however with increasing porosity and characteristic length, the effectiveness of the MPA diminishes (LSE 2 and 3). The low-absorption(-notch) increase is again visible. It is therefore advantageous to concentrate on many absorption peaks and/or a

certain high limit of absorption for the fitting, here 0.75 on the right flank of the α peaks. By doing so, one can minimize the error influence of the measurement system and can obtain a more realistic acoustic behavior.

In Fig. 3.4 (b) an MPA with $L_c = 60$ mm is compared to porous foam material, and foam plus MPP. One can see that the MPP plus the foam work less effective than the foam alone. Both absorber arrangements suffer from the sensitivity of foam material's absorption to mechanic stress and strain (frequency section between the two dotted lines). The foam specimen is deformed when being placed in the tube. Also, the limp frame of the porous media might be the cause of the altered absorption in the frequency region near $He = 0.5$. The MPA absorption notches could be compensated for by a second MPP in the backing cavity. It is remarkable that the MPA reaches a much higher maximum absorption below $He \approx 0.85$ than the porous foam. The foam, though, is much more broadband effective and reaches a comparable maximum absorption above $He = 1.0$.

3.1.4 Fitting results

The genetic material characterization was performed for all MPP types, and the results are listed in the tables in appendix A. The shown results for the design parameter tuples \boldsymbol{x} under the set limits for possible values resulted in good data match of the measured curves. The stopping criteria for the genetic algorithm are listed in 3.1.2. Some of the results of the real and the imaginary part of the reflection coefficient can be seen in Figs. 3.5, 3.6 and 3.7.

The diagrams show the effect of varying the design variable vector \boldsymbol{x} and the influence of using different models. Table 6.1 to 6.3 show the impact of changing the design variables for MPP type C. Table 6.4 and 6.5 list the fitted values of r_{pore} and ϕ for type B and LSE types. The most important conclusions are summarized in the following with the corresponding data readily extracted from the tables in the appendix. It is reminded here that strongly varying values for the tuples x_1, \dots, x_p in \boldsymbol{x} result in different values for $\rho_{\text{eq,scr}}$ and $K_{\text{eq,scr}}$ which in turn can produce different responses to an incoming sound wave.

Fitted MPP parameters depending on \boldsymbol{x} and acoustic models

The influence of differently sized \boldsymbol{x} and MPP types is very prominently displayed by a change in the viscous Biot frequency f_v . It is largely influenced by the characteristic pore size r_{pore} . The trends in the design variables from the collected data can be summed up to:

- a) Influence of temperature T_0 and size of \boldsymbol{x} (cf. Tab.3.1)
 - The temperature influences the fitted L_c , because it changes c_0 and thus λ ; this changes r_{pore} and thus f_v quite drastically.
 - Parameter b_{form} in the JCAPL has a strong influence on r_{pore} . Its value changes rather strongly (sensitivity of the model near $b_{\text{form}} = 0$), affecting the other design variables and changing the variance.

- The addition of three more design variables in the model, $(a, b, c)_{\text{JCAL}}$ (see (6.1)) increases the variance of the characteristic pore size and the porosity.
- *It must thus be deducted that to recover an accurate absorption behavior of the real material, one should choose few parameters, because an unrealistic synthetic impedance response to a diffuse sound field might be overlooked in the plane wave field.*

C - rear side	$t_{\text{MPP}} = 1.0 \text{ mm}$	$\mathbf{x} = (\phi/-$	$r_{\text{pore}}/\mu\text{m}$	L_c/mm	$b_{\text{form}}/-)$	f_v/Hz
$\ r\ $ - JCAL- II	$\alpha = [0.25; 1.0; 0.75], 18^\circ\text{C}$	0.063	67.3	140	–	4254
$\ r\ $ - JCAL- II	–, 20°C	0.055	71.8	140	–	3782
$\ r\ $ - JCAL- II	–, 25°C	0.046	80.3	140	–	3124
$\ r\ $ - JCAL- II	–, 18°C	0.060	68.8	139.7	–	4063
$\ r\ $ - JCAL- II	–, 20°C	0.060	69.2	140.4	–	4067
$\ r\ $ - JCAL- II	–, 25°C	0.060	70.3	141.7	–	4076
$\ r\ $ - JCAPL- II	$\alpha = [0.25; 1.0; 0.75]$	0.059	83.7	140	< 0.001	2826
$\ r\ $ - JCAPL- II	–	0.056	83.0	140	0.003	2874
$\ r\ $ - JCAL- II	–	0.076	65.6	140	–	4597
$\ r\ $ - JCAL- II	$a_{\text{JCAL}}, b_{\text{JCAL}}, c_{\text{JCAL}}$	0.12	53.3	141.2	–	6973
	$a_{\text{JCAL}}, b_{\text{JCAL}}, c_{\text{JCAL}}$					

Table 3.1: Table with specimen number (I-V) for comparison (a); entire set in appendix Tab. 6.2.

b) Influence of frequency range, L_c and size of \mathbf{x} (cf. Tab.3.2)

- Rear and front side have almost the same values of r_{pore} and ϕ .
- The least variance among specimens (I-V) is achieved if one only fits to r_{pore} and ϕ . Adding L_c as degree of freedom increases the variance among the aforementioned variables (cf. Tab. 3.2).
- The frequency ranges, "flanks", influence r_{pore} stronger than they influence ϕ . Omitting the resonance peaks (at $\alpha = 1.0$) produces a higher variance among r_{pore} .
- Different cavity lengths ($L_{c,60}, L_{c,140}$) produce almost the same values for r_{pore} if same frequency fitting range is chosen, however ϕ is changed more prominently, but with no influence on f_v .
- *The fitting frequency range must include the absorption peaks and more resonance peaks will make the fitting probable more accurate and robust. The difference in rear and front side is negligible. The porosity ϕ and cavity length L_c seem to be mutually-dependent.*

c) Influence of different models (cf. Tab.3.3)

3 Predictive design

C - front side	$t_{\text{MPP}} = 1.0 \text{ mm}$	$\mathbf{x} = (\phi/-$	$r_{\text{pore}}/\mu\text{m}$	L_{c}/mm	$b_{\text{form}}/-)$	f_{v}/Hz
r - JCAL- I	$\alpha = [0.25; 1.0; 0.75]$	0.057	72.1	141.7	–	3804
<hr/>						
C - rear side	$t_{\text{MPP}} = 1.0 \text{ mm}$					
r - JCAL- I	–	0.060	68.8	141.2	–	4175
<hr/>						
r - JCAL- II	$\alpha = [\text{all}]$	0.059	67.1	141.1	–	4393
r - JCAL- II	$\alpha = [0.75; 0.75]$	0.059	60.4	141.4	–	5408
r - JCAL- II	$\alpha = [0.25; 1.0; 0.25]$	0.058	68.1	141.0	–	4268
r - JCAL- II	$\alpha = [0.25; 0.75; 0.25]$	0.058	62.8	141.1	–	5018
<hr/>						
r - JCAL- IV	$\alpha = [\text{all}], L_{\text{c},60}$	0.067	67.0	61.5	–	4403
r - JCAL- IV	$\alpha = [0.25; 1.0; 0.75], L_{\text{c},60}$	0.063	68.7	61.2	–	4188
<hr/>						
r - JCAL- I	$\alpha = [0.25; 1.0; 0.75]$	0.050	75.9	140	–	3427
r - JCAL- II	–	0.050	76.0	140	–	3421
r - JCAL- III	–	0.052	75.9	140	–	3433
r - JCAL- IV	–	0.051	78.3	140	–	3226
r - JCAL- V	–	0.056	74.2	140	–	3590

Table 3.2: Table with specimen number (I-V) for comparison (b); entire set in appendix Tab. 6.1.

C - rear side	$t_{\text{MPP}} = 1.0 \text{ mm}$	$\mathbf{x} = (\phi/-$	$r_{\text{pore}}/\mu\text{m}$	L_{c}/mm	$b_{\text{form}}/-)$	f_{v}/Hz
r - JCAL- II	$\alpha = [0.25; 1.0; 0.75], \text{low}$	0.051	74.4	140	–	3576
r - JCAL- II	–, low	0.060	68.4	141.0	–	4231
r - JCAL- II	–, high	0.01	1.5	140	–	999999
r - JCAL- II	–, high	0.49	1.6	140.9	–	999999
<hr/>						
r - Wilson- II	–	0.058	135.4	140	–	1079
r - Wilson- II	–	0.069	124.4	141.0	–	1277
<hr/>						
r - Maa- II	–	0.050	77.4	140	–	3295
r - Maa- II	–	0.067	66.6	141.7	–	4459
<hr/>						
r - JCAL- II	–, $\mathcal{T}_{\text{eff},2}, L_{\text{c},2} = 2.5 \text{ mm}$ $a_{\text{JCAL}}, b_{\text{JCAL}}, c_{\text{JCAL}}$	0.49	36.7	140	–	14692
r - JCAL- II	–, $\mathcal{T}_{\text{eff},2}, L_{\text{c},2} = 2.5 \text{ mm}$ $a_{\text{JCAL}}, b_{\text{JCAL}}, c_{\text{JCAL}}$	0.21	56.1	138.1	–	6282

Table 3.3: Table with specimen number (I-V) for comparison (c); entire set in appendix Tab. 6.3.

- Simulation of two MPPs can recover the increasing absorption notch trend towards $He = 1.6$ (cf. Fig. 3.3 (a)). But the design variable values differ strongly

compared to the other models.

- The low-frequency JCAL limit model produces similar values as the standard JCAL model, with K_0 kept constant.
 - The high-frequency JCAL limit model produces strongly differing parameters r_{pore} and ϕ with a large difference to measured data in the low-frequency range (< 3000 Hz, c.f. 3.6).
 - The Maa model produces similar values as the JCAL model.
 - The Wilson model produces very different r_{pore} -values than the JCAL model and thus a strongly differing f_v .
- *For the thin MPP, it could be sufficient to simulate just the equivalent density and calculate the effective impedance with a constant K_0 . This would also reduce ambiguity in the plane wave solution for Z_{eff} , producing the synthetic sound field response. The characteristic pore size r_{pore} is very sensitive to the models chosen and the other design variables.*

All of the above parameter variations can recover the measured absorption curves with comparable minimal cost functions in the plane wave field. However, they can produce different characteristic impedances $Z_m(\omega)$ (cf. (3.4)) with varying ρ_m and K_m . However, in the cross-sectional homogeneous sound field (perpendicular sound incidents and plane-wave field) and the resulting local reaction of the MPA, the effects on the calculated reflection coefficient r are not too great.

Reflection coefficient results depending on model

Following the presented observations, the design variable values are plugged into the presented models for the comparison with measured reflection coefficient data of a single MPP type C specimen. For the fitting, the ambient temperature was assumed to be 22°C and $K_{\text{eq,scr}}$ was switched to a the constant value of K_0 . The cavity length was $L_c = 140$ mm. The frequency fitting range has been chosen to include absorption values within certain limits. These limits were $[0.25 < \alpha < 1.0]$ on the left flank of the α -peaks and $[0.75 < \alpha < 1.0]$ on the right flank (see Fig. 3.3 (a)). The intention for choosing this range was to avoid low absorption (high reflection) data values represented by the increasing notch absorption trend towards $He = 1.6$.

Figure 3.5 shows that a three-parameter fit ($\mathbf{x} = (\phi, r_{\text{pore}}, L_c)$) with the Maa, Wilson and JCAL model, keeping K_0 constant, produces a very similar approximation of the real part \Re of the reflection coefficient. There is a more discernable difference for the imaginary part \Im , especially the Maa model diverges from the other models. The JCAPL model recovers the real and imaginary part of r the best for $He < 0.25$. The absorption notch increase trend towards $He = 1.6$ cannot be recovered by any model and using one MPP. Since only one MPP was measured, it has to be a measurement error.

Comparing the low-frequency-limit model with the JCAL model in Fig. 3.6 reveals almost no

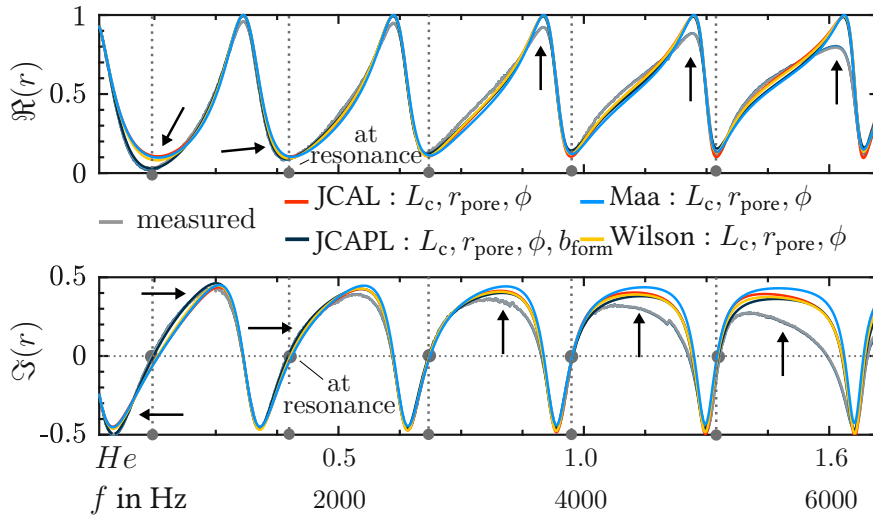


Figure 3.5: Real and imaginary part of the reflection coefficient depending on models and design variables used; with indicated resonance frequencies (grey dotted lines).

difference between the two models. The high-frequency limit model performs insufficiently in recovering the real and imaginary part of the reflection coefficient. The influence of simulating also $K_m(\omega)$ is visible beginning at around $He = 0.8$ or a frequency of 3500 Hz. This is also the frequency range of the Biot frequencies f_v and f_t computed with the fitted MPP parameters (see table 6.1 and 6.2). It marks the limit where viscosity and inertia drag effects are of the same order of influence on absorption (cf. Fig. 2.1). The high-frequency-limit model

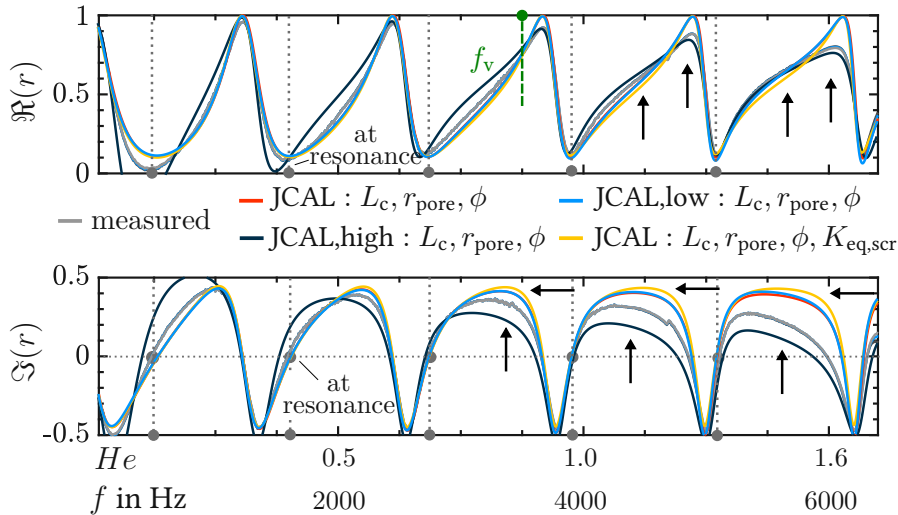


Figure 3.6: Real and imaginary part of r depending on models and design variables used.

can recover the real part of the reflection coefficient beyond the Biot frequency, but not the

imaginary part.

The absorption notch increase can only be simulated if one uses two MPPs instead of one in the 1D simulation (see Fig. 3.7). The two MPPs are 2.5 mm apart. Even better fits can be achieved if three additional parameter degrees of freedom $(a, b, c)_{\text{JCAL}}$ are added. They can increase or decrease the impact of the frequency f , r_{pore} and ϕ in $F(\omega)$ in (6.4) and (6.1). To get the best fit with the seemingly erroneous measurement data the compression modulus $K_{\text{eq,scr}}$ must be modeled as a frequency-dependent parameter.

The presented comparison of measured and simulated data leads to the following conclusions:

- The low-frequency JCAL model with constant K_0 is a sufficing model for the MPP emulation. However, the best impedance tube data agreement can be achieved with the usage of the JCAPL model.
- More MPPs (a thicker absorber volume) require the inclusion of a frequency dependent $K_{\text{eq,scr}}$.
- The usage of L_c in \mathbf{x} has a stronger influence on the fitted value of ϕ than on the fitted r_{pore} .
- The size of the fitted r_{pore} determines f_v , which separates the viscosity-dominated from the inertia-driven frequency range of the emulated MPP domain.

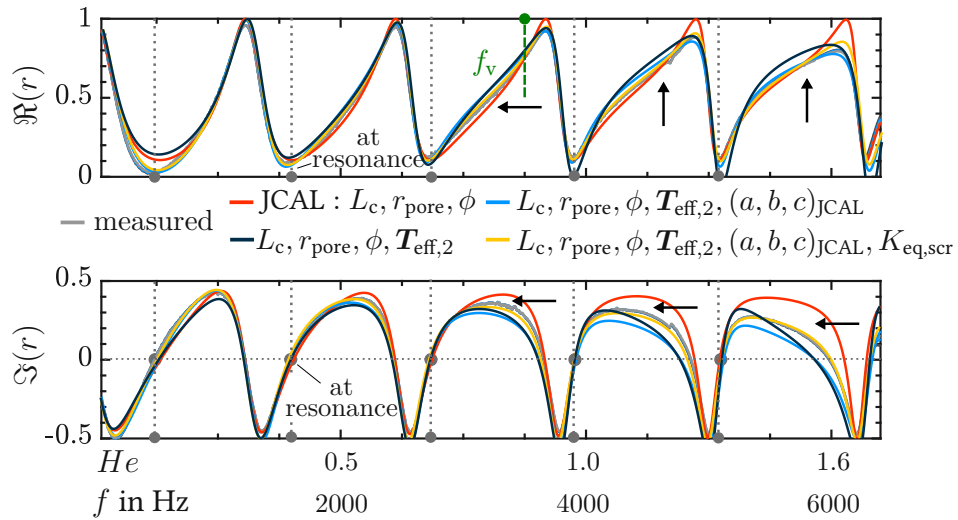


Figure 3.7: Real and imaginary part of r depending on models and design variables used for two MPPs, simulated with the JCAL model.

3.2 MPA measurements using an expansion chamber

In a room acoustics-like application scenario or a wave-guide application above its cut-off frequency, the sound field will be diffuse because the geometrical dimensions allow the excitation of many acoustic modes (the degree of spatial homogeneity depends on the frequency band and the modal density in the room). Therefore, sound wave fronts will impinge on the MPA from multiple directions. This might affect the effectiveness of the absorber in some frequency regimes because the MPA is not any more locally-reacting. It is important to keep in mind that the locally-reacting MPA at resonance has a very low reflection coefficient (see Fig. 3.5). The pore impedance in combination with the impedance of the cavity at resonance frequency are adjusted to Z_0 . The sound wave can easily enter the MPA, then is exposed to viscous plus inertia drag, depending on the frequency, respectively the boundary layer thickness δ_v , and the sound wave is attenuated.

3.2.1 Measurement setup

To assess different MPA configurations and compare them among each other as well as with the standard damping material, simulated and measured transmission loss (TL) data is obtained. With τ and r calculated from pressure data, the transmission loss of an absorber structure (brown section in Fig. 3.8 (a)) can be computed by

$$TL = 10 \log \left(\frac{1}{|\tau|^2} \right); |\tau|^2 = \frac{P_{a,t}}{P_{a,+}} = 1 - |r|^2 - \frac{P_{a,diss}}{P_{a,+}}. \quad (3.9)$$

The measurement setup allows to measure the TL of an expansion chamber (cf. Fig. 3.8 (b)) with different MPA structures. By wave decomposition, the incident sound power $P_{a,+}$ is separated from the reflected sound power $P_{a,-}$ [145]. At the other side, the same is done to obtain the transmitted sound power $P_{a,t}$. The measurements have to be performed twice with different end pieces (X,Y). The dimensions of the setup are the connecting duct dimension a_{ex} and microphone distance $d_{mic} = 18$ mm which allows measurements up to $f = 8500$ Hz. The expansion chamber with quadratic cross section is made up of the MPP plus cavity length L_c , length $l_{ex} = 300$ mm and chamber dimension b_{ex} . The transmission loss TL consists of a reflective and dissipative (absorbed) part [86, 141]

$$TL = TL_{abs} + TL_{refl} \quad (3.10)$$

$$TL_{refl} = 10 \log \left(\frac{1}{1 - |r|^2} \right) \quad TL_{abs} = 10 \log \left(\frac{1 - |r|^2}{|\tau|^2} \right). \quad (3.11)$$

Strictly speaking, the dissipated sound power in the expansion chamber is actually a combination of dissipated power and power lost by destructive interference. Due to the cross-section jumps at the beginning and end of the chamber, reflective interference damping at frequencies $f_{\lambda/4,i}$ ($i = 1, 3, 5, \dots$) will occur, calculated by $f_{\lambda/4,i} = c_0(4l_{ex})^{-1}(2i - 1)$ [117]. Here,

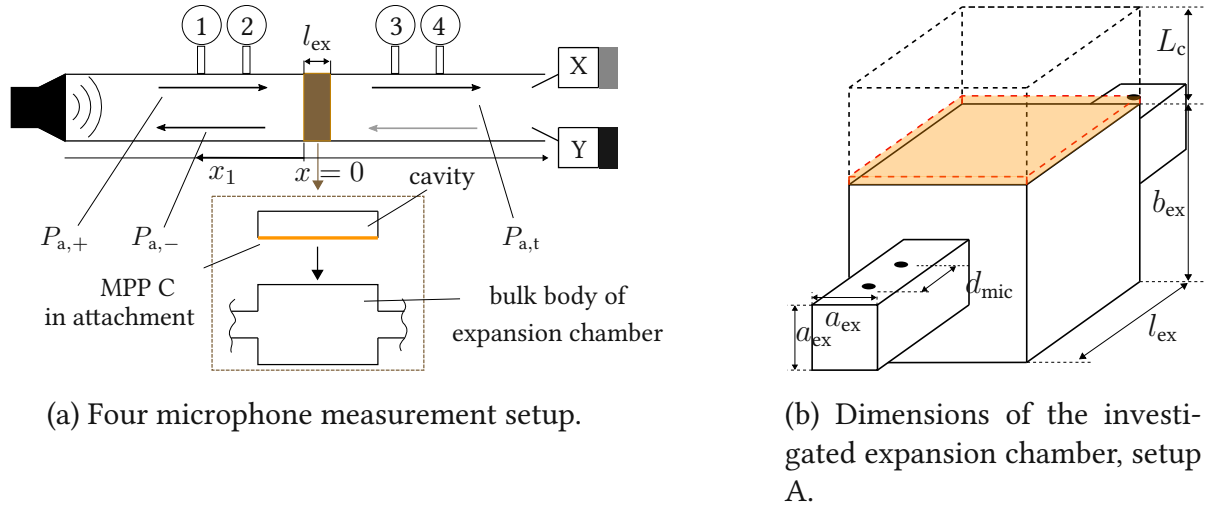


Figure 3.8: Measurement scheme and setup A for various MPAs for room acoustic application.

the transmission loss will be high due to the sudden geometry changes. For the expansion chamber with MPP certain frequency regions with different characteristic sound fields must be discerned:

- $f_c = 1900$ Hz is the first cut-on frequency of the expansion chamber: below it, only plane waves propagate in the chamber. Above it higher order modes propagate and the sound field in the chamber becomes more diffuse.
- $f_1 = 3800$ Hz is the second cut-on frequency of the expansion chamber: beyond it, the sound field becomes even more diffuse and the typical TL -lobes blur to smaller TL -peaks.
- $f_2 = 6400$ Hz marks the limit of the measured MPP specimen frequency behavior in the impedance tube, but also the diffusivity is very pronounced above that frequency (see Fig. 3.10)

The measured transmission and reflection coefficients are obtained from pressure data at microphones one to four in Fig. 3.8 (a) and calculated via [4, 37]

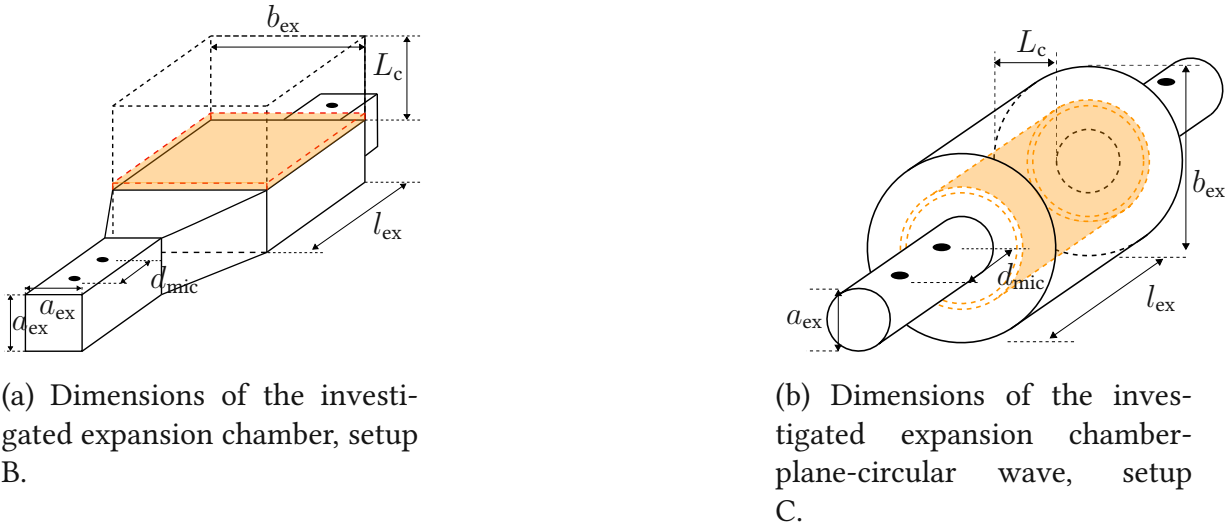
$$\tau = \frac{2e^{ik_0 l_{ex}}}{T_{11} + T_{12}/\rho_0 c_0 + \rho_0 T_{21} + T_{22}} \quad r = \frac{T_{11} - \rho_0 c_0 T_{21}}{T_{11} + \rho_0 T_{21}}, \quad (3.12)$$

where T_{ij} are the entries of the two-by-two transfer matrix, computed from pressure data of two measurements (X,Y). In the FE simulations, it is possible to enforce a non-reflecting boundary (PML or ABC, see [87]) condition instead of end pieces X and Y. So, only pressure data from microphones one to three are needed. The transmission and reflection coefficients

are calculated by [2, 162]:

$$\tilde{p}_{\text{in}} = \frac{\tilde{p}_1 - \tilde{p}_2 e^{-i2\pi f d_{\text{mic}} \tilde{k}_0}}{1 - e^{-i2\pi f d_{\text{mic}} \tilde{k}_0}} \quad \tau = \frac{\tilde{p}_3}{p_{\text{in}}} \quad r = \frac{H_{12} - e^{-ik_0 d_{\text{mic}}}}{e^{ik_0 d_{\text{mic}}} - H_{12}} e^{2ik_0 x_1}, \quad (3.13)$$

where \tilde{p}_1 , \tilde{p}_2 and \tilde{p}_3 are the overall pressures at the discrete microphone positions. The complex-valued pressures \tilde{p}_1 and \tilde{p}_2 at microphone one and two define the transfer function $H_{12} = \tilde{p}_2/\tilde{p}_1$. Three different chamber designs have been chosen to study the influence of geometry,



(a) Dimensions of the investigated expansion chamber, setup B.

(b) Dimensions of the investigated expansion chamber-plane-circular wave, setup C.

Figure 3.9: Measurement setup B and C for various MPAs for room acoustic application.

and thus the developing sound field, on the MPA's effectiveness. Setup A (Fig. 3.8 (b)) is the most versatile, because apart from the attachment, MPPs can be placed in the bulk expansion chamber as well. Here, the dimensions of the setup are $a_{\text{ex}} = 20$ mm, $b_{\text{ex}} = 90$ mm and $L_c = 60$ mm.

In setup B (Fig. 3.9 (a)) the bulk chamber geometry is rectangular with the goal of reducing skewed wave front (mode shape) in the direction of L_c . The Helmholtz numbers compute by $He = \tilde{k}_0 b_{\text{ex}}$ (A) and/or $He = \tilde{k}_0 a_{\text{ex}}$ (A,B) for the rectangular setups, and $He = \tilde{k}_0 (b_{\text{ex}} - 2L_c)$ for the circular setup C. In setup C (Fig. 3.9 (b)), $a_{\text{ex}} = 29$ mm, $b_{\text{ex}} = 190$ mm and L_c varies from 70 mm to 20 mm. In order to avoid near field effects, like short-time evanescence mode propagation and reactive sound fields, the sound source has a distance of at least five diameters to the first microphone (very small near field length N_{near}).

The acoustic pressure distributions in Fig. 3.10 show how the plane-wave field gradually develops into a diffuse sound field, consisting of many superposed acoustic modes, with increasing frequency. This depends strongly on dimension b_{ex} and the shape of the expansion chamber. A more rectangular cross-section setup suppresses skewed wave fronts in the direction L_c . The greatest difference concerning the sound field characteristic can be seen in setup C. The modes have a circular shape and the pressure distributions have the same phase

on the circumference. In contrast, setup A and B favor a spatially uncorrelated wavefront at the MPP interface. The wave fronts are strongly skewed and not in phase beyond f_1 . As the depiction of the modes (Fig.3.10) shows, the sound field in the high frequency regions is not really totally *diffuse* which would require a spatially homogeneous pressure distribution. But, it also not a *direct (far)* field which would require plane wave fronts. Hence, it is to be thought of as *diffuse* with strong *modal* components and one can assume an oblique incident impingement of the sound waves from many directions upon the MPA. The differences of the various MPA structures are expressed as transmission loss differences between a reference and comparative setup, computed by:

$$\Delta TL_{()} = TL_{(),reference} - TL_{(),comparative} \quad (3.14)$$

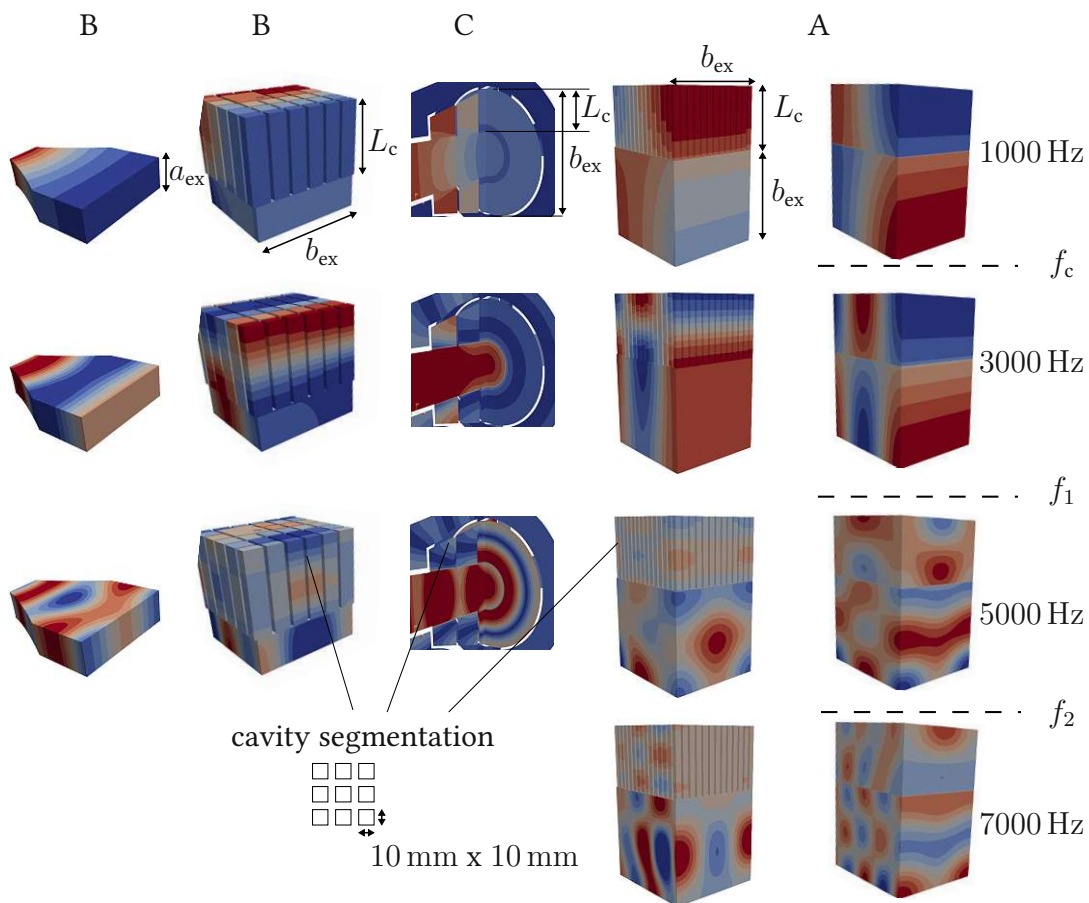












Figure 3.10: Modes simulated in setup B, C and A with segmented and unsegmented cavity within the frequency limits f_c , f_1 and f_2 .

3.2.2 Features of the measurement setup

The design of the expansion chamber test setup has the main goal of reproducibility and minimizing sensitivities of the measurements to the setup's boundary conditions. Therefore, the design includes the following features to reduce the mentioned bias errors of an impedance tube measurement system (cf. Chap. 3.1):

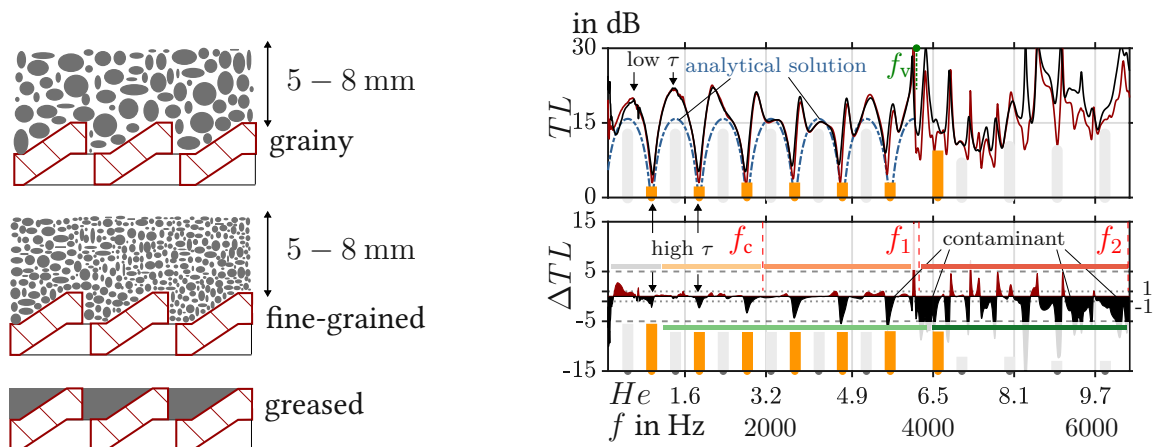
- The bulk body of the chamber and the connecting ducts are made of aluminum parts with a thickness of 1 cm to suppress structure-borne sound waves.
- Only the center part of the bulk chamber contains the MPA test configurations, the other parts of the setup remain unchanged.
- A smaller microphone distance $d_{\text{mic}} = 18$ mm allows a higher frequency range to be covered. However, there are portions of the frequency ranges prone to errors due to a high sensitivity to the pressure input data (cf. (3.1)).
- The cross-sections of the connecting ducts are 20x20 mm compared to 90x90 mm of the bulk chamber. This cross-section jump produces a relatively high transmission loss, and any additions or subtractions due to the MPA setup should be well visible.
- The microphones are located at least five diameters from the cross section jump or the loudspeakers to suppress the influence of evanescent modes. With a loudspeaker diameter of 25 mm, the near field length is kept small (for 6.4 kHz, $N_{\text{near}} = 5$ mm).
- The microphones have been calibrated with a pistophone. A microphone phase mismatch correction has been calculated. This should mainly affect the low-frequency portion of the measurement spectrum.

The setup's key features for the assessment of the MPA configuration's effectiveness are:

- A wide frequency range. Indicated by horizontal reddish colored bars (between f_c, f_1 and f_2 , , , ) in the following diagrams. Frequency portions with a higher error sensitivity are marked with horizontal grey bars ().
- Separation of viscous- and inertia-dominated frequency ranges; color-coded by light- and dark-green horizontal bars in the following diagrams (, ).
- Separation of the reflection and absorption portion of the transmission loss.
- Transmission loss peaks () and notches () are marked with grey and dark-yellow slim vertical bars, indicating the periodic effects at $f_{\lambda/4,i}$ (cf. Subchap. 3.2.1) due to the geometry (mainly dimension l_{ex}) on the acoustic power transmission.
- Colored areas (dark-red and black, , ) in the following diagrams signify positive or negative transmission loss differences between two setups.

3.2.3 Influence of pore obstructions

Using an MPA application in an air-duct system involves the consideration of pore contamination by dust or liquids. Therefore an MPA with one MPP C and $L_c = 60$ mm has been investigated at three levels of contamination. Case 1 involves grainy metal chips (> 1 mm), case 2 fine-grained wooden dust particles (< 1 mm) and in case 3 the pores are obstructed completely by grease (see 3.11 (a)). As described in [109], the contaminants have positive or negative effects on the MPA's performance, depending on frequency range, particle size or accumulation level and whether the pores are still passable by the acoustic air stream. The following figures show the transmission loss of three setups and the differences in TL between the MPA with one MPP with and without contaminant. The analytical solution to the trans-



(a) Close-up schematic of investigated pore obstructions.

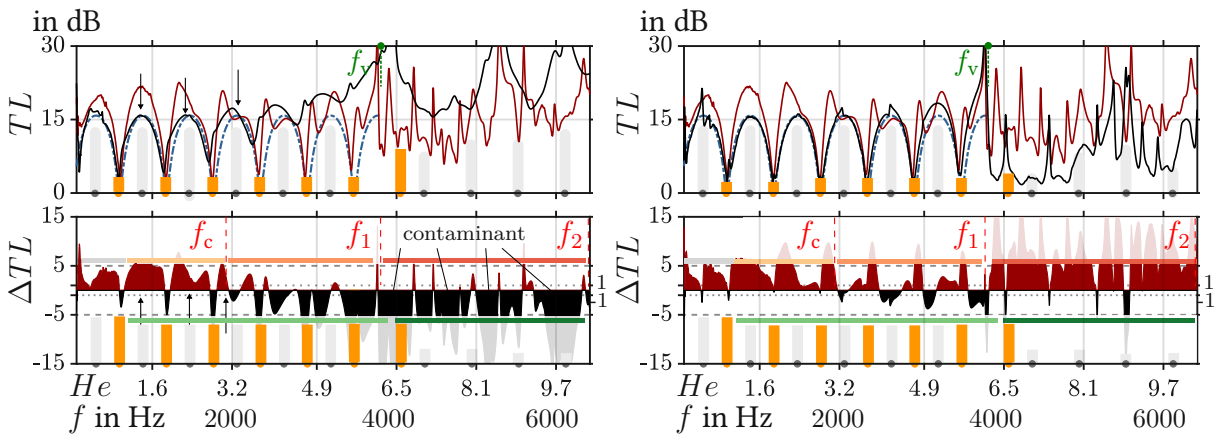
(b) TL of MPA reference setup (dark-red) compared to MPA covered with grainy metal contamination obstructing pores.

Figure 3.11: TL measurements of MPA, $L_{c,60}$, with different contaminants obstructing the pores; analytical solution for the bulk chamber without MPA.

mission loss without the MPA is indicated as the blue dashed line in Fig. 3.11 (b). The dark red line represents the MPA without contamination and the black line shows the contaminated case. Generally, the TL -plot of an expansion chamber reveals portions of the frequency spectrum with TL -peaks, where the transmission of acoustic power through the structure is low, and TL -notches, where the transmission of acoustic power is low. One can see the TL -notches (yellow dots) are affected by the presence of the grainy contaminant and that less sound power is transmitted (increasing black area in the ΔTL -plot). Also, the differences in transmission loss increase with higher frequencies. The fitting procedure (see Tabs. 6.1, 6.2) revealed an equivalent Biot frequency of $f_v \approx 3800$ Hz for the MPP. Depending on whether $\mathbf{x} = (\phi, r_{\text{pore}})$ or $\mathbf{x} = (\phi, r_{\text{pore}}, L_c)$ is used, the Biot frequency can be a little lower. Beyond that frequency (Stokes number significantly greater than unity), the acoustic

boundary layer thickness and the MPP characteristic pore size differ more strongly, and thus the inertia drag mechanism is more dominant. In the viscous regime, the viscous drag forces on the oscillatory flow should be proportional to pore size and particle velocity (correlated to the TL -peaks, marked with grey bars). So, if the contaminant would add to the reflection damping, one would see a larger change at the discrete frequencies indicated by the grey bars.

Since the TL -peaks, due to reflective-interference damping by the bulk chamber, seem to be unaffected by the contaminant, the distance of particles is probably too high to influence the wave motion through the MPP pores. But there might be a porous layer effect visible at the TL notches (dark-yellow bars), which are slightly higher than when the MPA without the contaminant is used. The TL -increase in the inertial drag regime is thus less likely caused by drag enforcement in the direction perpendicular to the MPP (augmenting reflective damping) and more likely by the drag addition of the porous (contaminant) layer itself in the direction parallel to the MPP. Anyway, the effects of the inertial drag component seem to be dependent on the thickness of the absorbent layer. The fitted MPP pore characteris-



(a) TL of MPA reference setup (dark-red) compared to MPA covered with fine-grained dust contamination obstructing pores; $He = \tilde{k}_0 b_{ex}$.

(b) TL of MPA reference setup (dark-red) compared to MPA covered with grease obstructing pores.

Figure 3.12: TL measurements of MPA, $L_{c,60}$, with different contaminants obstructing the pores; $He = \tilde{k}_0 b_{ex}$.

tic length is $r_{pore} \approx 70 \mu\text{m}$ (see Tab. 3.2) and $\delta_{v,500\text{Hz}} = 100 \mu\text{m}$, $\delta_{v,2000\text{Hz}} = 50 \mu\text{m}$ and $\delta_{v,6000\text{Hz}} = 30 \mu\text{m}$. The Stokes number varies from $St_{500\text{Hz}} = 1.073$, $St_{2000\text{Hz}} = 2.078$ to $St_{6000\text{Hz}} = 3.59$.



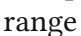

The fine-grained wooden dust seems to hinder sound waves penetrating the MPP pores (reduced TL in Fig. 3.12 (a) in the plane wave frequency range (orange bars)). But with increasing frequency the transmission loss increases. The loss in sound power is increased by the vis-

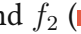
cous and inertia drag due to the contaminant (compare the increase of TL and position of f_v), even at the TL -notches compared to case of grease in the pores. Here (Fig. 3.12 (b)), the MPP is more or less unpassable, and the TL -trend resembles that of the bulk chamber without the MPA attachment. Also, the porosity of the contaminant layer in Fig. 3.12 (a) is greater than in the case of the metal chips layer, which most likely explains the broadband porous-absorber-like high transmission loss. One must assume that the MPP is actually unpassable in the fine-grained case, and the contaminant itself acts as the porous absorbing material.

3.2.4 Influence of cavity configuration, sound field character and MPP type

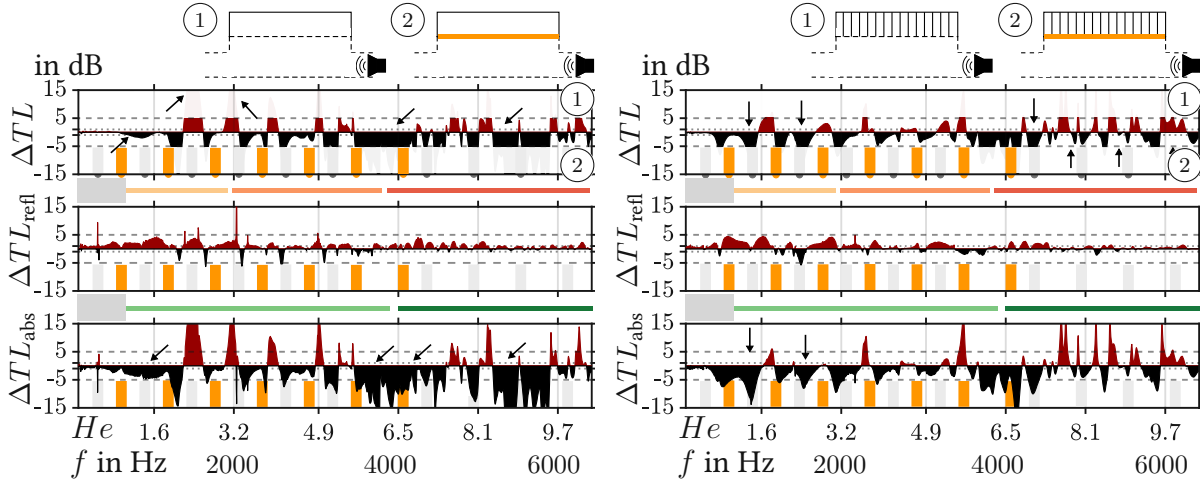
A porous foam material reacts for the most part locally to an impinging sound wave because the pores within the material are acoustically decoupled due to a large inner flow resistance. Therefore, the material absorbs sound wave power in a broad frequency range and causes a high transmission loss. The segmented (10 mm by 10 mm grid) and unsegmented MPA are compared to such a locally-reacting material by separating the power loss portions (see (3.11)). As can be seen in Fig. 3.10 setup A,B and C give rise to different diffuse mode shapes within the expansion chamber. To assess the MPA's effectiveness in expansion chamber's diffuse sound field, one must always discern relatively between two configurations and preferably the absorption portion of the TL . This is due to the fact that the reduction of acoustic transmission due to the reflection damping mechanism of an expansion chamber is, for the most part, a feature of the geometry of the expansion chamber (two cross-section jumps) and only to a small degree associated with the MPA setup within the chamber.

Setup A

First, the measured data of the empty attachment is compared to the MPA with one MPP (red vs. black areas in Fig. 3.13 (a)). The MPA adds significantly to transmission reduction above f_1 (frequency range ) and this is based on absorption (dissipation and/or destructive interference). But the transmission loss of the attachment without MPP is higher at two low frequency TL -peaks within the low He range (frequency range ). The empty attachment setup reflects more power. The difference in reflection is more prominent below f_c . Comparison at the TL -peaks and -notches (grey and yellow marked bars) above f_c (frequency range  and ) , the MPP adds broadband absorption (ΔTL_{abs}) at the notches and peaks. So at least, for the presented setup, the diffuse sound field in the cavity and in front of the MPP is rather beneficial to the MPA's effectiveness.

Segmenting the cavity (see Fig. 3.13 (b)) already causes a high transmission loss, but the MPP leads to a more broadband absorption at the analytical TL -peaks, not at the notches. This could mean that the interference damping mechanism is augmented by the segmented MPA. The largest differences can be seen below f_c and around f_1 . Between f_1 and f_2 () , in a developed diffuse sound field, adding the MPP is less effective and most of the absorbed energy is due to the cavity segmentation. The reflected power level differences are comparable the arrangement in (a).

The comparison of ΔTL_{abs} due to the segmented and unsegmented MPA (② in Figs. 3.13 (a,b)) reveals that in the viscous-drag-dominated frequency range (■), the segmentation increases the transmission loss at the grey-indicated peaks. However, not-segmenting the cavity increases TL in the inertia-driven frequency range (■).



(a) Expansion chamber with attachment without (reference, dark-red areas, ①) and with MPP (black areas, ②).

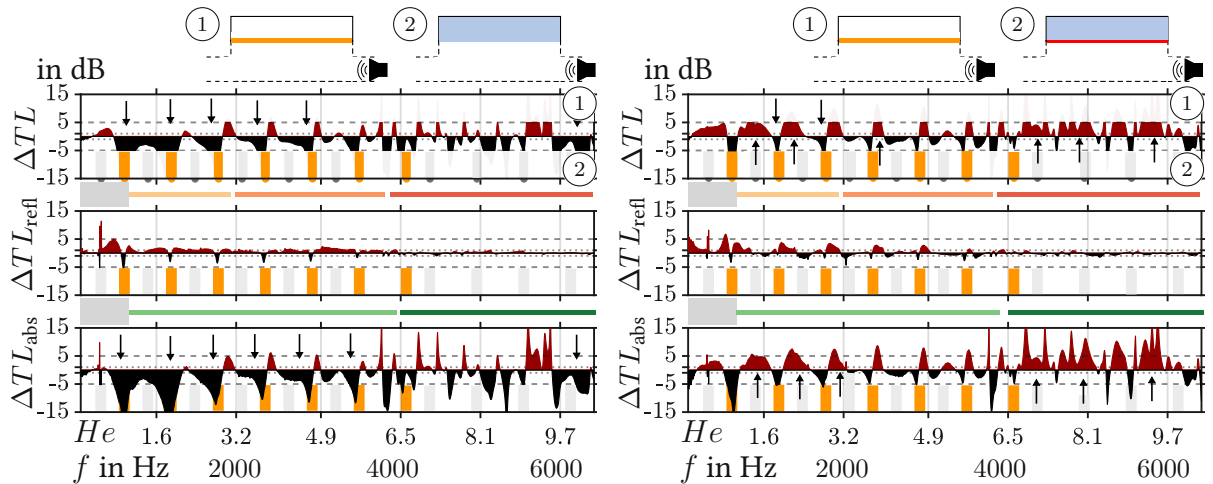
(b) Segmented attached cavity without (reference, dark-red areas, ①) and with MPP (black areas, ②).

Figure 3.13: Measured difference in TL -portions of the MPA, $L_{c,60}$ and setup A variations: empty attachment compared to attachment with MPP and segmented cavity without and with MPP; $He = \tilde{k}_0 b_{\text{ex}}$.

Now, the MPA with one MPP (dark-red areas in Fig. 3.14) are compared to an uncovered porous material filled cavity (a) and to the same porous material but covered with aluminum foil (b). The porous material leads to much more and broadband absorption at the analytical TL -notches up to f_1 (frequency range ■), but not at the analytical TL -peaks. This behavior is similar to the MPA covered with fine-grained dust contaminant (cf. 3.12 (a)). The porous material has a much smaller r_{pore} and thus a much wider viscous-drag-driven frequency range (■) which could explain the broadband transmission reduction.

Covering the porous material (Fig. 3.14 (b)) still leads to a more and broadband absorption at the TL -notches, but the TL -peaks are now reduced compared to the MPA. In the inertia-driven frequency range (■) of the covered foam material, the TL is extremely reduced. This can be explained by the surface of the foam not being air-penetrable anymore. With this finding and remembering that the empty attachment represents a larger impedance jump than the cavity filled with the porous material, it is stated that the MPP in setup A can add to the interference damping mechanism of the expansion chamber below f_c (■), but it might be equally effective for certain frequency ranges to omit the MPP (cf. 3.13 (a)). The opposite is the case above f_c (■ and ■), when the sound field becomes more and

more diffuse. Then the MPP becomes effective and is even more beneficial to absorption than the covered porous material. There are only minor changes in (a) and (b) in reflected sound power, because the setups (uncovered and covered porous material) are similar. Comparing TL_{abs} of the MPA and the covered foam in Fig. 3.14 (b), one can discern the viscosity-driven frequency range (orange), where the interference damping mechanism (by the geometry dimension l_{ex} and the cross section jumps) is visible by the TL -increase at grey peaks. The inertia-driven frequency range (green) can be observed by the broadband frequency behavior beyond $He = 6.5$.



(a) Attached cavity with MPP (reference, dark-red areas, ①) compared to porous material filled cavity (black areas, ②)).

(b) Attached cavity with MPP (reference, dark-red, ①) compared to covered porous material filled cavity (black areas, ②)).

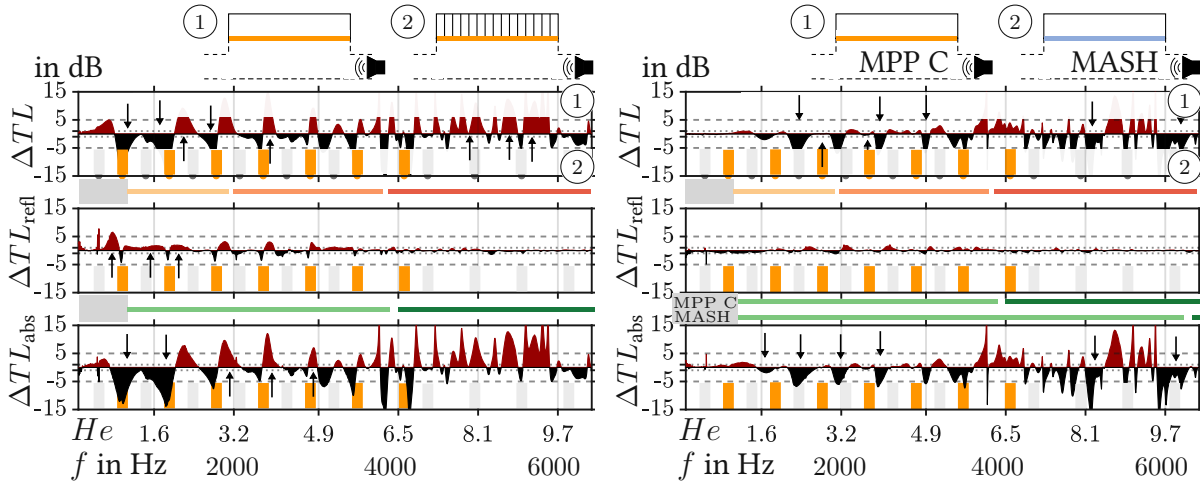
Figure 3.14: Measured difference in TL -portions of the MPA, $L_{c,60}$ and setup A variations: attachment with one MPP compared to uncovered and covered porous material filled cavity; $He = \tilde{k}_0 b_{\text{ex}}$.

Lastly, a direct comparison of the segmented and unsegmented MPA is made (Fig. 3.15 (a)). As observed before, the segmentation increases the absorption at the TL -notches in a broadband fashion in the viscous-driven frequency range (orange), most effectively below f_c (orange). The unsegmented MPA is more effective in reducing transmission of sound power above f_1 (red) and in the inertia-driven frequency range (green). As in the case of the porous material compared to the MPA, the segmentation reduces the TL -peaks below f_1 (orange).

In Fig. 3.15 (b), the MASH increases the sound power absorption at the TL -peaks over the entire frequency range. The MASH has a fitted $\phi = 0.098$ and $r_{\text{pore}} = 55$ mm (see 6.4) and thus a larger viscous-driven frequency range (orange). The conclusion is drawn that up to f_1 the type of MPP can influence the reflective damping effect of the expansion chamber (TL -peaks) and then the sound field diffusivity levels the different MPP types' effects. However,

a larger viscous-driven frequency range is beneficial for broadband and high transmission loss. The TL -notches are almost unaffected by the MPP type.

The segmentation reduces the reflected sound power up to f_1 compared to the segmented case. There is almost no difference in sound power reflection between MPP C and MASH in the attachment.



(a) Attachment with one MPP unsegmented (reference, dark-red areas, ①) to segmented case (black areas, ②).

(b) Attachment with one MPP type C unsegmented (reference, dark-red areas, ①) to MASH (black areas, ②).

Figure 3.15: Measured difference in TL -portions of the MPA, $L_{c,60}$ and setup A variations: unsegmented and segmented MPA with one MPP and compared MPP type C to MASH; $He = \tilde{k}_0 b_{ex}$.

So, summing up the findings leads to the following conclusions:

- The cavity segmentation is more ineffective in a diffuse sound field, but broadband-effective at low He -numbers where it enhances the reflection damping mechanism. An MPP with a wide viscous-driven frequency range can add to a high and broadband transmission loss at low He -numbers and in a diffuse sound field. In the inertia-diffuse frequency range it is beneficial not to segment the cavity (non-local reaction).
- For a wave guide MPA in a liner configuration, the reflected power portions are not negligible. Depending on the thickness, a contaminant layer can add to TL , but the pores must be permeable for optimal performance.
- An MPA is as effective as a covered porous foam absorber.

- MPPs add to sound absorption, but reduce maximum TL -peaks of the reflective interference damping due to cross section jumps at low He -numbers compared to the empty attachment. Filling the cavity reduces reflection.

Setup B

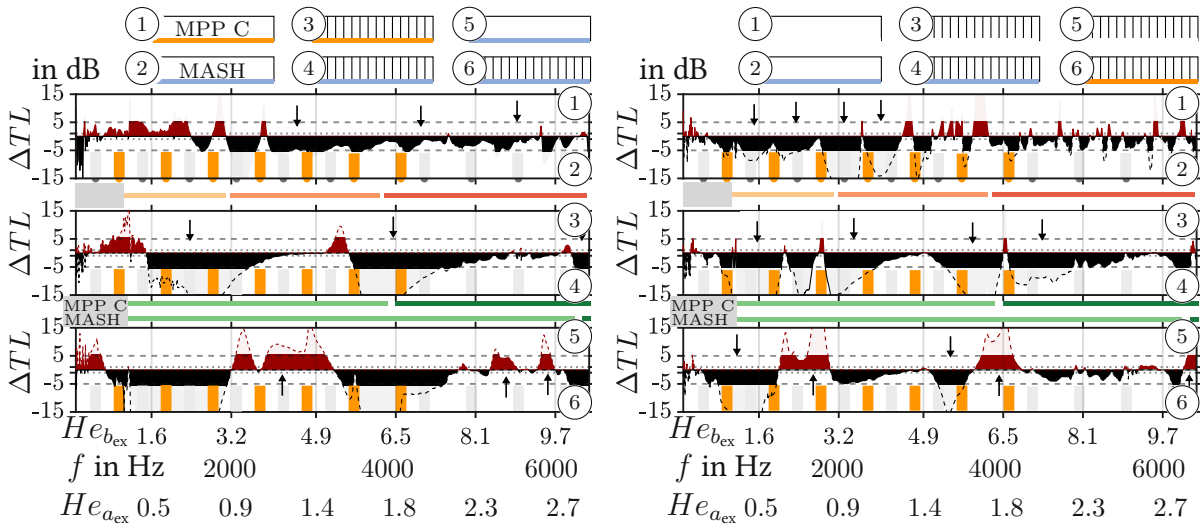
It has been established that most of the reduction in transmitted sound power in the expansion chamber setup is due to absorption (dissipation and/or reflective interference). Setup B with $L_{c,60} = 60$ mm now allows to assess the influence of a reduction in diffusivity on the MPA by solely looking at the difference in transmission loss. As can be seen in Fig. 3.10, the wave fronts in b_{ex} -direction are skewed, but in L_c -direction they are more or less plane, which corresponds to two Helmholtz numbers $He_{b_{ex}}$ and $He_{a_{ex}}$. The entire frequency range of setup B is like a magnification of the frequency range up to f_c (orange bar) in setup A, comparing the Helmholtz numbers (see Fig. 3.14 (a) and Fig. 3.16 (a)).

The upper plot in Fig. 3.16 (a) and Fig. 3.15 (b) shows the MASH's absorption advantage compared to MPP type C and that it can be augmented by a more plane-wave like sound field (low $He_{a_{ex}}$). Also, the wider viscosity-driven frequency range (green bar) of the MASH is visible. The segmentation (center plot) of the cavity in combination with a large porosity MPP and the MPA's cavity depth L_c , can then lead to a more broadband absorption over a frequency interval of up to 1000 Hz. The bottom plot shows the comparison of the MASH with an empty cavity and a segmented cavity. The large TL at the L_c -resonances is still there, but the broadband effect is slightly compromised. Again, a more diffuse sound field in b_{ex} -direction, beginning at f_c (orange bar and red bar), might play a role.

The typical TL -differences at TL -notches (dark-yellow bars) and peaks (grey bars) do not manifest as obvious as in setup A (compare Fig. 3.15 (b)). However in Fig. 3.16 (b), at low transversal Helmholtz numbers $He_{a_{ex}}$, the MASH augments some of the analytic TL -peaks significantly, but less prominent the TL -notches (upper plot) (orange bar and red bar). Broadband absorption is enforced by cavity segmentation (Fig. 3.16 (b), center), as well as a much higher TL than the segmented cavity alone. The maximum TL and broadband effectiveness is then determined by the MPP type (porosity and characteristic length) (see Fig. 3.16 (b), compare center and bottom).

Thus, summing up the findings leads to the following conclusions:

- A low transverse Helmholtz number ($He_{a_{ex}}$) is sufficient for a broadband MPA absorption behavior in the entire frequency range.
- MPP porosity and characteristic length (high Biot frequency f_v) determine optimal broadband effectiveness and maximum TL .
- A cavity segmentation is necessary for a maximum/optimal TL -loss (using the Cremer impedance, see [141]) in plane wave frequency range.
- A low Helmholtz number in a_{ex} - and b_{ex} -direction renders the highest MPA effectiveness in terms of sound absorption.



(a) Unsegmented cavity with MPP C (①) and MASH (②), segmented cavity with MPP C (③) and MASH (④), MASH with unsegmented (⑤) and segmented cavity (⑥).

(b) Empty cavity (①) compared to cavity with MASH (②), segmented cavity without (③) and with MASH (④), segmented cavity without (⑤) and with MPP type C (⑥).

Figure 3.16: TL differences in measurements of MPA, $L_{c,60}$; setup B with different cavity configurations.

3.2.5 Circular MPP in expansion chamber

Looking at the modes plot in Fig. 3.10, it is evident that the sound wave field in the circular expansion chamber arrangement is fundamentally different from the ones in setup A and B. The circumferential modes all have the same spatial phase at the edges, comparable to the field with a Helmholtz number $He_{a_{ex}}$ in setup B. The cavity length $L_{c,70-20}$, however, varies now from 70 mm to 20 mm.

Indeed as in setup B, Fig.3.17 (a) reveals that the segmentation already produces a high and broadband transmission loss. Adding MPP type C increases sound absorption merely below f_c (orange bar). The segmented cavity without MPP C reflects much more sound power.

If the MPP is added, the cavity structure does not make much of a difference (Fig.3.17 (b)) in terms of sound power reflection. However, the circular MPP seems to render the cavity segmentation broadband-absorption-ineffective above f_1 (frequency range orange bar and red bar). This is not observed in setup B (and less obvious in setup A). The MPP adds to absorption in combination with the segmented cavity below f_1 (frequency range orange bar and red bar).

Thus, summing up the findings up to now leads to following conclusions:

- In a circular mode sound wave field, the MPP does not impact so much on TL at medium to high He numbers (frequency range orange bar and red bar). The cavity structure already causes

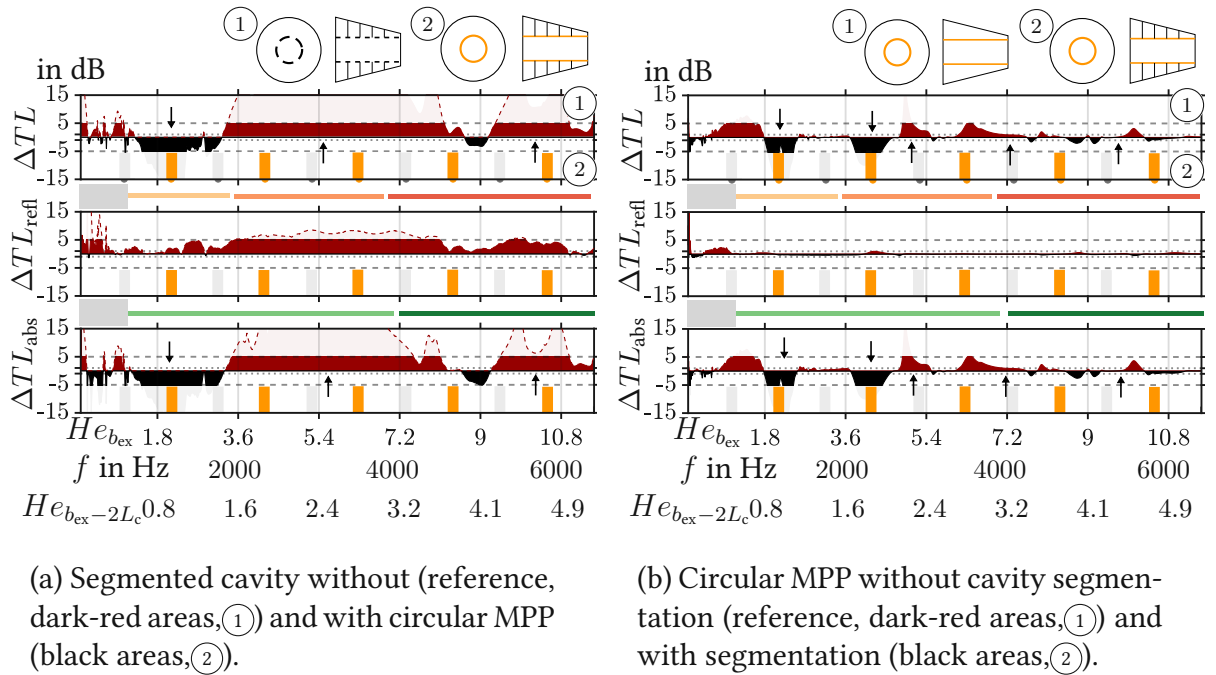


Figure 3.17: TL portion measurements of MPA, $L_{c,70-20}$, setup C with different cavity variations.

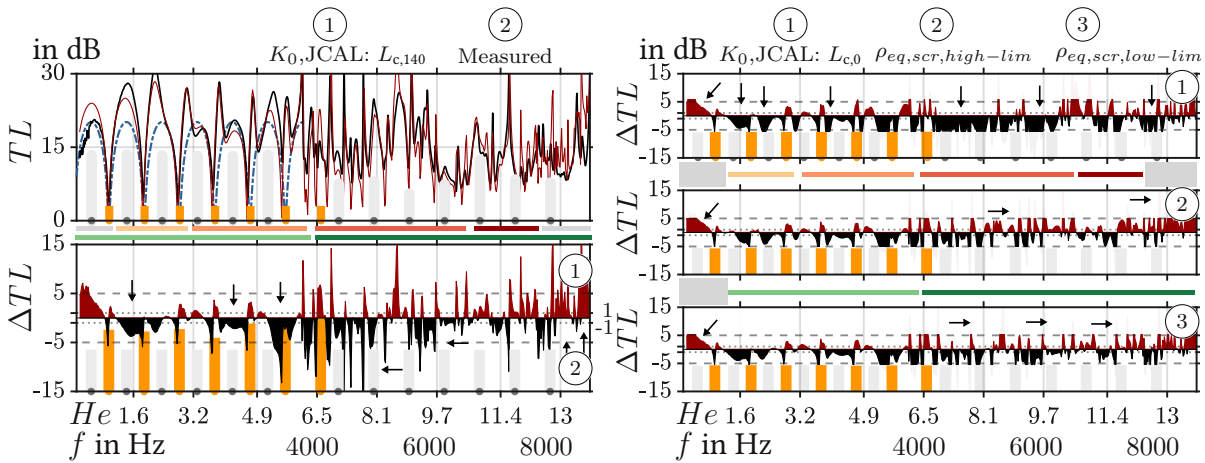
a very high transmission loss. In setups A and B (compare Fig.3.16 (b) and Fig.3.13 (b)) a much higher and broadband TL can be achieved at medium He numbers.

- The influence of the MPP is more prominent below f_c and with lower He numbers (■).
- The MPPs porosity and characteristic length might have been affected by the bending to the circular form (D_{MPA} , curvature radius).
- Comparing with setup A and B:
 - The MASH has a much smaller fitted characteristic length r_{pore} than MPP type C. This leads to much higher Biot frequency (3800 Hz vs. 6500 Hz)(compare Tab. 6.4 and Fig. 3.15 (b)), thus a much larger viscosity dominated frequency range, and this is beneficial for the augmentation of the TL peaks as well as the broadband absorption in the diffuse range. The MPP C's viscosity-dominated range could have been changed, e.g., by enlargement of the slits due to the bending.
 - In the circular MPA setup, the MPP with the segmented cavity affects the viscosity-dominated region much more than the inertia-dominated frequency region (compare Fig. 3.13 (a)) at higher He numbers. Which is comparable to the acoustic behavior of the MPA in Setup A and B.
But the benefit over the entire frequency range of using a segmented cavity instead of an unsegmented is much smaller than in setups A and B.

3.3 Characterization by simulation

3.3.1 Validation

To accurately recover the shown influences of the MPA on sound absorption with the equivalent fluid approach described in chapter 2.2.3 and chapter 3.1.2, it is necessary to investigate the modeling sensitivities. The robustness of the 1D-fitted equivalent fluid parameters will be tested in the benchmark setup A with one MPP type C in the unsegmented cavity and a frequency range up to 8500 Hz (additional frequency range ████████). The impedance tube data range frequency ends with 6400 Hz (range ████████). This time, two frequency regions with a larger error sensitivity to the microphone input data must be highlighted (████████, cf. f_{low} and f_{up} in (3.1)). It is also tested how much the modelling of $K_{eq,scr}$ influences the simulated and measured data agreement depending on the sound field character (cf. plane wave frequency range ████████ to diffuse ████████), the MPA configuration and its orientation to the sound source. First, the models used to fit equivalent density and compression modulus $\rho_{eq,scr}$ and $K_{eq,scr}$ to the impedance tube data are investigated. The basal design variable tuple is $\mathbf{x} = (\phi, r_{pore}, L_c)$.



(a) TL -differences of simulated setup (reference, dark-red areas) and measured (black areas); JCAL with fitting to $\mathbf{x} = (\phi, r_{pore}, L_{c,140})$ and constant K_0 ; analytical solution of bulk chamber without MPA (— —).

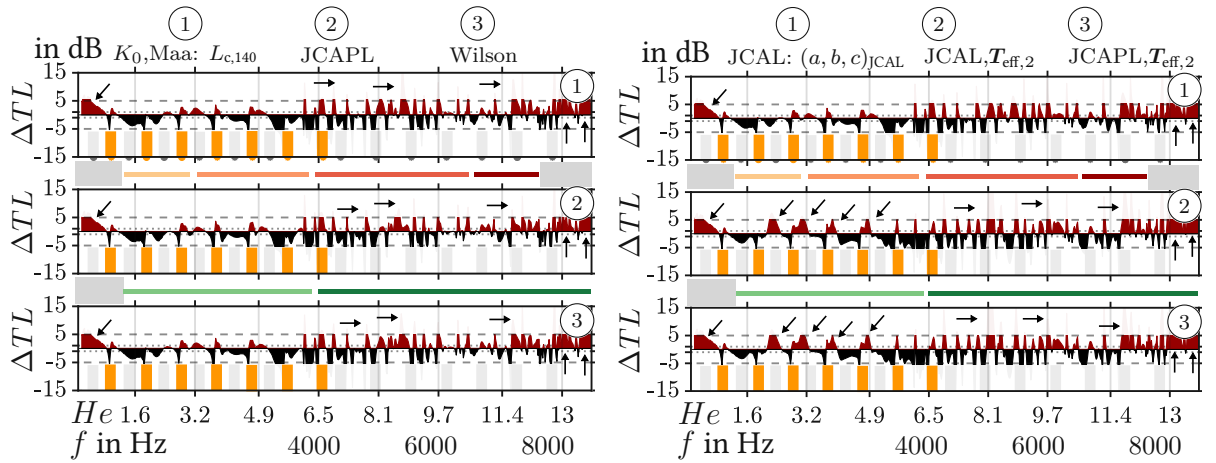
(b) TL -difference of simulation (reference, dark-red areas) to measured data (black areas); JCAL, K_0 , $\mathbf{x} = (\phi, r_{pore}, L_c):L_{c,0}$ (①), high-frequency-limit model- $L_{c,140}$ (②), low-frequency-limit model- $L_{c,140}$ (③).

Figure 3.18: JCAL modeled MPA in setup A compared to measurements and influences of the models used.

Models

Initially, only $\rho_{\text{eq,scr}}$ is modeled and K_0 is set to the constant ambient value. From the measurements above, it is known that most of the sound transmission reduction in setup A is due to absorption. The comparison plot in Fig. 3.18 (a) reveals that the model mostly underestimates sound absorption by the MPA. Larger differences occur in the highly-sensitive frequency range (grey) and in the highly-diffuse portion of the spectrum (red). Significant deviations are visible at the analytical TL -peaks (grey) and at the notches (orange) below f_c and at lower He numbers. Above f_2 the simulation overestimates sound absorption. Generally, the largest differences occur at the resonance peaks of the chamber and in the viscosity-driven frequency range (green).

Comparing $L_{c,0} = 0$ mm-fitting and the low- and high-frequency-limit models (cf. Fig. 3.18 (b)), shows that the largest error is introduced by fitting to impedance tube data without absorption peaks in the mid-high frequency range (orange and red). The low- and high-frequency-limit models render similar results as the full JCAL model. However, the low-frequency-limit model underestimates the sound absorption in a similar fashion as the full model. The differences below 500 Hz cannot be recovered by any model. It is attributed to a systematic measurement (phase) error due to a sensitivity to errors in input data from the microphones. The frequency range above 7700 Hz can be affected by the same principle (see the beginning of Chap. 3.1). Outside of these sensitive frequency portions the fit is generally well, even above the impedance tube data limit frequency 6400 Hz (frequency range red).



(a) TL -difference of simulation (reference, dark-red areas) to measured data (black areas); $K_0, \mathbf{x} = (\phi, r_{\text{pore}}, L_{c,140})$: Maa (①), JCAPL (②), Wilson (③).

(b) ΔTL simulation (reference, dark-red areas) to measured data (black areas); $K_0, \mathbf{x} = (\phi, r_{\text{pore}}, L_{c,140})$: JCAL + $(a, b, c)_{\text{JCAL}}$ (①), JCAL + $(a, b, c)_{\text{JCAL}} + \mathbf{T}_{\text{eff},2}$ (②), JCAPL + $(a, b, c)_{\text{JCAL}} + \mathbf{T}_{\text{eff},2}$ (③).

Figure 3.19: JCAL modeled MPA compared to measurement and influence of the model used.

For a fair comparison of the models, it helps to remember that each of the presented models recovered well the r -curves of the impedance tube data (cf. Subchap. 3.1.4). In Fig. 3.19, the TL -differences when using Maa or the Wilson model are small. The JCAPL-model produces minimally less differences at the TL -resonance peaks between f_1 and f_2 (■, see Fig. 3.19 (a)). All models perform equally worse below 500 Hz and beyond 7700 Hz (sensitive frequency range ■). Using more fitting parameters (see Fig. 3.19 (b)(①)) has no remarkable effect in setup A for the cavity with one MPP. In the frequency range below f_1 (■) using a double layer MPA for the impedance fitting procedure ($T_{\text{eff},2}$), introduces significant errors at the analytical TL -peaks (●). Also, these models cannot account for the errors below 500 Hz and beyond 7700 Hz.

Influence of fitting to L_c

In subchapter 3.1.4 it was proposed to fit the impedance tube data to as few model parameters as possible. The data in Fig. 3.19 (b) suggest that a higher number of fitting parameters only introduces more differences to the measurement at lower He numbers. Fig. 3.18(a) and Fig. 3.19 (b) showed that the JCAL, Maa and Wilson model produce similar results if only $\rho_{\text{eq,scr}}$ is modeled. The ansatz by Maa does not account for $K_{\text{eq,scr}}$ and Wilson's ansatz derives the equivalent density and compression modulus from the vorticity and entropy modes which results in quite different values for r_{pore} and thus f_v . In Tab. 6.3 and Tab. 3.3, these models' r_{pore} and ϕ vary rather strong if the cavity length is introduced as another design variable. However, an equivalent Z_{eff} is obtained in the impedance tube fitting; resulting in a good agreement in measured and simulated r -data (cf. Fig. 3.5) for low He numbers. Therefore, the model sensitivity to the third most important fitting parameter L_c is investigated in the expansion chamber MPA.

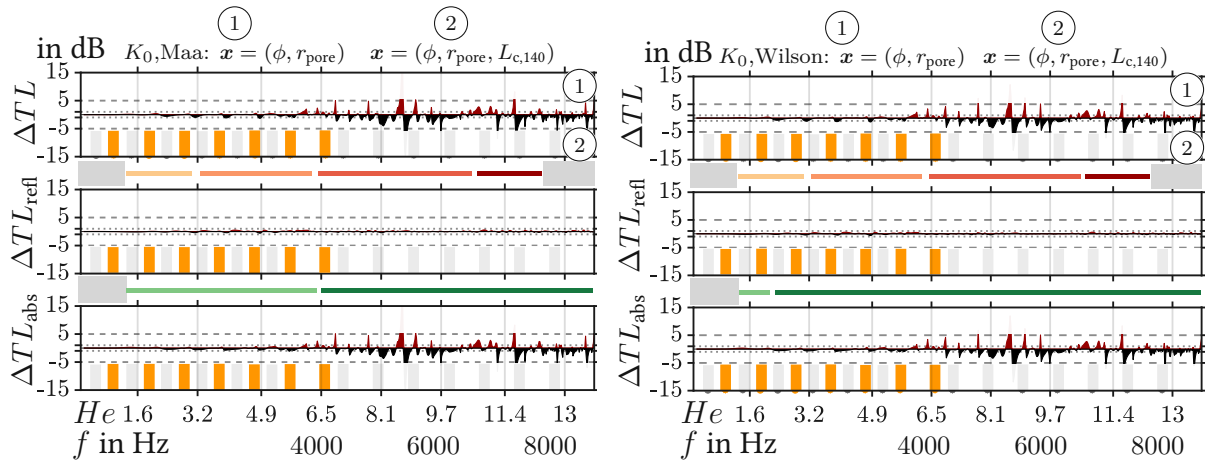
Both figures 3.20 (a,b) reveal that the three parameter modeling has a noticeable effect on sound absorption in a more diffuse sound field above f_1 (range ■, ■). The simulated sound absorption is reduced if the L_c -fitted equivalent density (with K_0 held constant) is used, since the simulation generally underestimates the measurement in that frequency range (cf. Fig. 3.18 (a)). Reflection is more or less unaffected by fitting to L_c . However, keep in mind that L_c as design variable can introduce more ambiguity to Z_{eff} , since L_c -fitting in the impedance tube is temperature sensitive and can compensate for a frequency-range and temperature change in the fitting with rather large variations in r_{pore} and ϕ (compare Tab. 3.1). In Fig. 3.20 (a,b), the differences in using Maa or Wilson with more design variables are not significant. They after all produce similar equivalent Z_{eff} , respectively $Z_{\text{eq,scr}}$. On the other hand, the comparison shows that the differentiation by a viscous- and inertia driven frequency range is not purposeful when using the same MPP (range ■, ■). These frequency ranges are only meaningful if different MPPs are compared (cf. 3.16 (b) and Tab. 6.5). This is because f_v is proportional to r_{pore} , and the latter changes significantly depending on the used model.

Thus, the following interim results are:

- The accuracy of the 3D-simulation is not dependent on the model if the 1D-fitting pro-

duced a good measurement data fit. This is probably due to the thinness of the MPP and that the models all emulate a similar effective surface impedance Z_{eff} and thus a similar characteristic impedance $Z_{\text{eq,scr}}$ of the MPP volume.

- The accuracy depends on the number of design variables. It is sufficient to use just $\boldsymbol{x} = (r_{\text{pore}}, \phi)$. The inclusion of L_c leads to a bit more undershooting of the measured data above f_1 (■, ■).
- However, if L_c is added to \boldsymbol{x} , its temperature sensitivity must be account for.
- The accuracy depends only in part on the character of the sound field; generally, the trends are recovered well over the entire frequency range, but the absolute height of the measured TL-peaks is mostly underestimated.
- The differentiation by viscous and inertia frequency range is best applied when different types of MPP are analyzed.



(a) TL-differences of Maa based simulated setup with $\boldsymbol{x} = (\phi, r_{\text{pore}}$ -fitting (dark-red areas,reference,(1)) to $\boldsymbol{x} = (\phi, r_{\text{pore}}, L_{c,140})$ -fitting (black areas, (2)).

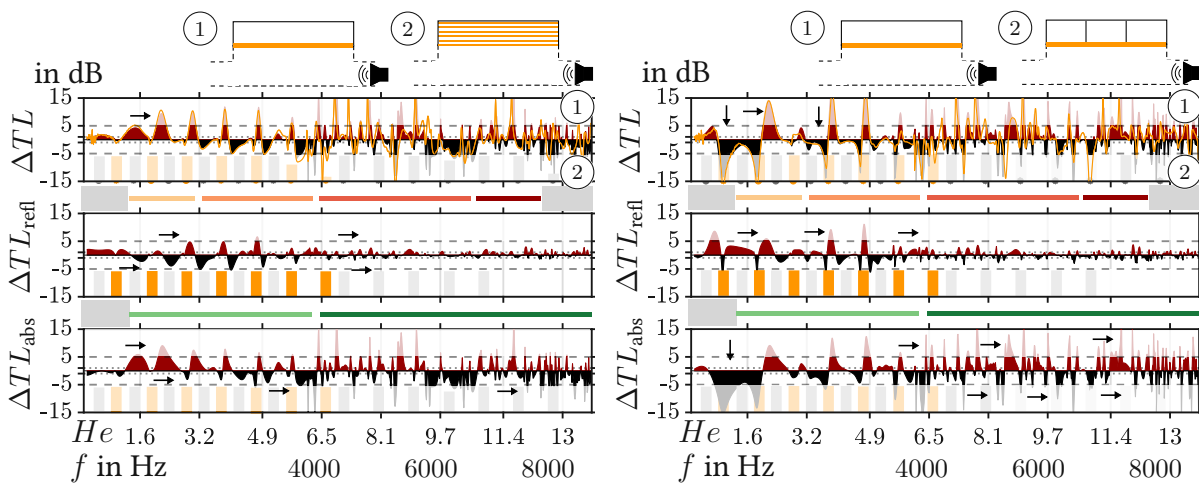
(b) TL-differences of Wilson based simulated setup with $\boldsymbol{x} = (\phi, r_{\text{pore}}$ -fitting (dark-red areas,reference,(1)) to $\boldsymbol{x} = (\phi, r_{\text{pore}}, L_{c,140})$ -fitting (black areas, (2)).

Figure 3.20: Influence on transmission loss portions by adding cavity length L_c to \boldsymbol{x} .

3.3.2 Changing the MPA configuration

The MPA predictive design involves the evaluation of MPP arrangement depending on the available space, sound field, and desired frequency range. The MPA in setup A with only one MPP type C might not be suitable for certain noise challenges, especially if one considers the sound energy portions (compare (3.11)).

If the cavity is filled with up to six MPPs (see Fig. 3.21 (a)), more absorption at the analytical TL-peaks is produced, beginning at f_c (range). With sound field being more diffuse above f_1 , the hexa-MPP arrangement absorbs significantly more sound. But sound absorption at the analytical TL-peaks below f_c is compromised (range). Also, more sound power is reflected here.



(a) Simulated and measured (yellow) TL; MPA configuration of one MPP with unsegmented cavity (dark-red areas, reference, (1)) compared to six MPPs in the cavity (black areas, (2)).

(b) Simulated and measured (yellow) TL; MPA configuration of one MPP with unsegmented cavity (dark-red, reference, (1)) to the cavity with three evenly spaced cavity chambers (black areas, (2)).

Figure 3.21: MPP in attachment and comparison of different cavity configurations.

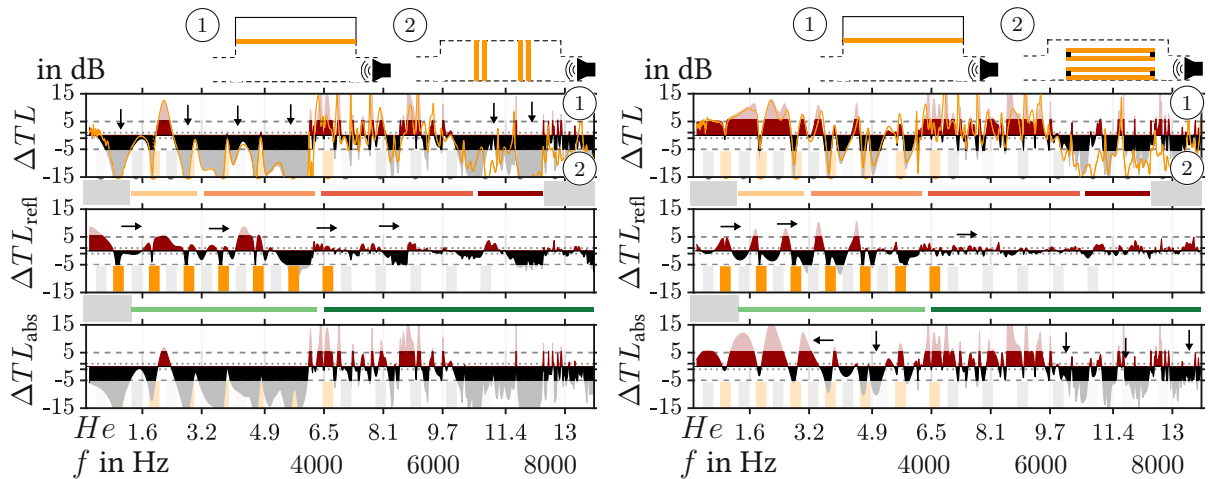
Compared to Fig. 3.21 (a) the triple segmentation of the cavity in Fig. 3.21 (b) is less effective in broadband fashion compared to the unsegmented cavity, but there are improvements below f_c (range). As shown before, the diffuse sound field renders the segmentation ineffective (range and).

To optimize the MPA for certain frequency ranges, a vertical and horizontal tetra-layer MPP arrangement are compared to the attached cavity with one MPP in Fig. 3.22 (a,b). The horizontal tetra-layer arrangement is the most effective absorber structure in terms of maximum and broadband absorption. Due to placing in direct line of sight to the noise source, there

is also a significant change in reflected sound power. The analytical TL -peaks are mostly unaffected.

The horizontal splitter-type arrangement increases sound absorption beyond f_2 (■), but loses performance below f_c and within f_1 and f_2 (ranges ■ and ■). The distance between a pair of tetra-layers was 10 mm.

The agreement of simulated and measured TL is very good for all investigated configurations up to f_1 (ranges ■ and ■). There is a good correlation in the frequency range up to f_2 , the limit of the impedance tube data fit (■). There are increasing differences between the measured and simulated data above f_2 , but the correlation is still sufficient. It appears that in the diffuse range (■ and ■) the correlation worsens if one MPP with the unsegmented cavity are simulated. If the tetra-MPPs in the bulk chamber are simulated, then a better fit to the measured data can be obtained.



(a) Simulated and measured (yellow ■); MPA configuration of one MPP with unsegmented cavity (dark-red, reference, (1)) to vertical tetra-layer arrangement in the bulk chamber (black areas, (2)).

(b) Simulated and measured (yellow ■); MPA configuration of one MPP with unsegmented cavity (dark red, reference) to horizontal tetra-layer arrangement (splitter-type) in the bulk chamber (black areas, (2)).

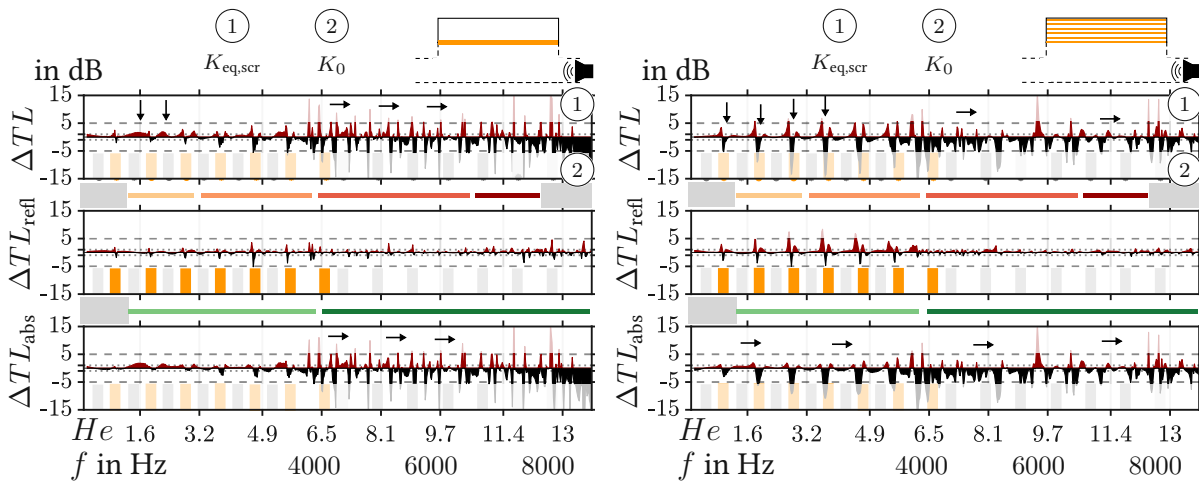
Figure 3.22: MPP in attachment and comparison of different MPP arrangements in the bulk chamber.

Influence of simulated compression modulus

So far the equivalent compression modulus has been set to the constant ambient value K_0 to avoid ambiguous fitting, because a non-unique $Z_{eq,scr}$ in the plane-wave case might result in very different synthetic sound field in the simulation with high He numbers (diffuse sound

field). Now, $K_{eq,scr}$ is modeled frequency-dependent and its influence on the four different MPA setups in Fig. 3.21 and Fig. 3.22 is assessed.

According to Fig.3.23 (a) the compression modulus controls the absorption notches below f_c (orange) and diffuse sound field peaks above f_1 (red, dark red). This effect is augmented if six MPPs are used (Fig. 3.23 (b)). Generally, simulated absorption is rather reduced if K_0 is used (more black area) which means that the simulation undershoots the measurement more (range orange, red, cf. 3.18 (a)). Comparing with Fig.3.18 (a), one can argue that using $K_{eq,scr}$ gives more realistic absorption peaks below f_c (orange). From these findings it is apparent that the thermal effects, simulated by the compression modulus, are smaller than in a conventional porous absorber (due to the thinness of the MPP volume), but have to be included if the least erroneous absolute value of absorption is sought. However, for general trends and relative comparisons among MPA configurations it should be sufficient to use just K_0 .



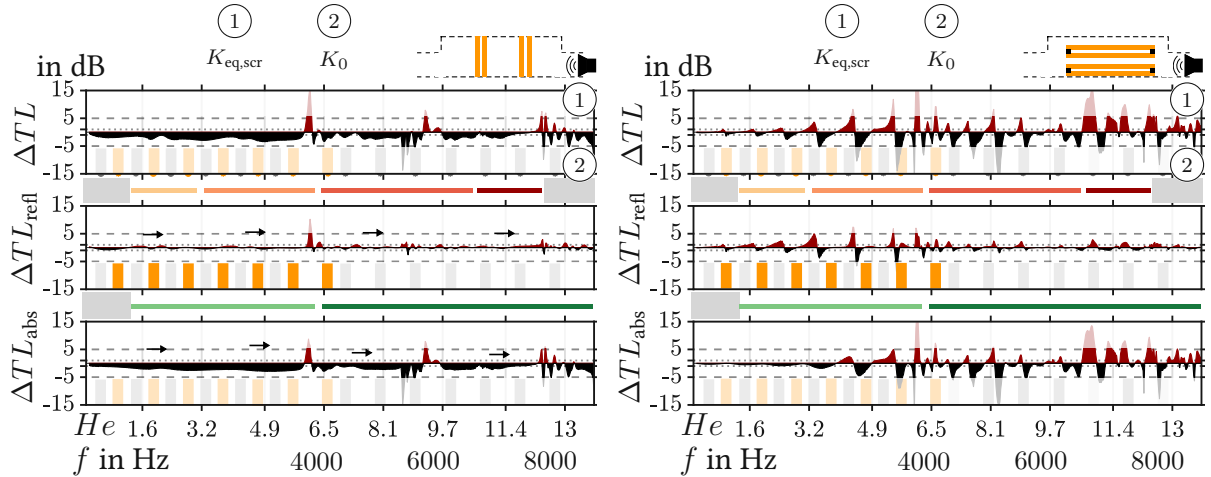
(a) Simulated MPA configuration of one MPP with $K_{eq,scr}$ (reference, dark-red areas, ①) and K_0 held constant (black areas, ②).

(b) Simulated MPA configuration with six MPPs in the cavity with $K_{eq,scr}$ (reference, dark-red areas, ①) and K_0 held constant (black areas, ②).

Figure 3.23: Influence of simulated compression modulus in different MPA configuration.

For the horizontal and vertical tetra-layer arrangements in Fig. 3.24 (a,b), the importance of including $K_{eq,scr}$ is also controlled by the number of MPPs (compare the viscous regime in Fig. 3.23 (a,b) and Fig. 3.24 (b), green). In Fig. 3.24 (a), the differences compared to using K_0 are rather large and occur in broadband frequency intervals. For the vertical layers there is almost no difference in reflected sound power, but in the case of the horizontal layers there are significant differences at the analytical TL -peaks (grey) and notches (orange). One can also conclude that if the sound wave impinges more perpendicular (Fig. 3.24 (a), entire frequency range), as well as in a more grazing incident sound field (Fig. 3.24 (b), range orange, red and in part red), where the TL -peaks due to the expansion chamber destructive interference

mechanism are dominant, $K_{eq,scr}$ apparently controls absorption and to smaller degree reflection more significantly.



(a) Simulated MPA with vertical tetra-layer arrangement in the bulk chamber with $K_{eq,scr}$ (reference, dark-red areas, ①) and K_0 held constant (black areas, ②).

(b) Simulated MPA with horizontal tetra-layer arrangement in the bulk chamber with $K_{eq,scr}$ (reference, dark-red areas, ①) and K_0 held constant (black areas, ②).

Figure 3.24: Influence of simulated compression modulus in different MPA configuration.

The results from the different MPA configuration studies thus far lead to the following conclusions:

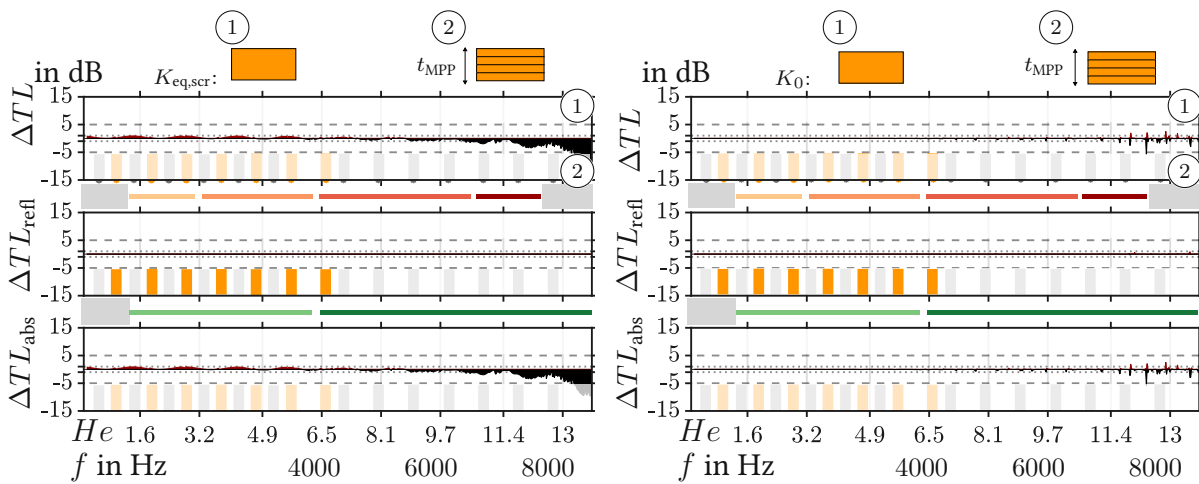
- The 1D-fitted data for $\rho_{eq,scr}$ and $K_{eq,scr}$ can emulate the acoustic absorption of more dedicated MPA configurations sufficiently well. Depending on the sought degree of accuracy, K_0 or a frequency-dependent $K_{eq,scr}$ can be used. In sum, using a constant K_0 or a frequency-dependent $K_{eq,scr}$ undershoots the measured TL for wide ranges of frequency.
- The differences in TL when using K_0 or $K_{eq,scr}$ depend on the MPA configuration, and number of MPP layers, and are, at least, in part dependent on the orientation of the source to the MPP volume. And thus also on the character of the sound field (plane or diffuse).
- Due to the thinness of the MPP volume, the influence of a frequency-dependent $K_{eq,scr}$ is small. Different combinations of $\rho_{eq,scr}$ and $K_{eq,scr}$ produce similar acoustic responses to the impinging sound wave. But, even if locally different, the same global acoustic response is reproduced.

3.3.3 Mesh sensitivity study

The simulations in Chap. 4 feature large geometries. Unnecessary large numbers of degrees of freedom (number of elements with corresponding nodes) cause large simulation times. The MPP volume solely introduces absorption and so, this region is the most sensitive to sound power artefacts caused by insufficient mesh resolution. It is therefore of interest how the mesh resolution affects the simulation results. For aforementioned and following FE simulations, the standard mesh size for all FE element volumes was $h = \lambda_{\min}/20$, with $\lambda_{\min} = c_0/f_{\max}$. The MPP thickness was $t_{\text{MPP}} = 1$ mm.

Conforming mesh - MPP thickness resolution

The simulations thus far, have been performed via a conforming spatial resolution of setup A and one element in MPP C depth direction. Fig. 3.25 (b) shows that keeping K_0 constant, introduces the fewest TL differences between one and four cell MPP depth resolution over the entire frequency range. There is no visible difference in the reflective transmission loss. If $K_{\text{eq,scr}}$ is modelled (Fig. 3.25 (a)), then sound absorption is reduced above f_2 (■) if four cells are used. If K_0 is used, then there is merely minimal differences in that frequency range between using one or four cells in depth direction. It could explain why the model choice has such a low impact above f_2 if K_0 is used (compare Fig.3.19), as well as that the influence of $K_{\text{eq,scr}}$ will be more prominent for thicker absorber volumes.



(a) Simulation with $K_{\text{eq,scr}}$; one cell (dark-red, reference, ①) to four cells (black areas, ②) in MPP depth direction.

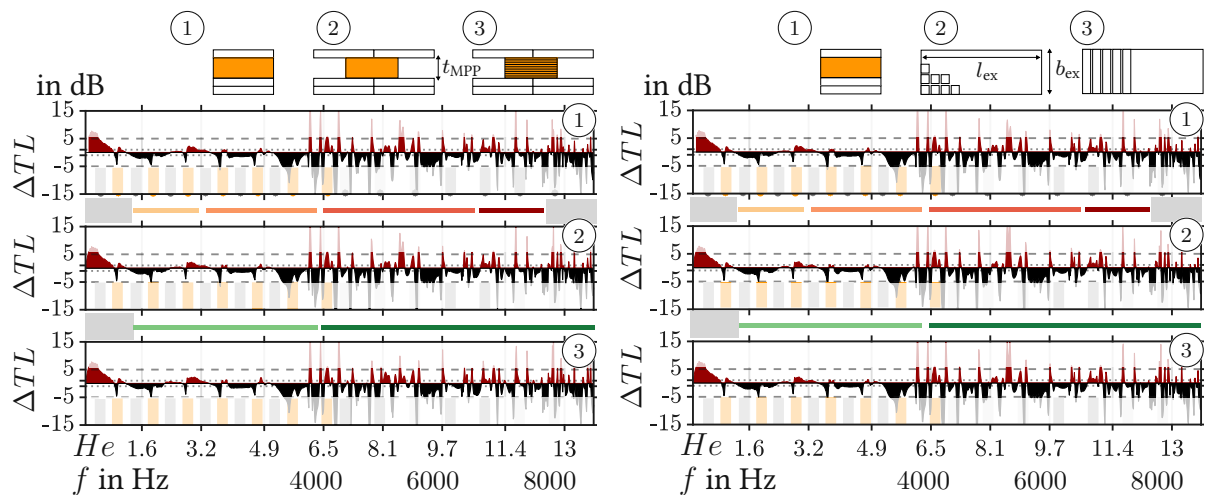
(b) Simulation with K_0 ; one cell (dark-red, reference, ①) to four cells (black areas, ②) in MPP depth direction.

Figure 3.25: Study of mesh resolution in MPP depth direction with K_0 held constant and $K_{\text{eq,scr}}$ simulated.

Non-conforming interfaces

The usage of non-conforming interfaces greatly simplifies the meshing effort and allows to split the MPP area in uncoupled smaller volumes. Thus, theoretically suppressing unwanted synthetic sound propagation perpendicular to the impinging sound wave and parallel to the MPP. Figures 3.26 (a,b) reveal, however, that with exception of certain resonance peaks, there is no significant distinguishable difference in using a conforming mesh or splitting the MPP volume into smaller volumes to suppress the wave propagation parallel and within the MPP volume.

This means that the synthetic wave propagation in the MPP domain can be neglected and non-conforming interfaces can be used with confidence for a wide frequency range. However, as has been shown before in Fig. 3.23 and Fig. 3.24, the number and placing of the MPP in the direction of the sound source, can introduce absorption differences and should also be accounted for with a frequency-dependent $K_{\text{eq,scr}}$ when using non-conforming FE meshes.



(a) Simulation with $K_{\text{eq,scr}}$ (dark-red areas, reference) and measured TL (black areas); conforming mesh (①), non-conforming with one cell in MPP depth direction (②), eight cells in MPP depth direction (③).

(b) Simulation with $K_{\text{eq,scr}}$ (dark-red areas, reference) and measured TL (black areas); conforming mesh and homogeneous MPP volume (①), 4x4 mm MPP rectangles (②), 4x90 mm MPP rectangles (③).

Figure 3.26: Influence of non-conforming interfaces and splitted MPP domain compared the measurement of setup A.

3.4 Review of the general findings

The observations thus far can support the investigations in the following chapters, but are also meant to give a general recommendation for the optimal design of more dedicated MPAs. The most relevant ones are:

- *MPA's do mainly augment sound absorption but the reflective behavior should be accounted for. The TL-portions depend on the geometry at hand.*
- *Pore contamination can support the MPA mechanism, but the pores must be passable by flow; here, a dependence on the viscous- and inertia-dominated frequency ranges is relevant.*
- *Cavity segmentation can help add to optimal usage by enforcing a local MPA reaction, but the broadband effectiveness depends to a large degree on the Helmholtz numbers parallel and perpendicular to the MPP. Also, the viscous- and inertia-dependent frequency ranges should be considered (Biot frequencies) for optimal MPP selection.*
- *For a circular MPP arrangement, an MPP with high porosity and small characteristic length should be chosen. The bending radius should be large so that the MPP pore geometry is unaltered.*
- **Modelling:**
 - *Choosing fewer fitting parameters renders accurate results compared to the measurements.*
 - *Fitting should be performed with an impedance tube cavity length that renders many absorption peaks.*
 - *If the most accurate result is sought, then the compression modulus must be modeled as frequency depended.*
- **Mesh sensitivity:**
 - *The MPP can be meshed with one cell in depth direction. Using a constant compression modulus reduces mesh sensitivity even further.*
 - *Non-confirming interfaces can be used with confidence and the MPP domain does not need to be segmented.*
- **MPA arrangement:**
 - *Horizontal, vertical, and multi-layer MPP arrangements in line of sight to the sound source can be applied for broadband-high-frequency sound (absorption) transmission loss.*
 - *The MPA liner can be optimized by already a few segmentations at low Helmholtz numbers. Fewer MPPs work more effective in a diffuse sound field (in front and in the cavity of the MPP) and with an unsegmented cavity.*

In-duct application adjacent to an axial fan

In this chapter, an MPA is applied in direct proximity to a low-pressure axial fan [8, 9, 49, 154]. Major parts of the following content have been published in [46, 57]. Here, a circular expansion chamber design was obtained using the workflow from Chap. 3 with non-conforming grids. The MPP type B was used and $K_{\text{eq,scr}}$ has been modeled as frequency-dependent. Type B has a slightly higher porosity than type C, but a roughly 30 % higher characteristic pore size r_{pore} (compare App. A Tab. 6.1 and Tab. 6.4). This results in a lower absorption coefficient than C, and the thinness and mounting of the type B specimen cause strong vibrations (compare Fig. 3.3 (b)). The scientific questions apart from the sound field sensitivity involve:

- So far, the MPA was located in the far-field of the sound source. How do the locations of the (aero-)acoustic sources in vicinity influence the MPA's effectiveness?
- How effective and how sensitive to its cavity configuration is the MPA if a background flow is present?
- How do the MPA, its location, and its cavity configuration influence the aerodynamics and thus the efficiency of the fan?
- Under which conditions or in which configuration will sound reduction be compromised by the MPP-fan-flow-interaction?
- How accurate is the simulative pre-characterization compared to the measurements?

The duct sound field characteristic is again cast into a Helmholtz number, He_R . It spans from the plane-wave range to the diffuse range, where it is comparable to setup C in Chap. 3. The aeroacoustic source mechanisms in combination with the rotating fan bring about a rotating

(spinning mode) pressure field. Higher order modes would propagate if the circumferential Mach number is supersonic; otherwise they are exponentially damped [34, 153]. These modes would then add to the far-field sound pressure at larger angles from the axis of fan rotation. In this case, due to the low tip-speed Mach number, higher order modes are theoretically propagated with a very low intensity along the duct into an anechoic chamber [28] or not propagated at all. The fan characteristics and sound emissions were measured in a test rig that features a homentropic steady inflow at discrete fan operational points with no relevant heat conduction at the duct walls.

With the major design parameter for dimensioning the MPA being the blade passing frequency, it is possible to pre-select an optimal cavity length. Due to its sources' coherent nature, the noise level emitted in the vicinity of f_{BPF} will be very high. The blade passing frequency for the fan(s) investigated is $f_{\text{BPF}} = 222.9 \text{ Hz}$, computed by $f_{\text{BPF}} = n_{\text{blade}} \cdot n_{\text{rot}}/60$, with number of blades $n_{\text{blade}} = 9$ and a rotational speed $n_{\text{rot}} = 1486 \text{ rpm}$. The relevant fan and flow dynamic parameters in the test rig are

- Volume flow range $\dot{V} = [0.2 : 2.1] \text{ m}^3 \text{ s}^{-1}$.
- Non-turbulent inflow Reynolds number range $Re = \frac{u_0 D_{\text{duct}}}{\nu_0} = [32000 : 320000]$;
 $Re_{\text{crit,plate}} = 5 \times 10^5$.
- Non-turbulent inflow plate Reynolds number range $Re = \frac{u_0 L_d}{\nu_0} = [79000 : 338000]$.
- Maximum background flow Mach number $Ma_{\text{back}} = \frac{\dot{V}_{\text{max}}}{A_{\text{duct}} c_0} = 0.03$.
- Fan tip speed Mach number $Ma_{\text{fan,tip}} = \frac{(n_{\text{rot}}/60)\pi D_{\text{fan}}}{c_0} = 0.11$.
- Angular speed $\Omega_{\text{fan}} = 155.6 \text{ s}^{-1}$
- Fan tip speed $U_{\text{fan,tip}} = 38.5 \text{ m s}^{-1}$ and circumference of the fan $C_{\text{fan}} = D_{\text{fan}}\pi$.

Convective effects on the acoustic mode's sound-propagation can be neglected ($Ma_{\text{back}} < 0.3$). Due to the many orders larger duct cross section ($D_{\text{duct}} = 500 \text{ mm}$) relative to the boundary layer thickness δ_v ($\mathcal{O}(\mu\text{m})$) and the short duct length of less than 1 m, its influence ($\alpha_{\text{cl}}, \alpha_{\text{walls}}$) on sound emissions is also neglected.

4.1 Measurement setup

The fan is operated in two versions, with forward-skewed (F) and backward-skewed (B) blades (see Fig. 6.3 in App. B). It has different distances to the nozzle (L_d , cf. Fig. 4.1), long and short which allows to assess the change in emitted sound pressure levels if the fan's noise sources are located within the MPA section. The details of the test rig can be found in the appendix (see App. B 6).

4.1.1 Fan setups

The MPA section has a length of $L_{\text{MPA}} = 440$ mm, a duct diameter $D_{\text{duct}} = 500$ mm, and the fan diameter is $D_{\text{fan}} = 495$ mm (see Fig. 4.4). The two latter dimensions represent the reference duct setup (tagged RFS and RFL in Fig. 4.1). It can be replaced by the MPA duct variant (MFS and MFL cf. Fig. 4.2). Therefore, the fan examined is either operated directly in the perforated duct section (MFS) or shortly downstream in the unperforated duct section (MFL). The relevant dimensions near the tip gap geometry are also depicted in Fig. 4.4 (a). The tip gap is $(D_{\text{duct}} - D_{\text{fan}})/2 = 2.5$ mm in width for the reference cases (RFS/RFL). The setup's name acronym consists of (R) for reference, (F) for free inflow and (S/L) for short or long duct (cf. Fig. 4.1 and Fig. 4.2). Deviations from the circular circumference at the joint of the MPP sheet (cf. red area in Fig. 4.4 (b)) need to be smaller than the tip gap clearance if the fan is operated above the micro-perforated sheet. The tip gap has a significant influence on both the efficiency of the fan and its aeroacoustic behavior [21, 92, 96]. First of all, the efficiency is affected, because a larger tip gap leads to increased blind flow affecting the pressure rise of the fan unfavorably. On the other hand, as stated previously, the sound sources in the tip gap are the dominant ones that can occur in the subharmonic (partial load range) range and at higher harmonics of the blade passing frequency. A larger tip gap can amplify these source mechanisms.

For the variant MFS, the perforated diameter was $D_{\text{MPP}} = 506$ mm in order to make sure that no contact of the fan blades with the sheet surface irregularities occurs. This is equal to a tip gaze size enlarged by 3 mm compared to the reference cases (RFS/RFL). In the short (S) duct version, the fan is operated at a distance $L_d = 520$ mm and in the long version at $L_d = 620$ mm from the nozzle. In the long version the fan is not operated within the MPA section, thus the tip gap clearance of the fan is the same as in the reference cases.

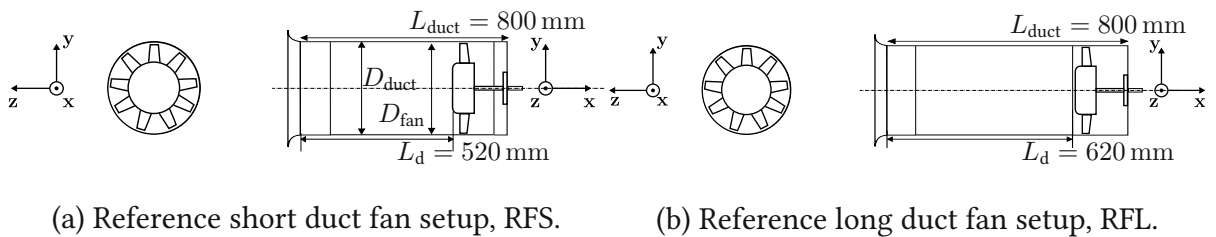


Figure 4.1: Schematic representation of the reference (R) duct design. F indicates that the inflow was undisturbed and S and L stand for the short $L_d = 520$ mm and long version $L_d = 620$ mm.

The duct length $L_{\text{duct}} = 800$ mm with two open endings can bring about duct resonances at 170 Hz, 350 Hz, 500 Hz, 690 Hz, 860 Hz according to $nc_0/(2L_{\text{duct}})$ with $n = 1, 2, 3, \dots$. The sound field character will be indicated by the Helmholtz number $He_R = \tilde{k}_0 R_{\text{duct}}$, where R_{duct} is the radius of the reference duct.

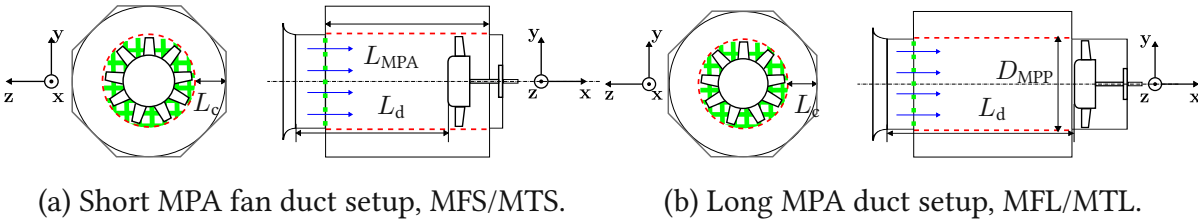


Figure 4.2: Schematic representation of the MPA duct design (M). Free inflow conditions (F) with long (L) as well as short (S) version (the same length as in reference case); $L_{MPA} = 440$ mm and indicated cavity length L_c , the turbulent flow with turbulence grid (light green indication) is marked with T (cf. [141]). The octagon shape is the realized geometry. The pre-characterization studies were performed on the circular shape.

4.1.2 MPA setups

The basal MPA with an empty cavity of length L_c (MFS/MFL) with free inflow conditions is compared to different variations of the cavity and under turbulent inflow conditions (.T.). According to [34, 131] the turbulence ingestion will create a broadband noise pattern. The different MPA cavity configuration are depicted in Fig. 4.3:

- Dummy: Fan hub without revolving fan. It shows the influence of the MPA on sound reduction (and production) without the influence of the revolving fan blades. The volume flow is created by the auxiliary fan (cf. Fig. 6.1 in App. B).
- MDFS: Tip gap clearance equal to RFS case. The sound sources in the tip gap of the fan are dominant sound sources, which occur mainly in the subharmonic range between the tonal peaks of the blade passing frequency. These sound sources are amplified due to the larger tip gap. The sound sources in the tip gap are particularly important in the unsteady operating range of the fan, i.e at low volume flow rates [90, 91, 96].
- MHFS: The cavity length is reduced to $L_c = 40$ mm with a honeycomb segmentation. This aims to enforce a local reaction, however the Helmholtz number $He_R = \tilde{k}_0 R_{duct}$ is rather high, even at lower frequencies below 1000 Hz (compare setups A,B and C in Chap. 3).
- MXFS: The axial segmentation of the cavity, parallel to the fan's axis of rotation, aims to broaden the sound reduction.
- MCFS: The reduced cavity length without segmentation $L_c = 35$ mm aims to reduce sound emissions in the higher-frequency range.
- MMFS: Adding an MPP with a larger flow resistivity aims to reduce bias flow through the MPP (see dark-green-dashed lines in Fig. 4.3).

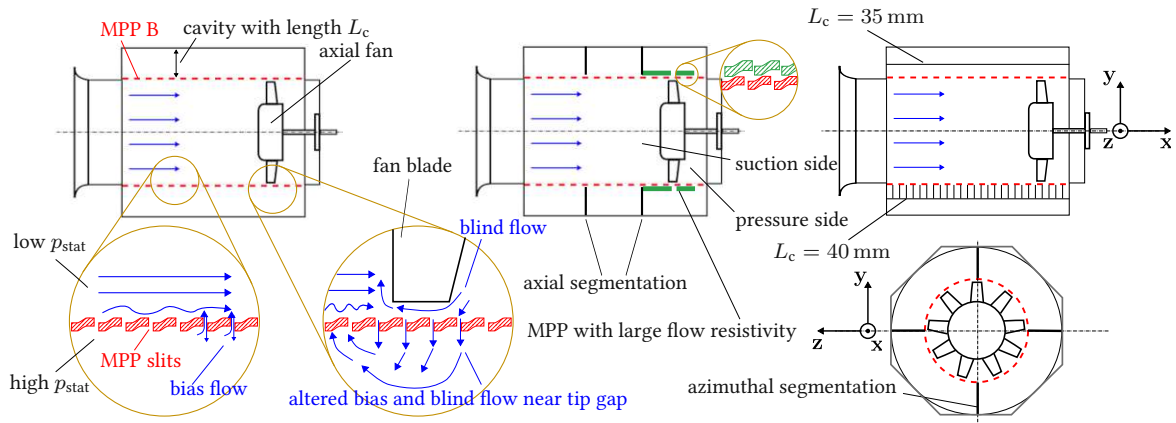


Figure 4.3: Schematic representation of the MPA cavity configurations.

4.2 Acoustic analysis - Duct setup pre-characterization

The design of the MPA is based on an heuristic and a numerical analysis according to the aeroacoustic sources of the fan. In addition, the MPA was laid out to compactness ($L_{c,max} = 200$ mm) and to be most effective at the blade passage frequency.

4.2.1 Aeroacoustic sources

The simulation framework proposed is not CAA, since resolving the MPP spatially within CFD simulations is unfeasible for parameter studies. The exact strength and distribution of acoustic sources remains unknown. To reflect the nature of aeroacoustic noise realistically, the distribution of sources for an axial fan in a duct was investigated [27, 28].

A theory of aeroacoustic analogies was first developed by Lighthill in [107], where he introduced the idea of replacing the flow field of a free unbounded jet with a sum of elementary sources. The resulting equation has the same form as the wave equation governing propagation of sound emitted by a quadrupole source with the strength of the turbulence stress tensor (Lighthill tensor) in a non-moving medium [65]. Thereby, he was able to calculate the sound power emitted and sound wave propagation into the far field by the integral formulation using Green's function of free radiation. Curle [44] gave a more general derivation taking solid surface effects into account in this integral equation [95]. Due to the flow's reaction forces on the blades' surface and the duct walls, dipole source behavior might be observed. These forces can be steady or unsteady, manifest on all all overflowed blade surfaces and cause "loading noise" [34]. Curle and Ffowcs-Williams and Hawkings [54][44] state that, at low Mach numbers, compact sources can be assumed and the contribution to the sound field from the dipoles should be greater than from the quadrupoles induced by the second spatial derivation of the Lighthill tensor. Monopole-like blade thickness noise (displacement noise) can also be disregarded due to the low Mach numbers. Thus, the source terms for the solution of (2.17) might be mimicked by dipole-like point sources near the blade tips and the duct surface.[57]

The fan test setup investigated was the basis for various computational aeroacoustic simulations and testing of different formulations of the inhomogenous wave equation [85]. Here, the fan was also revolving at $n_{\text{rot}} = 1486$ rpm. Figure 6.5 in App. B shows constant iso-surfaces at 220 Hz with phase and opposite phase parity that reveal predominant equivalent sources in the tip gap region. Also, the surface sources computed according to Curle reveal that the largest power levels occur at the leading edges of the blades and at the duct in the tip gap region (cf. Fig. 4.4). The shown simulation results from Fig. 6.5 [85] are based on DES CFD simulations and took up to several weeks to be completed. This corroborates unfeasibility for a parameter study, since the additional discretization effort needed for micro-perforations would increase simulation time even further.

Combined with the theory mentioned these simulation results led to the decision to mimic the equivalent sources and location by placing point sources at a small distance from each other near the tip of the blades (cf. black points in Fig. 4.4 (a,b)) and solve (2.17). The sources were placed on the blade tip region's surface 10 mm from the tip edge to direct acoustic radiation towards the anechoic chamber. To reflect the circumferential spatial distribution of the equivalent sources (cf. Fig. 6.5), the point sources were placed on each of the nine blades (cf. Fig. 4.4 (b)). The acoustic power emitted by the axial fan was estimated at to an amplitude $a_i \approx 94$ dB for the design point of the fan characteristic, with a volume flow rate of $1.4 \text{ m}^3 \text{ s}^{-1}$ and an average pressure rise of 150 Pa according to [1]. This value was used as constant source excitation strength for the point sources on the blades to solve (2.17). The duct to wavelength ratio L_{duct}/λ is much lower in the frequency range of $f_{\lambda/4,i}$ than in the diffuse range above 2 kHz. Therefore it is possible that some sound pressure portions of the (spinning) modes (order (m, r)), are detectable near the nozzle inlet.

To add this spinning mode behavior, one can calculate a varying source strength $\tilde{p}(\vartheta, t)$ by [34]

$$\tilde{p}(\vartheta, t) = \sum_{i=1}^{\infty} a_i \cos[in_{\text{blade}}(\vartheta - \Omega_{\text{fan}}t)], \quad i = 1, 2, \dots, \quad (4.1)$$

with t as the time it takes for one blade to revolve by 40° , ϑ as blade position in $^\circ$, Ω_{fan} as the angular speed of the fan, n_{blade} as the number of blades and i as the order for the harmonics of the base tone f_{BPF} , where $i = 1$).

The simulations showed no qualitative difference in using monopole (single point)-like or dipole (two points separated by a small distance plus π -phase difference)-like in the tip gap region. This observation is supported by previous investigations for low Mach number flows, showing that quadrupole sources near walls become dipole sources [62]. A significant difference manifests if one point source of the same strength as nine distributed sources on the blades in the tip gap region (cf. Fig. 4.4 (b)) is placed at the center of the fan body (cf. Fig. 4.8 (a) and Fig. 6.5 (b)). The spinning mode field can be discerned by the number of wave peaks in circumference direction (ϑ , order m) as well as in radial direction R_{duct} (order r). The plane wave mode, with order $(0, 0)$, is always propagated.

According to [34, 153], for a circumferential and/or radial spinning mode field to propagate,

the mode cut-off frequency (cf. (2.47)) must be surpassed, but also $Ma_{\text{fan,tip}} > \beta_{mr}/in_{\text{blade}}$ must be fulfilled [34], where β_{mr} is the argument for the Bessel function solution of the homogeneous version of (2.17) in the circular duct. This means that the fan tip would have to revolve with supersonic speed, which is not the case. The higher order spinning modes will then be exponentially damped with $8.685|\tilde{k}_x|$ dB per meter (cf. (2.47), [34]).

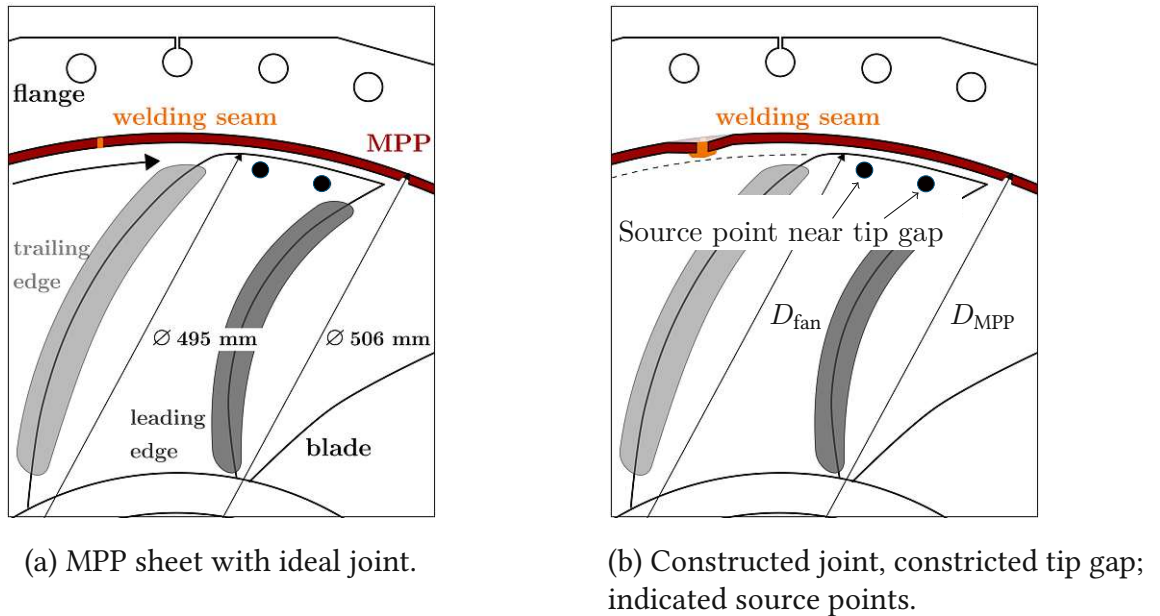


Figure 4.4: Dimensions and detail of tip gap region of forward skewed fan (F); front view.

4.2.2 Acoustic simulation setup

The material characterization in Chap. 3.1 provided MPP type B absorption behavior information in the frequency domain up to 1600 Hz. The cavity length of $L_c = 140 \text{ mm}$ proved to be a good compromise between a wide absorption frequency band and a high peak absorption performance with reasonable cavity length. Comparing Fig. 3.3 (b) and Fig. 3.4 (b), one can see the larger the cavity length, the narrower the absorption frequency bands. To reflect the acoustic behavior of the entire test setup more realistically, an FE simulation was conducted. Therefore, the duct section with fan and part of the sound-receiving air space were spatially discretized. Figure 4.6 (a) shows the rectangular settling chamber with the surrounding perfectly matched layer (PML), the attached nozzle section adjacent to the MPA section, and the axial fan section bordered by a second layer of PML, guaranteeing free radiation conditions on both sides of the duct. Figure 4.6 (b) shows an enhanced view of the non-conforming interfaces separating each of these sub-domains, which allows a much more flexible pre-processing (cf. [89]). Thereby, the open source research software openCFS [5, 87], using Nitsche-type mortaring [89] to solve (2.17) efficiently, has been applied. Since pre-design simulations aim to find an optimal trade-off between the cavity dimension L_c and a

large amount of absorption by comparing multiple simulation runs, a compromise between necessary spatial discretization and computational effort must be found. For harmonic simulations, an estimation formula for the necessary discretization exists. The relation between the element order q , the wave number \tilde{k} (complex valued \tilde{k} in MPP domain) and the spatial discretization size h is provided by [7]

$$q + \frac{1}{2} > \frac{\tilde{k}h}{2} + (\tilde{k}h)^{1/3}. \quad (4.2)$$

This inequality has to be fulfilled to obtain a pre-asymptotic error reduction by increasing the order q of the FE basis functions. In Fig. 6.6 (a,b) the resulting relations according to (4.2) for both the air domain and MPP domain are shown. The chosen discretization of $h = 0.01$ m for the nozzle, the MPA section and the axial fan domain (cf. Fig. 4.6) should be sufficient. The receiving air chamber elements were meshed with $h = 0.02$ m to reduce the number of degrees of freedom even further. Due to the complex valued material, the effective speed of sound in the MPP domain (cf. Fig. 6.6 (d)) is smaller than in the surrounding air (cf. Fig. 6.6 (b)), which results in a smaller required discretization as the wave number increases. However, the small thickness of the domain requires an element size of less or equal to 1 mm in the direction of the MPP depth.

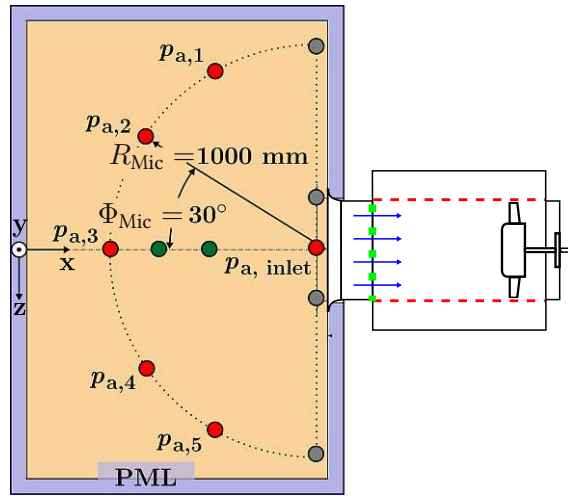


Figure 4.5: Monitoring points for simulations (●) and measurements (●) [57].

Therefore, as in the rest of the computational domain, an element order of one was chosen. The sound pressure field calculated was monitored at five locations in the receiving air chamber domain (cf. Fig. 4.5) and for comparison at the inlet of the nozzle. The pressure frequency results were spatially averaged and energetically summed up over monitoring points $p_{a,1-5}$ to obtain an overall simulated sound pressure level $\bar{L}_{p,sim}$. Each setup took roughly seventeen hours to compute on eight CPU cores with a total of 3.3 million elements. For the measurements, the averaging and summation was performed over monitoring points $p_{a,1-3}$

(●) and two additional microphones at the dark-green indicated positions (●). The additional microphones for the measurements (●) are located on a semicircle perpendicular to the plane of the points $p_{a,1-5}$ (see also App. B. Fig. 6.2). The microphones, respectively the monitoring points in the simulations, are located at a distance $R_{\text{Mic}} = 1$ m from the center of the inlet nozzle and are separated by $\Phi_{\text{Mic}} = 30^\circ$ in the simulations and $\Phi_{\text{Mic}} = 22.5^\circ$ in the measurements.

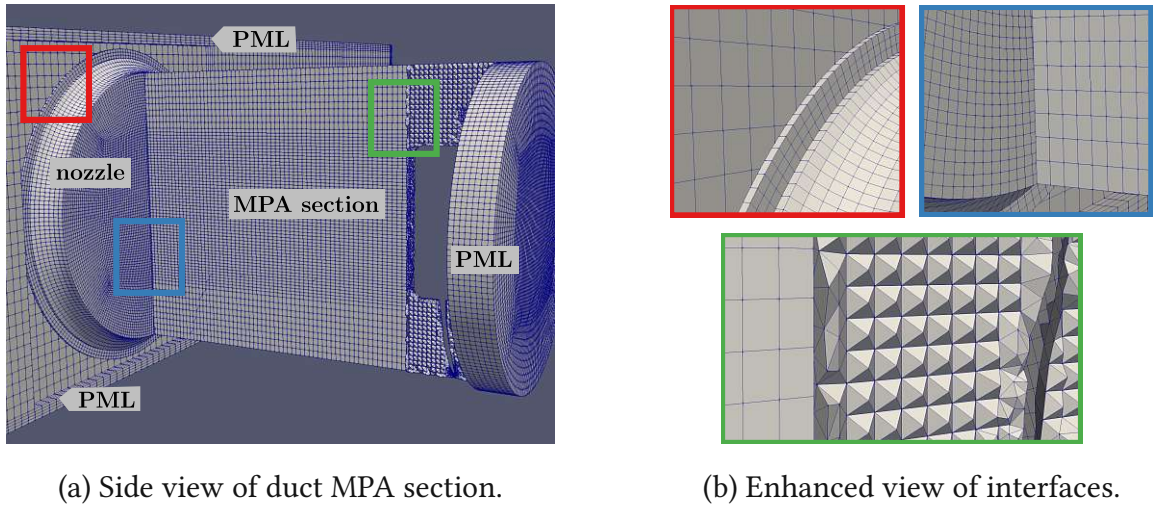


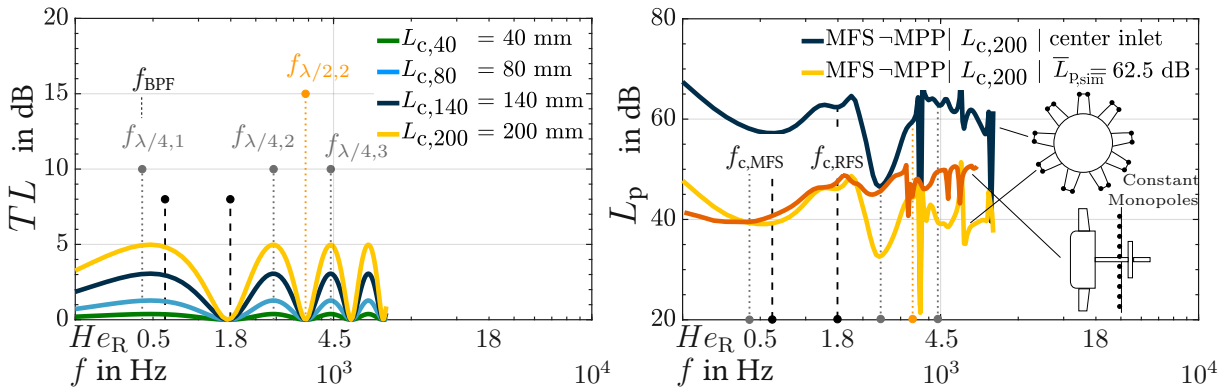
Figure 4.6: Finite Element subdomains with non-conforming interfaces [57].

4.2.3 Radiated sound and directivity

In this section, the described duct setup is investigated with the FE method. The aim is to assess the acoustic behavior of the duct-test-rig setup as well as to find equivalent spatial acoustic sources that mimic the real fan's aeroacoustic behavior. A design parameter input constraint was a maximum cavity length of $L_c = 200$ mm due to spatial constraints at the test rig. First, characterizing simulations of the geometry setup are shown in Fig. 4.7. A transmission loss computation of various cavity depths with transmission line theory (expansion chamber model, cf. [123] for details) shows only minor damping effects even at $L_c = 200$ mm. An FE simulation of the entire domain without MPP but with cavity length $L_c = 200$ mm and length $L_{\text{MPA}} = 440$ mm reveals that the sound emission spectrum at the duct nozzle center adjacent to the air chamber is qualitatively represented by the overall sound pressure level at the monitoring points (similar overall sound pressure trend over frequency) up to 1000 Hz (cf. Figs. 4.7 (b), 4.5). If one assumes plane wave fronts and free radiation conditions are present, we can verify the results in Fig. 4.7 (b) with the radiated sound power by comparing the sound pressure levels at the center inlet (cross section area A_{duct}) and at a distance of $R_{\text{Mic}} = 1000$ mm ($L_{p_{a,1-5}}$) over the half-sphere surface A_{D} [106] by

$$\Delta(L_{p, \text{inlet center}} - L_{p_{a,1-5}}) = 10 \log(A_{\text{D}}/A_{\text{duct}}) \text{ dB.} \quad (4.3)$$

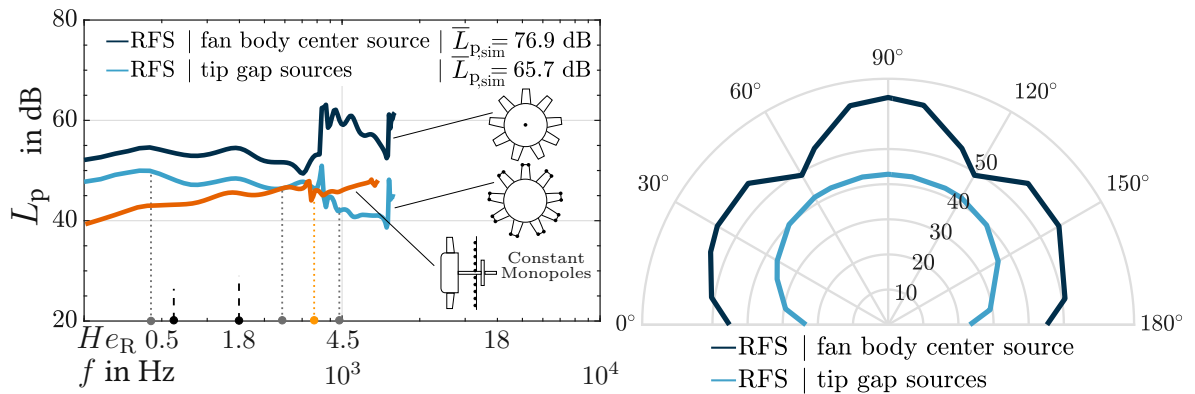
The sound pressure level between the center inlet microphone points and the points at distance R_{Mic} should decrease by about 15.1 dB at a 1000 mm distance from the nozzle inlet (cf. Fig. 4.5). This behavior is visible below 500 Hz, near the cut-off frequency of the first circumferential mode for the RFS setup. In the MFS case, the first cut-off frequency drops from $f_{c,\text{RFS}} = 402$ Hz to $f_{c,\text{MFS}} = 259$ Hz due to additional cavity length L_c . In Fig. 4.7 (a,b), certain resonance frequencies are highlighted. Below $f_{c,\text{MFS}} = 259$ Hz, all higher order modes are cut off. At $f_{\lambda/4,1} = 190$ Hz, $f_{\lambda/4,2} = 580$ Hz and $f_{\lambda/4,3} = 970$ Hz, the simulated TL spectra (cf. Fig. 4.7 (a)) show significant peaks that are associated with integer multiples of the cavity length dimension L_{MPA} . At $f_{\lambda/2,2} = 780$ Hz, the simulated spectrum reveals an additional narrower very pronounced dip (cf. Fig. 4.7 (b)). The expansion chamber shows $\lambda/4$ -reflection damping effects, and the TL at each of the indicated frequencies should be amplified by the MPP. The $\lambda/2$ -reflection frequency is mentioned, because the measurements will reveal a large sound reduction at this frequency.



(a) Analytically calculated transmission loss TL due to cross section changes; highlighted $\lambda/4$ - and $\lambda/2$ -resonance frequencies. (b) Simulated sound emission spectra; $L_{p_{a,1-5}}$ averaged over five microphone positions (cf. Fig. 4.5) and at the single center inlet point at the nozzle; indicated source positions on the fan (\bullet).

Figure 4.7: Pre-characterization simulations of the duct-fan geometry.

Additionally, the radiation strength and the directivity pattern of the reference duct with the nozzle were investigated. Figure 4.8 (a) reveals that with a single point source at the fan body center at a distance from the nozzle comparable to that of the nine point sources distributed across the blade tip region, the radiation strength is generally amplified, especially above $f_{\lambda/2} = 780$ Hz. Reflection at the duct walls begins to occur as soon as higher order modes can propagate. Higher order mode wave fronts not in phase parity tend to decrease propagating sound pressure levels by canceling out each other's portions of the wave fronts. The proximity of the point sources (Fig. 4.8 (a), in reality the tip gap equivalent sources) to the duct wall will most likely influence the sources' emission effectiveness by this reflection effect, since at frequencies below the cut-off frequencies $f_{c,\text{RFS}}$, $f_{c,\text{MFS}}$ and $f_{\lambda/2}$ (plane wave



(a) Simulated sound emission spectra with spatially varied point source (•) locations in the reference setup.

(b) Simulated sound emission directivity pattern at 1200 Hz with sound pressure level isolines.

Figure 4.8: Simulated radiation pattern and strength of point sources (•) located on the fan body center axis and on the blades in the fan's tip gap region.

frequency range), the radiation pattern and signal strength do not differ much.

In Fig. 4.8 (b), the more pronounced directivity pattern of the single point source far beyond the cut-off frequencies at 1200 Hz is depicted. Comparing Fig. 4.8 (a) and Fig. 4.7 (b) reveals that a lower-level non-monopole directivity behavior is present, indicating the emitted spectrum's qualitative and quantitative dependence on the source positioning. If the sources are placed behind the fan, then the radiation pattern is completely different to the aforementioned and measured patterns about to be presented. The simulated spectra in Fig. 4.8 (a) also corroborate the aforementioned dependence of the sound pressure emission trend on the ratio L_{duct}/λ . For a low ratio, meaning the frequency range below the first cut-off frequency $f_{c, \text{RFS}}$, the duct should not influence the fan's emission spectrum that much. However, with a high ratio, due to multiple reflection at the duct walls, the sound emission intensity and directivity are significantly influenced by the duct.

4.3 Overall measured sound reduction and fan efficiency

This subchapter is intended to clarify how the developed MPA duct affects the measured performance and sound radiation of different fans (forward- and backward-skewed, see also Fig.6.3 in App. B.). In addition, it will be analysed which differences in the operating behaviour of the fan occur when the fan operates directly within the MPA duct section or downstream in the unperforated part. A typical sound emission spectrum of a forward- and backward-skewed fan without an MPA is depicted in Fig. 6.4 in App. B.

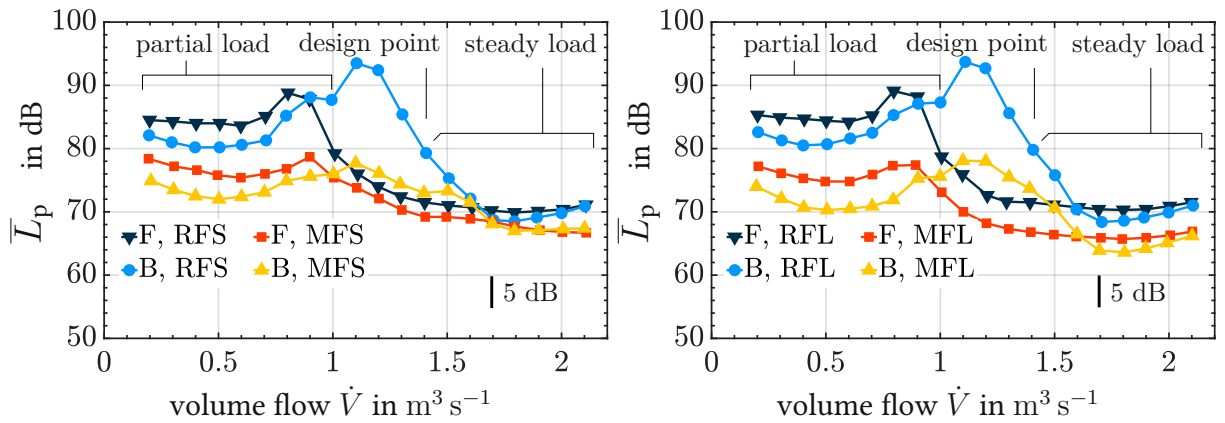
Fan blade skewness in the short and long duct

The overall sound emissions at all operational points of the fans' characteristic curves are shown in Fig. 4.9 (a,b). Additionally, the aerodynamic properties of the setup with a forward-skewed fan (F) and a backward-skewed fan (B) are depicted in Fig. 4.9 (c-f). The two fans were first investigated for the RFS and MFS variants, i.e. with free inflow and short duct (fan operates directly in the MPA duct section). The aerodynamic characteristics (Fig. 4.9 (c)) show that both fans have a lower pressure build-up in the case of the MFS. This can be connected to the larger tip gap. This is also reflected in a loss of efficiency for both fans (Fig. 4.9 (e)).

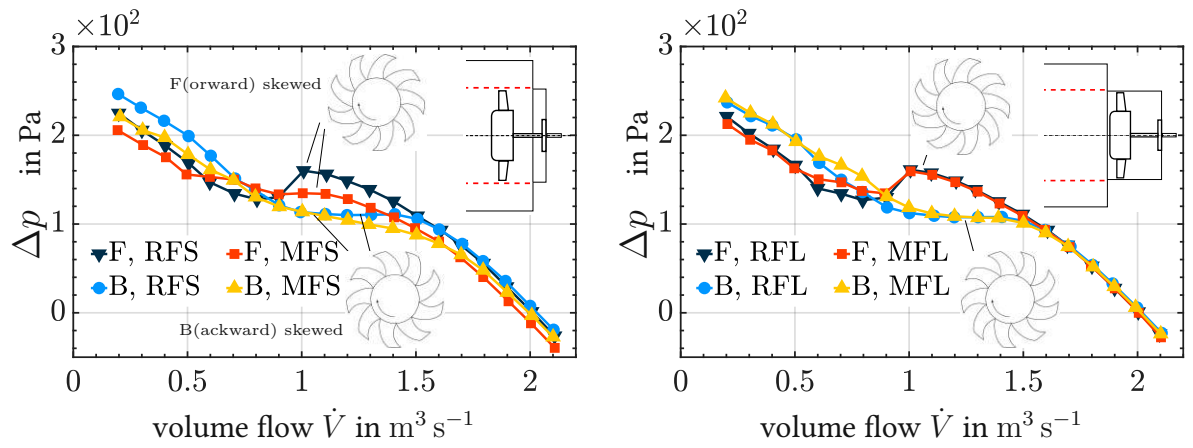
The noise reductions (Fig. 4.9 (a,b)) take place for both fans over the entire characteristic curve. However, the largest reductions in sound pressure level occur for the backward skewed fan (B). In the unsteady range of the characteristic curve, the sound sources are more dominant in this fan than in the forward skewed fan due to tip gap flow interactions. This is caused by the different radial velocity components of the skewed fan blades [39, 96, 166]. The noise reduction takes values of up to $L_p = 15$ dB (cf. Tab. 6.9) for the backward-skewed fan (B). The dominant peak (cf. Fig. 4.10 (a), Fig. 4.11 (a)) in the characteristic curve can thus be attenuated and the acoustic characteristic curve of the fans is much flatter. This indicates that the sound radiation in relation to the total sound pressure level becomes more independent of the volume flow rate \dot{V} . As a result, the noise level of the fan appears more constant when changing volume flows occur in a system.

The next step is to investigate the interaction of the MPA with the two fans in the long duct version. In this variant, the duct was extended and the fans operate behind the MPA in a standard duct section. The aerodynamic characteristics (Fig. 4.9 (b)) clearly show that the MPA no longer has a negative effect on the pressure build-up. In the partial load range an increase of the generated pressure difference can even be generated. In the long version of the duct the effects of the tip gap dimensions are the same for the reference case as for the case with MPA. According to this, the MPA seems to have a positive influence on the aerodynamics of the fan in the partial load range. This positive effect is visible in the efficiency curve (Fig. 4.9 (e)), which otherwise shows an identical course between reference case and MFL. In the case MDFS (cf. Fig. 4.20 (d)), the tip gap between reference case and MDFS was also identical, but nevertheless the efficiency was reduced due to the MPA. Since this is no longer visible here, it can be concluded that when the fan operates directly within the MPA section, the small pores of the absorber cause a larger backflow from the pressure side to the suction side of the fan, which reduces the efficiency. If the fan operates downstream the MPA, within a standard duct segment, the backflow is unchanged compared to the reference case.

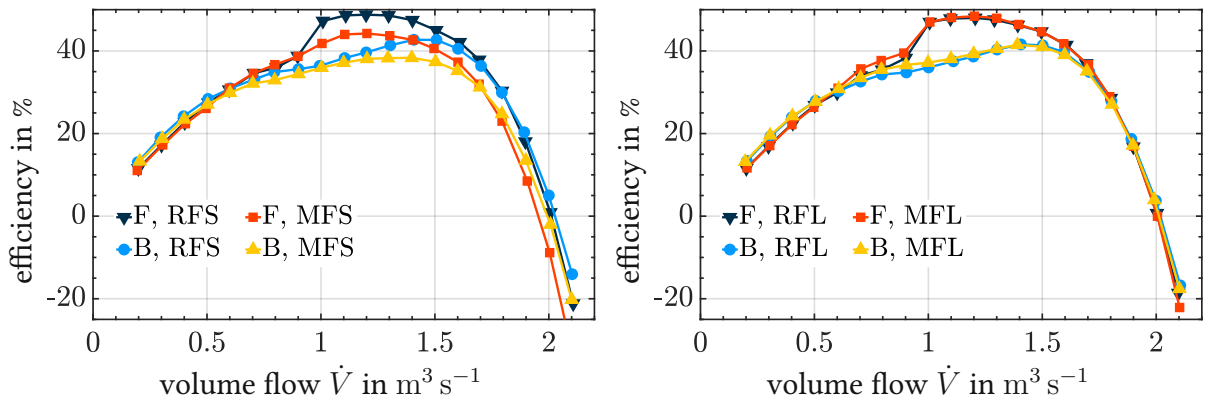
4.3 Overall measured sound reduction and fan efficiency



(a) Overall sound pressure level, RFS and MFS. (b) Overall sound pressure level, RFL and MFL.

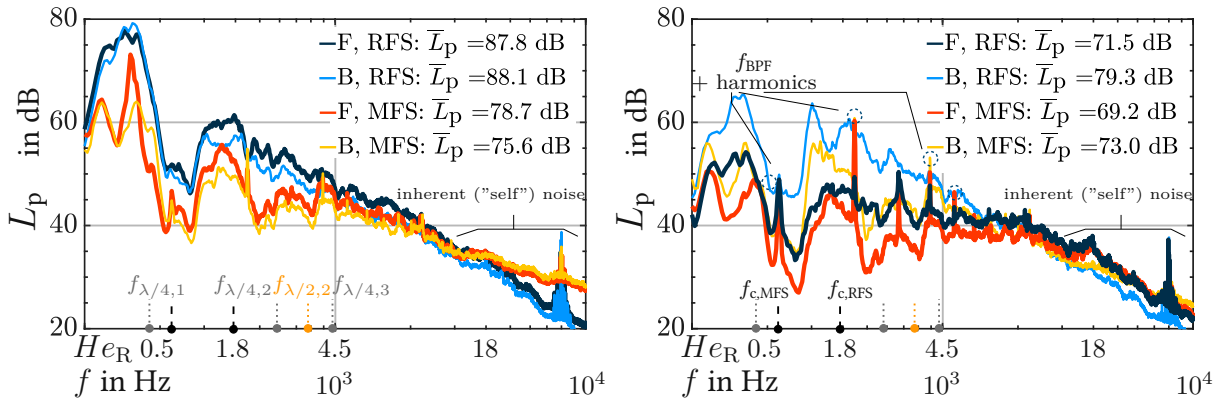


(c) Total-to-static pressure rise, RFS and MFS. (d) Total-to-static pressure rise, RFL and MFL.

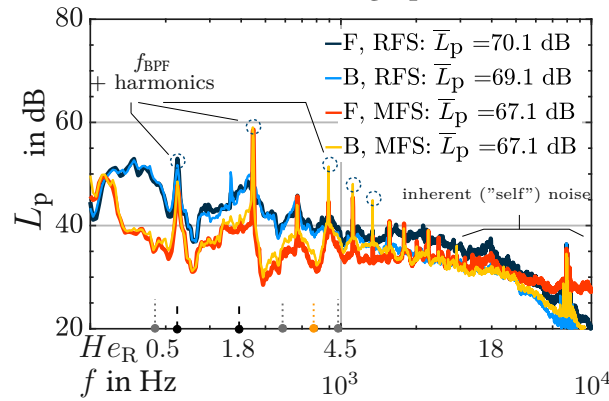


(e) Total-to-static efficiency, RFS and MFS. (f) Total-to-static efficiency, RFL and MFL.

Figure 4.9: Overall sound pressure levels, pressure rise and efficiency of F-B-RFS-MFS and F-B-RFL-MFL setup depending on the volume flow rate \dot{V} .



(a) Averaged L_p spectra at $\dot{V} = 0.9 \text{ m}^3 \text{ s}^{-1}$ (partial load). (b) Averaged L_p spectra at $\dot{V} = 1.4 \text{ m}^3 \text{ s}^{-1}$ (design point).

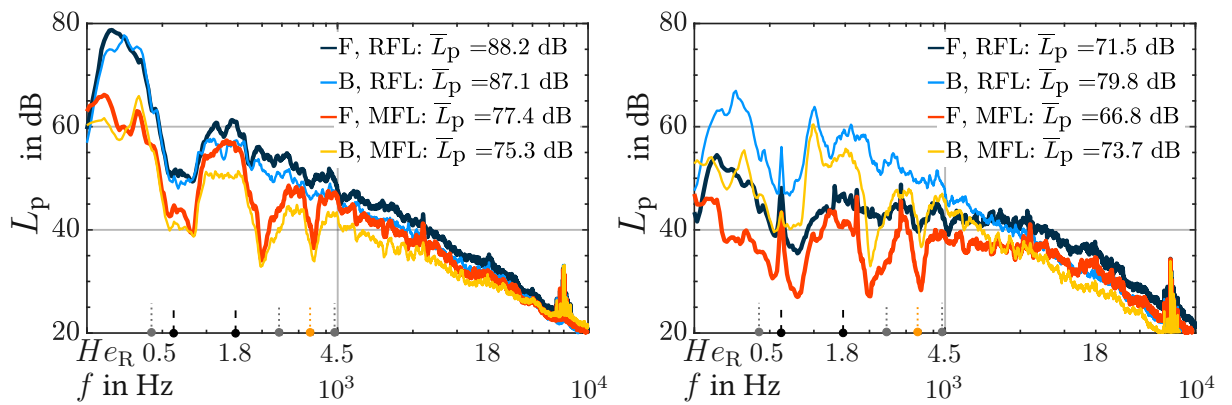


(c) Averaged L_p spectra at $\dot{V} = 1.9 \text{ m}^3 \text{ s}^{-1}$ (steady load).

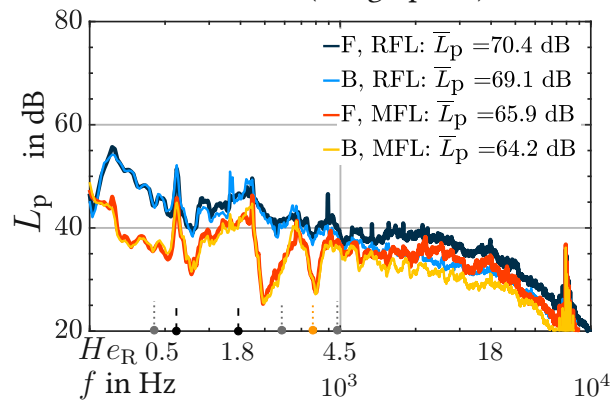
Figure 4.10: Results of the measurements of F-B-RFS-MFS setup.

Next, a more scrutinizing look is taken at selected operational points of the fan characteristics. The sound pressure spectra show that the reductions are independent of the operating point of the fan in the frequency range up to $f = 2 \text{ kHz}$. In the partial load range, both fans show a slight increase in the sound pressure spectra starting at $f = 3 \text{ kHz}$. This could also be determined in the case of the MDFS (see Fig.4.16 (b)), where the tip gap clearance is identical to the reference case (RFS). From this it can be concluded that this high-frequency rise is the inherent noise of the MPA, might be produced when the air flows through and over the absorber. Additionally, the inherent broadband sound emission by a fan's trailing edge could add to this effect [34, 60], since in the dummy setup at $\dot{V} = 1.9 \text{ m}^3 \text{ s}^{-1}$ the emitted self-noise spectrum can not be detected (cf. Fig. 4.17 (a)). This noise mechanism is increased if the inflow to the fan is more turbulent. A similar high-frequency noise could be detected during the flow over and through porous wings in the wind tunnel, which were also used for sound absorption in the literature [58, 59]. A similar inherent noise was also found by

Nelson [125] in basic experiments, who covered the openings of the perforations with cloth to identify the influence of the noise of the openings. This noise is highly dependent on the pressure difference Δp generated and the volume flow rate \dot{V} applied. In the (steady) overload range, sound pressure level of the forward skewed fan (F), which has acoustically poorer characteristics with regard to the sound sources on the trailing edge, is reduced by the MPA up to $f = 6$ kHz. At higher frequencies, this fan then experiences an increase of the emitted sound. The results allow the statement that the effects and interactions found between the MPA and the fan are basically applicable and transferable to different fans.



(a) Averaged L_p spectra at $\dot{V} = 0.9 \text{ m}^3 \text{ s}^{-1}$ (partial load). (b) Averaged L_p spectra at $\dot{V} = 1.4 \text{ m}^3 \text{ s}^{-1}$ (design point).



(c) Averaged L_p spectra at $\dot{V} = 1.9 \text{ m}^3 \text{ s}^{-1}$ (steady load).

Figure 4.11: Results of the measurements of F-B-RFL-MFL setup.

The sound reductions caused by the MPA in the long duct version (MFL) have been significantly increased compared to the MFS case with the short duct, although the effective absorber surface has remained the same. A reason could be that the absorber in the case of the long duct is no longer flowed through as strongly as in the short duct case. This is be-

cause the high-frequency component in the sound spectra (Fig. 4.11 (a-c)), which is caused by the inherent noise of the absorbers through which the air flows, is no longer present. The increased tonal components at the design point with the MFS case are no longer present (see Fig. 4.10 (c)). This is most probably influenced by the size of the tip gap clearance and/or the irregular weld seam of the MPA (cf. 4.4 (b), partially constricted tip gap clearance) when the fan blade has moved over it. In the MFL case, the tip gap has the same size as in the reference case.

The damping effects of the MPA are also limited over a larger frequency range up to $f = 7$ kHz in the partial load range and up to $f = 10$ kHz in the other operating points. The pronounced tonal components in the steady range of the fan from the case with short duct are also no longer visible in the sound pressure spectra (equal tip gap clearance and fan not moving over the constricted part of the gap). The frequencies of $f = 580$ Hz and $f = 780$ Hz are particularly significant in the sound pressure ranges, as these are where a strong noise reduction takes place. The obtained results from this subchapter can be summarized as follows:

- *The long duct segment, in which the fan operates downstream of the MPA, is a more effective variant in terms of noise reduction and more efficient in terms of aerodynamics.*
- *The short duct version causes inherent noise. This might be an effect of an enlarged tip gap clearance in combination with turbulence-induced trailing edge noise of the fan.*
- *All of the above findings apply to both fan types.*
- *A fan operated in the perforated section can cause additional tonal peaks at multiples of f_{BPF} . This effect seems to be very sensitive to the tip gap clearance.*
- *In the partial load and lower He number range, the absorber is very effective in both MPA versions (sound reduction of up to 15 dB). In the higher-frequency and steady load range, the sound emission reduction resembles the transmission loss of a single MPP specimen (2 – 5 dB) in an impedance tube.*
- *In case of the undisturbed inflow, at relatively low background flow Mach numbers ($Ma \ll 1$), and if the MPA is not placed in the vicinity of the fan, the functioning of the MPA is not compromised up to 3 kHz.*

4.4 MPA configuration effectiveness

In this subchapter, different MPA cavity configurations are evaluated in terms of sound reduction effectiveness and influence on the fan aerodynamics. The setups are compared at different operational points, representing the load ranges in the fan characteristics (cf. Fig. 4.9 (a,b)). The simulation framework's accuracy is shown by comparing simulated and measured sound emission spectra at the design point of the fans.

4.4.1 Simulated acoustics at the design point

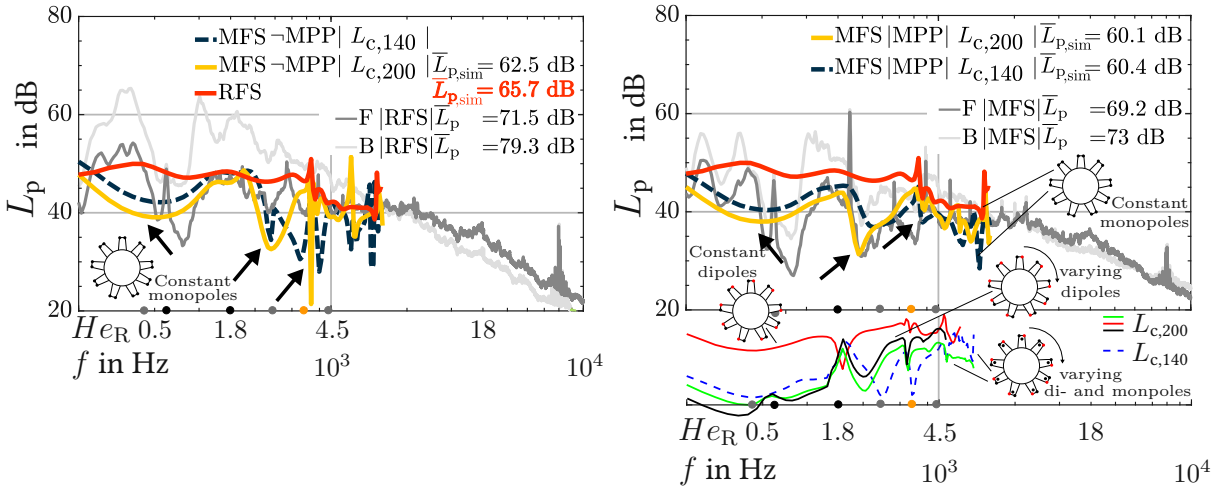
As shown in the pre-characterization of the fan-duct system (cf. Fig. 4.7 and 4.8), the location of the sources is key to obtain a qualitatively similar sound spectrum to the measurements. The emission spectra measured are dominated by sources due to the unsteady blade forces unable to be accounted for by the simulation. The source strength for each of the nine blades was therefore calculated for the design point with an empirical formula [1], using a.o. $\dot{V} = 1.4 \text{ m}^3 \text{ s}^{-1}$ and an averaged Δp to arrive at roughly $a_i = 94 \text{ dB}$. Additionally, (4.1) with $a_i = 94 \text{ dB}$, $\vartheta = 0$ and Ω_{fan} was used to emulate a spinning mode time-varying source strength as a means to reflect the measured data more qualitatively. When using the formula for the varying source strength, the emitted sound field is strongly influenced by the character of the source (monopole-like or dipole-like).

Simulation and measurement of different fan positions

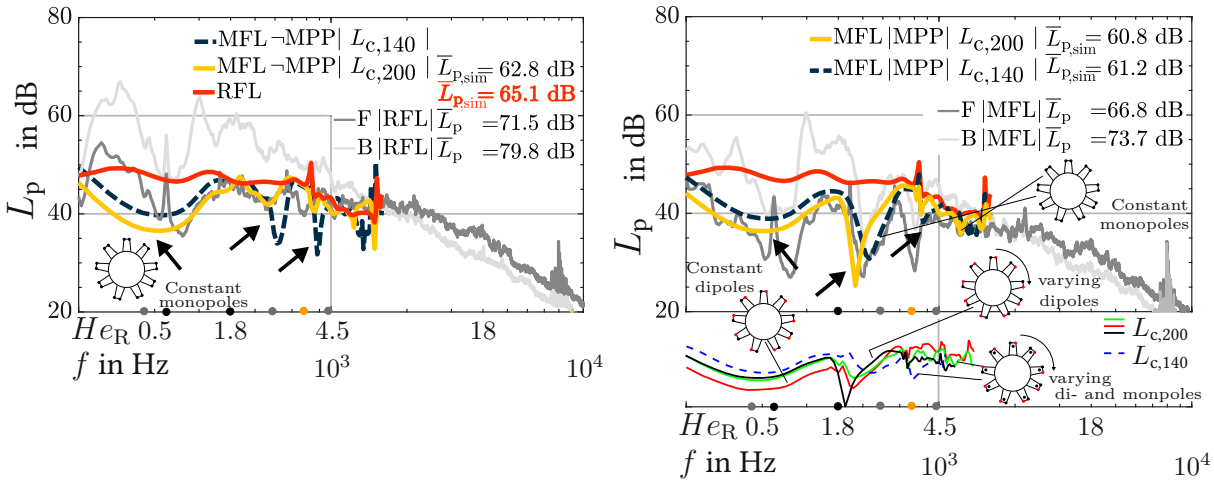
The simulated emission spectra at RFS/MFS (Fig. 4.12 (a,b)) reproduce the sound level trend qualitatively, but not quantitatively. In general, the sound level dip at $f_{\lambda/4,2}$ is more accurately represented by the simulation with constant tip gap sources than at $f_{\lambda/2,2}$. This dip seems to solely depend on L_{MPA} , being a half-wave resonator effect. This becomes later apparent by comparing setup MFS and MCFS (cf. 4.16 (a) or cf. 4.19 (a)). However, the sound emission dip at this resonance frequency can be better approximated if a varying source strength made of dipoles or a combination of dipoles and monopoles is used. Interestingly, using a cavity length of $L_c = 140 \text{ mm}$ represents the second dip better than the first. It is also possible that the geometry influences the MPA behavior more strongly than expected. The geometries in the experiment and simulations are not exactly identical; the shape of the MPA was changed from cylindrical in the simulation to an octagonal shape (cf. Fig. 4.2 (a,b)) for the sake of easier and more precise construction. The influence of the varying source and thus mode propagation could also indicate a strong dependence of the emission spectrum trends on the monitoring points' location.

The frequency shift at $f_{\lambda/4,2}$ when adding the MPP can be seen by comparing cavity without MPP (MFS|–MPP) to the case with MPP applied to the cavity (Fig. 4.12 (a,b)). This MPP-correlated shift is only slightly apparent for $f_{\lambda/2,2}$, which indicates again a sole half-wave resonance associated with the length of the MPA and less dependent on the MPP. Overall, the MPP type B adds about 3 dB to the sound reduction capability of the expansion cham-

ber (compare $\bar{L}_{p,sim}$ in Tab. 6.8 and Tab. 6.9). This corresponds to the results from Setup A in Chap. 3.2 for the TL -peaks in the low-frequency-low- He range (orange, in Fig. 3.13 (a)). Also, MPP type B does not have an α near one at the frequency range up to $f = 1$ kHz (cf. Fig. 3.3 (b)). This means that with an optimized MPP, the sound reduction should be higher.



(a) RFS emission spectrum at $\dot{V} = 1.4 \text{ m}^3 \text{ s}^{-1}$. (b) Emission spectrum at $\dot{V} = 1.4 \text{ m}^3 \text{ s}^{-1}$, MFS.



(c) RFL emission spectrum at $\dot{V} = 1.4 \text{ m}^3 \text{ s}^{-1}$. (d) Emission spectrum at $\dot{V} = 1.4 \text{ m}^3 \text{ s}^{-1}$, MFL.

Figure 4.12: Measured (grey, light grey) and simulated (red, yellow, blue, black) sound emission spectra of the RFS-MFS-RFL-MFL configurations; (a,c) show simulated cases without MPP and in (b,d) the MPP is added; qualitative trends in simulated sound emission spectra if the source type is changed (green, red, black, blue).

In the region near the blade passing frequency and its first harmonic (spectrum position cor-

responding roughly to f_{RFS} and f_{MFS}), the resonance at $f_{\lambda/4,1}$ produces large sound reduction even without the MPP. Comparing the cases of cavity length $L_{c,140}$ and $L_{c,200}$ without the MPP (cf. dark-blue and yellow curves in Fig. 4.12 (a)), reveals that the larger cavity produces more sound reduction near f_{BPF} . However, with cavity length $L_{c,140}$, the reduction of sound emissions appears in a broader frequency spectrum between $f_{\lambda/4,2}$ and $f_{\lambda/2,2}$. Such a behavior is not visible in the MFS setup with MPP (cf. dark-blue and yellow curves in Fig. 4.12 (b)). The MPP seems cause a broader sound reduction at $f_{\lambda/2,2}$. Yet, the source character and position is obviously very relevant for the peak height of the half-wavelength dip.

By comparing the simulated cases of MFS and MFL (Fig. 4.12 (a,b) and Fig. 4.12 (c,d)), one can see that the higher dip in the MFL case is reproduced by the simulation. Also, the largest portion of sound reduction in the MFS setup (source/fan position!) is due to the cavity length and depth, hence cross section jumps. The MPP amplifies absorption at resonance frequencies and to a small degree the reduction below the cut-off frequencies (cf. blue curves in Fig. 4.12 (a,b) and Fig. 4.12 (c,d)). This TL -increase by the MPP is higher in the MFS than in the MFL setup. Due to the high Helmholtz numbers in the rest of the spectrum, a high broadband absorption can not be achieved. Therefore, the MPA's main benefit in the application near the fan is its flow guiding ability. Nevertheless, at least for the low-frequency-low- He range, the MPP increases sound reduction significantly if the fan is not operated within the MPA section. The MPP has a high flow resistance, depending on r_{pore} and ϕ which can reduce the flow through the MPP (bias flow). Here, especially near the tip gap in the MFS setup. Probably, the main portion of the blind flow is associated with the flow cross section of the tip gap clearance. Thus, the high flow resistance of the MPP reduces pressure drops in the fan's characteristic curve and is, as such, favorable to the fan efficiency (cf. Fig. 4.9 (e) and Fig. 4.20 (d)).

Direct comparison of fan positions for forward skewed fan

The simulations, in agreement with the measurements, show that the source (=fan) location changes the emitted sound spectrum drastically. This can be better observed if the measured MFS and MFL setup are directly compared in Fig. 4.13. The measurements allow are more specific categorization of the observed effects of the fan location on the emitted sound spectrum. The spectrum is divided in a low-frequency portion, called "**subharmonic humps**". Here, the effect of an enlarged tip gap clearance manifests in an increased blind flow and causes an augmentation of unsteady blade forces. In the second portion of the spectrum " **$\lambda/4$, $\lambda/2$ and tonal peaks**" the quarter- and half-wave resonances caused by L_c and L_{MPA} are visible in the spectrum, and the enlarged tip gap presumably causes significant tonal peaks at multiples of f_{BPF} . However, as can be seen for the MDFS setup (Fig. 4.17 (b)), with a tip gap clearance equal to the reference case, the bias flow through the MPP might also contribute to the noise emission here. Because in the MDFS setup, the tonal components are detectable, but with a lower intensity.

The third spectral portion is termed "**self-noise**" because here, the fan emits a high-frequency broadband sound. It is presumed that the MPP induces turbulence in the boundary layer of

the grazing inflow and the now more turbulent flow interacts with the trailing edge of the fan. On the other hand, the "self-noise" might be caused merely by the MPA interacting with the grazing flow. Some evidence for an interaction of the fan-flow field and the MPP might be that the fan position also changes the self-noise spectrum to a higher more broadband intensity and that the inherent noise is not detected in the dummy setup (cf. 4.17 (a)). Additionally, the equal clearance in the MDFS case can not suppress this sound portion (cf. 4.14 (b)). The self-noise range and the subharmonic humps is strongly affected by the fan position within the MPA in the partial load range and the design point. The effects are most apparent in the partial load range. Here, also the highest sound reductions can be achieved. The MFL setup features the same tip gap clearance as the reference setup (RFS/RFL). Thus, this frequency portion of the fan characteristics can be optimally damped with the constraint of suitable (small) tip gap clearance.

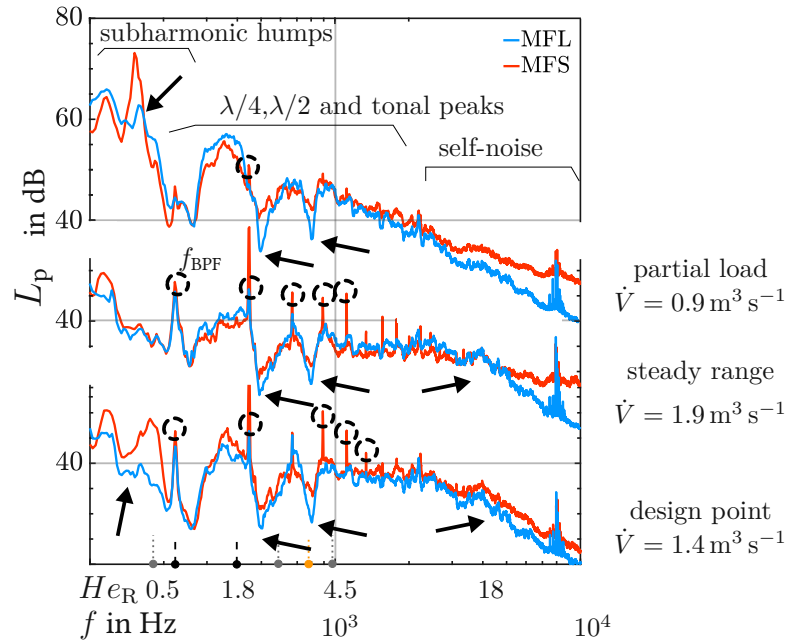


Figure 4.13: Direct comparison of the averaged L_p of the MFS and MFL configuration at three operating points of the forward-skewed fan.

The quarter- and half-wave resonance dips are obviously sensitive to the fan location. The position of the peaks does not change, but the absolute value of the dip does. Here, the difference between the MFS and MFL setup is more apparent in the lower operational range of the fan. In the steady load range, the fan position becomes more insignificant for the dips' depth. This is an indication that the grazing flow is less important for the change the MPA's absorption behavior compared to the changed bias (and/or blind) flow, which is only present in the MFS case, and significant for the noise emissions at lower volume flow rates. Also, it was found in Chap. 3.2 that the low Helmholtz number range is dominated by the MPP's viscous regime. MPP B's viscous-dominated regime ends with $f_v = 2$ kHz (cf. Tab.6.4 in

App. B.). It is readily known that flow in or above the pore increases the resistive part and decreases the reactive part of the MPP pore [9]. This might explain the drastic changes at the resonance dips, which in an MPA are dependent on the cavity length L_c . The MPP pores' reactive portion and the impedance of the cavity make up the reactive part of the MPA. The quarter-wavelength and half-wavelength resonance trends are more or less unaffected by the operational point of the fan. The changes in resonance dips occur most prominent for the highest sound pressure levels (partial load range). If a purely linear acoustic damping would occur the dip differences should be constant. Additionally, the tip gap (size-dependent) source mechanism presumably causes the tonal peaks and probably combined with the radial bias flow in part some of the "self-noise" portion.

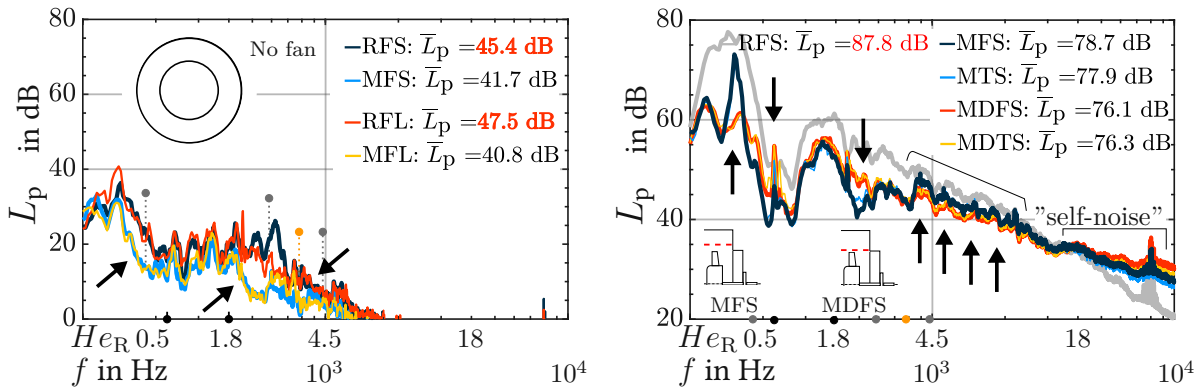
The inherent "self-noise" of the MPA is detectable in all operational points of the fan characteristic, but it depends on the fan noise source mechanism (enlarged tip gap or more broadband trailing edge noise influenced by the flow near the surface of the MPA) and operational point whether the effectiveness of the MPA is compromised (produces more sound than it reduces). Generally however, in the low-frequency-low- He part of the emission spectrum at low Ma numbers, the MPA is very effective in reducing the noise caused by the fan.

So far the findings for the unsegmented cavity configurations can be summarized to:

- Simulation
 - *The emissions of the forward skewed fan can be better reproduced than for the backward-skewed fan.*
 - *Constant sources are sufficient for simulating the overall emission reductions at the design point and for collapsing the sound emission trends. A varying source strength might improve those trends qualitatively.*
 - *The simulated sound emission spectrum is more sensitive to the type of source in the short duct version, when the sources are within the MPA section.*
 - *The MPP amplifies the $\lambda/4$ transmission loss peaks, but most of the sound reduction is caused by the expansion chamber cross section jumps themselves.*
- Measured differences depending on fan (=aeroacoustic sources) position
 - *The MFS' acoustic performance is compromised by tonal peaks and a larger subharmonic spectral portion. Bias flow and an increased blind flow due to a larger tip gap clearance might be responsible here.*
 - *The transmission loss peaks at $f_{\lambda/4,i}$ are reduced if the fan is operated within the MPA. Bias flow and an increased blind flow due to a larger tip gap clearance might be responsible here.*
 - *A flow speed dependent "self-noise" sound emission reduces the MPA's effectiveness in the higher-frequency range. This is presumably either caused by turbulence gusts induced by the MPA and interacting with the trailing edge noise mechanism of the fan; or the MPA causes this noise portion itself to a certain degree. Also, the bias flow through the MPP is theoretically a major "self-noise"-contributor.*

4.4.2 Unsteady (partial) load range

For a comparison of the overall sound reduction differences $\Delta \bar{L}_p$ caused by the different cavity configurations, the reader can refer to Fig. 6 in App. B. As a general result, it appears the MPA configuration changes the overall sound reduction just slightly. It is, therefore, more instructive to investigate specific points of the fan's operational range. The influence of changing the MPA setup is first shown for the partial load range ($\dot{V} = 0.9 \text{ m}^3 \text{ s}^{-1}$). Here, the overall sound reduction due to the presence of the MPA is the highest. The turbulent- and undisturbed-inflow reference cases (RFS/RFL) are compared in Fig. 6.7 in the App. B. They show that in the partial load range, the sound production due to unsteady blade forces is dominant and that only in the steady flow range, a broadband sound production due to the interaction of the (trailing edge of the) blades and the (turbulent) background flow occurs.



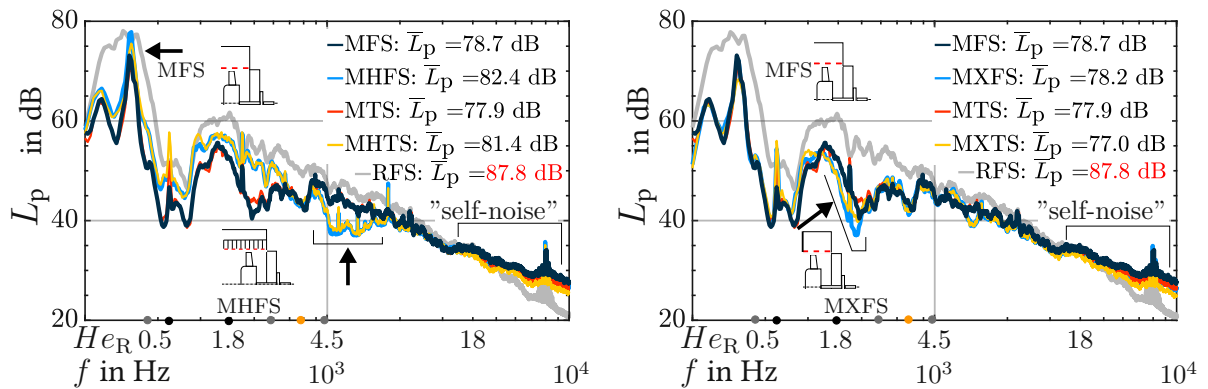
(a) Averaged L_p spectra of the dummy setup. (b) Averaged L_p spectra of MDFS/MDTS with a tip gap clearance equal to RFS.

Figure 4.14: Measurement results of no-fan-RFS/RFL-dummy and F(orward-skewed)-RFS/RTS-MDFS/MDTS setup.

The sound pressure spectra (Fig. 4.14 (b)) show that the sound pressure of the subharmonic humps is more pronounced in the MFS case than in the MDFS case. This is the effect of the increased tip gap. In addition, in the identified frequency range of tonal components due to the blade passing frequency, the average sound pressure level is increased in the MFS case compared to the MDFS. This could also be related to the weld seam (in the increased tip gap clearance) of the round MPP duct MFS, which, due to industrial fabrication, comes up against certain limitations of surface quality. The MPA duct consists of a plate of MPP, which is bent and then welded or glued to maintain the round shape of the duct. This weld seam is worse in the case of MFS than in the case of MDFS. These disturbances increase the turbulence of the flow locally, which in turn increases the unsteady forces on the blades. As a result, the sound pressure level at the blade passing frequency is increased [71, 120, 161]. On the basis of the results presented all relevant effects become apparent with the case MFS, although it has a slightly larger duct diameter. For a case with a suitable duct diameter corresponding to

the reference duct, i.e. MDFS, an improvement of the obtained results for the different cavity configurations regarding noise reduction (cf. Fig. 6.8) can be expected.[46]

The dummy setup (Fig. 4.14 (a)) already produces an overall sound reduction of 4 to 6 dB for the short and long duct. For comparison, the broadband transmission loss of an MPP specimen in an impedance tube using the four-microphone method, is 3 – 4 dB. Also, this corresponds to the overall reduction in the steady load range (compare Fig. 4.9 (a,b)). The "self-noise" in the high-frequency range due to the presumed MPP-flow interaction is not detectable. The major peaks in sound reduction already occur at $f_{\lambda/4,1} = 190$ Hz, $f_{\lambda/4,2} = 580$ Hz, $f_{\lambda/4,3} = 970$ Hz and $f_{\lambda/2,2} = 780$ Hz.



(a) Averaged L_p spectra of MHFS/MHTS configuration with $L_c = 40$ mm.

(b) Averaged L_p spectra of MXFS/MXTS with axial segmentation of the cavity.

Figure 4.15: Results of the measurements of F-RFS/RTS-MHFS/MHTS and F-RFS/RTS-MXFS/MXTS setup.

The reduced cavity length $L_c = 40$ mm with a honeycomb segmentation (Fig. 4.15 (a)) augments sound reduction in the range of 1000 Hz by 5 dB, with a cost of higher sound emission in the lower He -range, especially at the $\lambda/4$ peaks. The overall sound reduction is also worsened by around 2 dB compared to MFS at all operational points (cf. Fig. 6.8 (c) in App. B.), up to the design point for undisturbed inflow. If the inflow is turbulent, then sound reduction by the smaller cavity length is declined constantly by 2 dB (cf. Fig. 6.8 (c) in App. B.).

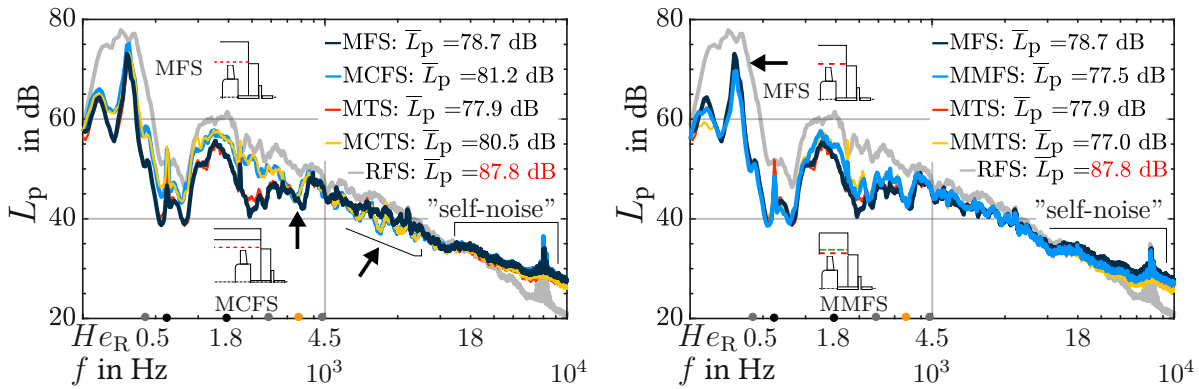
Similar to setup A in Chap. 3, the axial segmentation of the MPA cavity (Fig. 4.15 (b)) can broaden the sound reduction at the second cut-off frequency f_{MFS} without affecting the rest of the emission spectrum and the overall sound reduction at the operational points (cf. Fig. 6.8 (d)). However, the effect is localized in a small frequency interval due to the high Helmholtz numbers, respectively the very diffuse sound field, in the higher frequency range. This is also consistent with the results from Chap. 3. Nevertheless, if a local optimization of sound reduction is sought, the FE framework can provide a means for finding such a localized optimum.

Reducing the cavity length without a honeycomb segmentation (Fig. 4.16 (a)) is rather ineffective. However an influence is visible at around 2000 Hz. Still, the overall sound reduction

is declined by 2 dB compared to the honeycomb case (cf. Fig. 6.8 (e) in App. B). An interesting observation is that the sound reduction peak at $f_{\lambda/2,2}$ is maintained, which suggests that this peak is indeed a half-wavelength resonator effect, independent of the cavity length L_c .

The addition of an MPP with a larger flow resistivity in the segment the fan is running within (Fig. 4.16 (b)) reduces the subharmonic peak. The sound reduction in the rest of the frequency range is more or less unchanged. With the blind flow being the dominating aeroacoustic source mechanism, this leads to the conclusion that the adverse effects of an increased tip gap clearance and/or the bias flow through the MPP can be overcome with a suitable MPP choice. Remarkably, the self-noise production due to MPP-fan-flow interaction is reduced. Hinting that the MPP self-noise is correlated with tip gap blind flow and/or MPP bias flow. The slight reduction of "self-noise" can not be observed in the MHFS and MXFS where the second MPP is missing.

It is noteworthy that in both cases with a reduced L_c , the main portion of the sound reduction in the range of the subharmonic hump is maintained.



(a) Averaged L_p spectra of the MCFS/MCTS (b) Averaged L_p spectra of the MMFS/MMTS setup with $L_c = 35$ mm. setup with a second MPP.

Figure 4.16: Results of the measurements of the F-RFS/RTS-MCFS/MCTS and RFS/RTS-MMFS/MMTS setup.

4.4.3 High flow speed steady range

The influence of changing the MPA setup is now shown for the steady load range ($\dot{V} = 1.9 \text{ m}^3 \text{ s}^{-1}$). Here, the overall sound reduction is comparable to the dummy setup and rather constant. The influence of a turbulent disturbed inflow (T) is now apparent, and the MPA adds significant sound reduction of 6 dB (cf. Fig. 4.17 (b)). The disturbed inflow is generated via a turbulence grid (cf. Tab. 6.6). The forward skewed fan (F) is used for these investigations. This fan reacts more sensitively to a disturbed inflow than the backward-skewed fan. As will be apparent shortly, the influence of the cavity configuration is changed compared to the partial load range.

The aerodynamic curves are shown in Fig. 6.7 (a,b) in App. B and reflect the characteristics of the system (axial fan and installations). Accordingly, the pressure build-up is reduced by the turbulence grid, which represents an additional pressure loss in the system. This additional pressure loss is compensated by the auxiliary fan so that for the same volume flow, the fan operates at the same operating point with and without the grid. The acoustic characteristics show (cf. Fig. 6.7 (c)) that the turbulence grid has an influence on the emitted sound pressure level starting at a volume flow rate $\dot{V} = 1.0 \text{ m}^3 \text{ s}^{-1}$. The sound pressure level of the fan increases by $\Delta L_p = 6.5 \text{ dB}$ in the long duct and by $\Delta L_p = 9 \text{ dB}$ in the short duct. From previous studies, it can be assumed that the inherent noise of the turbulence grid only plays a minor role [96]. The sound pressure spectra (cf. Fig. 6.7 (d-e)) show that the increased inflow turbulence influences the sound pressure level of the fan up to a frequency of $f = 2 \text{ kHz}$. For higher volume flow rates \dot{V} this range increases up to $f = 3 \text{ kHz}$. The increased sound generation mechanism can be assigned to the leading edge (cf. Fig. 4.4) of the fan due to the low-frequency range [99, 160].

The reference MFS case and the cavity setups can be compared to the setups when inflow turbulence is generated by the upstream turbulence grid. This should clarify whether influences such as a disturbed inflow, which can be caused in real plants and systems, for example by dripping protective grids or pipe redirection, have an effect on the absorbing properties of the MPA. In the short duct, in which the fan operates directly within the perforated MPA section, the same effects of the MPA can be determined for both free and turbulent flow.

The sound emission curves (Fig. 4.17, Fig. 4.18, Fig. 4.19) show that the damping properties of the MPA have been increased in the case of a turbulent inflow independent of the cavity setup. This could be due to the fact that the overall sound pressure level was increased by the higher turbulence and the MPA absorbs better at a higher overall level. A further physical reason for the improved sound absorption properties of the MPA duct under turbulent inflow conditions could be that the increased turbulent kinetic energy also increases the fluctuation components of the flow perpendicular to the MPP surface. These additional fluctuations stimulate the air columns in the pores to oscillate further, which leads to higher dissipation inside the pores. Thus, the designed absorber counteracts a worsening of the flow and the resulting increased sound pressure level of the fan. In case of the turbulent inflow, a reduction of up to $\Delta L_p = 6 \text{ dB}$ on the sound pressure level at the operational points can be achieved. In case of the free inflow, this overall reduction was $\Delta L_p = 3.0 \text{ dB}$.

Using the dummy setup (cf. Fig. 4.17 (a)) reveals the effectiveness of the MPA at the quarter- and half-wavelength resonances. With no significant differences in the long and short duct setup. The self-noise-frequency range is slightly visible, but the MPA still reduces more sound than it produces. Therefore, the changed blind/bias flow (due to the tip gap difference) is necessary for the increased self-noise of the MPA. The MDFS (cf. Fig. 4.17 (b)), with the tip gap clearance equivalent to the reference case, reduces the tonal peaks of the higher harmonics. The tonal phenomenon is thus strongly correlated with the tip gap noise mechanism. Remarkably, the peak of the blade passage frequency is not reduced. The turbulent inflow causes a broadband noise and masks any tonal peaks. However, they are present, and an MPA with a higher sound reduction could make them reappear in the spectrum. The "self-noise" is gener-

ally of equal intensity at higher flow speeds compared to the setups in the partial load range.

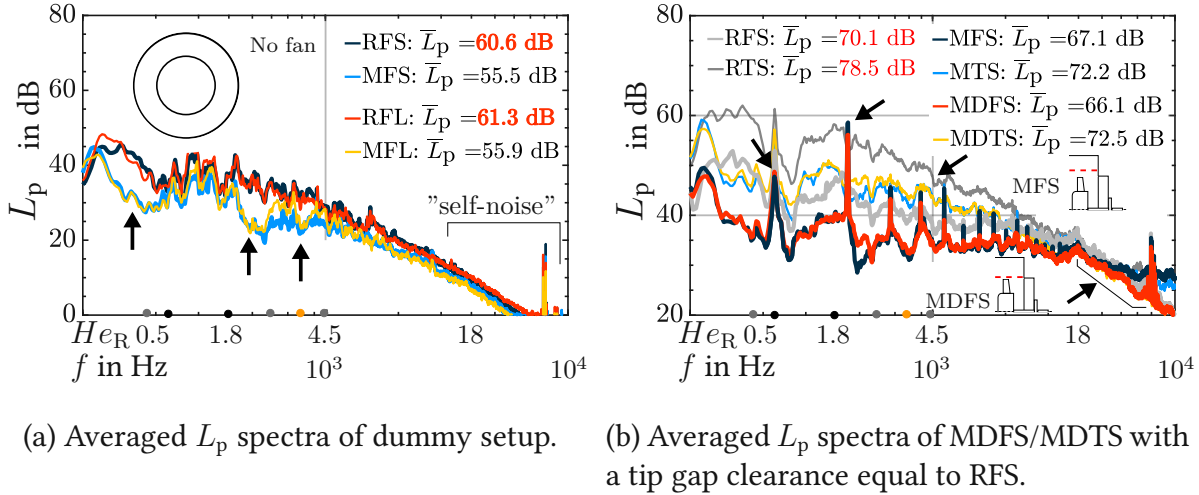


Figure 4.17: Measurement results of no-fan-RFS/RFL-dummy and F(orward-skewed)-RFS/RTS-MDFS/MDTS setup.

Compared to the free-inflow conditions, the honeycomb segmentation (Fig. 4.18 (a)) reduces sound in the specific frequency interval as well, but the tonal peaks are multiplied and augmented if the inflow is disturbed.

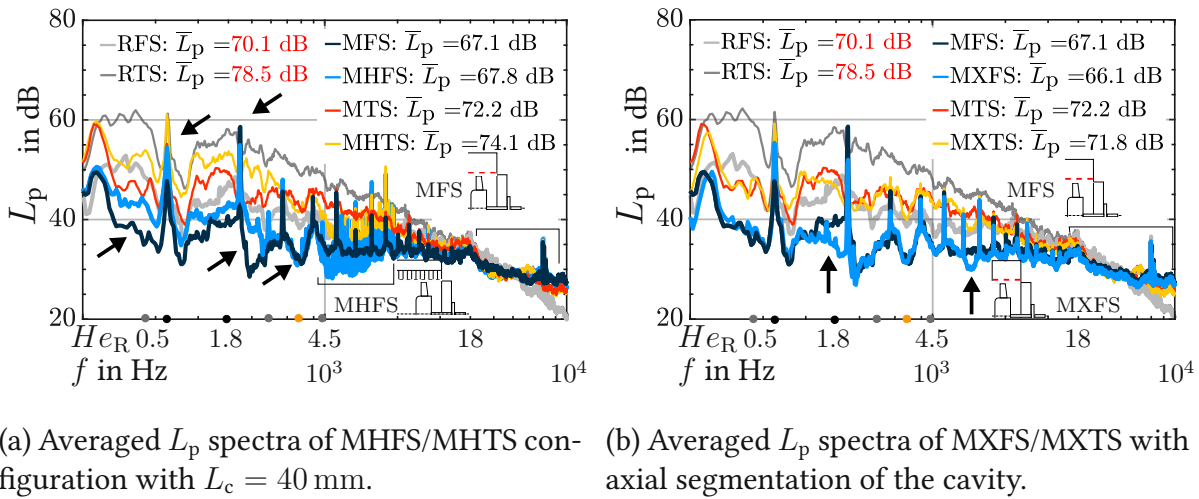
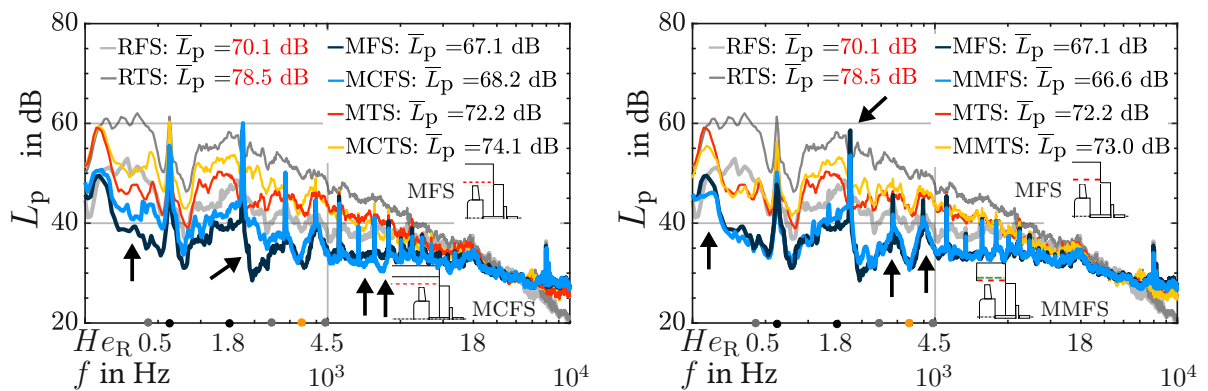


Figure 4.18: Results of the measurements of F-RFS/RTS-MHFS/MHTS and F-RFS/RTS-MXFS/MXTS setup.

The turbulence increases the Reynolds stress, and this stress surge in combination with the tip gap bias flow most probably increases the reaction forces on the blades. The reaction

forces of the blades on the flow are what causes sound production.

The triple axial back volume segmentation (Fig. 4.18 (b)) can help to reduce the second and third tonal peak in the frequency range correlated with $L_c = 40$ mm, but if the inflow is disturbed the effect is less apparent. Most probably, again masked by the broadband turbulence-induced sound emission. However, as seen above, the MPA and its cavity setup are vice-versa able to reduce sound over a broadband frequency range. Both setups seem to be more effective over a broader frequency range if the inflow is disturbed. The self-noise is slightly reduced. With a disturbed inflow, the impact of the smaller cavity is more or less undetectable (see Fig. 4.19 (a)). The sound reduction is declined compared to MTS over a broad frequency range. The tonal peaks are unaffected, as well as the self-noise frequency range. The same can be said if the MPP with a large flow resistivity is added to the chamber where the fan is running in (Fig. 4.19 (b)). Effects on the tonal peaks are present if the flow is undisturbed, but again, with the turbulence-induced Reynolds stress increase, the more broadband sound masks any effect the cavity setup might have on sound emission. Thus, it can be stated that the effectiveness of an MPA along a certain noise emission bandwidth rises and falls with the inflow conditions and the operational range of the fan.



(a) Averaged L_p spectra of the MCFS/MCTS setup with $L_c = 35$ mm.

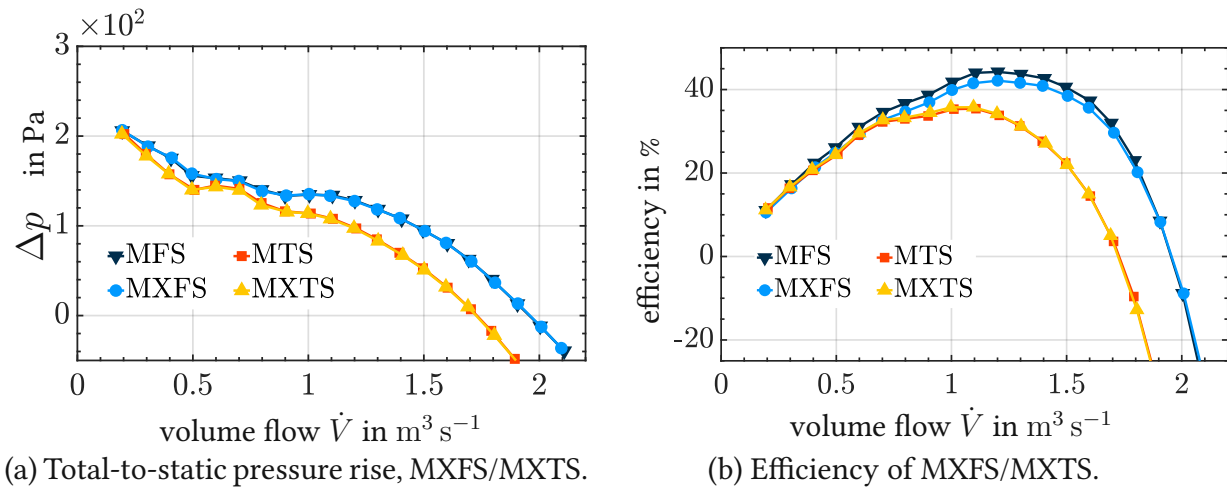
(b) Averaged L_p spectra of the MMFS/MMTS setup with a second MPP.

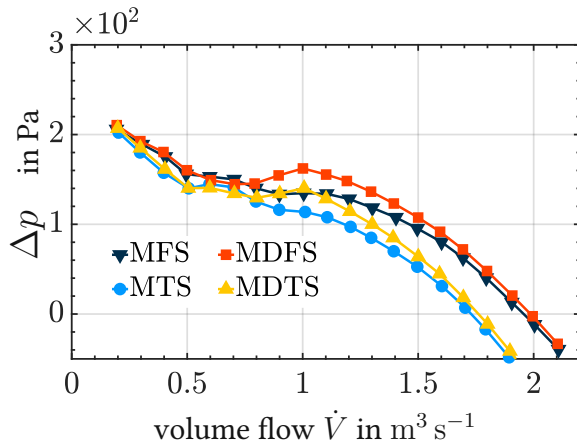
Figure 4.19: Results of the measurements of the F-RFS/RTS-MCFS/MCTS and F-RFS/RTS-MMFS/MMTS setup.

4.5 Cavity setup effects on fan aerodynamics

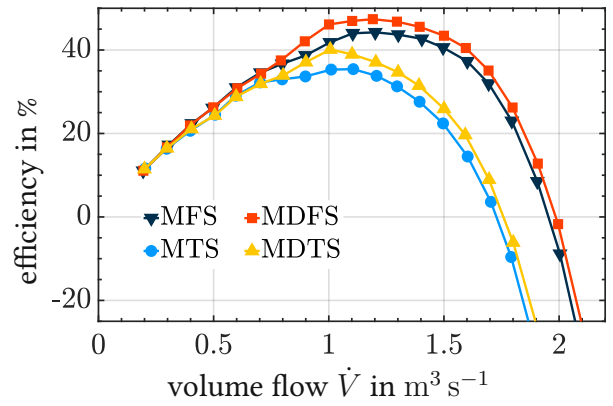
Significant effects on fan efficiency can only be observed for the MDFS, MXFS and MCFS setups. The reader is referred to App. B. (Fig. 6.9) to ascertain that efficiency is maintained for the other setups (MMFS, MHFS) compared to the MFS setup. The MDFS setups reaches a slightly lower efficiency than the reference setup (compare Fig. 4.9 (e,f)), but can recover most of the efficiency loss correlated to the larger tip gap clearance (cf. Fig.4.20 (c,d)). The reduced efficiency could be due to the fact that the boundary layer in the tip gap is increased because of the rough surface of the MPA and the fan needs a higher torque to be driven due to the increased impulse exchange in the boundary layer. In the same way, an increased back-flow through the pores of the MPP could explain the small difference in pressure build-up and be a cause for the reduced efficiency.

When the axial segmentation is applied, the pressure build-up is maintained, however slightly more torque is needed to drive the fan (cf. Fig.4.20 (a,b)). The same behavior is visible for the reduced cavity length (cf. Fig.4.20 (e,f)). This is only apparent for free-inflow conditions and most prominent in the partial load range. A measurement error can not be ruled out, but a possible physical explanation would be that only in these to configuration, the blind flow in the tip gap is affected by either the smaller cavity length or the cavity segmentation. This could indicate that a recirculation is present in the other setups, that is hindered in the MXFS and MCFS setups. Compare the "ported shroud" housing in turbo-chargers to improve the operating behavior at higher pressure differences and low volume flows [116].

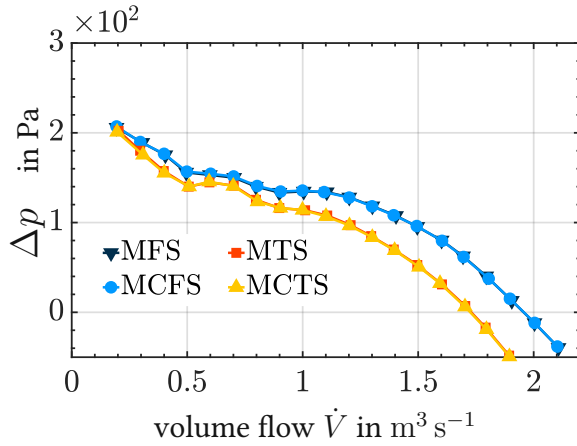




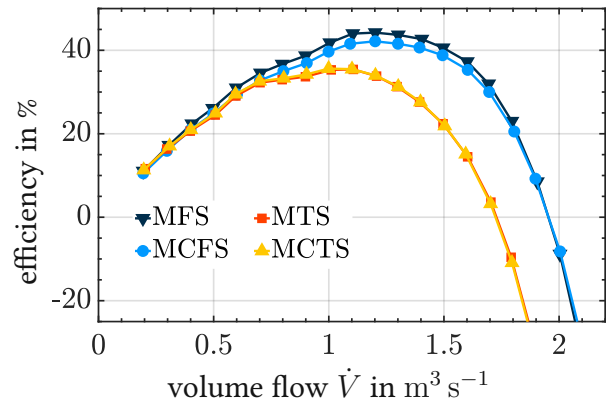
(c) Total-to-static pressure rise, MDFS/MDTS.



(d) Efficiency of MDFS/MDTS.



(e) Total-to-static pressure rise, MCFS/MCTS.



(f) Efficiency of MCFS/MCTS.

Figure 4.20: Overall sound levels of the different cavity setups and dummy.

4.6 Review of the general findings

The effectiveness of the MPA concerns broadband and tonal peaks, and its sensitivity to flow conditions. The cavity setups were evaluated whether the sound reduction is compromised or not. A major concern for a compact absorber in the present setup is the effect of fan location within the MPA. Designing the MPA depends on how accurate a pure acoustic simulation, without transient effects, can emulate reality compared to computationally costly aeroacoustic simulations. This involves mesh resolution, source approximation, and geometrical reduction.

- Simulation:

- The duct fan setup can be accurately and qualitatively simulated, using a PML for free-field conditions, an analytical mesh size estimation, and a source location comparable to the real source distribution.

- *The 1D-fitted MPP absorption character gives a good reproduction of the measured sound spectra with an MPP.*
 - *The quantitative accuracy depends on the calculation of the source strength. Stationary sources give a good estimation, but using spinning source strengths can add some qualitative improvement to the sound emission trends.*
 - *The simulation best represents the forward-skewed fan emission spectrum at the design point. The overall sound pressure level reduction is best approximated by the simulation for the long duct setup and the steady load range of the fan (cf. Tab.6.9).*
- Fan location:
 - *Since the forward-skewed fan is per se less load-sensitive than the backward-skewed fan, the sound reduction is higher for the latter.*
 - *If the fan is installed in the MPA section, tonal peaks are produced in the steady load range if the tip gap is increased. The fan efficiency can be maintained in the long duct version, and a suitable tip gap size improves sound reduction.*
 - *The highest sound reduction can be achieved in the partial load range, more or less independent of the fan location.*
 - *The MPA can compensate turbulent inflow adverse effects on sound emission in a broadband frequency range. If more sound is produced due to inflow conditions or the fans' location, then the MPA also reduces more sound.*
 - *Self-noise due to a presumed MPA-fan-flow interaction becomes significant for a fan installed in the MPA section in the partial load range and to minor degree in the steady load range. The evidence thus far suggests that the self-noise at the investigated flow speeds is strongly correlated with the fan's trailing edge noise mechanisms, influenced by changed flow phenomena (bias and blind flow) in the tip gap region next to the MPP. The extent of the influence of the (bias and/or blind) flow through the MPP pores remains unknown.*
 - MPA cavity setup and flow conditions:
 - *The MPA cavity setup is significant only in the partial load range and free-inflow conditions. More turbulent flow masks these specific effects because the noise spectrum is high and broadband. Also, large Helmholtz numbers can render cavity optimization efforts futile without the pre-characterization.*
 - *Fan efficiency is mostly affected by tip gap clearance associated blind-flow and the inflow conditions. However, a bias flow portion of that blind flow through the MPP is presumed.*

Evaluation in the free-far field and grazing flow

The MPP application in the preceding chapters was limited to a mere acoustic field, or the MPP was embedded in a background flow with a low Mach number ($Ma < 0.03$). In an HVAC application scenario, the Mach number can become significantly higher. Therefore, the following investigations aim to uncover acoustic and hydraulic interaction-effects that the MPP can have on the flow field and vice-versa at higher flow velocities. Therefore 1D-hot-wire-anemometer measurements have been conducted to assess the influence of the MPP on the hydraulic boundary layer. This is followed by acoustic measurements of the self-noise of the MPA when overflowed by an air stream. In the end an analytic model is presented that enables the acoustic engineer to predict such self-noise of the MPA.

5.1 Measurement setup and MPA configuration

Measurement setup

The setup is depicted in Fig. 5.1 (a,b). The MPP in the aluminum frame plate is fully embedded in the out-blowing flow from the nozzle and the plate is wide enough to suppress interactions of the outflow with the frame boundaries. The velocity profile has been measured in front, and after the MPP (○,●), because the waviness of the MPP's surface did not allow for the 1D-hot-wire probe to be positioned near enough to the MPP surface. In the cavity, one acoustic microphone has been placed on the bottom to detect cavity sound induced by the flow grazing over the MPP slits. A less sensitive Kulite pressure sensor has been placed in front of the MPP to detect the hydraulic wall pressure spectrum below the velocity boundary layer (Φ_{surf}). The investigated flow speeds ranged from 10 m s^{-1} to 30 m s^{-1} , which corresponds to $Ma = 0.03..0.09$. Acoustic free field conditions were provided by foam wedges placed on the walls of the measurement room, and the microphones were covered by a protective grid.

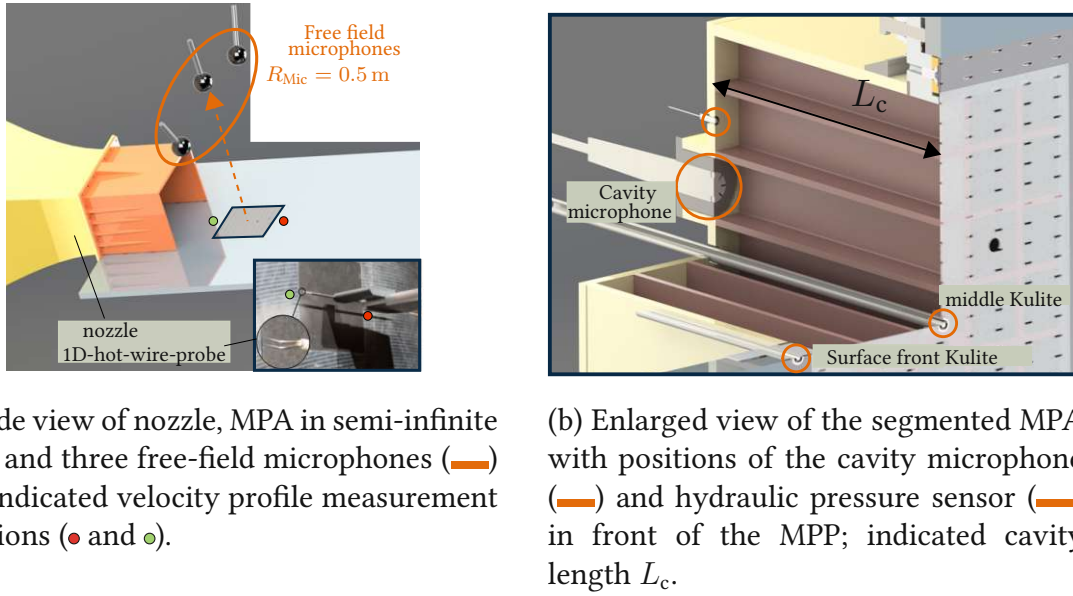


Figure 5.1: Position of the MPA in the outflow from nozzle and section view of the MPA inside.

The details of the MPA in the grazing flow conditions are depicted in Fig. 5.2. The first important feature is the position of the velocity profile, marked by a green and red "X", 20 mm in front and behind the MPP. Right after the front velocity probe position, a Kulite pressure sensor detects the hydraulic wall pressure fluctuations of the flow which then interacts with the MPP, respectively the MPA. Depending on the conditions, the MPA emits sound and influences the boundary layer, which is then measured 20 mm after the MPP. The MPA sound emissions are detected by the cavity microphone L_c remote from the MPP plate and by the free field microphones in the distance R_{Mic} of the MPP surface. The MPP is characterized by a pore width w_{pore} and length l_{pore} . The velocity probe allows to measure the speed of the bulk flow U_0 , the boundary layer thickness δ_{99} and the turbulent intensity Tu .

As described in the first chapter, the MPPs investigated are slotted. So, a width and length l_{pore}, w_{pore} must be discerned, depending on the flow direction. In contrast, the acoustic description is based on just one characteristic length r_{pore} . Therefore, the schematic view shows the "real" MPP geometry and the simplified geometry for the analytical description in the latter part of the chapter. For the modeling, the hydraulic interaction with the pores in plane 1-3 is key, causing the sound emissions in direction 2 towards the free-field microphones. Due to the semi-infinite plate setup, full embedment of the MPP in the flow field, and flow stationarity, the turbulence is assumed to be isotropic and "frozen" according to Taylor [148]. This hypothesis is valid if the turbulence intensity is less than 50 %, which justifies point temporal fluctuation measurements in lieu of spatial fluctuation measurements.

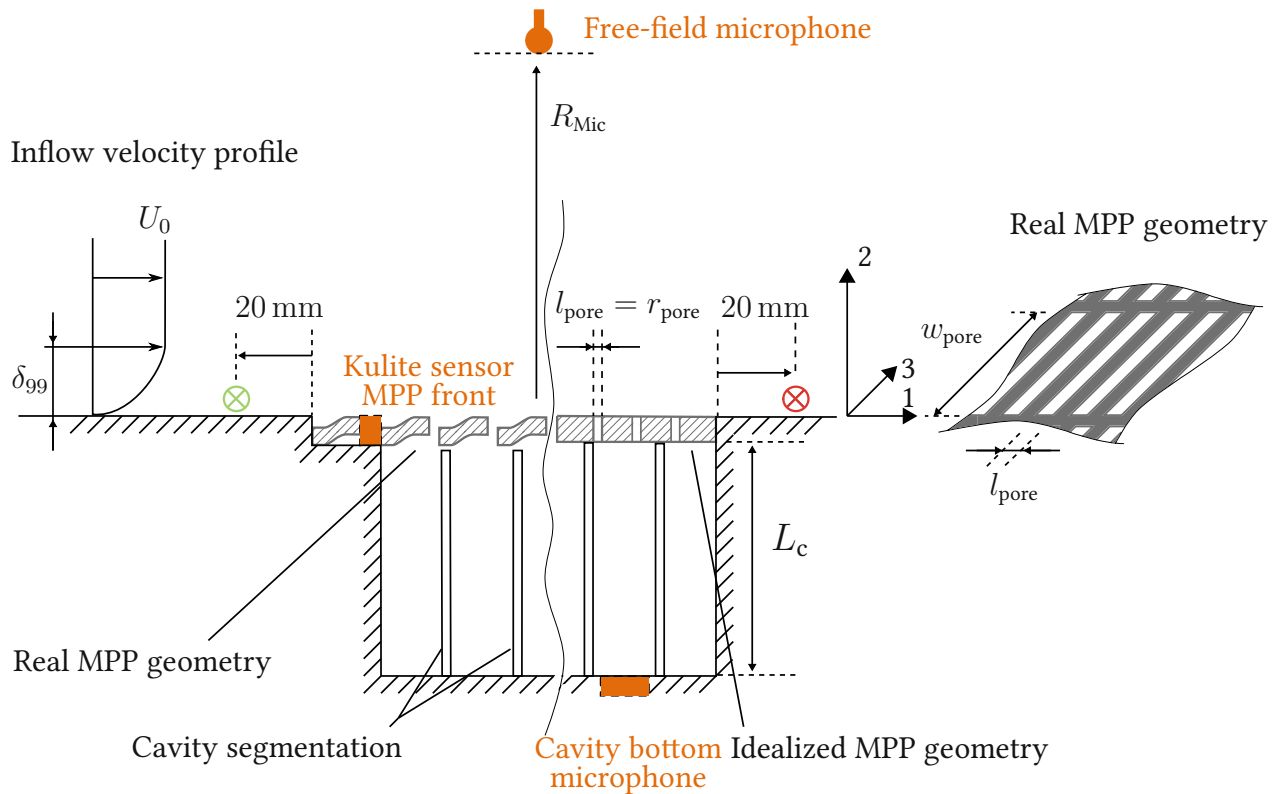


Figure 5.2: Detailed schematic of MPP in zero pressure gradient flow setup with indicated pressure sensor positions and velocity profile probing locations.

MPA configurations

The MPPs under consideration are referenced in Tab. 1.1 and Fig. 5.3 and differ in porosity ϕ and characteristic lengths l_{pore} and w_{pore} . l_{pore} has been derived by the fitting procedure described in the preceding chapters. w_{pore} is measured by hand and a ruler as reference and a camera with zoom. The orientation of the slits was changed, resulting in a smaller pore separation when the slits are parallel to the flow direction (cf. Fig. 5.3 and direction "1" in Fig. 5.2). By using a trip wire in the nozzle, the laminar inflow boundary layer along the plate was changed to a turbulent profile in front of the MPP. The absorption range of the MPA is changed by varying the length of the back volume L_c . Therefore, three different lengths have been employed to change the MPAs absorption range. It has to be emphasized that the porosity values for the hydraulic modeling are the values provided by the manufacturer and are therefore termed ϕ_{hydr} . In contrast, the acoustic (fitted) porosity is termed ϕ_{acou} . There is only one (acoustic) characteristic length which is fitted ($l_{\text{pore}} = r_{\text{pore}}$) because measuring in the sub-millimeter range is too inaccurate with a ruler. The investigations focus on the following issues:

- Influence of MPP porosity and characteristic length on the flow boundary layer and thus the character of the flow (laminar or turbulent). This has consequences on the efficiency of an adjacent turbo-machine.
- Intensity and frequency range of the self-noise which affects the effectiveness of the MPA.
- Providing measurement data for self-noise modeling based on models of Howe, Ffowcs-Williams, Golliard, Gloerfelt and Stein [53, 61, 66, 68, 77, 125, 146].

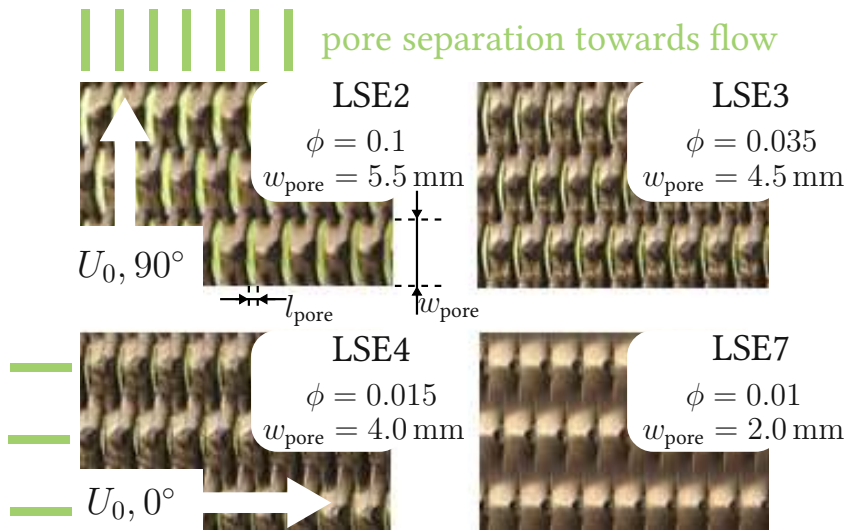


Figure 5.3: MPP type and orientation to flow with characteristic slit lengths.

5.2 Results

First, the results of the flow velocity profile measurements are shown. This is followed by the sound emission spectra of different MPA configurations with the flow parameter variations. The chapter is concluded by the analytical simulation ansatz developed for the presented MPA configurations.

5.2.1 Boundary layer measurements

The flow over the semi-infinite plate can be characterized by the bulk flow velocity U_0 , the velocity at the edge of the boundary layer U_e , the boundary layer thickness δ_{99} , the displacement thickness δ^* and the momentum thickness Θ . The form factor $H = \delta^*/\Theta$ can be used to characterize a laminar or turbulent flow. The displacement thickness is a measure for the

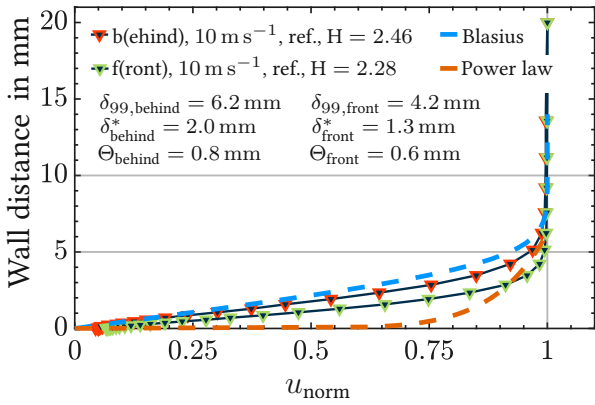
difference in volume flow rate between the non-viscous bulk flow and the viscous dominated near-wall flow, stating how far the streamlines of the bulk flow are displaced outward by the forming boundary layer [143]. The momentum thickness is a measure for the loss in momentum within the boundary layer due to friction compared to the bulk flow, thus quantifies the friction resistance [143].

In the Figs.5.4 (a-f), an undisturbed inflow grazes the MPP and reference plate. Comparing the form factors H in Figs.5.4 (a-d), one can see that the higher the porosity and slit width w_{pore} , then the more a turbulent velocity profile manifests. The profile in front of and after the plates is comparable to the Blasius profile, depending on the MPP geometrical parameters, and then develops into a profile describable with the power law (see Fig. 5.4 (b)). Also, the boundary layer thickness increases significantly with porosity and slit width, as does the displacement thickness. So, more fluid is displaced outward. The momentum thickness changes slightly with MPP parameters. Hence, one can deduce that the bulk flow along the MPP will experience a pressure drop, thus a higher flow velocity would be necessary for keeping the pressure gradient and vice-versa.

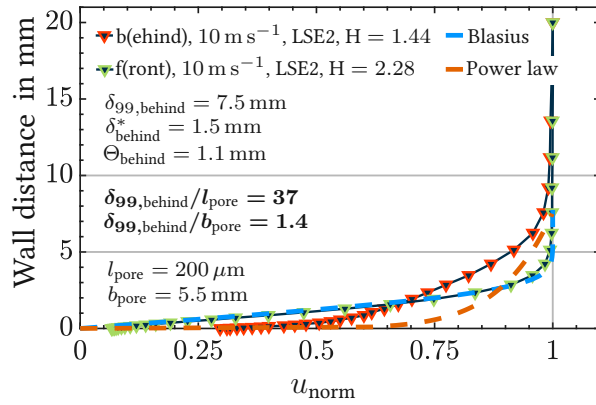
The turbulence level in front and behind the reference plate and MPP LSE2 is shown in Fig. 5.4 (e-f). For the reference plate, it is well below 10 % for almost all flow velocities, except for 20 m s^{-1} . With the MPP LSE2, more turbulence along the boundary layer thickness is introduced. This is however true only for lower flow velocities. By 30 m s^{-1} , the boundary layer is already turbulent-like. The Fig. 5.4 (e-f) also reveal that with an increase in flow velocities, the boundary layer thickness stays the same, but with the MPP, more fluid is displaced with increasing velocity, and more friction in the boundary layer introduced. The MPP, again depending on the geometrical parameters (compare Figs. 5.4 (a-d)), does not make the boundary layer more turbulent for undisturbed inflow conditions.

The influence of the MPP on the flow character changes when the inflow is disturbed, and already turbulent-like. This can be seen in Figs. 5.5 (a-f). With the lowest flow velocity, the differences in the velocity profile after the reference plate and MPP LSE2 are marginal considering the form factor and boundary layer thickness (cf. Figs. 5.5 (a,b)). However, more fluid is displaced, but the effect of the MPP on friction is almost non-existent (Θ_{behind} , cf. Figs. 5.5 (a-b)). The turbulence level in the inflow dominates over the effect of turbulence injection by the MPP surface. Figs. 5.5 (c-d) reveal that even an increase in flow velocity does not significantly change the turbulence level when the reference plate and MPP LSE2 are compared. Again, however, the displacement thickness changes rather strongly comparing MPP LSE2 and the reference plate. Friction effects are also increased (compare Θ in Figs. 5.5 (c-d)). These rather strong effects of the porosity and slit size vanish for MPP LSE4 (cf. Fig. 5.5 (e)). Here, the velocity profiles of the three flow velocities are almost congruent which is supported by the values of boundary layer thickness, displacement thickness and momentum thickness. The comparison of the orientation of the slits towards the flow shows that there is also only minor influences (cf. Fig. 5.5 (f)). The same behavior can be observed in the boundary layer characteristic lengths.

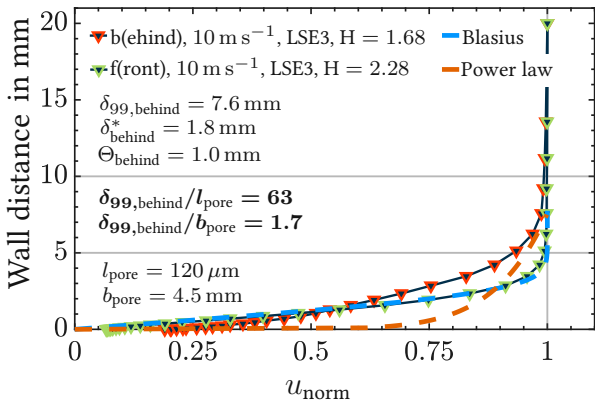
5 Evaluation in the free-far field and grazing flow



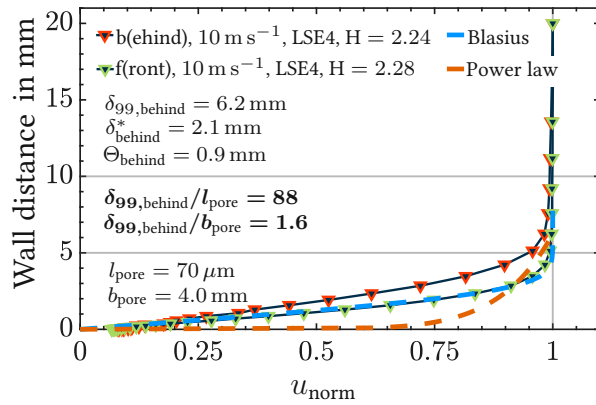
(a) Velocity profile of reference (ref.) plate at $U_0 = 10 \text{ m s}^{-1}$.



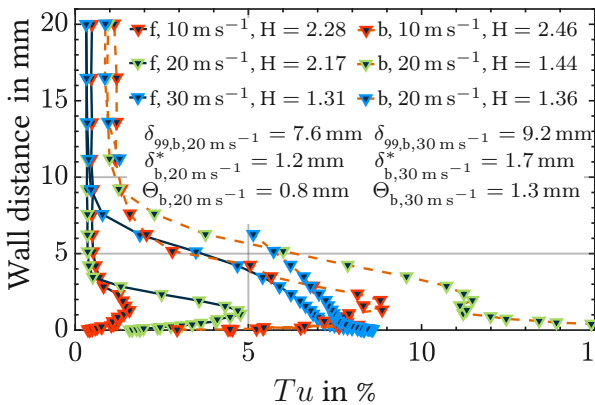
(b) Velocity profile b(ehind) and in f(front) of MPP LSE2 at $U_0 = 10 \text{ m s}^{-1}$.



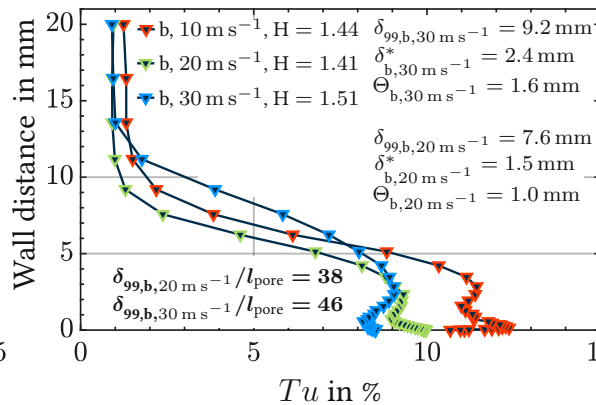
(c) Velocity profile b(ehind) and in f(front) of MPP LSE3 at $U_0 = 10 \text{ m s}^{-1}$.



(d) Velocity profile b(ehind) and in f(front) of MPP LSE4 at $U_0 = 10 \text{ m s}^{-1}$.

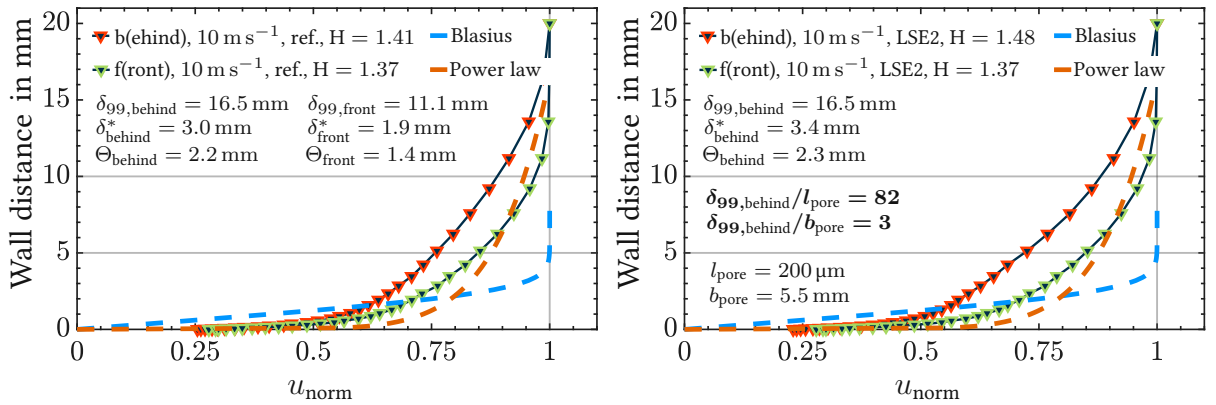


(e) Turbulence level Tu of reference plate;



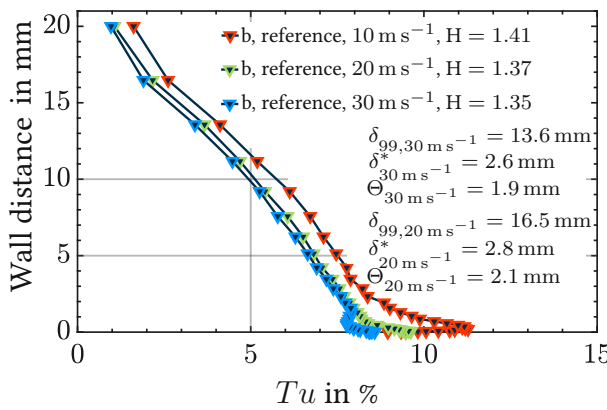
(f) Turbulence level Tu b(ehind) of MPP LSE2. b(ehind) and (f)ront.

Figure 5.4: Undisturbed inflow profiles grazing along MPP surface.

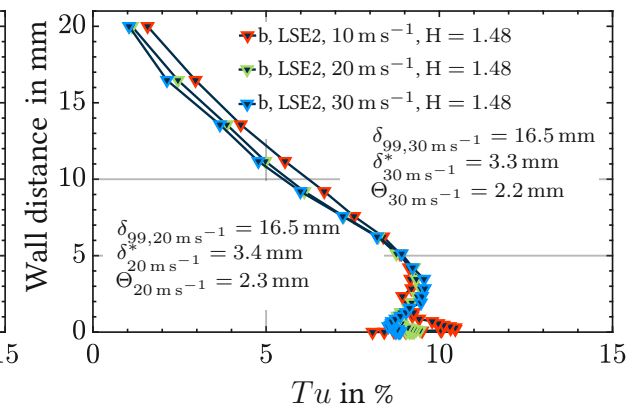


(a) Turbulent velocity profile of reference plate at $U_0 = 10 \text{ m s}^{-1}$.

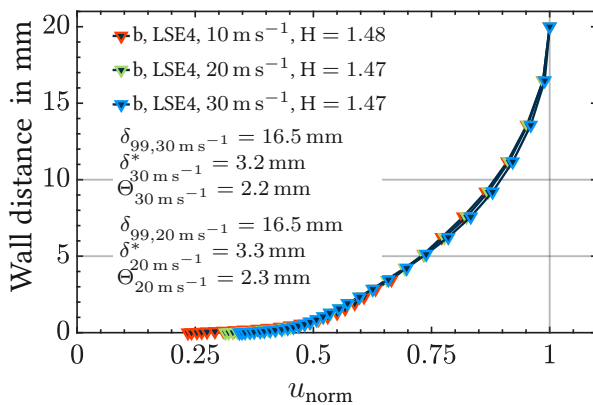
(b) Turbulent velocity profile of MPP LSE2 at $U_0 = 10 \text{ m s}^{-1}$.



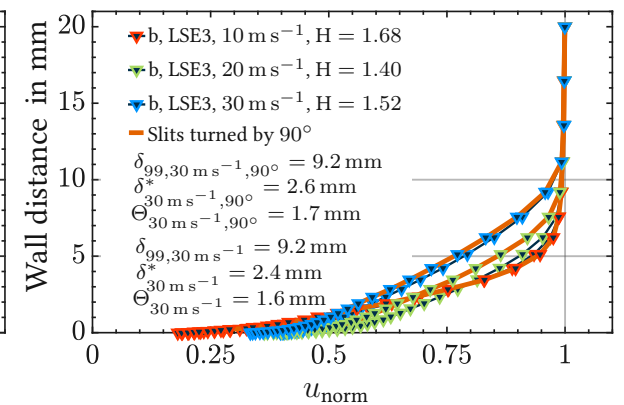
(c) Turbulence level Tu b(ehind) of reference plate.



(d) Turbulence level Tu b(ehind) LSE2.



(e) Turbulent flow profile b(ehind) MPP LSE4.



(f) Laminar-turbulent flow profile b(ehind) MPP LSE3; effects of slit orientation on boundary layer parameters.

Figure 5.5: Velocity profiles and turbulent intensity of disturbed flow grazing along MPP surface.

Die approbierte gedruckte Originalversion dieser Dissertation ist an der TU Wien Bibliothek verfügbar. The approved original version of this doctoral thesis is available in print at TU Wien Bibliothek.

The quiescent fluid in the cavity and the external moving fluid are separated by a shear layer in the cavity opening. The radiated sound is a result of the instability of this shear layer. One can discern a monopole-like source mechanism or dipole-like source, depending on whether acoustic modes are sustained by the cavity or not. The cause for the monopole is a time-varying net volume velocity in the opening. The cause for a dipole would be accordingly [27, 107] a resulting drag force on the fluid shear layer by the vortex impingement on the trailing edge of the opening. The monopole sound is expected to have a narrow band of frequencies due to its association with an acoustic cavity mode ($\lambda/4$). For dimensions of the opening smaller than the wavelength λ , the fluid displacement in the cavity represents a piston in a rigid baffle [27]. The goal is now to connect the fluid displacement velocity with the measured wall pressure spectrum as the input for an acoustic radiation model. A first step is the modification of the Goody formula for the near wall hydraulic pressure spectrum Φ_{surf} measured in front of the MPP or the reference plate:

$$\frac{\Phi_{\text{surf}}(\omega)U_e}{\delta_{99}\tau_w^2} = \frac{C_2(\omega\delta_{99}/U_e)^{0.8}}{[(\omega\delta_{99}/U_e)^{0.75} + C_1]^{1.7} + [C_3(\omega\delta_{99}/U_e)]^{4.8}} \quad (5.1)$$

With the constants $C_1 = 0.5$, $C_2 = 50.0$ and $C_3 = 1.1R_T^{-0.57}$, and R_T as a ratio of timescales (cf. [68] and (2.50) and (6.12)), the empirical model was fitted to the measured power spectral density.

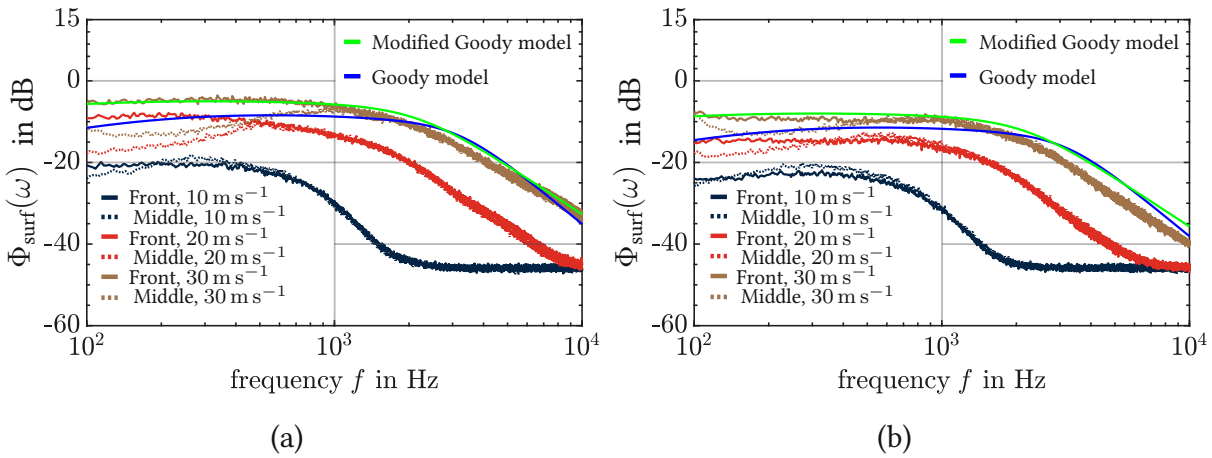


Figure 5.6: Wall pressure spectra $\Phi_{\text{surf}}(\omega)$ in front and on (middle) LSE4 surface (b) and on the reference plate (a); with (modified) Goody model simulated pressure spectra.

The fitted curve (—) shows that the modified Goody formula recovers the measured data better in the low-frequency part of the spectrum. The best fit can be achieved for the reference plate. However, the pressure spectrum is very sensitive to the sensor's flush placing in the plate wall. A too far recessed pressure sensor can significantly influence the higher frequency part of the wall pressure fluctuations. This is due to the additional cavity on the circumference of the sensor. This effect is especially visible at higher flow velocities. The measured and

analytical wall pressure spectra have a significant influence on the sound field at the cavity bottom and thus on the emitted self-noise of the MPA configuration.

5.2.2 Self-noise measurements

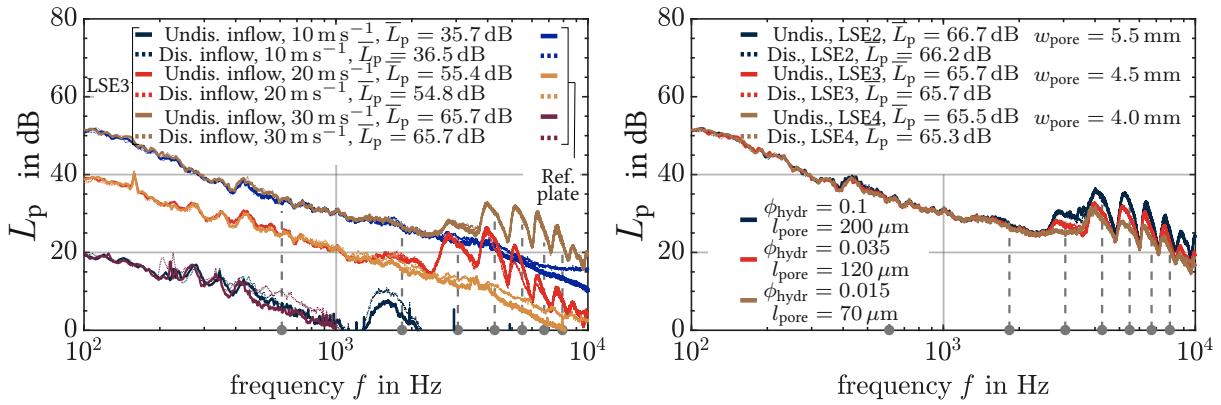
The MPA configurations have been varied to reveal the emitted sound's dependency on the flow character grazing the MPA. These configurations also served as validation cases for the modeling of the emitted sound spectra. The shown data in Fig. 5.7 (a-f) also allows to derive recommendations for MPP application in flow.

Figure 5.7 (a) clearly shows the dependence of the emitted sound intensity on the flow velocity. One can also discern a high-intensity low-frequency part below 1000 Hz and cavity tone dominated high-frequency portions. The cavity length here was $L_c = 143$ mm and MPP LSE3 was used. The diagram shows that the cavity sound, as well as the narrow band frequency peaks of the emitted sound, are associated with the $\lambda/4$ -resonance frequencies (cf. (d)). Figure 5.7 (a) also reveals that the low-frequency sound emission (< 1 kHz) is associated with the aeroacoustic sources within the flow itself and is independent of the MPP characteristics (compare reference plate emissions with MPA emissions). In Fig. 5.7 (b), the slits are tilted 0° towards the flow, and the cavity tones, beginning at 3000 Hz are correlated with MPP porosity and slit width. Whereby, the lower the porosity and smaller the slit width, the lower the emitted acoustic intensity. If the MPPs are tilted towards the flow by 90° , as shown in Fig. 5.7 (c), then the sound emission has a much more low-frequency portion, then in the 0° setup. The critical Strouhal number ($St = 0.2$) is reached much earlier due to effectively more slits (separation) tilting towards the incoming flow. It is worth noting that the peaks' intensity in the high-frequency range (above 3000 Hz) becomes lower, but due to the emergence of the peak at 2000 Hz, the overall emitted sound level would still be higher as in the 0° case.

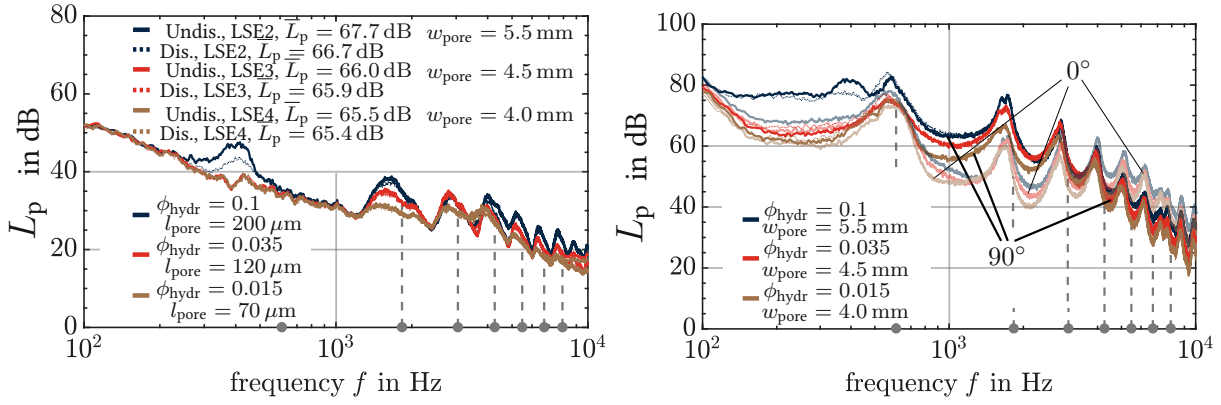
The sound in the cavity is changed significantly when the MPP is tilted from 90° to 0° . The low-frequency portion and the range up to 3000 Hz is strongly reduced. The high-frequency portion is increased. The location of the cavity tone peaks remains unchanged. Also, it is revealed that the cavity tones are clearly associated with the emitted narrowband peaks, beginning at 3000 Hz. The first two cavity peaks manifest in a corresponding emitted narrowband spectrum with the only exception of using MPP LSE2.

The last two diagrams show the influence of the cavity length L_c on the emitted SPL. In Fig. 5.7 (e), the MPP is tilted towards the flow by 0° and in Fig. 5.7 (f) by 90° . In first case the typical high-frequency spectrum occurs as shown in (b). For once, one can see that the cavity length does not change the intensity of the emitted sound. But more distinct peaks occur with increasing length. The shorter L_c , the more broadband the emitted sound field becomes. This effect is even more prominent when the MPP is tilted by 90° in the flow. The earlier excitation due to the smaller effective slit separation is now much more broadband, especially for the smallest cavity length. The overall sound pressure level should also be higher due to the higher low-frequency portions. The narrowband peak intensity, however is not changed significantly.

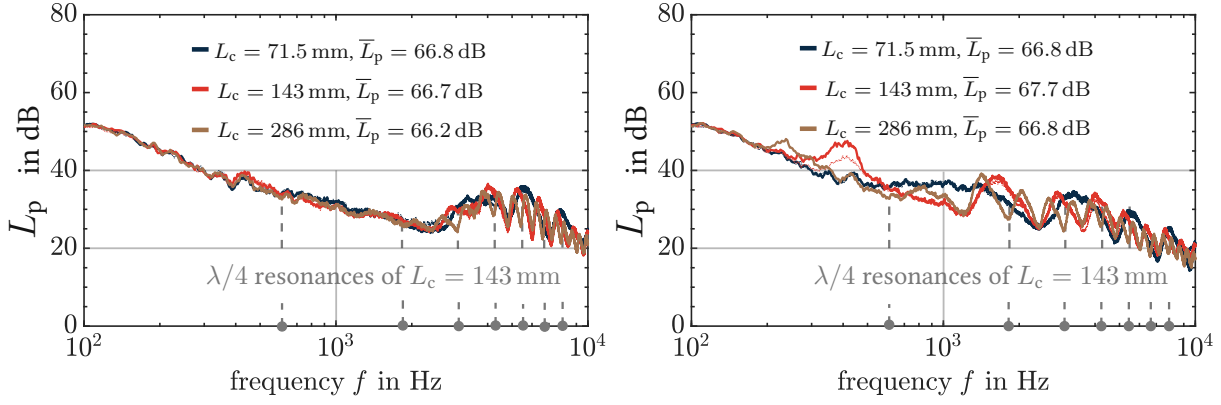
5 Evaluation in the free-far field and grazing flow



(a) Emitted spectrum L_p of MPP LSE3 at different flow velocities U_0 ; undisturbed (Undis.) and disturbed (Dis.) inflow. (b) Emitted spectrum L_p depending on ϕ and w_{pore} with $U_0 = 30 \text{ m s}^{-1}$ at 0° ; undisturbed (Undis.) and disturbed (Dis.) inflow.



(c) Emitted spectrum L_p depending on ϕ and w_{pore} with $U_0 = 30 \text{ m s}^{-1}$ at 90° ; undisturbed (Undis.) and disturbed (Dis.) inflow. (d) Sound spectrum in cavity with $U_0 = 30 \text{ m s}^{-1}$ at 90° and at 0° .



(e) Emitted spectrum L_p of LSE2 depending on L_c at 0° with $U_0 = 30 \text{ m s}^{-1}$. (f) Emitted spectrum L_p of LSE2 depending on L_c at 90° with $U_0 = 30 \text{ m s}^{-1}$.

Figure 5.7: MPP self-noise level dependence on MPA configuration parameters.

Die approbierte gedruckte Originalversion dieser Dissertation ist an der TU Wien Bibliothek verfügbar. The approved original version of this doctoral thesis is available in print at TU Wien Bibliothek.

The measurements show that the overall sound pressure levels \bar{L}_p are influenced the most by the flow velocity. Also, it has been established that the MPA will emit sound even without the presence of an adjacent fan. The "self-noise" phenomenon described in Chap. 4 can only in part be correlated to the overflowed MPA. A major part of this noise mechanism is presumably influenced by the trailing edge of the blades exposed to a turbulence flow field. Again, as mentioned in Chap. 4, the bias flow through the MPP, is probably a major contributor to this self-noise mechanism, but its scope and the underlying physical phenomena could not be further studied. However, the measurements above show that the MPA can ingest more turbulence into the grazing flow. In comparison to the large intensity portion around and below 1000 Hz, the narrowband noise peaks contribute only minor to the self-noise and thus would not worsen the MPA effectiveness. The lower-frequency portion is unaffected by self-noise (depending on MPP orientation and L_c) and thus the MPA effectiveness should not be compromised here. This, of course, might change when the flow velocity reaches values beyond $Ma = 0.1$.

An important observation is the presumed correlation between the ratio $\delta_{99}/l_{\text{pore}}$ and the effect of the MPP on the flow character. The boundary layer measurements in Fig.5.4 (b-d) show that if the ratio increases, the grazing flow maintains its laminar profile. If the inflow is disturbed and turbulent (cf. Fig.5.5 (b)), the boundary layer thickness and thus the ratio mentioned is also high. It can be seen that in this case also, that the wall bounded velocity profile character past the MPP remains unchanged. It appears that the scope of the influence of the MPP on the flow depends on this ratio. Additionally, the measurements in Fig. 5.7 (b,c) showed that the self-noise intensity also correlates with l_{pore} , but not with the character of the inflow velocity profile (disturbed or undisturbed, cf. Fig. 5.7 (b)). Thus, one could state for a first estimation for the level of MPP self-noise and the correlated influence on turbulence injection into the wall bounded flow (cf. Fig. 5.4 (f)), the ratio $\delta_{99}/l_{\text{pore}}$ can be used since the thickness of the hydraulic boundary layer can readily be estimated.

5.3 Simulations

As the measurements showed, the flow velocity is the most important factor for the emitted sound intensity. There are models that allow a rough estimation of the self-noise and cavity tone sound emission, which both can compromise the MPA effectiveness. The models presented are modifications of the single orifice models by Golliard, Stein and Gloerfelt [61, 66, 146] which are based on the works by Howe [77] and Goody [68], and on the perforated liner models by Nelson and Ffwocs-Williams [53, 125]. Only the modified models are shown here; the basal ansatzes can be found in Chap. 2 and in the literature mentioned.

5.3.1 Analytical models

Sound in the cavity

The first model to be presented is able to predict the sound pressure spectrum on the cavity bottom Φ_{bot} (cf. Fig. 5.2). It can be used to validate measured data or with a transfer function based on the lumped elements ansatz to calculate the emitted sound from the MPP surface. The surface hydraulic pressure field $\Phi_{\text{surf,front}}$ is averaged over one pore (respectively slit), with an area cross section $S_{\text{neck}} = l_{\text{pore}}w_{\text{pore}}$, by a shape function. The resulting force Φ_f due to the turbulent fluctuations excites the cavity eigenmodes ($\lambda/4$ -resonances), represented by $T(\omega)$.

$$\begin{aligned} \Phi_{\text{bot}}(\omega) &= |T(\omega)|^2 \Phi_f(\omega), & \Phi_f(\omega) &= \frac{1}{S_{\text{neck}}^2} \iint_{\infty} \Phi_{\text{surf,front}}(\omega) S(\tilde{\mathbf{k}})^2 d\tilde{\mathbf{k}}, \\ S_{\text{piston,rigid}}(\tilde{\mathbf{k}}) &= \text{sinc} \frac{\tilde{k}_1 l_{\text{pore}}}{2} \text{sinc} \frac{\tilde{k}_3 w_{\text{pore}}}{2}, \\ T(\omega) &= \left(\frac{1}{\sin \tilde{k}_0 L_c} \right) \left(\frac{1}{\cot \tilde{k}_0 L_c - \frac{1}{\phi_{\text{hydr}}} \tilde{k}_0 l_{\text{corr,H-S}} + \frac{1}{\phi_{\text{hydr}}} r_{\text{corr,H-S}}} \right), \\ l_{\text{corr,H-S}} &= \Re[S_{\text{neck}} / (K_{U_0=0} - K_R)], & r_{\text{corr,H-S}} &= \tilde{k}_0 \Im[S_{\text{neck}} / (K_R - K_{U_0=0})]. \end{aligned} \tag{5.2}$$

Since in this approach $\Phi_{\text{surf,front}}$ is independent of $\tilde{\mathbf{k}}$, l_{pore} and w_{pore} can be interchanged. The Rayleigh conductivity K_R is a function of $F(U_0, \omega, w_{\text{pore}}, l_{\text{pore}})$, J_1, J_0, Ψ (cf. Chap.2). The definition of the function Ψ governs the low-frequency and high-frequency behavior of the calculated cavity sound spectrum in a prominent way and can thus be used for tuning the data match. This also means it is necessary for future works to find a more appropriate function for Ψ . The differentiation between the "hydraulic" porosity ϕ_{hydr} and the fitted "acoustic" porosity ϕ_{acou} is emphasized here. The latter is fitted to acoustic measurements, whilst the former is measured and provided by the manufacturer. The hydraulic porosity is what the hydraulic pressure fluctuation wave "sees". The porosity governs the measured data agreement very sensitively in the high-frequency range and is therefore also a tuning parameter. From

an acoustic point of view the orientation of the slits (effective separation in flow direction), does not influence the MPA absorption behavior; the orientation of the slits does, however, matter from an hydraulic point of view and governs the source strength and frequency range (cf. Fig. 5.7).

Emitted sound

Because of $Ma \ll 1$, the sound field and the (hydraulic) source field exist on clearly separated length scales. The source has length scale l and the sound field l/Ma , with $l = 1/k'$. The basal model of Ffwocs-Williams [53], assumes that the small-scale turbulence is scattered by individual apertures into sound and that on sparsely perforated surfaces ("opaque") at each individual aperture, the turbulence drives an efficient monopole-like volume flow source. Which means a perforated plate with low porosity supports a monopole-like sound emission behavior. The model is further based on the assumption that at each aperture there is a piston that moves perpendicular to the plate surface with an average impedance Z_0 . Each piston is excited by a randomly fluctuating hydraulic pressure p' , now induces a monopole strength

$$Q_{\text{mono}} = \frac{2p' i \tilde{k}_0 b_{\text{pore}} l_{\text{pore}} \rho_0 c_0}{Z_0 z_{\text{rad}}}. \quad (5.3)$$

The acoustic emission is partly governed by the normalized radiation impedance of the piston $z_{\text{rad}} = z_{\text{res}} + i z_{\text{react}}$. The pressure on a rigid baffle is twice the pressure in the free field, therefore the hydraulic pressure in the equation is doubled. The calculation of the radiation impedance is shown in Appendix C. The far field sound pressure at a distance R_{mic} can then be calculated with,

$$\overline{\tilde{p}^2} = \frac{4}{\phi_{\text{acou}}^2} \Phi_{\text{surf,front}} \left| (1 - r) Q_{\text{mono}} \exp(-i \tilde{k}_0 R_{\text{Mic}}) / 4\pi R_{\text{Mic}} \right|^2. \quad (5.4)$$

Here, the equivalent acoustic coefficient $1 - r$ modulates the source excitation to recover the measured sound emission narrow band peaks in the higher-frequency spectrum. As shown in the measured emission spectra (cf. Fig. 5.7), the lower-frequency part (< 1 kHz) is unaffected by the MPA source mechanism. As the "acoustic" porosity ϕ_{acou} , $1 - r$ is calculated from the fitted equivalent compression modulus and density of the specific MPPs in combination with $\lambda/4$ -resonances due to the cavity length L_c . A broadband higher-frequency noise portion can be added by using [77]:

$$\overline{\tilde{p}_{\text{rough}}^2} = \frac{S_{\text{plate}} \phi_{\text{acou}}}{R_{\text{Mic}}^2} (\tilde{k}_0 t_{\text{rough}})^2 (\omega t_{\text{rough}} / U_c)^2 \Phi_{\text{surf,front}}, \quad (5.5)$$

where t_{rough} is the average height of the surface waviness and $U_c = 0.6U_0$ is the convection velocity of the largest eddies and S_{plate} is the surface area of the MPP plate.

5.3.2 Comparison to measurements

The aforementioned models have been applied to simulate the cavity and emitted sound spectrum of MPP LSE2 and LSE4. The results are shown in Figs. 5.8 (a-f). In Fig. 5.8 (a), the influence of different MPP geometry parameters on the simulated cavity sound at $U_0 = 30 \text{ m s}^{-1}$ and $L_c = 143 \text{ mm}$ can be observed. The basic trend of the spectrum is strongly dependent on the hydraulic pressure spectrum in front of or behind the MPP. The peak heights and positions can be changed with the porosity and slit lengths. There is a general better data agreement in the narrow parts between the peaks and in the higher-frequency range. In Fig. 5.8 (b), the simulated cavity spectrum below MPP LSE4 at $U_0 = 20 \text{ m s}^{-1}$ and $U_0 = 30 \text{ m s}^{-1}$ is shown. The model is able to produce a good correlation with the measure data, however the agreement worsens for the lower velocity. This is due to the fact that at lower velocities U_0 the hydraulic pressure spectrum in higher-frequency portion can not be accurately simulated by the modified Goody model.

The first emitted spectrum is shown in Fig. 5.8 (c). The modified model of Ffwocs-Williams can produce a good fit with the measured data at $U_0 = 30 \text{ m s}^{-1}$. The lower-frequency portion of the spectrum is overestimated. The adding of the simulated roughness noise can increase the broadband noise portion visibly in the measured spectrum for higher frequencies. At lower velocities the model significantly overestimates the lower-frequency part of the measured sound. For MPP LSE4 (cf. Fig. 5.8 (d)), the model performs similarly as for LSE2. Again, the lower-frequency spectrum portion is overestimated. But the peaks and general trend is captured well and can be mended accordingly by adding broadband noise induced by the roughness of the MPP surface. To show the robustness of the model, MPP LSE2 and LSE4 have been subjugated at $L_c = 71.5 \text{ mm}$ to the two flow velocities. The cavity model (cf. Fig. 5.8 (e)) can recover the measured spectra well. However, now the data fitting for the cavity sound is better in the lower-frequency spectrum portion. The peaks are however recovered with good correlation. The emitted spectrum (cf. Fig. 5.8 (f)) of the MPA with the smallest cavity length can be predicted with similar accuracy for MPP LSE4. The data fit can again be improved by adding the simulated roughness noise. All in all, the models can reproduce the observed sound sufficiently, keeping in mind that they mostly rely on empirical fitting parameters. The most important observation, however, is that at the absorption peaks of the MPA (calculated by the reflection coefficient r), there is also the highest level of "self-noise".

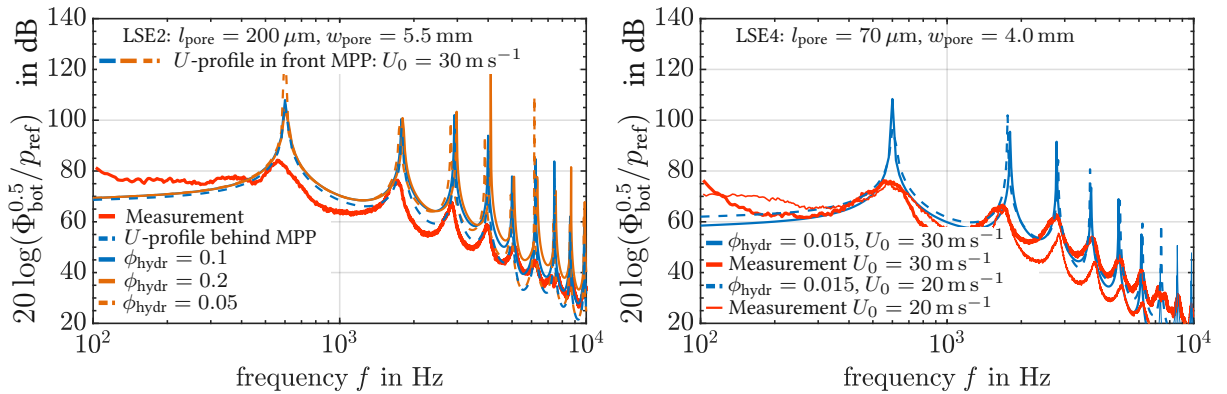
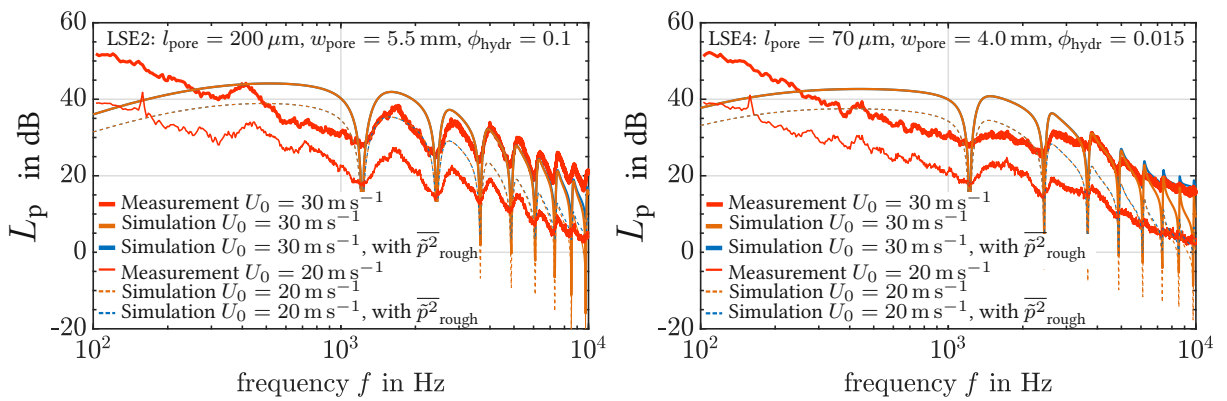
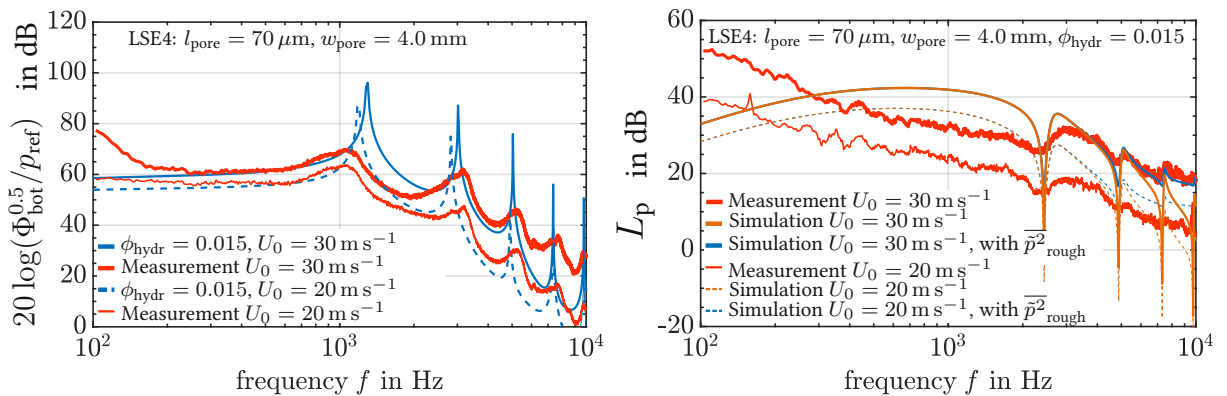
(a) Cavity sound for $L_c = 143$ mm and MPP type LSE2.(b) Cavity sound for $L_c = 143$ mm and MPP type LSE4.(c) Emitted sound L_p for $L_c = 143$ mm and MPP type LSE2.(d) Emitted sound L_p for $L_c = 143$ mm and MPP type LSE4.(e) Cavity sound for $L_c = 71.5$ mm and MPP type LSE4.(f) Emitted sound L_p for $L_c = 71.5$ mm and MPP type LSE4.

Figure 5.8: Simulated and measured spectra of the cavity and emitted sound pressure.

5.4 Consequences for MPA application in flow

The presented measurements and simulations allow now to derive some general recommendations for MPP application in flow:

- Results from the measurements
 - *At undisturbed inflow conditions, the MPPs introduce turbulence which might affect the efficiency of an adjacent turbo-machine.*
 - *The overflown MPAs emit resonance-based self-noise, which can be compensated and moved to a higher-frequency range with a change of orientation of the slits towards the flow direction.*
 - *The lower-frequency MPA effectiveness at the investigated Mach numbers is unaffected by the resonance self-noise mechanism.*
 - *If any, the MPP emits sound only at higher frequencies and low intensities compared to the high-intensity low-frequency sound due to the flow over the plate itself.*
 - *The intensity of the self-noise peaks is dependent on flow velocity, MPP geometrical parameters, and turbulence.*
 - *The narrowness of the peak frequency bands depends on the back volume length and the slit orientation towards the flow.*
 - *The location of the peaks can be tuned with the back volume length L_c .*
 - *At the absorption peaks, the MPA also emits relatively strong sound levels.*
- Results from the simulations based on the empirical models
 - *The analytical models are able to predict the overall sound spectrum trends and intensities.*
 - *The lower-frequency portion of the emitted spectrum is overestimated.*
 - Further studies certainly might investigate more detailed:
 - * The model performance at higher Mach numbers.
 - * The coupling of the hydraulic source mechanism to the emitted sound.
 - * The input Rayleigh conductivity correction terms for resistance and reactance.
 - * Usage of the models to investigate the change of acoustic impedance with flow which affects sound absorption.

Conclusion and outlook

The objectives of this thesis were to test an FE-based framework for dedicated MPA design and analyze its performance in various kinds of sound fields. Thereby, for MPA pre-characterization, an equivalent fluid approach has been applied. Here, obtaining accurate equivalent material parameters represents a challenging first step, which was solved by applying a genetic-algorithm based acoustic material parameter fitting. Several error influences within the fitting procedure could be identified, such as systematic measurement errors, over-fitting by too many design variables, and ambient influences. As such, the investigated MPP materials' acoustically relevant characteristic length was calculated, and allowed a performance ranking by using the viscous Biot frequency.

Next, modifying an expansion chamber test setup allowed for a wider frequency range by extending the standard MPA liner configuration from the plane-frequency range to the highly diffuse sound field range. Measurements revealed that the effectiveness of an MPA can be estimated by the Helmholtz number of the geometry at hand. Also, an MPP with high porosity and smaller characteristic length scale renders the highest sound reductions. The cavity configuration is key in tuning the MPA for certain noise frequency bands. To allow for high sound reduction at low Helmholtz numbers, the cavity should be segmented. However, the segmentation can have negative consequences at higher Helmholtz numbers. Here, a broadband sound reduction, comparable to the standard foam materials, can be achieved by leaving the cavity empty. If the MPP is bent into a circular shape, the sound reduction is declining at the higher-frequency portions. The equivalent MPP domain in more dedicated MPAs could be simulated with sufficient accuracy up to 8 kHz with the obtained 1D-absorption data. There, it could be shown that the orientation of the sound source should be considered for the optimal location of an MPA.

The in-flow application of an MPA using the presented pre-design steps revealed the importance of the location of MPA next to a low-pressure axial fan. For a performance evaluation,

the operational volume flow range has to be considered. The effectiveness of the MPA is best in the partial load range and becomes seemingly independent of the operational point with higher flow velocities. Noise mechanisms associated with the tip gap clearance are major contributors to high-intensity noise and can bring about unpleasant tonal noise components if the fan is operated within a micro-perforated section of the duct. The large-scale simulation of an MPA works well in the low Helmholtz number range. If the sound field consists of more and more modal components, the influence of the duct and MPA geometry, as well as the propagating modes, are significant for an accurate simulation.

The cavity configuration is significant in the partial load range in combination with low Helmholtz numbers. If the inflow is disturbed (turbulent), the MPA counteracts the turbulence-associated increase in broadband sound emissions. The fan's efficiency is mostly influenced by the tip gap clearance and associated to blind flow. The MPA, in presumed interaction with noise sources of the fan or vice versa, starts to emit self-noise beginning at 3 kHz, especially in the partial load range.

The investigated MPA-"self-noise" spectrum can be observed without the fan. Boundary layer and measurements of the emitted sound revealed that the emitted sound's intensity is correlated with higher flow velocity, MPP geometry parameters, the length of the MPA cavity, and to some degree on the ratio of the hydraulic near-wall boundary layer to the characteristic acoustic length. The orientation of the MPP slits towards the flow governs the affected frequency range. To complete the MPA design and evaluation, two analytical models for the sound in the MPA's cavity and the emitted sound spectrum have been developed from existing models. The formulas are based mainly on empirical factors, and a complete understanding of the underlying physical phenomena is missing. However, the modified models allow an estimation of the noise spectrum that an MPA is emitting under grazing flow conditions.

For future works, the tip-gap-MPA-associated noise mechanism should be studied. Furthermore, the conversion of the hydraulic fluctuating pressure field to an acoustic source at the MPA's slits should be investigated for higher Mach numbers and, as such, it is possible to derive a more generally applicable model.

Design variable constraints

Fitting constraints:

1. Frequency range
 - $\alpha = [\text{all}]$: frequency range from 100 Hz to 6400 Hz
 - $\alpha = [0.25; 1.0; 0.75]$: includes on left peak flank from 0.25 to 1.0 and on right flank 1.0 to 0.75
 - $\alpha = [0.75; 0.75]$: includes right peak flank from 0.75 to left peak flank 0.75, **without 1.0**
 - $\alpha = [0.25; 1.0; 0.25]$: includes on left peak flank from 0.25 to 1.0 and on right flank 1.0 to 0.25
 - $\alpha = [0.25; 0.75; 0.25]$: includes left peak flank from 0.25 to 0.75 and right peak flank from 0.75 to 0.25, **without peak 1.0**
2. Temperature: 18 °C, 20 °C, 22 °C, 25 °C
3. Models: JCAL, JCAPL, Wilson, Maa
4. Model parameters with applied ranges:
 - $r_{\text{pore}} = [1; 500]$, $\phi = [0.01; 0.5]$
 - $r_{\text{pore}}, \phi, L_c$
 - $r_{\text{pore}}, \phi, b_{\text{form}} = [0.0001; 1.0]$
 - $r_{\text{pore}}, \phi, b_{\text{form}}, L_c$
 - $r_{\text{pore}}, \phi, b_{\text{form}}, L_c, a_{\text{JCAL}} = [0.1; 3]$, $b_{\text{JCAL}} = [0.1; 3]$, $c_{\text{JCAL}} = [0.1; 3]$

- $T_{\text{eff},2} = T_{\text{MPP},2} \cdot T_{L_c,2} \cdot T_{\text{MPP},1} \cdot T_{L_c,1}$
- $K_{\text{eq,scr}}$ and K_0
- Low and high frequency limit for $\rho_{\text{eq,scr}}$ of the JCAL model

5. Specimens:

- I, II, III: measured on 29.3.2021 consecutively with the specimen glued in the mounting location
- IV: measured one week before I, II and III
- V: measured on 8.8.20 with specimen positioned loose in the mounting section and then fixed with a rubber band

6. $L_{c,60}$ and $L_{c,140}$

Fitting parameters $(a, b, c)_{\text{JCAL}}$ in the calculation of $\rho_{\text{eq,scr}}$

$$\rho_{\text{eq,scr}} = \frac{\alpha_{\infty} \rho_0}{\phi} \left[1 + \frac{\sigma \phi}{i \omega \rho_0 \alpha_{\infty}} \left(1 - b_{\text{form}} + b_{\text{form}} \sqrt{1 + i \frac{4 \alpha_{\infty}^2 \mu_0 \rho_0 \omega^a}{b_{\text{form}}^2 \sigma^2 \Lambda^b \phi^c}} \right) \right] \quad (6.1)$$

Different MPP C specimens

C - front side	$t_{\text{MPP}} = 1.0 \text{ mm}$	$\phi/-$	$r_{\text{pore}}/\mu\text{m}$	L_c/mm	$b_{\text{form}}/-$	f_v/Hz	f_t/Hz
$ r $ - JCAL- I	$\alpha = [0.25; 1.0; 0.75]$	0.057	72.1	141.7	—	3804	4047
$ r $ - JCAL- II	—	0.057	72.4	141.3	—	3370	4010
$ r $ - JCAL- III	—	0.059	71.8	141.3	—	3837	4082
$ r $ - JCAL- IV	—	0.064	71.5	142.2	—	3866	4112
$ r $ - JCAL- V	—	0.058	82.2	140.2	—	2925	3111
C - rear side	$t = 1.0 \text{ mm}$						
$ r $ - JCAL- I	—	0.060	68.8	141.2	—	4175	4441
$ r $ - JCAL- II	—	0.060	69.7	141.0	—	4072	4331
$ r $ - JCAL- III	—	0.061	69.8	140.9	—	4057	4315
$ r $ - JCAL- IV	—	0.066	69.0	141.5	—	4155	4419
$ r $ - JCAL- V	—	0.05	80.4	138.8	—	3059	3254
$ r $ - JCAL- II	$\alpha = [\text{all}]$	0.059	67.1	141.1	—	4393	4673
$ r $ - JCAL- II	$\alpha = [0.75; 0.75]$	0.059	60.4	141.4	—	5408	5752
$ r $ - JCAL- II	$\alpha = [0.25; 1.0; 0.25]$	0.058	68.1	141.0	—	4268	4539
$ r $ - JCAL- II	$\alpha = [0.25; 0.75; 0.25]$	0.058	62.8	141.1	—	5018	5338
$ r $ - JCAL- IV	$\alpha = [\text{all}], L_{c,60}$	0.067	67.0	61.5	—	4403	4683
$ r $ - JCAL- IV	$\alpha = [0.25; 1.0; 0.75], L_{c,60}$	0.063	68.7	61.2	—	4188	4455
$ r $ - JCAL- I	$\alpha = [0.25; 1.0; 0.75]$	0.050	75.9	140	—	3427	3646
$ r $ - JCAL- II	—	0.050	76.0	140	—	3421	3639
$ r $ - JCAL- III	—	0.052	75.9	140	—	3433	3651
$ r $ - JCAL- IV	—	0.051	78.3	140	—	3226	3431
$ r $ - JCAL- V	—	0.056	74.2	140	—	3590	3818

Table 6.1: Fitted parameters with JCAL and different specimens of MPP C, $L_c = 140 \text{ mm}$ and calculated viscous and thermal Biot frequencies f_v and f_t ; fitted to peaks at 22°C with at least 250 generations as time horizon. ρ_{eq} and K_0 are modeled. Specimen I-III were obtained the same day and consecutively with disassembling and reassembling the specimen mounting setup. Specimen IV was obtained a week earlier, and specimen V seven months earlier than I-III with also a less robust mounting arrangement.

C - rear side	$t_{\text{MPP}} = 1.0 \text{ mm}$	$\phi/-$	$r_{\text{pore}}/\mu\text{m}$	L_c/mm	$b_{\text{form}}/-$	f_v/Hz	f_t/Hz
$\ r\ $ - JCAL- II	$\alpha = [\text{all}]$	0.05	73.6	140	—	3654	3886
$\ r\ $ - JCAL- II	$\alpha = [0.25; 1.0; 0.75]$	0.05	76.0	140	—	3422	3640
$\ r\ $ - JCAL- II	$\alpha = [0.75; 0.75]$	0.048	65.8	140	—	4574	4866
$\ r\ $ - JCAL- II	$\alpha = [0.25; 1.0; 0.25]$	0.050	73.5	140	—	3659	3893
$\ r\ $ - JCAL- II	$\alpha = [0.25; 0.75; 0.25]$	0.05	67.2	140	—	4383	4662
$\ r\ $ - JCAL- II	$\alpha = [0.25; 1.0; 0.75], 18^\circ\text{C}$	0.063	67.3	140	—	4254	4574
$\ r\ $ - JCAL- II	—, 20°C	0.055	71.8	140	—	3782	4044
$\ r\ $ - JCAL- II	—, 25°C	0.046	80.3	140	—	3124	3296
$\ r\ $ - JCAL- II	—, 18°C	0.060	68.8	139.7	—	4063	4369
$\ r\ $ - JCAL- II	—, 20°C	0.060	69.2	140.4	—	4067	4350
$\ r\ $ - JCAL- II	—, 25°C	0.060	70.3	141.7	—	4076	4301
$\ r\ $ - JCAPL- II	$\alpha = [0.25; 1.0; 0.75]$	0.059	83.7	140	< 0.001	2826	3006
$\ r\ $ - JCAPL- II	— $a_{\text{JCAL}}, b_{\text{JCAL}}, c_{\text{JCAL}}$	0.056	83.0	140	0.003	2874	3057
$\ r\ $ - JCAPL- II	—	0.073	73.2	141.1	0.025	3687	3922
$\ r\ $ - JCAPL- II	— $a_{\text{JCAL}}, b_{\text{JCAL}}, c_{\text{JCAL}}$	0.080	70.4	141.1	0.1	3993	4248
$\ r\ $ - JCAL- II	— $a_{\text{JCAL}}, b_{\text{JCAL}}, c_{\text{JCAL}}$	0.076	65.6	140	—	4597	4890
$\ r\ $ - JCAL- II	— $a_{\text{JCAL}}, b_{\text{JCAL}}, c_{\text{JCAL}}$	0.12	53.3	141.2	—	6973	7417

Table 6.2: Fitted parameters with JCAL or JCAPL and different specimens of MPP C, $L_c = 140 \text{ mm}$ and calculated viscous and thermal Biot frequencies f_v and f_t ; fitted to peaks at 22°C (if not indicated otherwise) with at least 250 generations. ρ_{eq} and K_0 are modeled.

C - rear side	$t_{\text{MPP}} = 1.0 \text{ mm}$	$\phi/-$	$r_{\text{pore}}/\mu\text{m}$	L_c/mm	$b_{\text{form}}/-$	f_v/Hz	f_t/Hz
$ r $ - JCAL- II	$\alpha = [0.25; 1.0; 0.75], \text{ low}$	0.051	74.4	140	—	3576	3804
$ r $ - JCAL- II	—, low	0.060	68.4	141.0	—	4231	4501
$ r $ - JCAL- II	—, high	0.01	1.5	140	—	999999	99999
$ r $ - JCAL- II	—, high	0.49	1.6	140.9	—	999999	99999
$ r $ - Wilson- II	—	0.058	135.4	140	—	1079	1147
$ r $ - Wilson- II	—	0.069	124.4	141.0	—	1277	1358
$ r $ - Maa- II	—	0.050	77.4	140	—	3295	3505
$ r $ - Maa- II	—	0.067	66.6	141.7	—	4459	4743
$ r $ - Wilson- II	—, $T_{\text{eff},2}, L_{c,2} = 2.5 \text{ mm}$	0.16	114.1	140	—	1520	1617
$ r $ - Wilson- II	—, $T_{\text{eff},2}, L_{c,2} = 2.5 \text{ mm}$	0.11	136.4	138.1	—	1062	1130
$ r $ - JCAL- II	—, $T_{\text{eff},2}, L_{c,2} = 2.5 \text{ mm}$ $a_{\text{JCAL}}, b_{\text{JCAL}}, c_{\text{JCAL}}$	0.49	36.7	140	—	14692	15627
$ r $ - JCAL- II	—, $T_{\text{eff},2}, L_{c,2} = 2.5 \text{ mm}$ $a_{\text{JCAL}}, b_{\text{JCAL}}, c_{\text{JCAL}}$	0.21	56.1	138.1	—	6282	6682
$ r $ - JCAPL- II	—, $T_{\text{eff},2}, L_{c,2} = 2.5 \text{ mm}$ $a_{\text{JCAL}}, b_{\text{JCAL}}, c_{\text{JCAL}}$	0.49	38.4	140	0.57	13439	14295
$ r $ - JCAPL- II	—, $T_{\text{eff},2}, L_{c,2} = 2.5 \text{ mm}$ $a_{\text{JCAL}}, b_{\text{JCAL}}, c_{\text{JCAL}}$	0.12	79.9	138.0	0.002	3102	3300

Table 6.3: Fitted parameters with JCAL or JCAPL and different specimens of MPP C, $L_c = 140 \text{ mm}$ and calculated viscous and thermal Biot frequencies f_v and f_t ; fitted to peaks at 22°C (if not indicated otherwise) with at least 250 generations. K_0 and different models in comparison.

MPP B specimens

B - front side	$t_{\text{MPP}} = 1.0 \text{ mm}$	$\phi/-$	$r_{\text{pore}}/\mu\text{m}$	L_c/mm	$b_{\text{form}}/-$	f_v/Hz	f_t/Hz
$\ r\ $ - JCAL	–	0.063	101.7	140	–	1911	2033
$\ r\ $ - JCAL	–	0.081	89.9	141.7	–	2446	2601
$\ r\ $ - JCAPL	–	0.063	101.7	140	1.0	1911	2033
$\ r\ $ - JCAPL	–	0.09	104.5	141.8	< 0.001	1809	1924
<hr/>							
B - rear side	$t = 1.0 \text{ mm}$						
$\ r\ $ - JCAL	–	0.065	94.0	140	–	2236	2379
$\ r\ $ - JCAL	–	0.078	85.4	140.2	–	2713	2886
$\ r\ $ - JCAPL	–	0.065	93.9	140	0.97	2239	2381
$\ r\ $ - JCAPL	–	0.086	84.9	141.2	0.51	2742	2917
<hr/>							
MASH -	$t = 1.0 \text{ mm}$	$\phi/-$	$r/\mu\text{m}$	L_c/mm	$b/-$	f_v/Hz	f_t/Hz
$\ r\ $ - JCAL	–	0.098	54.8	140	–	6598	7018
$\ r\ $ - JCAL	–	0.14	45.5	142.2	–	9552	10161
$\ r\ $ - JCAPL	–	0.13	51.3	140	0.19	7521	8000
$\ r\ $ - JCAPL	–	0.2	40.8	142.3	0.057	11872	12628

Table 6.4: Fitted parameters with JCAL and JCAPL and MPP B and MASH $L_c = 140 \text{ mm}$ and calculated viscous and thermal Biot frequencies f_v and f_t ; fitted to peaks at 22°C with at least 250 generations. ρ_{eq} and K_0 are modeled.

MPP LSE specimens

LSE 2 - rear side	$t_{\text{MPP}} = 1.0 \text{ mm}$	$\phi/-$	$r_{\text{pore}}/\mu\text{m}$	L_c/mm	$b_{\text{form}}/-$	f_v/Hz	f_t/Hz
$ r $ - JCAL	—	0.13	194.7	140	—	521	554
$ r $ - JCAL	—	0.18	154.7	141.7	—	826	878
$ r $ - JCAPL	—	0.13	194.7	140	0.999	521	554
$ r $ - JCAPL	—	0.18	164.6	141.7	0.63	730	776
<hr/>							
LSE 3 - rear side	$t = 1.0 \text{ mm}$						
$ r $ - JCAL	—	0.074	112.6	140	—	1558	1657
$ r $ - JCAL	—	0.1	95.4	142.1	—	2171	2309
$ r $ - JCAPL	—	0.078	141.7	140	< 0.001	984	1047
$ r $ - JCAPL	—	0.1	95.9	142.2	0.64	2151	2288
<hr/>							
LSE 4 - rear side	$t = 1.0 \text{ mm}$	$\phi/-$	$r/\mu\text{m}$	L_c/mm	$b/-$	f_v/Hz	f_t/Hz
$ r $ - JCAL	—	0.044	74.4	140	—	3571	3799
$ r $ - JCAL	—	0.061	63.7	142.0	—	4881	5192
$ r $ - JCAPL	—	0.05	72.5	140	0.45	3758	3997
$ r $ - JCAPL	—	0.077	65.4	142.1	< 0.001	4624	4918
<hr/>							
LSE 7 - rear side	$t = 1.0 \text{ mm}$						
$ r $ - JCAL	—	0.28	14.0	140	—	100000	100000
$ r $ - JCAL	—	0.5	10.8	142.1	—	170000	181000
$ r $ - JCAPL	—	0.24	15.2	140	0.98	86000	92000
$ r $ - JCAPL	—	0.5	10.8	142.0	0.999	170000	181000

Table 6.5: Fitted parameters with JCAL and JCAPL and MPP B and MASH $L_c = 140 \text{ mm}$ and calculated viscous and thermal Biot frequencies f_v and f_t ; fitted to peaks at 22°C with at least 250 generations. ρ_{eq} and K_0 are modeled.

Additional content B

Test rig - schematic

The experimental investigations were carried out in an axial fan test rig standardised according to DIN EN ISO 5801 [3]. The test rig has an anechoic chamber on the suction side of the test axial fan, which makes it technically possible to determine the sound emissions of the fan. A cross-section of the inlet test rig is shown in Figure 6.1. The air is drawn in through a standardized inlet nozzle. The volume flow is determined via this nozzle. For the adjustment of the operating point the test stand has an auxiliary fan and a butterfly throttle. Before the air enters the anechoic chamber, it is made quiet by splitter-type silencers. The anechoic chamber on the suction side of the axial fan has a volume of $V = 22 \text{ m}^3$ and has a quiescent sound pressure level $L_p = 28 \text{ dB}$ for the frequency range of $f \in [0.1 \text{ kHz}; 10 \text{ kHz}]$. The walls of the chamber are built in a sandwich structure, which consists of 80 mm thick acoustic foam, 20 mm acoustic heavy foam and 2.5 mm acoustic heavy foil inside. These are mounted on acoustic sound insulation panels. The cut-off frequency of the anechoic chamber is $f_c = 254 \text{ Hz}$ and has reverberation times in the range of $[0.03 \text{ s}; 0.19 \text{ s}]$. Just before the inlet nozzle of the axial fan there is a ring pressure tap which is connected to a differential pressure sensor (Setra, type 2391-500LB-1F-2B-02-9-NN) with the ambience to measure the total static pressure difference p_{ts} of the fan. The pressure sensor has a measurement inaccuracy of $\pm 0.073 \%$ on the measured value. The inlet nozzle of the fan is connected to the test bench wall. The duct in which the fan operates is variable so that the length can be changed. At a distance of $S_{\text{grid}} = 220 \text{ mm}$ from the inlet nozzle it is possible to insert generic turbulence grids into the flow. Numerous studies on the induced flow field of the used turbulence grid can be found in the literature [55, 96, 97]. The characteristic data of the grid are shown in Tab. 6.6. After the turbulence grid a replaceable duct section is located. This duct section has a length of $L_{\text{MPA}} = 440 \text{ mm}$ and represents in the reference variant a straight duct with the diameter $D_{\text{duct}} = 500 \text{ mm}$. In the second variant this duct section is replaced by a micro-perforated duct. The diameter of the micro-perforated tube is $D_{\text{MPA}} = 506 \text{ mm}$

and thus slightly larger than the standard reference duct. Depending on the variant, the examined axial fan is operated directly in the perforated duct or shortly downstream in an unperforated duct section. The fan is supported by 4 non-centric support struts, which lower the rotor-stator-interaction [96]. Outside the duct is the motor drive unit. This is equipped with a torque and speed sensor (burster, typ 8861), so that the power and efficiency of the fan can be determined. The measurement uncertainty of the torque sensor is 0.1 % on the measured value. The torque values of the fan are corrected with a predetermined torque offset M_s , which includes momentum due to bearing friction. For more detailed information on the test rig and the turbulence grid used, please refer to the literature [45, 96, 98][46].

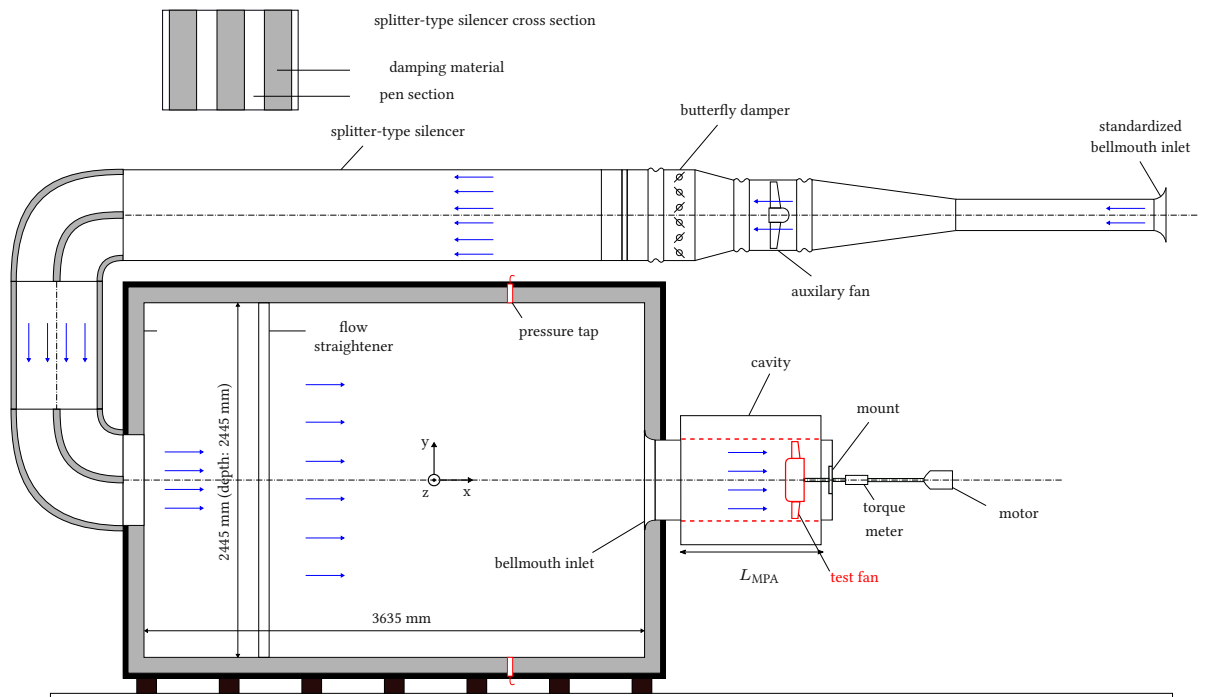


Figure 6.1: Inlet test chamber designed according to ISO 5801 [3] [46].

Table 6.6: Parameters of turbulence grid.

Parameter	Value
bar width T_{bar}	16 mm
clearance T_{cl}	80 mm
mesh size T_{m}	96 mm
solidity σ	0.31

Test rig - anechoic chamber

The radiated sound field of axial fans is determined on the suction side of the turbomachinery. For this purpose five free-field microphones (Brüel & Kjær, type 4189-L-001) with preamplifier (Brüel & Kjær, type 2669-L) are used within the anechoic chamber. The microphones are connected to a microphone amplifier (Brüel & Kjær, type Nexus 2690-A) and are calibrated with a microphone calibrator (Brüel & Kjær, type 4231) before measurement. A PXIe-1075 front-end (NI) chassis with a high-precision 24-bit PXIe-4492 (NI) data acquisition module was used to acquire the measurement data. The components of the measurement technology were controlled by the software LabView (NI). The microphones used have a free field response of ± 1 dB over the frequency range of $f \in [10 \text{ Hz}; 8 \text{ kHz}]$ and the microphone preamps of ± 0.5 dB over the frequency range of $f \in [3 \text{ Hz}; 200 \text{ kHz}]$. The microphones are all located at a distance of $R_{\text{Mic}} = 1000$ mm from the fan inlet bellmouth. The arrangement of the microphones is shown schematically in Fig. 6.2(a) and the Fig. 6.2(b) shows a photograph of the experimental setup with built-in turbulence grid and forward skewed fan. One microphone (M3) is located on the rotation axis of the fan and two microphones (M1-M2) are located on a horizontal quarter circle to the rotation axis of the fan. The microphones (M3-M5) are arranged on a vertical quarter circle. The angle segments between the individual microphones are each $\Phi_{\text{Mic}} = 22.5^\circ$. As soon as a stable operating point is reached, the sound pressure is measured parallel to the determination of the aerodynamic characteristics of the fan. The sound pressure is measured for a measuring time of $t_{\text{samp}} = 30$ s with a sampling frequency of $f_{\text{samp}} = 48$ kHz. The resulting sound pressure level spectrum is calculated from the energetically averaged sound pressure of all five microphones (M1-M5). The total sound pressure level of each measurement is calculated from the average sound pressure spectrum for the frequency range of $f \in [0.1 \text{ kHz}; 10 \text{ kHz}]$. For details we refer to [45, 46, 96].

Fans - blade skewness

The influence of the MPA on the noise emissions of axial fans is investigated on two different fans. The two fans are identical and differ only in the fan blade skew. Thus a backward skewed fan with the sweep angle of $\lambda_{\text{fan}} \in [0^\circ; -55^\circ]$ and a forward skewed fan with sweep angle of $\lambda_{\text{fan}} \in [0^\circ; 55^\circ]$ are investigated. A sweep angle of $\lambda_{\text{fan}} = 0^\circ$ is applied to the hub of both fans. This sweep angle changes its value linearly over the span of the blade. The fans used are shown in the Fig. 6.3. These two fans were chosen because there is a large database of aerodynamic and acoustic properties of the two fans in the literature [45, 55, 72, 96, 97]. Furthermore, backward and forward skewed fans are frequently used in technical systems. The axial fans were designed according to the blade element theory [34, 35, 130]. Both of them have $n_{\text{blade}} = 9$ blades and are configured for optimal operation for a volume flow rate of $\dot{V} = 1.4 \text{ m}^3 \text{ s}^{-1}$ and a rotational speed of $n_{\text{rot}} = 1486 \text{ min}^{-1}$. The most important dimensions of the fans are listed in the Tab. 6.7. The behaviour of the two fans has already been experimentally examined in several studies. It was found that at the design point the forward skewed fan is the quieter version of the two fans. In addition, the backward skewed

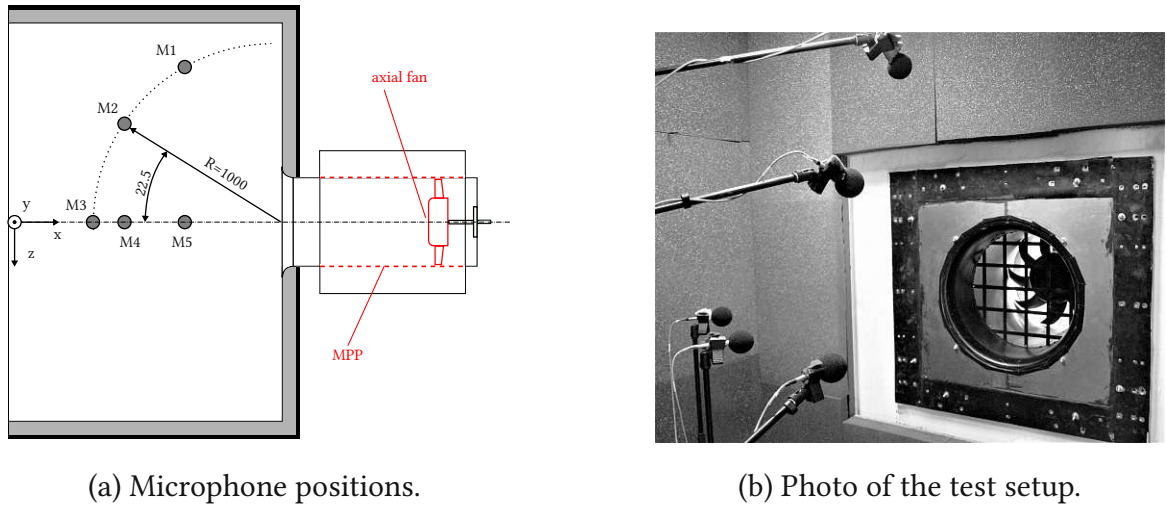


Figure 6.2: Representation of the experimental setup for characterization of the sound field, (a) schematic drawing with microphone positions (M1-M5) and (b) photo of the experimental setup with installed turbulence grid [46].

fan showed higher sound sources, which are due to the interaction of the blade tips with the tip gap flow. The forward skewed fan was found to be more sensitive to disturbed inflow conditions [45, 96, 167]. Figure 6.4 shows the sound pressure spectra of the used fans for free and turbulent inflow operating in a short duct at two different operation points (part load range $\dot{V} = 0.9 \text{ m}^3 \text{ s}^{-1}$, design point $\dot{V} = 1.4 \text{ m}^3 \text{ s}^{-1}$). The increased turbulence was generated with a turbulence grid upstream of the fans. From the spectra shown, the acoustic properties of the fans can be identified. In the partial load range (see Fig. 6.4 (a) and (b)) subharmonic components are visible in the spectra, which are caused by the formation of coherent flow structures in the tip gap and interact with the leading edge of the fan. These sound sources are usually amplified with increasing tip gap [90, 96]. Furthermore, these sound sources are influenced by the operating point of the fan and the blade shape. For example, it can be seen that this sound mechanism for the backward skewed fan is still present in the region of the design point, whereas this is not the case for the forward skewed fan (see Fig. 6.4 (c) and (d)). The tonal components of the fans used are more pronounced from the design point onwards. These are increased by turbulent inflow for both fans. In addition, turbulent inflow leads to an increase in broadband sound up to $f = 3 \text{ kHz}$ for these fans (leading edge sound). It can be seen that the forward skewed fan reacts much stronger to the changed inflow than the backward skewed fan at the design point. With their different characteristics, these two fans are particularly suitable for obtaining a general applicability of the results. The acoustic properties shown can change further with varying duct lengths, because these affect the inflow and acoustic propagation of duct modes [96, 124][46].



(a) Forward skewed fan (F).



(b) Backward skewed fan (B).

Figure 6.3: Photography of the axial fans, (a) fan F with forward skewed fan blades and (b) fan B with backward skewed blades [46].

Table 6.7: Design parameters of the axial fans.

Parameter	Value
Number of fan blades n_{blade}	9
Total fan diameter D_{fan}	495 mm
Duct diameter D_{duct}	500 mm
Hub diameter	247.5 mm
Tip gap size $(D_{\text{duct}} - D_{\text{fan}})/2$	2.5 mm
Design volume flow \dot{V}	$1.4 \text{ m}^3 \text{ s}^{-1}$
Design speed n_{rot}	1486 min^{-1}
NACA-profile	NACA 4510 [6]

Fans - sound pressure characteristics

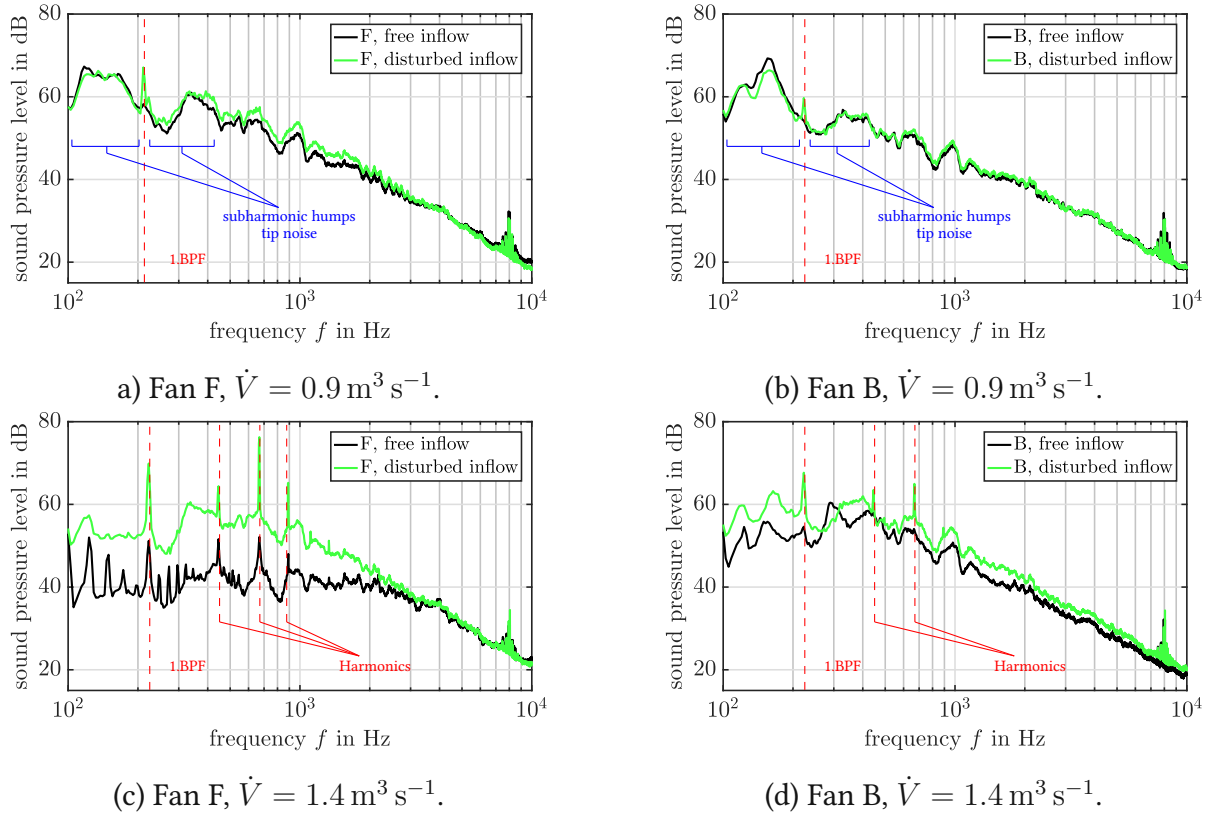


Figure 6.4: Averaged sound pressure spectra of fans F (a and c) and B (b and d) operating in a short duct with different inlet turbulence at the design point ($\dot{V} = 1.4 \text{ m}^3 \text{ s}^{-1}$) and in the part load range ($\dot{V} = 0.9 \text{ m}^3 \text{ s}^{-1}$). Red dashed lines indicate the blade passing frequency (BPF) and its harmonics. The areas in blue brackets represent the subharmonic humps in the spectrum, which mainly occur in the partial load range and are caused by the interaction of the leading edge of the blade with the vortex structures in the tip gap of the fan [46].

Aeroacoustic sources - simulated emitted power

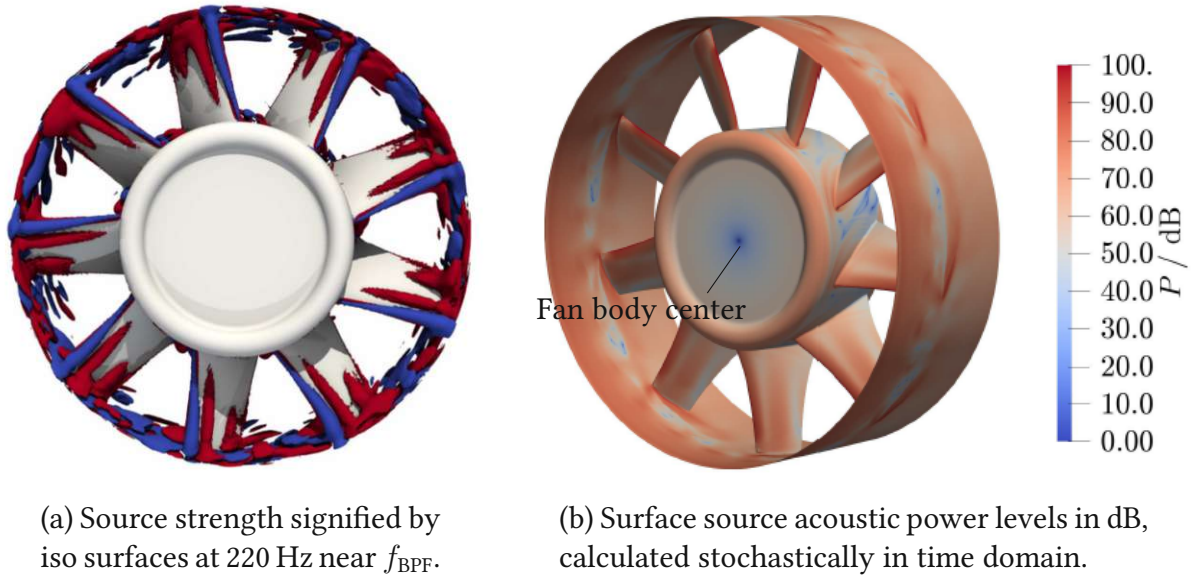
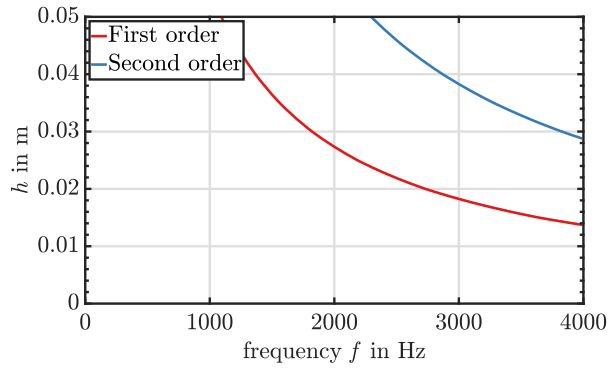
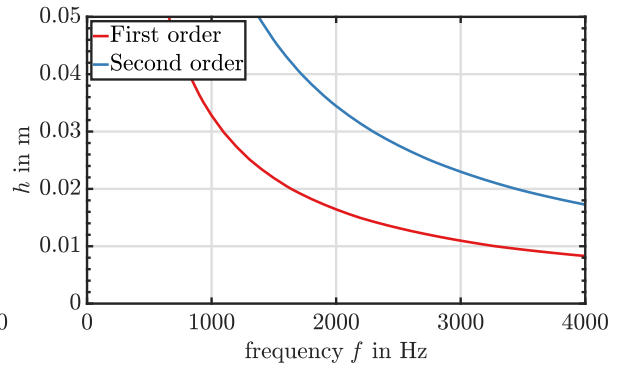


Figure 6.5: Constant iso surfaces of the acoustic power source terms at 220 Hz and surface source power levels obtained from aeroacoustic simulation of an unskewed fan, [85].

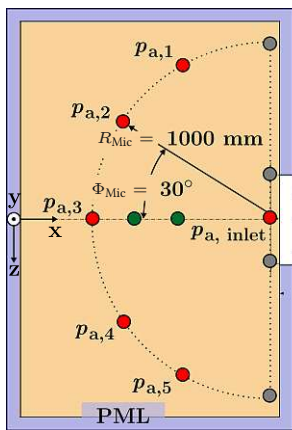
Meshed geometry - non-conforming interfaces



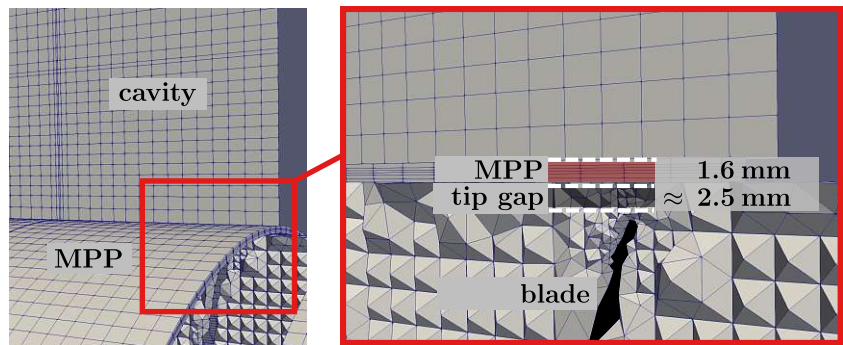
(a) hq -relation for air domain according to (4.2).



(b) hq -relation for MPP domain at largest simulated frequency 1600 Hz with effective speed of sound of 205 m s^{-1} .



(c) Pressure monitoring points in measurement plane.



(d) MPP with cavity and enhanced view of the non-conforming interfaces.

Figure 6.6: Discretization of the volume domains, monitoring points and enhanced view of MPP - cavity intersections [57].

Table 6.8: Measured and simulated \bar{L}_p at different operating points of the fan in RFS and RFL setup [57].

\dot{V} in m^3s^{-1}	Setup	\bar{L}_p in dB	$\bar{L}_{p,\text{sim}}$ in dB
0.8	F,RFS	88.8	65.7
	B,RFS	85.8	-
1.0	F,RFS	79.2	-
	B,RFS	87.7	-
1.2	F,RFS	74.0	-
	B,RFS	92.4	-
1.4	F,RFS	71.5	-
	B,RFS	79.3	-
1.9	F,RFS	70.1	-
	B,RFS	69.1	-
-	MFS, \neg MPP, $L_{c,140}$	-	62.9
-	MFS, \neg MPP, $L_{c,200}$	-	62.5
0.8	F,RFL	89.1	65.1
	B,RFL	85.3	-
1.0	F,RFL	78.7	-
	B,RFL	87.3	-
1.2	F,RFL	72.6	-
	B,RFL	92.7	-
1.4	F,RFL	71.5	-
	B,RFL	79.8	-
1.9	F,RFL	70.4	-
	B,RFL	69.1	-
-	MFL, \neg MPP, $L_{c,140}$	-	63.2
-	MFL, \neg MPP, $L_{c,200}$	-	62.8

Table 6.9: Measured and simulated \bar{L}_p at different operating points of the fan in MFS and MFL setup [57].

\dot{V} in m^3s^{-1}	Setup	\bar{L}_p in dB	$\bar{L}_{p,\text{sim}}$ in dB	$\Delta(\text{RFS-MFS})$
0.8	F,MFS	76.8	-	12.0
	B,MFS	74.9	-	10.9
1.0	F,MFS	75.4	-	3.8
	B,MFS	76.0	-	11.7
1.2	F,MFS	72.1	-	1.9
	B,MFS	76.1	-	16.3
1.4	F,MFS	69.2	-	2.3
	B,MFS	73.0	-	6.3
1.9	F,MFS	67.1	-	3.0
	B,MFS	67.1	-	2.0
-	MFS,MPP, $L_{c,140}$	-	60.4	5.3
-	MFS,MPP, $L_{c,200}$	-	60.1	5.6
-	-	-	-	$\Delta(\text{RFL-MFL})$
0.8	F,MFL	77.3	-	11.8
	B,MFL	71.9	-	13.4
1.0	F,MFL	73.1	-	5.6
	B,MFL	75.6	-	11.7
1.2	F,MFL	68.2	-	4.4
	B,MFL	78.0	-	14.7
1.4	F,MFL	66.8	-	4.7
	B,MFL	73.7	-	6.1
1.9	F,MFL	65.9	-	4.5
	B,MFL	64.2	-	4.9
-	MFL,MPP, $L_{c,140}$	-	61.2	3.9
-	MFL,MPP, $L_{c,200}$	-	60.8	4.3

Reference setup with turbulent inflow - fan characteristics and overall sound pressure

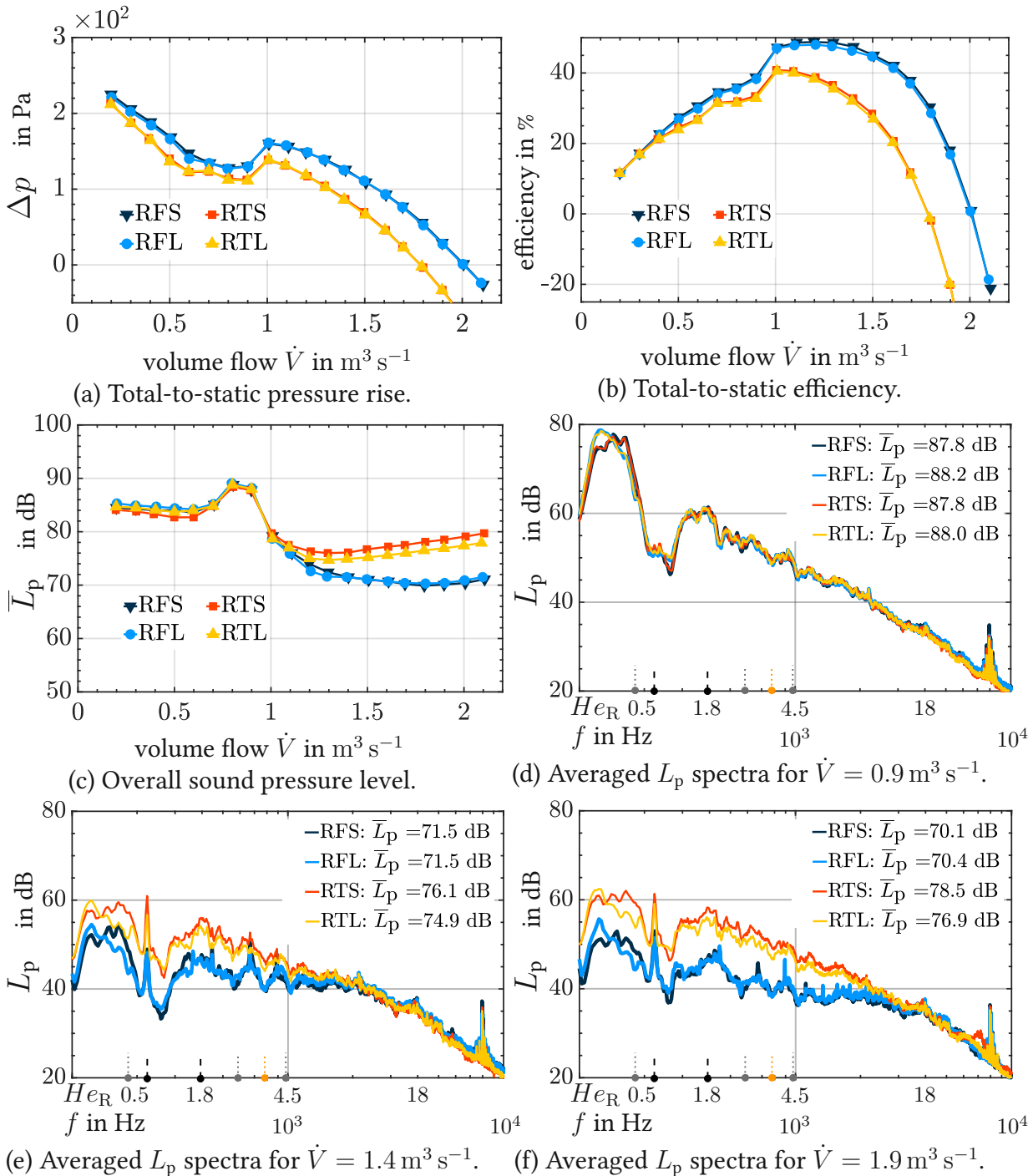


Figure 6.7: Results of the measurements of RFS-RFL-RTS-RTL setup.

Overall sound reduction of the compared cavity setups

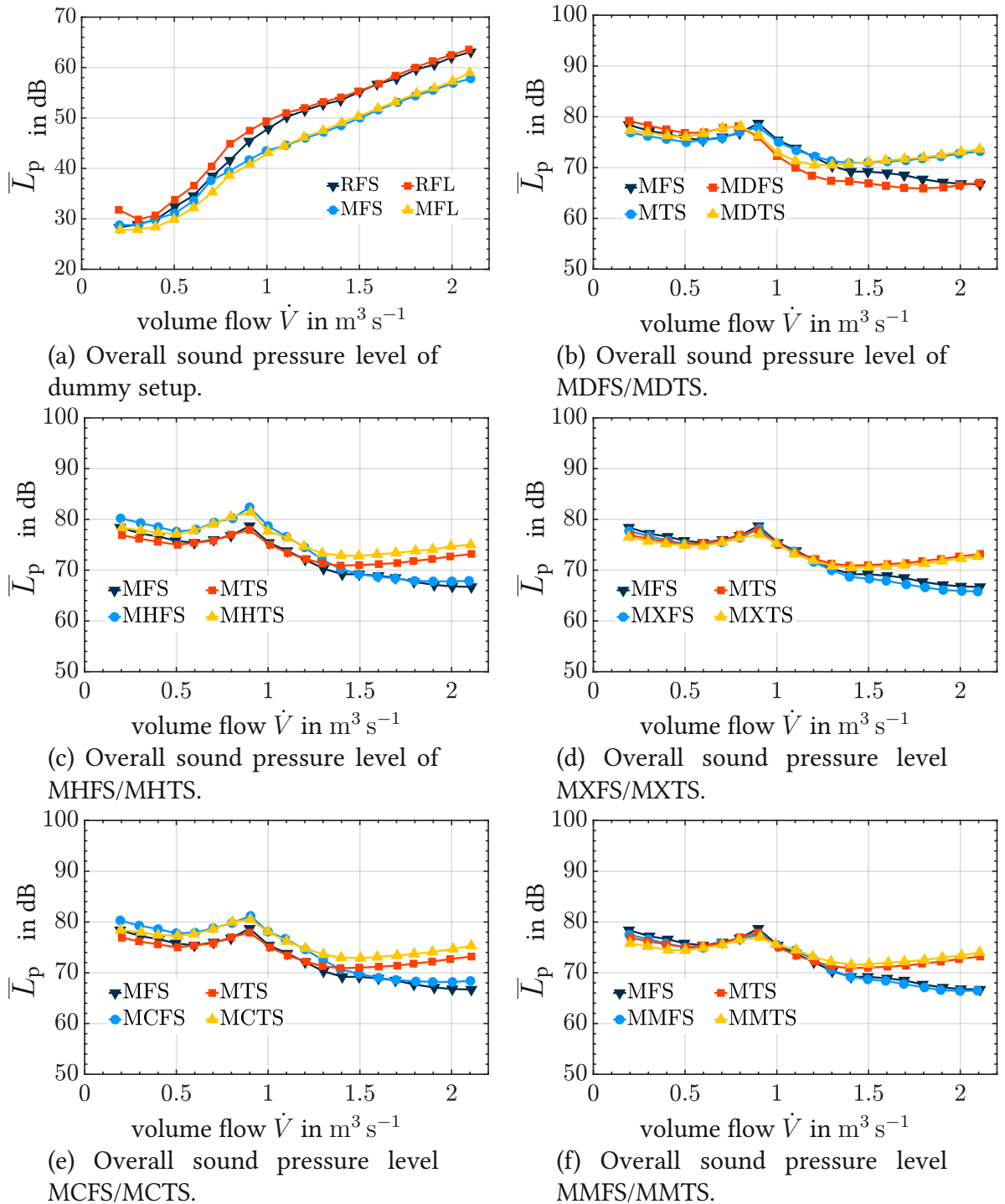
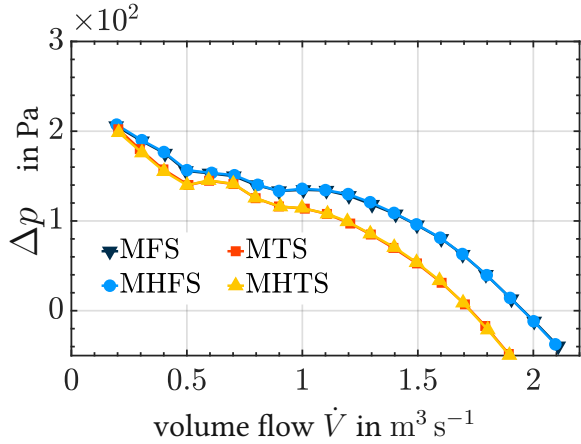
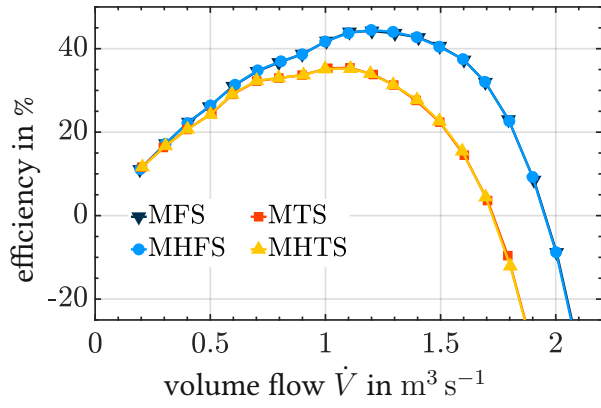


Figure 6.8: Overall sound pressure levels of the different cavity setups and the dummy setup.

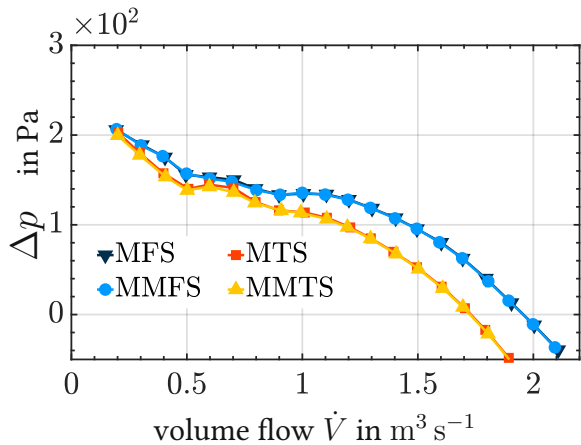
Effects on fan aerodynamics - efficiency - other setups



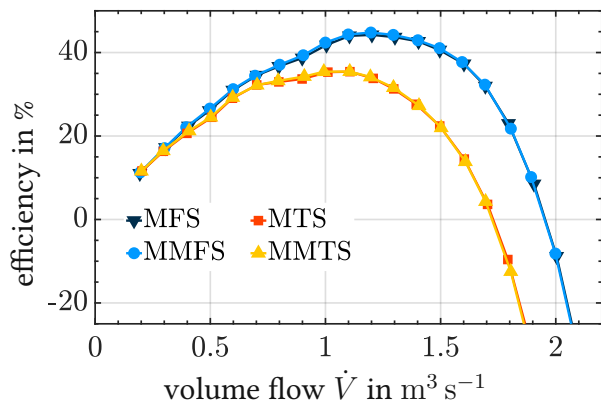
(a) Total-to-static pressure rise of MHFS/MHTS.



(b) Total-to-static efficiency of MHFS/MHTS.



(c) Total-to-static pressure rise of MMFS/MMTS.



(d) Total-to-static efficiency of MMFS/MMTS.

Figure 6.9: Pressure rise and total-to-static efficiency of the MHFS/MHTS and MMFS/MMTS setup.

Additional content C

Calculation of the slit radiation impedance

The entire derivation and formulas for the calculation of the radiation impedance of a rectangular piston in a rigid baffle can be found in [117]. Here only the fast calculation formulas are presented:

$$\begin{aligned}
 \frac{Z_{\text{res}}}{Z_0} &= 1 - \frac{2}{\pi \tilde{k}_0^2 ab} [1 + \cos(\tilde{k}_0 \sqrt{a^2 + b^2}) + \tilde{k}_0 \sqrt{a^2 + b^2} \sin(\tilde{k}_0 \sqrt{a^2 + b^2}) \\
 &\quad - \cos(\tilde{k}_0 a) - \cos(\tilde{k}_0 b)] + \frac{2}{\pi} \hat{I}_a, \\
 \frac{Z_{\text{react}}}{Z_0} &= \frac{2}{\pi \tilde{k}_0^2 ab} [\tilde{k}_0 (a + b) + \sin(\tilde{k}_0 \sqrt{a^2 + b^2}) - \tilde{k}_0 \sqrt{a^2 + b^2} \cos(\tilde{k}_0 \sqrt{a^2 + b^2}) \\
 &\quad - \sin(\tilde{k}_0 a) - \sin(\tilde{k}_0 b)] - \frac{2}{\pi} \hat{I}_b,
 \end{aligned} \tag{6.2}$$

where $b = l_{\text{pore}}$ and $a = w_{\text{pore}}$ and with the integrals

$$\begin{aligned}
 \hat{I}_a &= \int_1^{\sqrt{1+(b/a)^2}} \sqrt{1-1/x^2} \cos(x\tilde{k}_0 a) dx + \int_1^{\sqrt{1+(a/b)^2}} \sqrt{1-1/x^2} \cos(x\tilde{k}_0 b) dx, \\
 \hat{I}_b &= \int_1^{\sqrt{1+(b/a)^2}} \sqrt{1-1/x^2} \sin(x\tilde{k}_0 a) dx + \int_1^{\sqrt{1+(a/b)^2}} \sqrt{1-1/x^2} \sin(x\tilde{k}_0 b) dx.
 \end{aligned} \tag{6.3}$$

Additional content D

General form of JCAL and JCAPL models

The final expressions (2.38) and (2.39) if further scrutinized reveal [12, 102, 114]:

$$\begin{aligned}
 \alpha(\omega) &= \alpha_\infty \left[1 + \frac{1}{i\bar{\omega}} F(\omega) \right] & \text{with} & & F(\omega) &= 1 - b_{\text{form}} + b_{\text{form}} \sqrt{1 + \frac{M}{2b_{\text{form}}^2} i\bar{\omega}}, \\
 i\bar{\omega} &= \frac{i\omega \rho_0 k_0 \alpha_\infty}{\mu_0 \phi} & \text{and} & & M &= \frac{8k_0 \alpha_\infty}{\phi \Lambda^2}
 \end{aligned} \tag{6.4}$$

$$\begin{aligned}
 \beta(\omega) &= \gamma - (\gamma - 1) \left[1 + \frac{1}{i\bar{\omega}'} F'(\omega) \right]^{-1} & F'(\omega) &= 1 - b'_{\text{form}} + b'_{\text{form}} \sqrt{1 + \frac{M'}{2b'_{\text{form}}{}^2} i\bar{\omega}'} \\
 M' &= \frac{8k'_0}{\phi \Lambda'^2}, \quad i\bar{\omega}' = \frac{i\omega \rho_0 Pr k'_0}{\mu_0 \phi} & b'_{\text{form}} &= \frac{M'}{4(\alpha'_0 - 1)} = \frac{2k'_0}{\phi \Lambda'^2 (\alpha'_0 - 1)}
 \end{aligned} \tag{6.5}$$

In (6.4) and (6.5), M is a shape factor and $\bar{\omega}$ is the reduced frequency (as a measure of unsteadiness or another shape factor). For identical cylindrical pores with characteristic length $r_{\text{pore}} = d/2$, then the viscous and thermal problem happen to have the same mathematical form and the following relations hold [102]:

$$\begin{aligned}
 k'(\omega) &= k(Pr\omega) & M &= M' & \Lambda &= \Lambda' = r_{\text{pore}} \\
 k_0 &= k'_0 = \phi r_{\text{pore}}^2 / 8 & \sigma &= 8\mu_0 / (\phi r_{\text{pore}}^2) & b_{\text{form}} &= b'_{\text{form}} = 1
 \end{aligned} \tag{6.6}$$

Here, the superscript $()'$ signifies a thermal acoustic model parameter.

Details on JCAPL

The drag within pores of variable shape is considered in this model, with a relative fluid flow defined by

$$\mathbf{v}(\mathbf{r}) = \tilde{\mathbf{u}}(\mathbf{r}) - \bar{\mathbf{u}}_s. \quad (6.7)$$

Thereby, $\tilde{\mathbf{u}}(\mathbf{r})$ is the non-averaged fluid velocity in the tube-like channel, with $\mathbf{r} = f(y, z)$ as the distance from the tube axis (in x-direction of the pore channel) in 2D and $\bar{\mathbf{u}}_s$ is the average solid frame velocity. The two Biot frequency domains defined in (2.36) control the nature of the relative flow (viscous or inertia dominated). If one defines the local Strouhal number with

$$Sr_{\text{local}} = \frac{|\bar{\mathbf{u}}_s \cdot \nabla \mathbf{v}|}{|\partial \mathbf{v} / \partial t|}, \quad (6.8)$$

and assumes a constant-width of the circular pore channels, the convection term is zero, but nonzero for relative flow in channels that possess a half-width function $h(z)$, then one can establish estimates for a variable-width flow channel where the local Strouhal and Reynolds number tend to zero in the limit of high and low frequencies:

$$Sr_{\text{local}} \approx \frac{1}{h_0} \left| \frac{dh}{dz} \right| \frac{\varepsilon c_0}{\omega} \quad \text{and} \quad Re_{\text{local}} = \frac{\omega}{\omega_v} Sr_{\text{local}}. \quad (6.9)$$

Here, the parameter ε is the wave strain (the strain of the surface area covered by the fluid), h_0 is the mean channel half width and $|dh/dz|$ is a characteristic (flow-controlling) channel-wall or streamline slope. The form drag always contributes to drag forces if there is a non-constant channel width. Thereby, the contribution increases with increasing slope of the channel walls. Friction drag mainly appears in the smallest apertures (pores).[133]

Influence of plate vibration

The equations (2.28) and (2.29) account for the situation when the porous frame material is allowed to move and air phase and solid material produced a coupled response to an impinging sound wave. It has been established that a coupled response (dilatational and rotational waves) can be ruled out due to the low decoupling frequency (2.30). But, if the influence of a vibrating frame is to be considered, one can add the elastic properties of the frame with a structural impedance of the panel Z_p . The structural impedance is a function of the eigenfrequencies, frame mode shapes and the modelling of the relative motion of the frame to the envisioned moving air plug in the pore. For only plane air wave coupling with the frame, the structural-acoustic coupling can be cast in the form [32, 38, 147, 151]:

$$Z_{\text{eff}} = \frac{Z_{\text{eq,scr}} Z_p}{Z_{\text{eq,scr}} + Z_p} - iZ_0 \cot(\tilde{k}_0 L_c), \quad \text{with } Z_{\text{eq,scr}} = Z_m. \quad (6.10)$$

Additional content E

Calculation of Kelvin-Helmholtz wavenumbers

The function $F(\sigma_1, \sigma_2)$ is defined by [61]

$$F(\sigma_1, \sigma_2) = \frac{-\sigma_1 J_0(\sigma_2)[J_0(\sigma_1) - 2W(\sigma_1)] + \sigma_2 J_0(\sigma_1)[J_0(\sigma_2) - 2W(\sigma_2)]}{\sigma_1 W(\sigma_2)[J_0(\sigma_1) - 2W(\sigma_1)] - \sigma_2 W(\sigma_1)[J_0(\sigma_2) - 2W(\sigma_2)]}, \quad (6.11)$$

with $W(x) = ix(J_0(x) - iJ_1(x))$.

Definition of the ratio of timescales of the hydraulic pressure

The ratio of timescale of the random (hydraulic) pressure is defined in [68] by

$$R_T = \frac{\delta_{99}/U_e}{\nu_0/u_\tau^2}, \quad (6.12)$$

with $u_\tau = (\tau_w/\rho_0)^{0.5}$ as the friction velocity.

Bibliography

- [1] *Noise generation and noise reduction in air-conditioning systems*. VDI 2081, 2001.
- [2] *DIN EN ISO 10534 Acoustics - Determination of sound absorption coefficient and impedance in impedance tubes - Part 2: transfer function method*. Berlin Beuth Verlag, 2010.
- [3] *DIN EN ISO 5801 Fan - Performance testing using standardized airways*. Berlin Beuth Verlag, 2017.
- [4] *ASTM E1050-19, Standard Test Method for Impedance and Absorption of Acoustical Materials Using a Tube*. ASTM International, West Conshohocken, PA, 2019.
- [5] openCFS, 2021. Online; accessed 13-September-2021; <https://www.opencfs.org/index.html>.
- [6] I. H. Abbott and A. E. Von Doenhoff. *Theory of wing sections, including a summary of airfoil data*. Courier Corporation, 1959. ISBN 0486605868.
- [7] M. Ainsworth. Discrete dispersion relation for hp-version finite element approximation at high wave number. *IAM J. Numer. Anal.*, 42(2):553–575, 2004. doi: 10.1137/S0036142903423460.
- [8] S. Allam and M. Åbom. Experimental characterization of acoustic liners with extended reaction. *AiAA*, December 2008. doi: 10.2514/6.2008-3074.
- [9] S. Allam and M. Åbom. A new type of muffler based on micro-perforated panels. *J. Vib. Acoust.*, 133(3):031005–031005–8, 2011. doi: 10.1115/1.4002956.
- [10] S. Allam and M. Åbom. Fan noise control using micro-perforated splitter silencers. *Journal of Vibration and Acoustics*, 136(3), 2014. doi: 10.1115/1.4027245.

- [11] S. Allam and M. Åbom. Noise reduction for automotive radiator cooling fans. *FAN 2015*, 2015.
- [12] J. F. Allard. *Propagation of Sound in Porous Media*. Elsevier, London, 2015. doi: 10.1002/9780470747339.
- [13] J. F. Allard and Y. Champoux. New empirical equations for sound propagation in rigid frame fibrous materials. *Journal of the Acoustical Society of America*, 91(6):3346–3353, 1991. doi: 10.1121/1.402824.
- [14] N. Atalla and F. Sgard. Modelling of perforated plates and screens using rigid frame porous models. *Journal of Sound and Vibration*, 303(2):195–208, 2007. doi: 10.1016/j.jsv.2007.01.012.
- [15] N. Atalla and F. Sgard. Modeling of perforated plates and screens using rigid frame porous media. *Journal of Sound and Vibration*, 303:195–208, 2007. doi: 10.1016/j.jsv.2007.01.012.
- [16] N. Atalla, R. Panneton, and P. Ddebergue. A mixed displacement-pressure formulation for poroelastic materials. *Journal of the Acoustical Society of America*, 103(3), 1998. doi: 10.1121/1.424355.
- [17] M. Avellanda and S. Torquato. Rigorous link between fluid permeability, electrical conductivity, and relaxation times for transport in porous media. *Physics of Fluids: Fluid Dynamics*, 3(11):2529–2540, 1991. doi: 10.1063/1.858194.
- [18] T. Bäck, D.-B. Fogel, and Z. Michalewicz. *Handbook of Evolutionary Computation*. IOP Publishing Ltd., 1st edition, 1997.
- [19] G. K. Batchelor. *An Introduction to Fluid Dynamics*. Cambridge University Press, 2000. ISBN 978-3-540-71342-5.
- [20] A. B. Bauer and R. L. Chapkist. Noise generated by boundary-layer interaction with perforated acoustic liners. *14th AIAA/ Aeroacoustic Science Meeting, AIAA*, 14(2), 1977. doi: 10.2514/6.1976-41.
- [21] M. Becher, R. Krusche, M. Tautz, M. Mauß, N. Springer, F. J. Krömer, and S. Becker. Influence of the gap flow of axial vehicle cooling fans on radiated narrowband and broadband noise. *Acta Acustica united with Acustica*, Volume 105(1), feb 2019. doi: 10.3813/AAA.919326.
- [22] F. X. Bécot and L. Jaouen. An alternative biot’s formulation for dissipative porous media with skeleton deformation. *Journal of the Acoustical Society of America*, 134(6), 2013. doi: 10.1121/1.4826175.

- [23] W. M. Beltman. *Viscothermal wave propagation including acousto-elastic interaction*. doctoralthesis, University of Twente, Department of Mechanical Engineering, 1998.
- [24] M. Berggren, A. Bernland, and D. Noreland. Acoustic boundary layers as boundary conditions. *Journal of Computational Physics*, 371:633–650, 2018. doi: 10.1016/j.jcp.2018.06.005.
- [25] M. A. Biot. Theory of propagation of elastic waves in a fluid-saturated porous solid. i. low-frequency range. *Journal of the Acoustical Society of America*, 28(2):168–178, 1956. doi: 10.1121/1.1908239.
- [26] M. A. Biot. Theory of propagation of elastic waves in a fluid-saturated porous solid. ii. higher frequency range. *Journal of the Acoustical Society of America*, 28(2):179–191, 1956. doi: 10.1121/1.1908241.
- [27] W. K. Blake. *Mechanics of Flow-Induced Sound and Vibration, Volume 1 General Concepts and Elementary Sources*. Elsevier Academic Press, 2017. ISBN 978-0-12-809273-6.
- [28] W. K. Blake. *Mechanics of Flow-Induced Sound and Vibration, Volume 2*. Elsevier Academic Press, 2017. ISBN 978-0-12-809274-3.
- [29] T. Blickle and L. Thiele. A comparison of selection schemes used in evolutionary algorithms. *Evolutionary Computation*, 4(4):361–394, 1996. doi: 10.1162/evco.1996.4.4.361.
- [30] H. Bodén and M. Åbom. Influence of errors on the two-microphone method for measuring acoustic properties in ducts. *Journal of the Acoustical Society of America*, 79(2): 541–549, 1986. doi: 10.1121/1.393542.
- [31] J.-S. Bolton. *Microperforates: A Review*. Publications of the Ray W. Herrick Laboratories. Paper 163, 2017. <http://docs.lib.purdue.edu/herrick/163>; accessed on 29.05.20.
- [32] T. Bravo, C. Maury, and C. Pinhède. Absorption and transmission of boundary layer noise through flexible multi-layer micro-perforated structures. *Journal of Sound and Vibration*, 395:201–223, 2017. doi: 10.1016/j.jsv.2017.02.018.
- [33] M. Butteltmann and B. Lohmann. Optimierung mit genetischen algorithmen und eine anwendung zur modelreduktion. *Automatisierungstechnik*, 52(4):151–163, 2004.
- [34] T. Carolus. *Ventilatoren - Aerodynamischer Entwurf, Schallvorhersage, Konstruktion*. Springer Vieweg, Wiesbaden, 3rd edition, 2013. doi: 10.1007/978-3-8348-2472-1.
- [35] T. H. Carolus and R. Starzmann. An aerodynamic design methodology for low pressure axial fans with integrated airfoil polar prediction. In *ASME 2011 Turbo Expo: Turbine Technical Conference and Exposition*, pages 335–342. American Society of Mechanical Engineers, 2011. doi: doi:10.1115/GT2011-45243.

- [36] Y. Champoux and J. F. Allard. Dynamic tortuosity and bulk modulus in air saturated porous media. *Journal of Applied Physics*, 70(4), 1991. doi: 10.1063/1.349482.
- [37] J. Y. Chung and D. A. Blaser. Transfer function method of measuring in-duct acoustic properties. II. experiment. *J. Acoust. Soc. Am.*, 68(3):914–921, 1980. doi: 10.1121/1.384779.
- [38] P. Cobo and F. Simón. Multiple-layer microperforated panels as sound absorbers in buildings: A review. *Buildings Journal*, 53(9), 2019. doi: 10.3390/buildings9020053.
- [39] A. Corsini and F. Rispoli. Using sweep to extend the stall-free operational range in axial fan rotors. *Proceedings of the Institution of Mechanical Engineers, Part A: Journal of Power and Energy*, 218:129–139, 2004. doi: 10.1243/095765004323049869.
- [40] A. Cortis, D. M. J. Smeulders, J.-L. Guermont, and D. Lafarge. Influence of pore roughness on high-frequency permeability. *Physics of Fluids*, 15(6):1766–1775, 2003. doi: 10.1063/1.1571545.
- [41] T. J. Cox and P. D’Antonio. *Acoustic Absorbers and Diffusers - Theory, Design and Application*. CRC Press, 2017. ISBN 0978-1-4987-4099-9.
- [42] M. J. Crocker. *Handbook of Noise and Vibration Control*. Wiley & Sons Inc., 2007. ISBN 978-0-471-39599-7.
- [43] A. Cummings. Impedance tube measurements on porous media: The effects of air-gaps around the sample. *Journal of Sound and Vibration*, 151(1):63–75, 1991.
- [44] N. Curle. The influence of solid boundaries upon aerodynamic sound. *Proceedings of the Royal Society of London. Series A, Mathematical, Physical and Engineering*, 231 (1187):505–514, 1955. doi: 10.1098/rspa.1955.0191.
- [45] F. Czwielong, F. Krömer, and S. Becker. Experimental investigations of the sound emission of axial fans under the influence of suction-side heat exchangers. In *25th AIAA/CEAS Aeroacoustics Conference*, volume AIAA 2019-2618 Session: Acoustic/Fluid Dynamics Interactions X, 2019. doi: 10.2514/6.2019-2618.
- [46] F. Czwielong, S. Floss, S. Becker, and M. Kaltenbacher. Influence of a micro-perforated duct absorber on sound emission and performance of axial fans. *Applied Acoustics*, 174 (-):107746, 2021. doi: 10.1016/j.apacoust.2020.107746.
- [47] S. R. De Groot and P. Mazur. *Non-Equilibrium Thermodynamics*. Dover Publications Inc. New York, 1984. ISBN 978-0486647418.
- [48] H. Denayer, V. Korchagin, W. De Roeck, and W. Desmet. Multi-port characterization of a modal filter containing micro-perforated panels. *22th AIAA/CEAS Aeroacoustic Conference*, volume AIAA 2016, 2016. doi: 10.2514/6.2016-2850.

- [49] B. Dong, D. Xie, F. He, and L. Huang. Noise attenuation and performance study of a small-sized contra-rotating fan with microperforated casing treatments. *Mechanical Systems and Signal Processing*, 147:107086, 2021. doi: 10.1016/j.ymssp.2020.107086.
- [50] F. Durst. *Fluid Mechanics*. Springer-Verlag Berlin Heidelberg, 2008. ISBN 978-3-540-71342-5.
- [51] EEA. *Noise in Europe 2014*. -, EEA Report No 10/2014: Copenhagen, 2014.
- [52] EN ISO 5136. *Acoustics – Determination of sound power radiated into a duct by fans and other air-moving devices – In-duct method*. -, Beuth Verlag Berlin, 2009.
- [53] J. E. Ffowcs Williams. The acoustics of turbulence near sound absorbent liners. *Journal of Fluid Mechanics*, 51(4):737–749, 1972. doi: 10.1017/S0022112072001338.
- [54] J. E. Ffowcs Williams and D. L. Hawkings. Sound generation by turbulence and surfaces in arbitrary motion. *Philosophical Transactions of the Royal Society of London. Series A, Mathematical and Physical Sciences*, 264(1151):321–342, 1969. doi: 10.1098/rsta.1969.0031.
- [55] Z. Florian, H. Gert, and B. Stefan. Acoustic characterization of forward-and backward-skewed axial fans under increased inflow turbulence. *AIAA Journal*, pages 1241–1250, 2017. doi: <https://doi.org/10.2514/1.J055383>.
- [56] S. Floss, M. Kaltenbacher, and G. Karlowatz. Application and simulation of micro-perforated panels in HVAC systems. In *Conference: 10th International Styrian Noise, Vibration & Harshness Congress: The European Automotive Noise Conference*, June 2019. doi: 10.4271/2018-01-1514.
- [57] S. Floss, F. Czwielong, M. Kaltenbacher, and S. Becker. Design of an in-duct micro-perfoated panel absorber for axial fan noise attenuation. *Acta Acustica*, 24(5):–, 2021. doi: 10.1051/aacus/2021015.
- [58] T. Geyer, E. Sarradj, and C. Fritzsche. Measurement of the noise generation at the trailing edge of porous airfoils. *Experiments in fluids*, 48(2):291–308, 2010. doi: 10.1007/s00348-009-0739-x.
- [59] T. F. Geyer and E. Sarradj. Self noise reduction and aerodynamics of airfoils with porous trailing edges. *Acoustics*, 1(2):393–409, 2019. doi: 10.3390/acoustics1020022.
- [60] S. Glegg and W. Devenport. *Aeroacoustics of Low Mach Number Flows*. Elsevier Academic Press, London, 2017. ISBN 978-0-12-809651-2.
- [61] X. Gloerfelt. *Cavity Noise*. Lecture notes, Arts et Métiers ParisTech, France, 2007.

- [62] X. Gloerfelt, F. Pérot, C. Bailly, and D. Juvé. Flow-induced cylinder noise formulated as a diffraction problem for low mach numbers. *Journal of Sound and Vibration*, 287: 129–151, 2005. doi: 10.1016/j.jsv.2004.10.047.
- [63] L. Goines and L. Hagler. Noise pollution: A modern plague. *Southern Medical Journal*, 100:287–294, 2007. doi: 10.1097/SMJ.0b013e3180318be5.
- [64] D.-E. Goldenberg. *Genetic algorithms in search, optimization and machine learning*. Addison Wesley, Reading: MA, 1989.
- [65] M. Goldstein. Unified approach to aerodynamic sound generation in the presence of solid boundaries. *Acoustical Society of America*, 56(2):497–509, 1974. doi: 10.1121/1.1903283.
- [66] J. Golliard. *Noise of Helmholtz-resonator like cavities excited by a low Mach-number turbulent flow*. doctoralthesis, University of Poitiers, 2002.
- [67] S. Gombots. *Acoustic source localization at low frequencies using microphone arrays*. doctoralthesis, TU Wien, 2020.
- [68] M. Goody. Empirical spectral model of surface pressure fluctuations. *AIAA Journal*, 42(9), 2004. doi: 10.2514/1.9433.
- [69] R. E. Graves and B. M. Argrow. Bulk viscosity: Past to present. *Journal of Thermophysics and Heat Transfer*, 13(3):337–342, 1999. doi: 10.2514/2.6443.
- [70] E. A. Guggenheim. *Thermodynamics - An Advanced Treatment for Chemists and Physicists*. Elsevier Science Publishers, 1967. ISBN 978-0444869517.
- [71] D. B. Hanson. Spectrum of rotor noise caused by atmospheric turbulence. *The Journal of the Acoustical Society of America*, 56(1):110–126, 1974. doi: 10.1121/1.1903241.
- [72] G. Herold, F. Zenger, and E. Sarradj. Influence of blade skew on axial fan component noise. *International Journal of Aeroacoustics*, 16(4-5):418–430, 2017. doi: 10.1177/1475472X17718740.
- [73] J.-H. Holland. *Adaption in natural and artificial systems; an introductory analysis with applications to biology, control and artificial intelligence*. MIT Press, 1992.
- [74] K. V. Horoshenkov. A review of acoustical methods for porous material characterisation. *International Journal of Acoustics and Vibration*, 22(1), 2017. doi: 10.20855/ijav.2017.22.1455.
- [75] K. V. Horoshenkov and et al. Reproducibility experiments on measuring acoustical properties of rigid-frame porous media (round-robin tests). *International Journal of Acoustics and Vibration*, 122(1), 2007. doi: 10.1121/1.2739806.

- [76] M. S. Howe. The damping of sound by wall turbulent shear layers. *Journal of the Acoustical Society of America*, 98:1723–1730, 1995. doi: 10.1121/1.414408.
- [77] M. S. Howe. *Acoustics of Fluid-Structure Interactions*. Cambridge University Press, Cambridge, 1998. ISBN 0-521-63320-6.
- [78] A. K. M. Hussain and W. C. Reynolds. The mechanics of an organized wave in turbulent shear flow. *Journal of Fluid Mechanics*, 41(2):241–258, 1970. doi: 10.1017/S0022112070000605.
- [79] K. U. Ingard and H. Ising. Acoustic nonlinearity of an orifice. *Journal of the Acoustical Society of America*, 42(1), 1967. doi: 10.1121/1.1910576.
- [80] L. Jaouen and F.-X. Bécot. Acoustical characterization of perforated facings. *Journal of the Acoustical Society of America*, 129(3):1400–1406, 2011. doi: 10.1121/1.3552887.
- [81] L. Jaouen and F. Chevillotte. Length correction of 2d discontinuities or perforations at large wavelengths and for linear acoustics. *Acta Acustica united with Acustica*, 104, 2018. doi: 10.3813/AAA.919166.
- [82] X. Jing, X. Sun, J. Wu, and K. Meng. Effect of grazing flow on the acoustic impedance of an orifice. *38th AIAA/ Aeronautics Conference*, AIAA, 39(8), 2001. doi: 10.2514/2.1498.
- [83] D. L. Johnson, J. Koplik, and R. Dashen. Theory of dynamic permeability and tortuosity in fluid-saturated porous media. *Journal of Fluid Mechanics*, 79:379–402, 1987. doi: 10.1017/S0022112087000727.
- [84] M. G. Jones, W. R. Watson, D. M. Nark, and N. H. Schiller. Optimization of variable-depth liner configurations for increased broadband noise reduction. *22nd AIAA/CEAS Aeroacoustics Conference*, 2016. doi: 10.2514/6.2016-2783.
- [85] C. Junger. *Computational aeroacoustics for the characterization of noise sources in rotating systems*. TU Wien, doctoral thesis, 2019.
- [86] R. Kabral. Optimum sound attenuation in flow ducts based on the exact cremer impedance. *Acta Acustica United with Acustica*, 102:851–860, 2016. doi: 10.3813/AAA.918999.
- [87] M. Kaltenbacher. *Numerical Simulation of Mechatronic Sensors and Actuators - Finite Elements for Computational Multiphysics*. Springer Berlin, 3 edition, 2015. doi: 10.1007/978-3-642-40170-1.
- [88] M. Kaltenbacher. *Fundamental equations of acoustics, Computational Acoustics*. Springer International Publishing, vol. 579 edition, 2018. doi: 10.1007/978-3-319-59038-7-1.

- [89] M. Kaltenbacher and S. Floss. Nonconforming finite elements based on nitsche-type mortaring for inhomogenous wave equation. *J. Theor. Comput. Acoust.*, 26(3): 1850028–1–18, 2018. doi: 10.1142/S2591728518500287.
- [90] F. Kameier and W. Neise. Experimental study of tip clearance losses and noise in axial turbomachines and their reduction. *Journal of Turbomachinery*, Volume 119(3): 229–243, 1997. doi: 10.1115/1.2841145.
- [91] F. Kameier and W. Neise. Rotating blade flow instability as a source of noise in axial turbomachines. *Journal of Sound and Vibration*, 203(5):833–853, 1997. doi: 10.1006/jsvi.1997.0902.
- [92] F. Kameier and W. Neise. Rotating blade flow instability as a source of noise in axial turbomachines. *Journal of Sound and Vibration*, 203:833–853, 1997. doi: 10.1006/jsvi.1997.0902.
- [93] M. Knutsson and M. Åbom. Sound propagation in narrow tubes including effects of viscothermal and turbulent damping with application to charge air coolers. *Journal of Sound and Vibration*, 320:289–321, 2008. doi: 10.1016/j.jsv.2008.07.006.
- [94] S. Knutsson and M. Åbom. The effect of turbulence damping on acoustic wave propagation. *Journal of the Sound and Vibration*, 329:4719–4739, 2010. doi: 10.1016/j.jsv.2010.05.018.
- [95] F. Krömer. *Sound emission of low-pressure axial fans under distorted inflow conditions*. FAU Erlangen, doctoral thesis, 2017. doi: 10.25593/978-3-96147-089-1.
- [96] F. J. Krömer. *Sound emission of low-pressure axial fans under distorted inflow conditions*. doctoralthesis, FAU University Press, 2018.
- [97] F. J. Krömer and S. Becker. Off-design sound emission of low-pressure axial fans under distorted inflow conditions: An experimental study. *Acta Acustica united with Acustica*, Volume 105(1), feb 2019. doi: 10.3813/AAA.919291.
- [98] F. J. Krömer, A. Renz, and S. Becker. Experimental investigation of the sound reduction by leading-edge serrations in axial fans. *AIAA Journal*, 56:1–5, January 2018. doi: 10.2514/1.J056355.
- [99] F. J. Krömer, S. Moreau, and S. Becker. Experimental investigation of the interplay between the sound field and the flow field in skewed low-pressure axial fans. *Journal of Sound and Vibration*, 442:220–236, 2019.
- [100] P. K. Kundu, I. M. Cohen, and D. R. Dowling. *Fluid Mechanics*. Elsevier Academic Press, 2016. ISBN 978-0-12-405935-1.

- [101] D. Lafarge. *Propagation du son dans les matériaux poreux à structure rigide saturés par un fluide viscothermique*. doctoralthesis, L'Université du Maine, 1993.
- [102] D. Lafarge, P. Lemarinier, and J. F. Allard. Dynamic compressibility of air in porous structures at audible frequencies. *Journal of the Acoustical Society of America*, 102(4), 1997. doi: 10.1121/1.419690.
- [103] Z. Laly, N. Atalla, and S. A. Meslioui. Characterization of micro-perforated panel at high sound pressure levels using rigid frame porous models. *Journal of the Acoustical Society of America*, 30:030005, 2017. doi: 10.1121/2.0000599.
- [104] S. Lee. *Application of microperforated elements in axial fan noise control and silencer design*. Purdue University Libraries. Open Access Dissertations. 1308., 2015. online; accessed on 25.04.20; https://docs.lib.purdue.edu/open_access_dissertations/1308.
- [105] Y. Y. Lee, E.-W.-M. Lee, and C. F. Ng. Sound absorption of a finite flexible micro-perforated panel backed by an air cavity. *Journal of Sound and Vibration*, 287:227–243, 2005. doi: 10.1016/j.jsv.2004.11.024.
- [106] R. Lerch, G. M. Sessler, and D. Wolf. *Technische Akustik*. Springer-Verlag Berlin Heidelberg, 2009. doi: 10.1007/978-3-540-49833-9.
- [107] M. J. Lighthill. On sound generated aerodynamically 1: General theory. *Proceedings of the Royal Society of London. Series A, Mathematical, Physical and Engineering*, 211 (1107):564–587, 1952. doi: 10.1098/rspa.1952.0060.
- [108] J. Lin, C. Scalo, and L. Hesselink. Bulk viscosity model for near-equilibrium acoustic wave attenuation, 2017. <https://arxiv.org/abs/1707.05876>.
- [109] J. Liu and D. Herrin. Effect of contamination on acoustic performance of microperforated panels. *SAE Int. J. Passeng. Cars - Mech.Syst.*, 4(2):1156–1161, 2011. doi: 10.4271/2011-01-1627.
- [110] J. Liu, X. Hua, and D. Herrin. Estimation of effective parameters for microperforated panel absorbers and applications. *Applied Acoustics*, 75:86–93, 2013. doi: 10.3397/1/3761043.
- [111] Y. Liu, A. P. Dowling, and H.-C. Shin. Measurement and simulation of surface roughness noise using phased microphone arrays. *Journal of Sound and Vibration*, 314(1-2): 95–112, 2008. doi: 10.1016/j.jsv.2007.12.041.
- [112] D. Y. Maa. Theory and design of microperforated panel sound absorbing constructions. *Scientia Sinica*, 18:55–71, 1975. doi: 10.1360/ya1975-18-1-55.
- [113] D. Y. Maa. Potential of microperforated panel absorber. *Journal of the Acoustical Society of America*, 104:2861–2866, 1998. doi: 10.1121/1.423870.

- [114] Matelys. APMR, 2021. Online; accessed 23-September-2021; <https://apmr.matelys.com/PropagationModels/MotionlessSkeleton/JohnsonCham-pouxAllardPrideLafargeModel.html>.
- [115] Mathworks. Matlab optimization toolbox, 2020. Online; accessed 25-December-2020; <https://www.mathworks.com/discovery/genetic-algorithm.html>.
- [116] P. Mayer. *Investigation of flow stabilization in inlets of turbocharger compressors*. TU Wien, bachelor thesis, 2020.
- [117] F. Mechel. *Formulas of Acoustics*. Springer International Publishing, second edition edition, 2008. ISBN 978-3-540-76832-6.
- [118] T. H. Melling. The acoustic impedance of perforates at medium and high sound pressure levels. *Journal of Sound and Vibration*, 29(1):1–65, 1973. doi: 10.1016/S0022-460X(73)80125-7.
- [119] Y. Miki. Acoustic properties of porous materials - modifications of delany-bazley. *Journal of the Acoustical Society of Japan*, 11(1):19–42, 1990. doi: 10.1250/ast.11.19.
- [120] R. Minniti, III, W. Blake, and T. Mueller. Determination of inflow distortions by interpreting aeroacoustic response of a propeller fan. In *4th AIAA/CEAS Aeroacoustics Conference*, page 2286, 1998. doi: 10.2514/6.1998-2286.
- [121] M. J. Moran and H. N. Shapiro. *Fundamentals of Engineering Thermodynamics*. John Wiley & Sons Inc., 2006. ISBN 978-0-470-03037-0.
- [122] P. M. Morse and K.-U. Ingard. *Theoretical Acoustics*. McGraw-Hill Book Company, New York, 1968. ISBN 978-0691024011.
- [123] M. Möser and G. Müller. *Handbook of Engineering Acoustics*. Springer-Verlag Berlin Heidelberg, 2013. doi: 10.1007/978-3-540-69460-1.
- [124] W. Neise and U. Michel. Aerodynamic noise of turbomachines. *Deutsche Forschungsanstalt für Luft-und Raumfahrt, eV, DLR, Institut für Strömungsmechanik, Abt. Turbulenzforschung, Berlin*, 5, 1994. doi: 10.13140/2.1.3408.9760.
- [125] P. A. Nelson. Noise generated by flow over perforated liners. *Journal of Sound and Vibration*, 83:11–26, 1982. doi: 10.1016/S0022-460X(82)80072-2.
- [126] X. Olny and R. Panneton. Acoustical determination of the parameters governing thermal dissipation in porous media. *Journal of the Acoustical Society of America*, 123(2), 2008. doi: 10.1121/1.2828066.

- [127] A. J. Otaru. Review on the acoustical properties and characterisation methods of sound absorbing porous structures: A focus on microcellular structures made by a replication casting method. *Metals and Materials International*, (26):915–932, 2019. doi: 10.1007/s12540-019-00512-y.
- [128] R. Panneton and X. Olny. Acoustical determination of the parameters governing viscous dissipation in porous media. *Journal of the Acoustical Society of America*, 119(4), 2006. doi: 10.1121/1.2169923.
- [129] R. L. Panton. *Incompressible Flow*. John Wiley & Sons Inc., 2013. ISBN 978-1-118-01343-4.
- [130] C. Pfeleiderer. *Strömungsmaschinen*. Springer-Verlag, 2013. ISBN 978-3-540-22173-9. doi: 10.1007/b138287.
- [131] A. D. Pierce. *Acoustics - An Introduction to Its Physical Principles and Applications*. McGraw-Hill Inc., London, 1980. ISBN 978-3-030-11213-4.
- [132] D. Pilon and R. Panneton. Behavioral criterion quantifying the effects of circumferential air gaps on porous materials in the standing wave tube. *Journal of the Acoustical Society of America*, 116(1), 2004. doi: 10.1121/1.1756611.
- [133] S. R. Pride, F. D. Morgan, and A. F. Gangi. Drag forces of porous-medium acoustics. *Physical Review B - covering condensed matter and materials physics*, 47(9), 1993. doi: 10.1103/PhysRevB.47.4964.
- [134] R. T. Randeberg. *Perforated Panel Absorbers with Viscous Energy Dissipation Enhanced by Orifice Design*. doctoralthesis, Norwegian University of Science and Technology, 2000.
- [135] S. N. Reschevkin, O. M. Blunn, and P. E. Doak. *A Course of Lectures on The Theory of Sound*. A Pergamon Press Book, New York, 1963.
- [136] S. W. Rienstra. *Fundamentals of Duct Acoustics*. Lecture Notes, Technical University Eindhoven, 2015.
- [137] R. Roncen, Z. E. A. Fellah, D. Lafarge, F. Simon, E. Ogam, M. Fellah, and D. Depollier. Acoustical modeling and bayesian inference for rigid porous media in the low-mid frequency regime. *Journal of the Acoustical Society of America*, 144(6), 2018. doi: 10.1121/1.5080561.
- [138] D. Ronneberger and C. D. Ahrens. Modelling of perforated plates and screens using rigid frame porous models. *Journal of Fluid Mechanics*, 83(3):433–464, 1977. doi: 10.1017/S0022112077001281.

- [139] T. Rossing. *Handbook of Acoustics*. Springer Berlin, 1 edition, 2007. doi: 10.1007/978-0-387-30425-0.
- [140] S. Sack, M. Åbom, and G. Efraimsson. On acoustic multi-port characterisation including higher order modes. *J. Vib. Acoust.*, 102(5):834–850, 2016. doi: 10.3813/AAA.918998.
- [141] S. Sacks and M. Åbom. Modal filters for mitigation of in-duct sound. *Acoustical Society of America*, 29(-), 2016. doi: 10.1121/2.0000473.
- [142] M. Sadouki and M. Fellah. Measuring static thermal permeability and inertial factor of rigid porous materials. *Journal of the Acoustical Society of America*, 130(5):2627–2630, 2011. doi: 10.1121/1.3641402.
- [143] H. Schlichting and K. Gersten. *Boundary-Layer Theory*. Springer, 8th edition, 2000. doi: 10.1007/978-3-642-85829-1.
- [144] A. Schulz. *Die akustischen Randbedingungen perforierter Wandauskleidungen in Strömungskanälen – Physikalische Modelle und Eduktion*. doctoralthesis, Technischen Universität Berlin, Fakultät V – Verkehrs- und Maschinensysteme, 2018.
- [145] B. H. Song and J. S. Bolton. A transfer-matrix approach for estimating the characteristic impedance and wave numbers of limp and rigid porous materials. *Journal of the Acoustical Society of America*, 107(1131), 2000. doi: 10.1121/1.428404.
- [146] L. Stein and J. Sesterhenn. An acoustic model of a helmholtz resonator under a grazing turbulent boundary layer. *Acta Mech*, 230:2013–2029, 2019. doi: 10.1007/s00707-018-2354-5.
- [147] D. Takahashi and M. Tanaka. Flexural vibration of perforated plates and porous elastic materials under acoustic loading. *Journal of the Acoustical Society of America*, 112(4): 1456–1464, 2002. doi: 10.1121/1.1497624.
- [148] G. I. Taylor. The Spectrum of Turbulence. *Proceedings of the Royal Society of London Series A*, 164(919):476–490, Feb. 1938. doi: 10.1098/rspa.1938.0032.
- [149] P. A. Thompson. *Compressible-Fluid Dynamics*. McGraw-Hill Inc, 1988. ISBN 978-0070644052.
- [150] H. Tijdeman. On the propagation of sound waves in cylindrical tubes. *Journal of Sound and Vibration*, 39(1):1–33, 1975. doi: 10.1121/1.1911130.
- [151] M. Toyoda, R. L. Mu, and D. Takahashi. Relationship between helmholtz-resonance absorption and panel-type absorption in finite flexible micro-perforated panel absorbers. *Applied Acoustics*, 71(4):315–320, 2009. doi: 10.1016/j.apacoust.2009.10.007.

- [152] C. Y. Tsui and G. Flandro. Self-induced sound generation by flow over perforated duct liners. *Journal of Sound and Vibration*, 50(3):315–331, 1977. doi: 10.1016/0022-460X(77)90486-2.
- [153] J. M. Tyler and T. G. Sofrin. Axial flow compressor noise studies. In *Pre-1964 SAE Technical Papers*. SAE International, jan 1962. doi: 10.4271/620532.
- [154] Z. B. Wang, Y. Chiang, Y. S. Choy, and Q. Xi. Noise control for a dipole sound source using micro-perforated panel housing integrated with a herschel–quincke tube. *Applied Acoustics*, 148:202–211, 2019. doi: 10.1063/1.1423934#.
- [155] C. Weng. *Modeling od sound-turbulence interaction in low-Mach-number duct flows*. doctoralthesis, KTH The Marcus Wallenberg Laboratory for Sound and Vibration Research, 2015.
- [156] WHO. *Burden of disease from environmental noise – Quantification of healthy life years lost in Europe. 2011, The WHO European Center for Environment and Health*. Bonn Office, WHO Regional Office for Europe: Copenhagen, 2010. ISBN 978-92-890-0229-5.
- [157] WHO. *Environmental Noise Guidelines for the European Region*. -, WHO Regional Office for Europe: Copenhagen, 2018. ISBN 978-92-890-5356-3.
- [158] D. K. Wilson. Relaxation-matched modeling of propagation through porous media, including fractal pore structure. *Journal of the Acoustical Society of America*, 94(2), 1993. doi: 10.1121/1.406961.
- [159] D. K. Wilson. Simple, relaxational models for the acoustical properties of porous media. *Applied Acoustics*, 50(3):171–188, 1997.
- [160] S. Wright. The acoustic spectrum of axial flow machines. *Journal of Sound and Vibration*, 45(2):165–223, 1976.
- [161] T. Wright and W. Simmons. Blade sweep for low-speed axial fans. *Journal of Turbomachinery*, 1990. doi: 10.1115/1.2927413.
- [162] T. W. Wu, P. Zhang, and C. Y. R. Cheng. Boundary element analysis of mufflers with an improved method for deriving the four-pole parameters. *Journal of Sound and Vibration*, 217:767–779, 1998. doi: 10.1006/jsvi.1998.1800.
- [163] Q. Xi, Y. S. Choy, L. Cheng, and S. K. Tang. Noise control of dipole source by using micro-perforated panel housing. *Journal of Sound and Vibration*, 362:39–55, 2016. doi: 10.1016/j.jsv.2015.09.047.
- [164] Z. Xiaoqi and C. Li. Acoustic impedance of micro-perforated panels in a grazing flow. *Acoustical Society of America*, 145:2461, 2019. doi: 10.1121/1.5098785.

- [165] Z. Xiaoqi and C. Li. Acoustic silencing in a flow duct with micro-perforated panel liners. *Applied Acoustics*, 167, 2019. doi: 10.1016/j.apacoust.2020.107382.
- [166] L. Yang, H. Ouyang, and Z.-h. Du. Experimental research on aerodynamic performance and exit flow field of low pressure axial flow fan with circumferential skewed blades. *Journal of Hydrodynamics, Ser. B*, 19(5):579–586, 2007. doi: 10.1016/S1001-6058(07)60156-5.
- [167] F. J. Zenger, A. Renz, M. Becher, and S. Becker. Experimental investigation of the noise emission of axial fans under distorted inflow conditions. *Journal of Sound and Vibration*, 383:124–145, 2016. doi: <https://doi.org/10.1016/j.jsv.2016.07.035>.
- [168] Q. Zhang and D. J. Bodony. Direct numerical investigation of acoustic liners with single and multiple orifices grazed by a mach 0.5 boundary layer. *46th AIAA/ Fluid Dynamics Conference , AIAA 2016-3626*, 2016. doi: 10.2514/6.2016-3626.
- [169] T. G. Zieliński. Normalized inverse characterization of sound absorbing rigid porous media. *Journal of the Acoustical Society of America*, 137(6), 2015. doi: 10.1121/1.4919806.
- [170] T. G. Zieliński, F. Chevillotte, and E. Deckers. Sound absorption of plates with micro-slits backed with air cavities: Analytical estimations, numerical calculations and experimental validations. *Journal of Applied Acoustics*, 146, 2018. doi: 10.1016/j.apacoust.2018.11.026.

Curriculum Vitae

Personal Data

Name: Sebastian Floß
Date of Birth: October 20, 1984
Place of Birth: Munich, Germany

Education

10/2010 – 11/2014 Bsc. Mechanical Engineering
TU Wien
Vienna, Austria
11/2014 – 04/2017 Msc. Mechanical Engineering
TU Wien
Vienna, Austria
04/2017 – 01/2022 Doctor of Technical Sciences
TU Wien
Vienna, Austria

Professional Experiences

05/2016 – 02/2022 Research and Teaching, and Project Assistant, Institute of
Mechanics and Mechatronics, Research Group of Technical
Acoustics, TU Wien, Austria